TYCO

C 1.

TYCO LABORATORIES, INC., BEAR HILL, WALTHAM, MASSACHUSETTS 02154 TELEPHONE 617 [illegible]

Development of Cathodic Electrocatalysts for Use in Low Temperature H_2/O_2 Fuel Cells with an Alkaline Electrolyte

Contract No. NASW-1233

Q-4

Fourth Quarterly Report
Covering July 1, 1965
Through June 30, 1966

for

National Aeronautics and Space Administration
Headquarters, Washington, D. C.

NOTICE

This report was prepared as an account of Government sponsored work. Neither the United States, nor the National Aeronautics and Space Administration (NASA), nor any person acting on behalf of NASA:

A) Makes any warranty or representation, expressed or implied, with respect to the accuracy, completeness, or usefulness of the information contained in this report, or that the use of any information, apparatus, method, or process disclosed in this report may not infringe privately owned rights; or

B) Assumes any liabilities with respect to the use of, or for damages resulting from the use of any information, apparatus, method or process disclosed in this report.

As used above, "person acting on behalf of NASA" includes any employee or contractor of NASA, or employee of such contractor, to the extent that such employee or contractor of NASA, or employee of such contractor prepared, disseminates, or provides access to, any information pursuant to his employment or contract with NASA or his employment with such contractor.

Requests for copies of this report should be referred to:

National Aeronautics and Space Administration
Office of Scientific and Technical Information
Attn: AFSS-A
Washington, D. C. 20546

DEVELOPMENT OF CATHODIC ELECTROCATALYSTS FOR USE IN LOW TEMPERATURE H_2/O_2 FUEL CELLS WITH AN ALKALINE ELECTROLYTE

Contract No. NASW-1233

Q-4

Fourth Quarterly Report

Covering July 1, 1965

Through June 30, 1966

for

National Aeronautics and Space Administration

Headquarters, Washington, D. C.

DEVELOPMENT OF CATHODIC ELECTROCATALYSTS FOR USE IN LOW TEMPERATURE H_2/O_2 FUEL CELLS WITH AN ALKALINE ELECTROLYTE

CONTRACT OBJECTIVES

The research under contract NASW-1233 is directed towards the development of an improved oxygen electrode for use in alkaline H_2/O_2 fuel cells. The work is being carried out for the National Aeronautics and Space Administration, with Mr. E. Cohn as technical monitor. Principal investigators are R. J. Jasinski, J. Giner and A. C. Makrides.

CONTENTS

This report summarizes the work carried out under this contract between June 16, 1965, and July 1, 1966. It contains all information given previously in quarterly reports 1 through 3, in addition to data obtained in the fourth quarter of this program.

CONTENTS

LIST OF TABLES

LIST OF TABLES (Cont.)

I. SUMMARY AND CONCLUSIONS

The development of an improved oxygen electrode for use in alkaline H_2/O_2 fuel cells involves first a study of the intrinsic activity of new materials and then the optimization of the structure of oxygen electrodes made from promising materials. In the first phase of this program, transition metal alloys, intermetallic compounds, and transition metal carbides, nitrides, borides, and silicides were surveyed for intrinsic activity in catalyzing the electrochemical reduction of oxygen. Measurements were taken on rotating disc electrodes operated at 75°C in 2N KOH saturated with oxygen. The results are summarized below.

A. The Elements

The first phase of the oxygen electrocatalyst screening program was a survey of the metals of Groups IV B, V B, VI B, VII B (except Tc), VIII B, and I B, over the potential range of + 1200 to 0 mv (vs. RHE). The compatability of these materials with 2N KOH at 75°C was determined, as well as their activity for catalyzing the cathodic reduction of oxygen. These experiments defined a set of reference curves for describing the activity of transition metal alloys and compounds and also established the relative activities of some metals (e.g. Os, Re) for which only a minimal literature exists.

The activity for complete reduction of O_2 to OH^- was essentially as reported in the literature, i.e. Pt > Pd > Au ~ Ag > Mn > C. Of the remaining elements Fe, Re, Ir, and Rh were active below + 675 mv; Ni, Ti, and Cu were active below + 360 mv on the DHE scale*. Osmium showed a cathodic current at a potential more positive than platinum by 75 mv. However, the reaction is apparently incomplete in this potential region and HO_2^- is probably a stable intermediate. Complications are also introduced by a small but detectable corrosion of osmium to a soluble ion.

---

* DHE scale - Dynamic Hydrogen Electrode is about - 30 mv in Reversible Hydrogen Scale.

Metals most active for oxygen reduction are generally those the surface oxides of which are easily reduced. The principal exception is manganese: a substantial O_2 reduction current was observed on MnO_2 at about + 900 mv.

B. Alloys and Intermetallic Compounds of Transition Metals

The materials examined were alloys of transition metals. They are discussed under five groupings, alloys of (1) platinum, (2) palladium-silver, (3) nickel, (4) Ti, Zr, Hf, and (5) Ta.

1. Platinum Alloys

Alloys of platinum with base metals were generally less active than platinum, although a number of alloys equalled platinum in activity, e.g. Pt_2Ta and PtMn.

Alloys of platinum with metals that corroded in the pure state often developed a roughened or etched surface. However, the extent of corrosion was far less than for the pure, base metal. For example, Pt_2Nb corroded at a substantially smaller rate than Nb; similarly, Pt_3Co did not form the surface oxides found with pure cobalt. Alloys showing corrosion (e.g. PtNb) may show a high apparent activity because of surface roughening.

2. Palladium-Silver Alloys

A series of palladium-silver alloys (70% to 10% silver) was studied. Little corrosion was observed, as expected. The alloys generally showed an initial potential for O_2 reduction less than that of pure palladium. Perhaps the most significant finding in this series of experiments was that the $E_{\frac{1}{2}}$ values (the potential at half the diffusion-limited current) were approximately 100 mv more positive for the alloys than for pure silver.

3. Nickel Alloys

Of the nickel-based metal alloys studied, only those with manganese and cobalt were significantly active for the reduction of O_2. In the former system the activity is associated with manganese. The activity of $NiCo_2$ is probably due to the formation of a surface layer of nickel-cobalt spinel. The activity is enhanced by holding the starting potential above + 1200 mv, where Co^{+3} is formed. Apparently Co^{+3} is

reduced to Co^{+2} below +750 mv and the activity noted above this potential disappears below +750 mv. Returning the electrode to high potentials restores its performance. This effect was not observed for pure cobalt.

One of the more interesting characteristics of nickel alloys is the effectiveness of nickel in suppressing corrosion of the alloyed constituents. These effects were observed for alloys of at least 50 wt % nickel and either Mn, Co, Al, Nb, or Mo.

4. Titanium, Zirconium, and Hafnium Alloys

The corrosion behavior of these alloys was similar to that of nickel. No pronounced enhancement of O_2 activity was noted for alloys containing base metals. In fact, the small amount of activity associated with nickel was inhibited in Zr_2Ni and suppressed in $TiNi_3$.

The activity of $TiPt_3$ was less than that of platinum, while Ti_3Au was more active for the reduction of O_2 than gold, being comparable to platinum. The surface area of Ti_3Au increased with time, apparently yielding a surface with a higher Ti/Au ratio than the bulk material. In spite of the higher surface concentration of nonnoble metal, activity of the sample also increased. $ZrAu_3$, richer in gold than is Ti_3Au, showed a lower activity than gold itself and a stable surface.

5. Tantalum Alloys

The performance of alloys of tantalum showed very little interaction between the metals; i. e. the corrosion and O_2 activity were approximately that expected from a mixture of the pure metals. $TaPt_2$ and $TaPd_3$ are essentially as active as platinum and palladium, respectively.

C. Carbides, Nitrides, Borides, and Silicides of Transition Metals

1. Carbides and Nitrides

There were no systematic trends in corrosion behavior. The corrosion of VC, VN, NbC, and TiN was lower than that of the metals, while Cr_3C_2, TiC, and TaC were more prone to oxidation than the parent metals.

The carbides were all more active than the parent metal for oxygen reduction. Even if the metal itself were inert (e.g. Zr, Hf, Ta, Cr) its carbide showed some activity for oxygen reduction. Except for the titanium compounds, the nitrides were less active than the carbides.

The highest activities were observed for TiN, VC, Fe_2C, and Ni_3C. Of these the most active carbide was Ni_3C, although its performance is still approximately 100 - 200 mv lower than platinum. It is not clear whether this high activity is an inherent property of the material or whether it is due to a high surface area.

2. Borides and Silicides

Corrosion currents were generally observed for the borides and silicides of the refractory metals. Of interest are the high corrosion rates for the borides and silicides of metals which themselves are inert in 2N KOH, e.g. Zr, Hf, and Ta. The three group VIII borides studied (Ni_2B, Ni_3B, and Pt_2B) were relatively resistant to corrosion. The measurements of O_2 activity indicated no enhancement due to the presence of boron.

D. Dispersed Materials

Replicate runs on commercial electrodes have demonstrated that the "floating electrode" test system yields reproducible results for testing O_2 electrodes, and its performance is equivalent to that obtained in working fuel systems.

Electrodes prepared from coprecipitated Pt-Au alloys are essentially equal in performance to the platinum black electrodes prepared in a similar manner and are superior to palladium-gold electrodes. Silver electrodes of comparable activity were also prepared.

The electrodes prepared from the iron carbides were less active, partly because of an abnormally high ohmic drop. Ni_3C was more active than Ni_3N, sustaining 185 ma/cm^2 at + 700 mv, and both are orders of magnitude more active than pure Ni.

II. INTRODUCTION

The intrinsic factor which determines the reactivity of an oxygen electrode is its atomic composition and the subordinate crystal structure. The composition ultimately determines both the desirable properties (viz. electrocatalytic activity for reduction of oxygen) and the undesirable properties (viz. corrosion or other time-dependent failure mechanisms which limit the efficiency or life of the electrode). The electrode activity may be an inherent characteristic of the pure electrode surface, or it may be conditioned by reactions with the electrolyte, e.g. through specific adsorption of ions. Selection of appropriate electrolytes (e.g. KOH) can eliminate undesirable effects of the solution or, at any rate, reduce them to a minimum.

The selection of alloys for experimental investigation as electrocatalysts for oxygen reduction must be carried out in a systematic way. Random selection is a questionable procedure, since the number of possible systems is extremely large. For example, even if one restricts the choice to about 30 transition metals which are generally good catalysts, there are about 400 binary systems, 4,000 ternary systems, 28,000 quaternary systems, and so on, for a total of about a hundred million systems. If we consider that in addition there are distinct intermetallics and that even solid solutions of different concentration may have qualitatively different properties, it is clear that in the forseeable future we can study only a tiny fraction of the possible compositions.

Previous work on catalysis has been treated within a theoretical framework based on a consideration of two extreme points of view concerning the source of surface activity. According to one view (which can be called the "atomic approach") the reactivity is determined by the intrinsic chemical properties of the individual surface atoms and is only slightly influenced by the neighboring atoms in the crystal bulk. The other extreme view (which can be called the "continuum approach") is that reactivity is determined primarily by the electronic energy states of the material as a

whole, with the specific atomic chemistry being secondary. This approach has been used extensively to interpret chemisorption and catalysis on transition metal alloys where the surface activity has been correlated with d-band occupancy.

The oxygen reaction is admittedly a more complex process, the mechanism of which (i. e. the precise sequence and relative rates of the various elementary steps) still remains unresolved[1]. However, there is ample evidence for the existence of a special kind of oxygen-metal interaction during the electrolytic reduction of oxygen, even if knowledge of the precise nature of this interaction is scanty.

There is also little doubt that the disruption of the oxygen-to-oxygen bond is the slowest step in the over-all process and that hydrogen peroxide appears as an intermediate or by-product during reduction in alkaline solutions[2]. Without going into the details of the reaction, we can thus safely assume that (a) electronic factors play an important role in the kinetics and (b) geometric factors are probably also involved in the catalytic breaking of the oxygen bond.

Catalysts were selected with both the "continuum" and "atomic" approaches in mind. Alloys of noble metals (Pt, Au) which are good catalysts for O_2 reduction with base metals were investigated, as well as alloys containing only base metals. The materials examined encompass a variety of crystal types; a partial listing is given in Table I. A series of essentially stoichiometric carbides, nitrides, silicides and borides were also studied and can be considered within this "continuum vs. atomic" framework. The validity of the continuum approach to the electrocatalysis of oxygen reaction would be established by alterations of the noble metal activity through alloy formation and/or by the development of high activity through alloying of low activity base metals.

The results of this survey program are presented in four parts. Part I summarizes the performance of most of the transition metals; part 2 is concerned with alloys and intermetallics; part 3 deals with carbides, nitrides, borides, and silicides of the transition metals; and part 4 is devoted to results obtained with dispersed electrodes.

III. EXPERIMENTAL

A convenient method of testing a material for corrosion resistance and catalytic activity was to use it as a solid ingot. As such, it could be mounted in an alkali resistant resin and tested potentiostatically as a rotating disc electrode run consecutively in N_2- and O_2- saturated KOH-solution.

By potentiostatic measurement of the corrosion current under an inert atmosphere, it was possible to measure the corrosion rate over the whole potential region relevant to an oxygen electrode.

The advantages of this method are that the samples can be prepared with relative ease and have well-defined surfaces. They could therefore be tested unequivocally for corrosion and for O_2-activity under well-defined transport conditions (Levich equation). The main disadvantage of the method is the sensitivity of the electrode, with its low roughness factor, to poisoning by impurities. This disadvantage is minimized by the high electrode potential at which O_2 is reduced and by continuous surface renewal due to the small corrosion current present in most cases. The low concentration of surface defects on solid electrodes, in contrast to that on dispersed electrodes, may lead to lower specific activity, but this difference is probably irrelevant in a comparative study of the relative activity of a series of materials.

A. Testing of Solid Ingots as Rotating Discs

1. Preparation of the Disc Electrode

Carefully weighed mixtures of pure elements were arc-melted in a furnace with six water-cooled copper heaters (each one-inch in diameter) using a tungsten tip under an argon atmosphere. A Ti getter was fired before each run in order to eliminate traces of O_2. A maximum of six ingots weighing 5 to 10 grams could be obtained in one run.

If the alloy or compound was formed peritectically (i. e. during solidification the composition of the solid phase differs from the composition of the liquid phase), the ingot was annealed, generally overnight, at a

convenient temperature. If the alloy or compound was formed congruently (i.e. the solidifying phase had the same composition as the molten phase), the ingot could be used without any subsequent thermal treatment.

The ingot had a button shape when removed from the furnace and was cut with a boron carbide or chromonel saw in order to expose two parallel flat circular faces. One part of the sawed button was used for metallographic analysis, according to standard procedures.

The part of the button with the two parallel flat circular planes was incorporated as shown in Fig. 1a with "Koldmount," (an acrylic resin (including methylmethacylate monomer) used for metallographic work, which erroded less than 0.05 mg/cm^2 in 2N KOH at 80°C over a period of 80 hrs). This arrangement, besides isolating the electrical contact to the electrode from the electrolyte, also constituted an ideal configuration for controlling precisely mass transport to the electrode.

Electrical contact to the button was made by screwing a metal rod down on a spring-loaded contact in the threaded shaft of the Koldmount. The rod, spring, and contact were gold-plated and the rod was covered with heat shrinkable Teflon tubing (Fig. 1a). The electrode assembly was mounted in a Sargent 600 rpm synchronous motor designed for voltammetry with solid electrodes. Contact between the stirring rod and the fixed lead was made by dipping a wire into a pool of mercury in the hollow top of the rod.

A series of ductile materials was also tested in a demountable assembly described by Stern and Makrides[3] with only Teflon and glass exposed to the solution (Fig. 1b). Ductile materials tested in both electrode assemblies gave basically the same results. This confirms that the acrylic resin used in the rotating disc had no poisoning effect on the results.

2. Test Cell

The cell shown in Fig. 2 was used. In this cell all the frits were eliminated since they dissolve in caustic solution. The lack of a frit between working and counter electrodes did not introduce a significant error, since during the cathodic oxygen reduction (with oxygen

saturated solution) only oxygen was evolved at the counter electrode. The hydrogen evolved at the counter electrode during the corrosion test (N_2-saturated solution) which could dissolve and reach the working electrode was largely swept away by nitrogen and therefore did not contribute significantly to the measured current.

The reference electrode was a Dynamic Hydrogen Electrode (DHE) (X), which under the cell operating condition adopted a potential 30 mv $\pm$ 5 mv negative to the RHE[4].

The temperature of the cell was regulated $\pm$ 0.5°C by a heating mantle and a regulator with a temperature sensor inside the electrolyte. A temperature of 75°C was selected for the experiments.

The electrolyte concentration was set at 2M KOH after preliminary experiments with 35% (8.4 M) KOH. This concentration had a more favorable transport factor (D x C) than 8.3 M KOH solutions used in fuel cells. Since the screening electrolyte was milder, the chances of missing a possible catalyst were reduced.

3. Electrochemical Measurements

i(E)-curves were generated by imposing a linear potential scan on the working electrode by means of a slow linear potential signal to a Wenking potentiostat. The slow function generator was constructed with two standard batteries, two 10 turn, 10 K potentiometers, and a synchronous motor (Insco Corp., Groton, Mass.). The motor has a basic speed of 4 rpm and six gear ratios of 1:1, 2:1, 5:1, 10:1, 20:1, and 50:1. By changing these gear ratios and the peak voltage, scanning rates from 10 mv/min to 800 mv/min could be obtained. For the initial routine screening, a rate of 50 mv/min was selected.

The current-potential curve was recorded directly on an x-y recorder. Current-time curves at constant potential for relatively long times could be recorded on the same recorder by using the slow function generator to feed the y-axis of the recorder.

Before an activity test experiment, the corrosion current under inert gas (N_2) was measured at a series of potentials. This corrosion current had to be measured with stirring in order to subtract it quantitatively from the O_2 reduction current. It was also measured without

stirring in order to apply the results to a practical electrode. Also, the possibility of a decrease of the corrosion rate with time had to be investigated. As long as the corrosion current was small compared with the expected O_2-current, the O_2-curve was run, even if the corrosion rate was higher than useful for a practical cell.

In order to ascertain whether an observed performance represented the intrinsic activity of a material and not a mere increase of the surface area, the real surface area of the electrode had to be estimated. The only practical method of doing this during screening of a large number of flat electrodes was by measuring the double layer capacity of the electrode.

For the capacity measurements a method was selected in which a triangular wave of 50 cycles/sec and a peak-to-peak voltage of 100 mv (i.e. a sweep rate of 10 volts/sec), biased by a convenient dc voltage, was fed to the signal input of the potentiostat. The dc voltage was selected so that Faradaic currents were avoided. If the electrode behaves as a perfect capacitor (no Faradaic or ohmic resistance), the small triangular potential wave is transformed into a square current wave, with a peak-to-peak value which is proportional to the electrode capacity and therefore to the real surface.

Procedure

The following procedure was used for routine screening:

1. N_2 Saturation

A freshly prepared 2M KOH solution was saturated with pure nitrogen for at least 45 minutes. The electrode was kept inside the cell but not exposed to the electrolyte until N_2 saturation was complete.

2. Corrosion i(E) Curve

The electrode was introduced into the solution at a potential of E = 0 mv. The potential scan was initiated within a minute at a rate of 50 mv/min and 600 rpm rotation. The potential scan was reversed between E = 0.8 volt and E = 1.23 volts, depending on the extent of corrosion in this

range. If there was a high corrosion rate at the lower potentials, higher potentials were still investigated since there could be a region of passivation in the potential range of interest.

At several points of the i(E)-curve, stirring was stopped for 1 or 2 minutes without stopping the potential sweep (in order to see the effect of stirring on corrosion).

3. Measurements of the Double Layer Capacity

At several points in the i(E)-curve under N_2 the recording was interrupted and a double layer capacity measurement was made as described above.

The electrode potential was never left uncontrolled in order to control the history of the electrode from the moment it was immersed in solution. If, in addition to the i(E)-curve, the electrode had to be left for some time at a known potential, the time at this potential was kept as short as possible and noted. The electrode was removed from the solution during extended periods of inactivity, and any attached electrolyte was removed by rotating the electrode in the gas phase for a short time (about half a minute).

4. O_2-Saturation

If the corrosion current was within tolerable limits, the test for O_2-activity was carried out. The electrode was removed from the system and repolished, and the solution was saturated with O_2 (at least 45 min).

5. i(E)-Curve for O_2-Reduction

The repolished sample was introduced into the electrolyte at a high, passive potential where possible, but below any current wave (usually between 0. 8 volt and 1. 23 volt), and the i(E)-curve was initiated in the direction of decreasing potentials. At E = 0, the direction of the potential sweep was reversed.

6. Measurements of the double layer capacity in the region of the limiting current were necessary when doubts existed about the real surface increase during recording of the i(E)-curve.

7. After recording the i(E)-curves, a micrograph of the electrode surface was taken and the sample was filed for subsequent study.

8. The data presented in tabular form are corrected to the reversible hydrogen electrode (RHE) in the same electrolyte by subtracting 30 $\pm$ 5 mv from the recorded potentials (DHE).

B. Testing of Finely Divided Catalysts

Some materials showing negligible corrosion and O_2-activity in the previous test or materials which are known from previous experience (including literature) for activity in O_2-reduction were tested as finely divided powders. Specific preparation methods are described below. After preparation, the real surface of the resulting finely divided material was measured using the B. E. T. (krypton) adsorption system.

The electrode was made by mixing the material with a suitable amount of Teflon powder (Teflon - 30), sintering or drying, and bonding to a fine mesh Ni-screen for electrical contact.

The electrode was tested in a "floating electrode"[5] system (Fig. 3). This cell consisted of an electrode ($\sim$ 1 cm^2 area) placed on the surface of the electrolyte over which reactant gas was passed and simulates the operation of a half-cell without the complications of cell construction and operation in a contained electrolyte. The time required for characterization with O_2 was about 1/2 hour, a considerable saving over experimental fuel cell testing.

The body of the cell was a 500 ml resin reaction kettle. The cover supported the working electrode, reference electrode, and gas inlet. The gas exited from the cell through the threads in the level adjust screw. The reference electrode and the working electrode holder were made in one piece so that the capillary tip was always at the same distance from the electrode. With this arrangement, the resistance included in the electrode potential measurement was constant for a given electrolyte and needed to be measured only once. This was a distinct advantage, since otherwise, it is very difficult to adjust the capillary tip for each individual electrode so that a constant iR drop is included in the polarization measurements.

The electrode holder was fitted into the center tube with a screw device which permitted a fine control on the level of the electrode with respect to the electrolyte. It was found that raising or lowering the electrode from a position level with the electrolyte surface by 3 mm made less than 2% change in the current and thus the elevation of the electrode with respect to the solution was not critical.

C. Preparation of Interstitials of the Group VIII Metals

In general, careful control of the temperature and gas composition had to be exerted in preparing these compounds so as to remain in the range of thermodynamic stability. In order to prepare the compounds, three furnace tubes equipped to operate under CO and NH_3 atmospheres were constructed.

1. Iron Carbides and Nitrides

The preparation of a sample of Fe_2C (Hagg carbide) is briefly described below. Four iron carbides have been described in the literature[6-8]: (a) "FeC," (b) the hexagonal iron carbide (Fe_2C or Fe_3C) of controversial formulation, (both discovered in Fischer-Tropsch catalysts), (c) Hagg carbide (Fe_2C), and (d) cementite (Fe_3C). The three last carbides can be obtained separately by treating finely divided iron with CO and regulating the temperature. At temperatures under 170°C, and very long reaction periods hexagonal close packed carbide is obtained; between T = 170°C and 300°C, Hagg carbides are formed; and at temperatures higher than 300°C, cementite is the only carbide found. If hydrogen is used prior to carburization (CO treatment) - or still better, simultaneously with carburization - contamination by oxygen is eliminated. The specific experimental details involved in the preparations together with the results of physical characterization are summarized in Table II.

2. Nickel Carbides and Nitrides

The preparation of nickel nitride has been described in the open literature[9,10]. Apparently it is necessary to maintain a close control over reaction temperature and space velocity to obtain substantial yields of products. Juza and Sachze recommended heating 10-20 mg of nickel for

TABLE II

Preparation of Iron Carbides and Nitrides

Run #	Material Sought	
1	Fe_2C	Pure Fe sponge was carburized with CO at 150° - 275°C for 27 hours. X-ray analysis - iron and iron oxide.
2	Fe_2C	Pure Fe sponge was reduced with H_2 at 325°C for 15 hours and carburized with CO at 170° - 300°C for 30 hours. X-ray analysis - iron, iron oxide, traces of Fe_2C, Fe_3C.
3	Fe_2C	Pure Fe sponge was reduced with hydrogen for 20 hours at 325°C and carburized with CO at 200 - 275°C for 96 hours. X-ray analysis - iron, iron oxide, traces of Fe_2C, Fe_3C.
4	Fe_2C	Pure Fe sponge was reduced with hydrogen at 350°C for 28 hours and carburized with CO at 200 - 250°C for 32 hours. X-ray analysis - Fe_2C - Fe_3C; B. E. T. surface area - 162 m^2/gm.
5	Fe_2C	Pure Fe sponge was reduced with H_2 at 500°C for 28 hours and carburized with CO 200 - 350°C for 56 hours. X-ray analysis - iron, iron oxide, trace Fe_2C, Fe_3C.
6	Fe_3C	Fe_2C - Fe_3C from prep. #4 was heated under N_2 to 475°C for 4 hours. X-ray analysis - Fe_3C, Fe; B. E. T. surface area - 143 m^2/gm.
7	Fe_3C	Iron salt of mellitic acid was decomposed in vacuo at 450°C for 4 hours[13,14]. X-ray analysis - Fe_3C, traces Fe_3O; B. E. T. surface area - 8.4 m^2/gm.

TABLE II (Cont.)

Run #	Material Sought	
9	Fe_2N	Pure Fe sponge was reduced with hydrogen at 300°C for 24 hours and nitrided with NH_3 at 300°C for 7 hours. X-ray analysis - Fe, oxides, Fe_4N, Fe_3N.
10	Fe_3N	Pure Fe sponge was reduced with H_2 at 450°C for 24 hours and nitrided with NH_3 at 950°C for 48 hours. X-ray analysis - Fe_3N.

---

3 hours at 445°C $\pm$ 2° in an ammonia stream flowing at 22 cc/sec. The preparation is cooled under NH_3. The material is then carefully ground and treated again for 2 hours under the same conditions. The preparation is reported to have the theoretical composition (7.37% N). It has been claimed[10] that small amounts of iron (< 1%) in nickel improve the rate of nitride formation as well as the yield.

Nickel carbide can be prepared[11] by thermal decomposition of aliphatic acids, in particular of nickel acetate. A reported preparation involved heating nickel acetate powder at 289° to 337°C under vacuum for times up to one hour. Carbide, carbon, and oxide were found. It has also been reported that Ni_3C can be formed by treating nickel with carbon monoxide at 250°C[12], the carbide decomposing at 380 - 420°C.

The experimental procedures employed to prepare these materials are summarized in Table III. To obtain Ni_3N, the method described by Juza and Sachze was followed as closely as possible. Since the nitriding conditioning were quite critical, it was necessary to make several preparation attempts with slight variations of the parameters (especially temperature). Ni_3C was easily obtained by thermal decomposition of Ni acetate[11]. The method of Bahr and Bahr could not be reproduced in our attempts to prepare Ni_3C by CO-carburization.

TABLE III

Preparation of Ni_3N and Ni_3C

Run #	Material Sought	Method and Results
14	Ni_3N	Carbonyl nickel pwd was reduced with H_2 at 400°C for 21 hours and then nitrided with NH_3 at 400°C for 40 hours. X-ray analysis - nickel and trace Ni_3N.
17	Ni_3N	Carbonyl nickel was reduced with H_2 at 350°C for 24 hours and nitrided with NH_3 at 350°C for 48 hours. X-ray analysis - major phase nickel.
18	Ni_3N	Carbonyl nickel was reduced with H_2 at 450°C for 24 hours and nitrided with NH_3 at 450°C for 48 hours. X-ray analysis - major phase nickel.
19	Ni_3N	Carbonyl nickel was reduced with H_2 at 300°C for 24 hours and nitrided with NH_3 at 300°C for 48 hours. X-ray analysis - two major phases Ni, Ni_3N. Chemical analysis indicated 58% Ni_3N.
20	Ni_3C	Decomposition of NiAc at 200°C under N_2, 3 hours; 275°C, 4 hours; 300°C, 4 hours. X-ray analysis - two major phases Ni, Ni_3C. Assuming no free carbon, chemical analysis revealed 68% Ni_3C.
21	Ni_3C	Decomposition of NiAc at 250°C under N_2, 3 hours. X-ray analysis - two major phases Ni, Ni_3C. Chemical analysis showed more than the stoichiometric proportion of C in the sample for 100% Ni_3C.
22	Ni_3C	Carbonyl nickel powder was carburized with $H_2 + CO$ at 250°C for 24 hours. X-ray analysis - nickel.
23	Ni_3C	Carbonyl nickel powder was carburized with $H_2 + CO$ at 300°C for 24 hours. X-ray analysis - nickel.

TABLE III (Cont.)

Run #	Material Sought	Method and Results
24	Ni_3C	Carbonyl nickel powder was carburized with $H_2 + CO$ at 350°C for 24 hours. X-ray analysis - nickel.
28	Ni_3N	0.050 gm Ni was placed between two plugs of glass wool and subjected to H_2 for 18 hours at 445°C and NH_3 for 5 hours at 445°C. The sample was cooled in NH_3, ground in agate mortar, treated again with NH_3 for 2 hours at 445°C, cooled in NH_3, and ground. X-ray - two major phases, Ni and Ni_3N.
29	Ni_3N	0.050 gm Ni was placed between two Ni impregnated nickel screen disks in H_2 gas for 1 hour at 445°C and NH_3 for 3 hours at 445°C, cooled in NH_3, ground in agate mortar and again treated with NH_3 for 2 hours at 445°C. The sample was cooled in NH_3 and ground. X-ray - only phase, Ni.
31	Ni_3N	0.5 gm Ni and Ni ingot were treated according to the following sequence: H_2 for 5 hours at 445°C, NH_3 for 16 hours at 445°C (cooled in NH_3 - ground), NH_3 for 3 hours at 445°C (cooled in NH_3 - ground), NH_3 for 2 hours at 445°C (cooled in NH_3 - ground*).
32	Ni_3N	Ni ingot and Ni wire were heated in NH_3 for 2 hours at 350°C. The ingot changed from shiny appearance to satin gray. X-ray - not completed.
33	Ni_3N	Ni ingot and Ni wire were heated in NH_3 for 1.5 hours at 300°C. The ingot changed from shiny appearance to satin gray. X-ray - not completed.
34	Ni_3N	Ni ingot and Ni wire were heated in NH_3 for 1.5 hours at 250°C. The ingot turned satin gray; the wire broke up into many pieces during heating.

* The 2-hour heating was done five times. After each heating, the sample was X-rayed. The X-ray studies have not been completed. Appearance of ingot remained unchanged.

3. Cobalt Carbide

It has been reported[15] that extended treatment of finely divided cobalt with carbon monoxide at atmospheric pressure and 226° - 230°C increased the carbon content to 9.3 percent corresponding to the formula Co_2C. The reaction was slow under these conditions and required about 500 hours for completion. When the reaction temperature was increased above 230°C, the reaction rate was also increased and the amount of carbon deposited was no longer limited to 9.3 percent. This product was prepared also by Hofer and Peebles[16] who did a thorough characterization by X-ray diffraction. Jack[17] reported that this compound can be easily formed by carburizing cobalt nitride.

Co_2O_3 obtained from the thermal decomposition of $Co(NO_3)_2$ was reduced with H_2 at 230°C for 68 hours and carburized with CO at 230°C for 220 hours (prep. #10). X-ray analysis indicated Co_2C with traces of Co and Co_3O_4. This material when treated with water and aqueous caustic decomposed with the formation of a blue solution.

4. Manganese Carbide

Since the carburization technique was successful in preparing carbides of iron and cobalt, it was also applied to manganese. The finely divided metal was first treated with hydrogen and then carbon monoxide. Temperatures of 550°, 400°, and 450°C were used; contact time was held constant at 24 hours. Carbide formation was not observed, (Table IV, prep. #25, 26, 27).

5. Ni-Co Spinels

Mixed nitrates of nickel and cobalt were heated under N_2 at 200°C. X-ray analysis indicated the formation of the spinel ($NiO \cdot Co_2O_3$). The B. E. T. surface area was 25.7 m^2/gm.

D. Presentation of Data

The voltage-current curves obtained in the manner described are presented in Appendix I. It is desirable for purposes of discussion and comparison to reduce these data to a minimum number of parameters which represent the activity of the particular catalyst under study.

TABLE IV

Preparation of Manganese Carbide

Run #	
25	2 gm Mn metal was heated in H_2 for 24 hours at 350°C and CO for 24 hours at 350°C. X-ray - major phase, α-Mn.
26	2 gm Mn metal was heated in H_2 for 24 hours at 400°C, followed by CO for 24 hours at 400°C. X-ray - α-Mn.
27	2 gm Mn metal was heated in H_2 for 24 hours at 450°C and CO for 24 hours at 450°C. X-ray - α-Mn.

The reduction of oxygen is an irreversible process and in absence of concentration polarization the current potential curve is described by

$$i = i_o \exp\left(\frac{\alpha z F}{RT}\ \eta\right) \qquad (1)$$

where i_o is the exchange current, α the transfer coefficient, $z = \frac{n}{\nu}$ where n is the number of electrons involved in the electrode reaction and ν the stoichiometric number, F is Faraday's constant, R the gas constant, and T the absolute temperature.

If, in addition to activation polarization, concentration polarization appears due to O_2 depletion at the electrode, equation (1) converts to:

$$i = i_o \left(\frac{C^E}{C^B}\right)^{z'} \exp\left(\frac{\alpha z F}{RT}\right)\eta \qquad (2)$$

where C^E and C^B are the concentrations of oxygen at the electrode and in the bulk of the solution, respectively, and z' the stoichiometric factor[18] for the oxygen molecule in the reduction reaction.

Equation (2) can be rewritten as

$$\eta = \frac{RT}{\alpha z F} \ln \frac{i}{i_o} + \frac{z' RT}{\alpha z F} \ln \left(\frac{C^B}{C^E} \right) \tag{3}$$

It can be easily demonstrated that in case of diffusion controlled limiting current (as is the case in most of our experiments) at the half wave potential (i. e. when $i = i_{d/2}$) $C^E = \frac{C^B}{z}$

Equation (3) can then be rewritten as

$$\eta = \eta_{act} + \frac{z' RT}{\alpha z F} \ln 2 \text{ (4), or at } T = 75°C$$

$$\eta = \eta_{act} + \frac{z'}{\alpha z} 0.018 \text{ (volt)} \tag{5}$$

Thus at the half wave potential of a diffusion limited wave, the over-voltage ($\eta_{\frac{1}{2}} = E_{\frac{1}{2}} - E_o$) is equal to pure activation polarization plus a small numerical term which depends on the transfer coefficient, stoichiometric factor, and stoichiometric number.

It is apparent that the half wave potential is a very appropriate quantity for comparing catalysts studied under identical conditions since the normalization of the current to this potential is not subject to errors made in the measurement of electrode area.

In this system there are two complications which limit the rigor with which such a comparison can be made:

(1) The passivating effect of oxides and chemisorbed oxygen. Because of this effect, it is frequently found that above a given potential no current is seen, while below the potential at which the "oxide" is reduced, a very steep (purely diffusion controlled) wave appears. It is therefore possible that electrodes with little "oxide passivation" but large overvoltage due to other causes show a more negative half wave potential than electrodes with very steep waves but with an "oxide inhibition" at low polarizations.

(2) The formation and accumulation of HO_2^- by partial reduction of O_2 during the following reaction sequence:

$$O_2 + H_2O + 2\,e^- \rightarrow HO_2^- + OH^- \qquad (6)$$

$$HO_2^- + H_2O + 2\,e^- \rightarrow 3\,OH^- \qquad (7)$$

It is possible in principle that an electrode with completely reversible step (6) and very irreversible step (7) (i. e. with a very low half wave potential for the 4-electron O_2-reduction over-all wave) shows much more negative half wave potential than an electrode with less reversible reaction (6) but a more reversible reaction (7).

In order to eliminate this uncertainty, we have included in the tabulation the initial potential, i. e. the potential at which a net cathodic current is observed. This value is, at best, semiqualitative since it is dependent on the sensitivity of the ammeter and the presence or absence of corrosion current. Even with these limitations, it is a good complement to the half wave potential for comparing catalyst performance.

IV. RESULTS

Classification of Materials

The performance of the specific materials studied during the first year of the program is given in detail in subsequent sections of this report. Here, the data are summarized according to level of anodic corrosion and according to activity for O_2 reduction.

Materials which show neither anodic corrosion current nor cathodic current for the reduction of O_2 are listed in Table V. Materials which corrode only above + 800 mv are listed in Table VI, while those corroding below +800 mv are listed in Table VII.

Catalysts active for O_2 reduction are listed in Table VIII. The potential at which substantial net cathodic current was first observed for the activation controlled reduction of O_2 to HO_2^- and/or OH^- was the criterion for classifying them in five general groups. The particular voltage ranges chosen represent clusters of data points. There was generally minimal ambiguity in classifying materials, except for the HO_2^-/OH^- problem discussed elsewhere in this report.

The most active catalysts (Group I) are further divided into subclasses according to activity. Since the differences among catalysts are smaller than in the other groups, the HO_2^-/OH^- complication becomes more serious. We have therefore formed two collections. In the first, the catalysts are ordered according to $E_{\frac{1}{2}}$, thereby representing the activity for complete reduction of O_2 to OH^- (Table IX). The second collection, ordered according to initial potential, emphasizes catalysts which generate cathodic current from O_2, even though the reaction may be incomplete.

TABLE V

Materials Inert Between 0 and + 1200 mv

Zr	Zr_2Ni
Hf	Hf_2Co
Ta	HfN

TABLE VI

Materials Showing Anodic Current Between + 800 and + 1200 mv

Cr	Co_2NiAl_3	TiC	TaC	Cr_2B	Cr_3Si
Re	$TiCr_2$	VN	Cr_2N	Cr_3B	
Os	$TiCr_4$	VC	Cr_3C_2	Cr_4B	
Ag	$TaCr_2$	NbC	CrB	$CrSi_2$	
Rh	Ti_3Au				

TABLE VII

Materials Showing Anodic Current Below + 800 mv

V	NbPt (low)	TiCu*	ZrN	$TiSi_2$	TaB_2	W_2B
Nb	MoPt (low)	$TiCu_3$	HfC*	ZrB_2	$TaSi_2$	W_2B_5
Mo	Nb_3Pt	TiCo	NbN	$ZrSi_2$	Ta_5Si_3	WSi_2
W	Mo_3Pt	TaV_2	TaN	VB_2	CrB_2	$MnSi_2$
Co*	Co_2NiAl_3	$TaFe_2$	Mo_2C	VSi_2	Cr_5B_3	$CoSi_2$
Cu*	$ZrMo_2$	MnNi*	WC	NbB	MoB	
Mn*	$HfMo_2$		WC-Co	NbB_2	MoB_2	
	ZrW_2		TiB_2	$NbSi_2$	$MoSi_2$	
	HfW_2		Ti_5Si_3	TaB	WB	

* Apparent insoluble oxide.

TABLE VIII

Materials Active for O_2 Reduction

Potential Region of Activation Control Current

> + 700 mv			+ 700 to + 450		+ 450 to + 250		+ 250 to + 100		≤ + 100
Pt	$TiPt_3$	Co_2Ni	Re	MoPt	Ni*		Ti	Ti_2Cu	Cr
Pd	$TaPt_3$	$ZrAu_3$	Fe	$TaNi_3$	Cu	ZrC	Nb	$TiNi_3$	$TiCr_2$
Ag	VPt_3	Ti_3Au	Ru	$TiIr_3$	Ni_3Nb*	HfC	Ni_3Ti	$TiCr_4$	TiCo
Au	$CoPt_3$	$TaPd_3$	Ir	TiC	TiCu	NbC	NiTa	NbN	ZrN
Mn	$TaPt_2$	C		TiN	$TiCu_3$	Ni_3N*	$TaNi_2$	$CrSi_2$	HfN
Os	$NbPt_2$	Pt_2B		VC	$TaFe_2$	Cr_5B_3*	Ni_4Mo	Ni_2B	VN
	NbPt			TaC			NiAl	Ni_3B	TaN
	MnPt			Cr_3C_2			Ni_3Al*	B_4C	Cr_2N
	PtPd			Fe_2C			Alnico*		TiB_2
	Pd-Ag			Ni_3C*					$TiSi_2$**
	MnNi (3:1)			Ti_5Si					
	MnNi*			Cr_2B					

* The placement of these materials is not well defined by the data.

** Considerable corrosion also observed in this potential range.

TABLE IX

Classification of O_2 Reduction Catalysts According to $E_{\frac{1}{2}}$

(Materials Showing Activity Above + 700 mv)

Class 1

Material	E_1	$E_{\frac{1}{2}}$
Pt	+ 925	+ 845
Pt_2Ta	920	840
Pt:Pd	900	840
Ti_3Au	900	840
Pt_3Ta	870	840
Os	970	400*

* Low $E_{\frac{1}{2}}$ due to slow reduction of HO_2^-

Class 2

Material	E_1	$E_{\frac{1}{2}}$
Pd	900	835
$TaPd_3$	890	835
Pd_xAg_y	880	825
Pt_2B	875	830

TABLE IX (Cont.)

Class 3

Material	E_1	$E_{\frac{1}{2}}$
PtMn	920	820
Mn	900	820*
Pt_3V	880	820
Pt_3Ti	870	820
Pt_2Nb	870	820
Pt_3Co	900	815
$NiCo_2$	870	800*

* Limiting current was not observed due to oxide reduction.

Class 4

Material	E_1	$E_{\frac{1}{2}}$
Au	900	785
Ag	900	760

Class 5

Material	E_1	$E_{\frac{1}{2}}$
$ZrAu_3$	875	575
MnNi (3:1)	830	700
MnNi	820	150
C	810	370
$TiIr_3$	750	560

TABLE X

Classification of O_2 Reduction Catalysts According to Initial Potential

Material	E_1
Class 1a	
Os	+970
Pt	925
Pt_2Ta	920
PtMn	920
Class 2a	
Pd	900
Ag	900
Au	900
Mn	900
Pt:Pd	900
Ti_3Au	900
Pt_3Co	900
PtMn	900

TABLE X (Cont.)

Material	E_1
Class 3a	
$TaPd_3$	890
Pd:Ag	880
Pt_3V	880
Pt_2B	875
Zr_3Au	875
Pt_2Nb	870
Pt_3Ti	870
$NiCo_2$	870
Pt_3Ta	870
Class 4a	
Mn:Ni (3:1)	830
Mn:Ni (1:1)	820
C	810
$TiIr_3$	750

V. DISCUSSION

A. Transition Metals

The thermodynamic data are taken from reference (19); the potentials are given vs. a hydrogen electrode in the same solution.

1. Group IV B

a. Titanium. The thermodynamic behavior of titanium and its oxides in 2N KOH is described by the following equations:

$$Ti + H_2O = TiO + 2H^+ + 2\,e^- \qquad E = -1.306$$

$$2TiO + H_2O = Ti_2O_3 + 2H^+ + 2\,e^- \qquad E^* = -1.123$$

$$Ti_2O_3 + H_2O = 2TiO_2 + 2H^+ + 2\,e^- \qquad E^* = 0.556$$

These oxides, hydrated or anhydrous, are relatively insoluble, i.e. log C is less than 10^{-4}.

The current-potential curves for titanium are shown in Fig. 4. A low corrosion current was observed; the capacitance of 100 $\mu f/cm^2$ indicates a slightly etched surface. Titanium is active for oxygen reduction below + 300 mv; a slight hysteresis is observed when scanning back from 0 mv to + 1200 mv.

According to the equations presented above, titanium should be coated with an oxide layer throughout the potential region studied. Thus, O_2 reduction current must occur on an oxide layer.

The apparent diffusion limited current is approximately half that observed for Pt, Pd, Ag, and Au. The implication then is that O_2 is reduced to HO_2^-, as it is on graphite. Indeed, extension of the O_2 reduction curve to more negative voltages indicates a second wave associated with reduction of HO_2^- to OH^-.

b. Zirconium and Hafnium

$$Zr + 2H_2O = ZrO_2 + 4H^+ + 4\,e^- \qquad E^* = -1.553$$

$$Hf + 2H_2O = HfO_2 + 4H^+ + 4\,e^- \qquad E^* = -1.685$$

---

* The oxides are taken to be anhydrous.

The oxides are also relatively insoluble, e.g. log ($HZrO_3^-$) = - 4.3. As shown in Figs. 5, 6, both Zr and Hf show little corrosion and negligible activity for the reduction of O_2.

2. Group V B

a. Vanadium. The electrochemical behavior of vanadium is quite complex, involving valence states from 0 to +5 and involving a variety of soluble oxides. The thermodynamic reactions pertinent to the system under study are

$$2V + H_2O = V_2O_2 + 4H^+ + 4e^- \qquad E = - 0.82$$

$$V_2O_2 + H_2O = V_2O_3 + 2H^+ + 2e^- \qquad E = - 0.549$$

$$V_2O_3 + H_2O = V_2O_4 + 2H^+ + 2e^- \qquad E = + 0.20$$

$$V_2O_4 + H_2O = V_2O_5 + 2H^+ + 2e^- \qquad E = + 0.666$$

Both the quadrivalent and pentavalent oxides are appreciably soluble in 2N KOH, i.e. log ($HV_2O_5^-$) = + 4 and log ($H_3V_2O_7^-$) = + 9.6.

The observed performance of vanadium under a nitrogen atmosphere is shown in Fig. 7. Pronounced corrosion is observed at 0 mv and above, as expected. A minor passivation effect was observed at + 250 mv. An O_2 reduction curve was not taken because of the excessive corrosion.

The potential dependence of the corrosion current involving formation of V^{+4} is given by E_o = - 0.90 + 0.0295 log ($HV_2O_5^-$). Since the ($HV_2O_5^-$) term is most likely less than its equilibrium value, it is to be expected that the corrosion reaction will take place at potential values more negative than 200 mv for the transition.

b. Niobium. The expected behavior of niobium is described by the following relations:

$$Nb \xrightarrow{-0.73} NbO \xrightarrow{-0.63} NbO_2 \xrightarrow{-0.29} Nb_2O_5.$$

The observed behavior is shown in Fig. 8 . The sample is inert below + 150 mv as expected, presumably covered by a film of NbO_2 or Nb_2O_5. However, substantial corrosion current is observed at higher potentials; the absence of a passivation current implies a soluble reaction product, most likely potassium niobate.

Oxygen reduction was observed below + 150 mv prior to extension corrosion. This is also an example of O_2 reduction on an oxide film.

c. Tantalum. The thermodynamic behavior of tantalum in base is

$$2\,Ta + 5H_2O = Ta_2O_5 + 10H^+ + 10\,e^- \qquad E = -0.750$$

The observed data are shown in Fig. 9 ; a slight anodic current is observed below + 200 mv. To all intents and purposes, tantalum is inert.

3. Group VI B

a. Chromium. This element, like vanadium, possesses a variety of oxidation states from 0 to + 6. The pertinent reactions are

$$2\,Cr + 3H_2O = Cr_2O_3 + 6H^+ + 6\,e^- \qquad E = -0.654$$

$$Cr_2O_3 + H_2O = CrO_2 + 2H^+ = 2\,e^- \qquad E = +1.28$$

Cr_2O_3 is relatively insoluble; however, quadrivalent chromium exists essentially as $CrO_4^=$. The equilibrium potential equation for the formation of Cr^{+6} is given by $E_o = +1.386 - 0.0985\ pH + 0.0197 \log (CrO_4^=)$.

The observed behavior is shown in Fig. . There is little corrosion below + 900 mv, reflecting the passivating effect of Cr_2O_3. Above + 900 mv, the corrosion current increases with the formation of $CrO_4^=$. A small amount of O_2 reduction current is observed below + 200 mv, i.e. on an oxide surface.

b. Molybdenum. The thermodynamic equations for oxide formation are given by the following:

$$Mo + 2H_2O = MoO_2 + 4H^+ + 4\,e^- \qquad E = -0.72$$

$$MoO_2 + H_2O = MoO_3 + 2H^+ + 2\,e^- \qquad E = -1.091;\ +0.32$$

The exact value for the equilibrium potential depends on whether hexavalent molybdenum is present as H_2MoO_4 (-1.09) or anhydrous MoO_3 (+0.32). This difference in state is also reflected in the predicted solubility of Mo^{+6}.

The observed behavior is shown in Fig. 11. Pronounced corrosion is observed above +300 mv, apparently reflecting the formation of soluble $MoO_4^=$. Below this potential the surface is passive.

c. Tungsten. The thermodynamics of the W/OH^- system are similar to molybdenum. The reactions involved are

$$W \xrightarrow{-0.119} WO_2 \xrightarrow{-0.03} W_2O_5 \xrightarrow{-0.029} WO_3$$

In base, WO_3 is reported to be appreciably soluble, $\log (WO_4^=) = +14$.

The observed performance of tungsten under nitrogen indicates that the surface is passive below +200 mv even though "soluble" oxide should exist on the surface; corrosion is observed only at higher positive potentials with the apparent formation of $WO_4^=$ (Fig. 12).

4. Group VII B

a. Manganese. The calculated equilibria for the Mn/OH^- system are given by the following equations:

$$Mn + 2H_2O = Mn(OH)_2 + 2H^+ + 2\,e^- \qquad E = -0.73$$

$$Mn(OH)_2 + H_2O = Mn_3O_4 + 2H^+ + 2\,e^- \qquad E = 0.46$$

$$Mn_3O_4 + 9H_2O = 3Mn(OH)_3 + 9H^+ + 9\,e^- \qquad E = 2.01$$

$$Mn(OH)_3 = MnO_2 + H_2O + H^+ + e^- \qquad E = 0.573$$

The observed behavior is shown in Fig. 13. Below +350 mv, a small anodic current is observed. The anodic-cathodic couple observed at +700 mv is associated with the redox behavior of MnO_2. Also shown is the activity of the material for the reduction of oxygen. It is interesting to note that MnO_2 catalyzes the reduction of O_2 at +900 mv; however, activity diminishes significantly with the reduction of MnO_2 below +750 mv. This is another example of a surface oxide active for the reduction of O_2.

b. Rhenium. Rhenium should form a series of oxides at +0.227 (Re_2O_3), +0.375 (ReO_2), +0.399 (ReO_3), and the water-soluble heptavalent oxide (Re_2O_7/ReO_4^-) by the following reaction:

$$Re + 4H_2O = ReO_4^- + 8H^+ + 7\,e^- \qquad E = -0.676 + 0.008 \log ReO_4^-$$

The current-potential behavior observed in practice is shown in Fig. 14. A high corrosion current is observed above +730 mv, presumably due to the formation of ReO_4^-. At less positive voltages, the surface is stable, i.e. the formation of the lower valent oxides was not detected which may be due to thin films of oxide.

Activity for oxygen reduction was noted in the potential region where corrosion was not detected, i.e. below +730 mv. In this region the appearance of the curve is very similar to that of graphite.

5. Group VIII B

a. Iron. The pertinent thermodynamic reactions are

$$Fe + H_2O = FeO + 2H^+ + 2\,e^- \qquad E = -0.047$$

$$3Fe + 4H_2O = Fe_3O_4 + 8H^+ + 8\,e^- \qquad E = -0.085$$

$$Fe + 3H_2O = Fe(OH)_3 + 3H^+ + 3\,e^- \qquad E = 0.059$$

$$FeO + 2H_2O = Fe(OH)_3 + H^+ + e^- \qquad E = 0.271$$

The observed corrosion curve is shown in Fig. 15. An anodic current is observed at + 50 mv, corresponding to surface oxidation. As seen from the curve, the oxide surface is significantly active for the reduction of oxygen below + 650 mv. As with Ti and C, limiting current is substantially less than that for platinum, implying low activity for peroxide decomposition.

b. Cobalt. The oxide-forming reaction of cobalt are

$$Co + H_2O = CoO + 2H^+ + 2\,e^- \qquad E = +0.095$$

$$3CoO + H_2O = Co_3O_4 + 2H^+ + 2\,e^- \qquad E = +0.77$$

$$2Co_3O_4 + H_2O = 3Co_2O_3 + 2H^+ + 2\,e^- \qquad E = +1.018$$

The observed performance is shown in Fig. 16. A detailed explanation of the observed oxide formation-reduction reactions is beyond the scope of the present work. The activity for a reduction was negligible.

c. Nickel. At low potentials, the principal Ni/OH^- reaction is

$$Ni + H_2O = NiO + 2H^+ + 2\,e^- \qquad E = +0.11$$

The low activity observed for oxygen reduction at this temperature is consistent with the data of others (Fig. 17).

d. Ruthenium. The thermodynamic reactions pertinent to the oxidation of ruthenium are

$$2Ru + 3H_2O = Ru_2O_3 + 6H^+ + 6\,e^- \qquad E = +0.738$$

$$Ru_2O_3 + H_2O = 2RuO_2 + 2H^+ + 2\,e^- \qquad E = +0.937$$

$$RuO_2 + 2H_2O = RuO_4 + 4H^+ + 2\,e^- \qquad E = +1.387$$

The observed behavior of ruthenium is shown in Fig. 18. Cathodic current is observed below + 500 mv; however, anodic current corresponding to the re-oxidation of the surface is not observed. Such would be the case if the oxide layer is small and thickens as higher potentials are reached. The large hysteresis of + 350 mv is consistent with this explanation.

O_2 reduction current is observed below + 700 mv. An additional 100 mv are needed before the reactions become rapid. This polarization puts the sample into the potential region where, thermodynamically, the material should be free of oxide.

e. Rhodium. The thermodynamically expected reactions for the Rh/OH^- system are as follows:

$$2Rh + H_2O = Rh_2O + 2H^+ + 2\,e^- \qquad E_o = +0.796$$

$$Rh_2O + H_2O = 2RhO + 2H^+ + 2\,e^- \qquad E_o = +0.882$$

$$Rh_2O + 2H_2O = Rh_2O_3 + 4H^+ + 4\,e^- \qquad E_o = +0.877$$

$$2RhO + H_2O = Rh_2O_3 + 2H^+ + 2\,e^- \qquad E_o = +0.871$$

$$Rh_2O_3 + H_2O = 2RhO_2 + 2H^+ + 2\,e^- \qquad E_o = +1.730$$

The observed behavior of rhodium is shown in Fig. 19. Current corresponding to oxide reduction and formation is not observed, as would be expected if the oxide is insoluble and nonporous. Substantial anodic current is observed above + 1100 mv due to the formation of a soluble material, presumably $RhO_4^=$. Discoloration of the solution was also observed.

O_2 reduction current is observed below + 820 mv. As with other metals of this group, the reaction rate does not become appreciable until the potential region is reached in which oxide should be absent. A significant hysteresis is observed, most likely associated with reduction of surface oxide.

f. Palladium. The equally well established behavior of palladium from 0 to + 1200 mv is shown in Fig. 20. Again, it is only after the surface oxide has been reduced that substantial activity is observed for the reduction of O_2.

Palladium is less active than Pt by approximately 10 mv.

g. Osmium. The thermodynamics of the Os/OH^- system are as follows:

$$Os + 2H_2O = OsO_2 + 4H^+ + 4\,e^- \qquad E_o = +0.687$$

$$OsO_2 + 2H_2O = OsO_4 + 4H^+ + 4\,e^- \qquad E_o = 1.005$$

The tetroxide is soluble in caustic, e.g. $\log (HOsO_5^-) = +4$. The observed behavior is shown in Fig. 21. Corrosion of osmium is observed above + 830 mv, presumably to form $HOsO_5^-$. In comparing this corrosion rate to other materials, account must be taken of the expanded current scale.

O_2 reduction current is first detected at approximately + 1040 mv; however, because of the background corrosion, net cathodic current is observed at + 970 mv. The O_2 reduction curve involves two well-separated waves; an additional overpotential of approximately 400 mv is apparently required for the rapid reduction of HO_2^-. The current at + 870 mv is stable with time; no change was observed during a 15 min hold at this potential. The current in this potential region is not particularly affected by stirring, which is reasonably since the current is only 10% of the diffusion-limited current.

A current-potential curve was taken at a scan rate of 480 mv/min. Intermediate oxide formation is not observed. The anodic current in the 500-100 mv range indicates that osmium is also active for the oxidation of H_2.

h. Iridium. The reversible thermodynamic potential for the Ir/IrO_2 couple is + 0.926 mv. The observed behavior is shown in Fig. 22. There is no indication of the formation or reduction of this oxide. Either the system is highly irreversible, or the oxide layer is very thin. The fact that the surface has been altered below + 700 mv is indicated by the 175 mv hysteresis for the O_2 reduction curve.

i. Platinum. The well known behavior of platinum in the reduction of O_2 is shown in Figs. 23 and 24. A slight hysteresis is noted in both curves; Fig. 24 indicates the small amount of current associated with the formation of platinum oxide. A small hysteresis loop, approximately 5 mv, was observed when the scans were terminated at 0 mv and + 500 mv. It is probable that Pt is an active catalyst only after the surface oxide has been reduced.

6. Group I B

a. Copper. The thermodynamic equilibria for the Cu/OH^- system are given by:

$$2Cu + H_2O = Cu_2O + 2H^+ + 2\,e^- \qquad E_o = + 0.471$$

$$Cu_2O + H_2O = 2CuO + 2H^+ + 2\,e^- \qquad E_o = + 0.669$$

The observed corrosion behavior is shown in Fig. 25. The principal corrosion reactions are apparently those listed above. It is apparent, from the cathodic scan that activity is not observed for the reduction of O_2 until copper metal is formed.

b. Silver. The oxide-forming reactions of silver have been thoroughly studied in conjunction with work on Ag/Zn batteries. The thermodynamic data on these reactions are

$$2Ag + H_2O = Ag_2O + 2H^+ + 2\,e^- \qquad E_o = +\,1.173$$

$$Ag_2O + H_2O = 2AgO + 2H^+ \qquad E_o = +\,1.398$$

The solubility of Ag_2O is given by $\log (AgO^-) = -\,3.3$.

The observed performance is given in Figs. 26 and 27. Oxide formation takes place at a high rate above + 1100 mv and is preceded by a small anodic current above + 900 mv. Oxygen reduction is observed below + 900 mv, i.e. on the reduced metal surface. A hysteresis loop of 50 mv is observed.

c. Gold. Gold is the most noble of metals. Oxide formation is observed only above + 1.457 mv, so that the O_2 reduction process does take place on the reduced metal surface. The solubility of AuO_3 is given by $\log (H_2AuO_3^-) = -\,3$. The performance curve for gold is shown in Fig. 28. A two-stage reduction is apparent, which is generally associated with differences in rate between the reactions

$$O_2 \rightarrow HO_2^-$$

$$HO_2^- \rightarrow OH^-$$

This two-step process is more apparent in Fig. 29. At more positive potentials, gold is less active than platinum by approximately 25 mv. This difference becomes greater below + 800 mv because of the poorer activity of gold in catalyzing the decomposition of HO_2^-.

General Discussion

It is possible to place the elements into a number of categories in describing their performances in 2H KOH saturated with N_2 or O_2. The first grouping contains those metals which either corrode substantially or are inert over the potential range 0 to + 1000 mv. These metals are listed in Table XI.

TABLE XI

Elements Not Active as Oxygen Electrodes

Corrode	Inert
V	Zr
Nb*	Hf
Ta	Cr**
Mo	
W	
Co	

* Active where corrosion is observed

** Corrodes above + 900 mv

In a number of cases, the observed corrosion behavior was other than predicted by thermodynamics. Consider the following specific examples:

a) Vanadium corroded at negative potentials, presumably due to the formation of $HV_2O_5^-$. A slight passivation occurred at + 200 mv; the predicted transition to V_2O_5 or $H_3V_2O_7^-$ at about 600 mv was not observed.

b) Niobium is reported to be covered by an insoluble oxide at positive potentials. However, corrosion of niobium was observed above + 250 mv, presumably because of a soluble reaction product.

c) The formation of soluble $WO_4^=$ is predicted to occur at negative potentials. However, the formation of a soluble corrosion product was not observed below + 200 mv.

The remaining transition elements show some activity for O_2 reduction. Table XII lists elements which catalyze O_2 reduction above + 800 mv.

TABLE XII

Transition Metals Active for O_2 Reduction Above + 800 mv

Mn	Ag
	Au
Pd	C
Pt	Os

The performance curves indicate the order of activity (based on initial potential): Os > Pt > Pd > Au = Ag > Mn > C.

Of the remaining elements, Fe, Re, and Ir are active below + 675 mv; Ni, Ti, and Cu are active below + 360 mv.

A parallel grouping of the metals can be formed according to whether oxygen is reduced on an oxide or on "bare" metal. This correlation is shown in Table XIII.

The performances of the transition metals are summarized in Table XV, according to position in the periodic table. The limiting current i_l is also given.

The most active elements are those for which the metal itself catalyzes the O_2 reduction process. The low limiting currents and the slope of the performance curves for Fe, Ti, and possibly Ni and Re indicate that these materials have a low activity for the decomposition

TABLE XIII

Oxygen Reduction Activity vs. Surface Composition

Oxide Surface	Metal Surface
Ti	Pd
Nb	Pt
Fe	Ag
Mn	Au
Ni	Cu

of HO_2^-. Nb also shows a two-step reduction; however, some ambiguity is introduced by corrosion.

Manganese dioxide is the one oxide which shows activity for oxygen reduction at high potentials.

Elements showing a hysteresis loop of 100 mv or more are listed in Table XIV. In the sense used here, the hysteresis is given by the difference in current at the half-wave potential between the scans from + 1200 to 0 and from 0 to + 1200.

TABLE XIV

Hysteresis for Oxygen Reduction

Element	V (mv)
Nb	100
Re	100
Ru	350
Ir	175
Fe	50 - 150
O_s	300
Ni	180
Rh	250
Ag	120
Au	100

TABLE XV

O_2 Reduction Properties of the Elements

Group	Metal	E_i**	$E_{\frac{1}{2}}$	i_1 (ma/cm^2)	Hysteresis* (mv)
IV B	Ti	250	160	0.66	20
	Zr		inert		
	Mf		inert		
V B	V		corrode		
	Nb		(~ 190), corrode	1.36	100 mv (max)
	Ta		inert		
VI B	Cr	~200	< 0, corrode, > + 950		
	Mo		corrode		
	W		corrode		
VII B	Mn	900	~820		oxide reduction limited
	Re	820	340	1.32	100
VIII B	Fe	645	300	0.80	50
	Ru	720	450	----	350
	Os	970	400	1.6	300
	Co		"corrodes"		
	Rh	820	450	1.1	250
	Ir	675	544 (RHE)	1.37	175
	Ni	340	< 90	1.0	180
	Pd	900	835	1.2	50
	Pt	925	845	1.35	15
I B	Cu		oxide formation	1.33	
	Ag	900	760	1.45	120
	Au	900	785	1.34	100
graphite		810	370	0.89	---

* Hysteresis at $E_{\frac{1}{2}}$

** E_i is the potential at which O_2 reduction is first detected.

It is not possible, with the information developed within this study, to offer a detailed explanation of this effect. In all cases, the anodic scan showed a higher activity than the forward scan. Generally, this improvement was temporary; with time, the performance decayed to that of the cathodic scan. Obviously, taking the metals to less positive potentials alters the surface, rendering it more active. Generally, most improvement results for the section of the reduction curve attributed to the reduction of HO_2^-.

In the cases of Nb, Re, Fe, Ni, and possibly Ir, this effect could be attributed to "thinning" of the oxide surface.

Osmium is unique in that it shows activity for the reduction of oxygen at potentials more positive than platinum. Unfortunately, the use of this metal in working electrodes is complicated by the corrosion of this material to form soluble ($HOsO_5^-$).

B. Alloy Electrocatalysts

The materials investigated are discussed below. The order is somewhat arbitrary and was chosen primarily to represent the smallest number of groups. A regrouping according to experimentally determined correlations will be made after the presentation of results. The metallurgical characterization of selected intermetallic compounds is given in Appendix B.

1. Platinum Based Alloys

a. Pt_3Ti. The performance curve is shown in Fig. 30. Negligible corrosion is observed; the electrolyte capacitance is somewhat higher than usually observed, probably indicating a roughened surface. O_2 reduction activity is observed below + 870 mv (RHE).

b. Pt_3Ta. The performance of this material is shown in Fig. 31. The anodic current observed at the more positive potentials is anomalous in view of the stability of Ta and Pt. Nevertheless, it is apparent that the material is no more active than platinum.

c. Pt_3V. The performance curve is shown in Fig. 32. The corrosion reaction of vanadium is much reduced, although some corrosion is observed above +750 mv; however, the surface passivates at higher potentials. Pt_3V is active for O_2 reduction below +880 mv.

d. Pt_3Co. The surface oxide reactions noted for cobalt are not observed in this system. The activity of this material for the reduction of O_2 is somewhat less than that of pure platinum (Figs. 33, 34).

e. Pt_2Ta. The performance of this material is shown in Figs. 35, 36. Corrosion is negligible over the potential range studied, as would be expected from the stability of elements themselves. This compound is active for O_2 reduction below +920 mv, which is essentially equivalent to platinum.

f. Pt_2Nb. The performance of this material is shown in Fig. 37 . The corrosion reaction noted for Nb metal has been almost entirely suppressed, although the capacitance of 133 $\mu f/cm^2$ indicates a slightly roughened surface. O_2 reduction activity is observed below $\pm$ 870 mv.

g. PtNb. A pronounced anodic current is observed particularly during the scan from 0 to +1200 mv. A large cathodic current is present below +200 mv. Oxygen reduction activity is observed below +925 mv. The electrolyte capacitance is also high (820 $\mu f/cm^2$), indicative of a significantly roughened or etched surface (Fig. 38, 39).

h. PtMo. Corrosion is also observed for this material. O_2 reduction activity is observed below +800 mv. The high anodic current observed in the presence of O_2 has not been explained (Fig. 40).

i. Pt:Mn. Anodic current is observed above +850 mv and is higher on the anodic scan. Activity for O_2 reduction is observed below +920 mv: little hysteresis is present. The lower value of $E_{\frac{1}{2}}$ is possibly due to a slow reduction of HO_2^-, i.e. the curve is similar in form to that for gold. At higher potentials the material is at least equivalent to platinum (Fig. 41).

j. Pt:Pd. The oxygen reduction curve for this alloy is shown in Figs. 42, 43. Activity is present below + 900 mv.

k. $PtNb_3$, $PtMo_3$. The corrosion reactions are particularly pronounced as expected from the high atomic percent of the base metal (Figs. 44, 45).

Discussion

Platinum alloys containing the metals Nb and Mo show varying degrees of corrosion, depending upon composition. Table XVI summarizes the capacitance data for the alloys containing niobium and molybdenum.

TABLE XVI

Corrosion of Nb and Mo Alloys with Pt

Alloy	Capacitance ($\mu f/cm^2$)
Pt	58
Pt_2Nb	133
PtNb	400
$PtNb_3$	> 600
PtMo	350
$PtMo_3$	> 600

The corrosion products of Nb and Mo are soluble in the electrolyte. The absence of a large anodic current for Pt_2Nb could be ascribed to depletion of Nb at the surface of the metal. At higher concentrations of the alloying constituent, the corrosion current becomes more pronounced. This apparent suppression of the base metal-surface oxide reactions by alloy formation was noted for Pt_3Co, PtMn, and Pt_3V. The capacitance data for Pt_3Co (133 $\mu f/cm^2$) indicate a slightly roughened surface, possibly due to etching of the cobalt.

This surface roughening or etching will, of course, complicate the evaluation of activity for oxygen reduction since the current is proportional to the real area of exposed surface, except in the diffusion-limited range. It is therefore necessary to consider the activity of corrodable alloys (Table XVI) as upper limits to the "true" specific activities of the material.

The variation in $E_{\frac{1}{2}}$ introduced by this problem can be small (10-15 mv) at capacitances less than 150 $\mu f/cm^2$. The usual form of the current-potential curve is such that a large change in current density is accompanied by only a small shift in potential. E_I, the potential at which a net cathodic O_2 reduction current is first observed, is more sensitive to this surface area effect. If the capacitance is higher than 150 $\mu f/cm^2$, an effect on activity is observed. For example, the measured activity of PtNb was higher than platinum at the more positive potentials (Fig. 38) and equivalent to platinum at the less positive potentials. This is shown in Table XVII.

TABLE XVII

O_2 Reduction on PtNb

E (mv)	Current Density ($\mu a/cm^2$)	
	Pt	PtNb
950	+ 21	- 45
900	- 46	- 170
850	- 530	- 602
800	-1077	-1090

The capacitance data (400 $\mu f/cm^2$) for PtNb indicate highly roughened surface, which most likely explains the observed higher activity.

The performance of these electrodes in order of activity ($E_{\frac{1}{2}}$) is given in Table XVIII.

TABLE XVIII

Activity of Pt Based Catalysts

Alloy	E_I	$E_{\frac{1}{2}}$	Capacitance (at + 400 mv) ($\mu f/cm^2$)
Pt	925	845	45
Pt_2Ta	920	840	24
Pt:Pd	900	840	44
Pt_3Ta	870	840	
PtMn	920	820	145
Pt_3Ti	870	820	132
Pt_3V	880	820	132
Pt_2Nb	870	820	133
Pt_3Co	900	815	133

If synergistic effects do exist in these alloy systems, they are minor. None of these materials is more effective than platinum, although a number of alloys approach this level of activity. Pt-Mn is as effective at potentials more positive than $E_{\frac{1}{2}}$. The use of these alloys as practical O_2 electrodes therefore depends on other factors - for example, on the possible resistance of these alloys to sintering. Of particular interest are the platinum-tantalum and platinum-manganese alloys. The corrosion rate is low as expected, and yet the activity is comparable to platinum.

In some cases the electrocatalytic activity was decreased, e.g. for Pt_3V, Pt_2Nb, and Pt_3Ti. Alloys with metals which corrode in the pure state develop a roughened or etched surface. However, the observed anodic current for Pt_2Nb was very small and the surface oxide reactions of cobalt were not apparent with Pt_3Co.

2. Palladium-Silver Alloys

The O_2 reduction activity of a series of palladium-silver alloys is summarized in Table XIX and Figs. 46-50.

TABLE XIX

O_2 Reduction Activity of Pd-Ag Alloys

Alloy	E_I	$E_{\frac{1}{2}}$	i_L (ma/cm^2)	ΔE
Pd	900	835	1.2	50
Pd-Ag (9:1)	870	815	1.4	58
(4:1)	880	820	0.96	40
(2.1:1)	880	830	0.91	--
(1:1)	880	820	1.4	40
(1:2.1)	880	820	1.36	--
Ag	900	730	1.45	120

Little corrosion is observed for this series, as expected. Except for the (1:2.1) Pd-Ag sample, all alloys show an increase in cathodic current as the hydrogen deposition region is approached and a significant anodic current on the subsequent scan from 0 to + 1200 mv. In this respect the alloys resemble palladium.

Alloy formation generally leads to a lower initial potential for oxygen reduction; the half wave potentials are also 10-15 mv less positive than that of palladium. Perhaps the most significant point of this series is that the $E_{\frac{1}{2}}$ values for the alloys are approximately 100 mv more positive than for pure silver. Evidently, the rate of peroxide reduction is much faster on the alloys.

3. Nickel Based Alloys

The performance of a variety of nickel alloys as oxygen electrodes is shown in Table XX and Figs. 51-65.

TABLE XX

O_2 Reduction Activity of Nickel Alloys

Alloy	E_I	$E_{\frac{1}{2}}$	i_L	ΔE
Ni	250-650	~ 200	---	~ + 150
Ni_3Nb	~ 800	~ 200	---	~ + 200
Ni_3Ti	250	~ 100	---	~ + 100
$NiZr_2$	-----	-----	inert	-----
NiTa	+ 210	+ 105	1. 2	+ 200
Ni_2Ta	+ 210	+ 175	-----	~ + 275
Ni_3Ta	+ 700	~ 250		
NiMn (1:3)	+ 830	~"700"		~ + 300
NiMn (1:1)	+ 820	+ 150	0. 8	+ 150
Ni_4Mo	+ 250	+ 150		
$NiCo_2$	+ 870	"800"		
NiAl	+ 280	+ 100		
Ni_3Al		+ 100		
$NiCo_2Al_3$	-----	-----		
Alnico	~ + 400	~ 175		

Nickel shows activity for O_2 reduction below + 200 mv. Alloys of nickel with Nb, Ti, Zr, Ta, and Mo were no more active than nickel;

$NiZr_2$ was inert. The Ta-Ni series can be considered as a series of diluted nickel samples; i. e. there is no indication of synergistic interactions.

a. Nickel-Manganese. The performance curves for the two alloys studied are shown in Figs. 57 and 58. There is some evidence of the complex surface oxide reactions characteristic of pure Mn with the NiMn (1:3) alloy, while these reactions are essentially suppressed in the 1:1 alloy. O_2 reduction activity is observed for both alloys, although the level is somewhat below that of pure manganese. The shape of the curve implies a slow rate for the reduction of HO_2^-; this type of curve is observed with metals which are covered with an oxide layer.

b. Nickel Cobalt. The data for $NiCo_2$ are shown in Fig. 60. The surface oxide reactions of cobalt are also suppressed. The O_2 reduction activity observed below + 900 mv is apparently associated with the formation of a surface spinel. (See Discussion.)

Discussion

Of the nickel-base metal alloys studied, only those with manganese and $NiCo_2$ were active for the reduction of O_2. In the former system the activity is probably associated with manganese. The activity of the alloy is less than that of pure Mn.

It is reasonable to ascribe the cathodic current of $NiCo_2$ to the reduction of O_2 catalyzed by a surface layer of spinel, the active component being trivalent cobalt. This activity is enhanced by holding the potential above + 1200 mv where the formation of Co^{+3} is expected. Apparently Co^{+3} is reduced to Co^{+2} below + 750 mv and the activity of the material disappears on scanning from 0 to + 1200 mv. Returning the electrode to high potentials restores its performance.

Perhaps the most interesting characteristic of the nickel alloys is the effectiveness of nickel in suppressing corrosion. This is particularly true of alloys containing over 50 at % nickel. For example, the redox behavior of manganese and cobalt involves a complex series of surface

reactions. There is little evidence for these reactions in the alloys NiMn and $NiCo_2$, although the (1:2) NiMn alloy did show some evidence of surface reactions.

Suppression of corrosion was also observed in the nickel-aluminum series. Pure aluminum dissolves anodically in caustic solution; $NiAl_2$ and $NiAl_3$ also dissolve readily. However, both NiAl and Ni_3Al are stable over the entire potential range studied.

The pure metals Nb and Mo corrode severely in 2N potassium hydroxide. Corrosion of the alloys Ni_3Nb and Ni_4Mo is negligible. The low double layer capacities of these alloys indicate that the surface is not roughened. Actually, the low values of 17 and 19 $\mu f/cm^2$ imply relatively thick oxide films.

4. Alloys Containing Group IV B Metals

The alloys surveyed can be divided into two broad groups: those which contain noble metals and those which do not. The specific alloys studied are listed in Table XXI.

TABLE XXI

Alloys of Ti, Zr, Hf with Nonnoble Metals

$ZrMo_2$	Hf_2Co	Ti_2Cu	Ti_3Au
ZrW_2	$HfMo_2$	TiCu	$TiPt_3$
Zr_2Ni	HfW_2	$TiCu_3$	$ZrAu_3$
		TiCo	$TiIr_3$
		$TiNi_3$	
		$TiCr_2$	
		$TiCr_4$	

a. Nonnoble Metal Alloys

(1) Zr and Hf Alloys

As seen in Figs. 66 - 70, substantial corrosion was observed for $ZrMo_2$, $HfMo_2$, HfW_2 and ZrW_2. However

the surface oxide reactions were suppressed in Hf_2Co (Fig. 69) which was inert over the potential range studied. Zr_2Ni (Fig. 53) was also inert, not showing the activity associated with pure nickel.

(2) Titanium Alloys

(a) Base Metal Alloys

The performance of the titanium-copper alloys are shown in Figs. 71 , 72 , and 73. The surface reactions of copper become more pronounced as its concentration is increased. The curves are similar to those observed for pure copper, except that the surface oxide reactions are apparently much more irreversible; i. e. distinct cathodic waves are not observed. Ti_2Cu shows cathodic activity for O_2 reduction below + 250 mv, while TiCu and $TiCu_3$ show a net cathodic reduction of O_2 (in excess of the anodic corrosion current) below + 500 mv. Actually, the corrosion current is displaced to more cathodic values by O_2 reduction at somewhat higher potentials (+ 750 mv) in the case of $TiCu_3$. Some O_2 activity is observed for $TiNi_3$, although it is substantially less than that of nickel. The low capacitance (15 $\mu f/cm^2$) implies a relatively thick oxide film.

The behavior of the titanium-chromium alloys resembles that observed for pure chromium. Formation of chromate is apparent at high potentials; there is a little activity for O_2 reduction on $TiCr_4$ (Figs. 74, 75). There is some evidence for the surface reactions of cobalt in TiCo; the O_2 activity is low (Fig. 76).

Discussion

To a first approximation, the corrosion behavior of the alloys studied is controlled by the major constituent, as illustrated by the Ti-Cu series and the cobalt alloys of Hf and Ti. The corrosion of Mo and W in the hafnium alloys is displaced to more positive potentials.

No enhancement of O_2 activity was noted with any of these alloys. In fact, the small activity associated with nickel was inhibited in Zr_2Ni and in $TiNi_3$. A small activity was noted on $TiCr_4$.

b. Noble Metal Alloys

The activity of alloys of group IV B and the noble metals is summarized in Table XXII.

TABLE XXII

Activity of Ti and Zr Alloys with Noble Metals

Alloy	E_I	$E_{\frac{1}{2}}$	i_L (ma/cm^2)
Pt	925	850	1.36
Au	870	735	1.34
$TiPt_3$	870	820	1.05
$TiIr_3$	750	560	1.26
Ti_3Au	900	840	1.05
$ZrAu_3$	875	575	1.8

The $TiPt_3$ alloy was discussed previously. The performance of $TiIr_3$ was essentially the same as that for iridium itself (Fig. 77). The O_2 reduction activity was neither enhanced nor suppressed by the presence of 25 at % Ti.

$ZrAu_3$ showed some activity; the form of the voltage-current curve implies a pronounced difference in rate between the two stages in O_2 reduction. The curve resembles those noted for oxide covered surfaces (Fig. 78).

Ti_3Au was active for the reduction of oxygen, unlike other alloys with a high content of nonnoble metal (Fig. 79). The catalytic activity of electrodes increased with time after immersion in KOH. This effect is summarized in Tables XXIII and XXIV. After measuring the initial activity (Fig. 80) the sample was held potentiostatically at + 1200 mv for 24 hours. As mentioned, an anodic current is initially observed in this potential region down to approximately + 950 mv (Fig. 80). This current declines with time and is essentially absent in the voltage current curve measured after the 24 hour treatment (Fig. 81). A comparison of activity is made in Tables XXIII and XXIV and Fig. 82.

TABLE XXIII

Activity of Ti_3 Au as a Function of Time

Sample	E_I	$E_{\frac{1}{2}}$	Capacitance ($\mu f/cm^2$ at 200 mv)
Pt	925	850	58
Ti_3Au (initial)	900	840	87
Ti_3Au (final)	990	880	720

TABLE XXIV

Activity of Ti_3Au as a Function of Potential

Potential	Current Density ($\mu a/cm^2$)		
	Pt	Ti_3Au (initial)	Ti_3Au (final)
950	+ 21	+113	- 47
900	- 46	+ 9	-357
850	- 530	- 432	-686
800	-1077	-696	-874

The initial performance of Ti_3Au is slightly below that of platinum; however, with time this performance increases to a level higher than platinum. This increase is accompanied by pronounced increase in electrical capacitance, implying a roughening or etching of the surface. Indeed an anodic current is observed which would correspond to surface corrosion reaction. Electron micrographs (Figs. 83 and 84) taken of the surface before and after treatment also indicate a pronounced etching of the sample.

The chemical composition of the surface was studied with an electron beam microprobe. The sample was cut perpendicular to the surface exposed to the solution. The electron beam was then scanned onto the surface and the Ti/Au ratio determined. This data indicates that this surface film has a thickness of at least one micron and that the surface has a higher titanium/gold ratio than the bulk of the material.

In summary, the activity of $TiPt_3$ is less than that of platinum; Ti_3Au is more active for the reduction of O_2 than gold, being comparable to platinum. The surface area of this material increases with time, probably yielding a surface with a higher Ti/Au ratio than the bulk material. In spite of this higher superconcentration of nonnoble metal, activity of the sample also increases. $ZrAu_3$, richer in gold, shows a lower activity than gold itself and a stable surface.

5. Tantalum Based Alloys

The following alloys of tantalum have been studied:

TABLE XXV

Tantalum Alloys

TaV_2	TaNi	$TaPd_3$
$TaCr_2$	$TaNi_2$	$TaPt_2$
$TaFe_2$	$TaNi_3$	$TaPt_3$

The performance curves for alloys of tantalum and base metals show very little evidence of interaction between the metals; i. e. the corrosion and O_2 activity are what was expected from the pure metals themselves (Figs. 85-88).

The tantalum-platinum alloys were discussed elsewhere.

The performance of $TaPd_3$ is shown in Figs. 89, 90. The pertinent activity data are as follows:

E_I = 890; $E_{\frac{1}{2}}$ = 835; i_L = 1.6 ma/cm^2; ΔE = + 50;

capacitance = 100 μf/cm^2.

This activity is essentially equal to that of palladium, consistent with the lack of interactions noted for other tantalum alloys.

C. Carbides, Nitrides, Borides, and Silicides of Transition Metals

Borides, silicides, carbides, and nitrides of the transition metals have been surveyed for their corrosion behavior and their activity for catalyzing the electrochemical reduction of oxygen.

The data accumulated is displayed in two sections, the first dealing with carbides and nitrides, the second dealing with borides and silicides. The performances of materials within each grouping is discussed in terms of modifying the properties of the parent transition metal. The relationships and trends among carbides and between classes will be discussed subsequently.

1. Carbides and Nitrides

a. Ti, TiN, TiC. The performances of these materials are shown in Figs. 91, 92, and 93. A slight anodic corrosion current is observed for titanium. This current is much less for TiN even though the surface area of the nitride is much greater, as indicated by the capacitance (540 μf/cm^2). Substantial corrosion of TiC is observed above + 830 mv. Judging from the absence of a passivating current, the reaction product is either partly soluble or porous.

The O_2 reduction activity of TiN is substantially higher than that of Ti. The current-potential curve has two waves, implying a difference in rate for O_2 and HO_2^- reduction noted for oxide coated metals. This material was also studied with a graphite counter electrode to eliminate the possibility of contamination of TiN by dissolved platinum. No difference in activity was found (Fig. 94).

TiC is slightly more active than titanium and some O_2 reduction current is noted at + 820 mv. However, its performance is less than that of TiN. Some of this could be ascribed to the large difference in surface area.

b. Zr, ZrN, ZrC. As noted previously, Zr does not corrode nor reduce O_2 over the potential range studied. ZrN shows a slight activity and possibly corrosion at potentials above + 600 mv (Fig. 95).

Corrosion is not observed for ZrC; the material shows cathodic current for O_2 reduction below + 400 mv (Fig. 96).

c. Hf, HfN, HfC. Hafnium, like Zr, is inert over the potential range studied. The low capacitance (2 $\mu f/cm^2$) is consistent with an insulating oxide film. HfN is also essentially inert although there is a slight indication of activity below + 500 mv (Fig. 97).

HfC shows an anomalous anodic current peak at + 630 mv. O_2 reduction is observed at potentials less positive than + 500 mv (Fig. 98)

d. V, VN, VC. Vanadium corrodes under the conditions of the experiment, presumably with the formation of a soluble product (Fig. 7). Anodic corrosion current is observed for VN above + 180 mv and a small amount of oxygen activity is observed below + 180 mv (Fig.99) These corrosion reactions are further suppressed in VC. Anodic current is observed only above + 820 mv; the low capacitance (60 $\mu f/cm^2$) at + 600 mv is consistent with a stable surface. Cathodic O_2 reduction current is observed below this potential (Fig. 100).

e. Nb, NbN, NbC. As shown in Fig. 8 , niobium corrodes above + 170 mv. This metal is also active for O_2 reduction; net cathodic current was observed below + 270 mv. The corrosion behavior of NbN is similar to that of the metal; the O_2 activity may be less, although this point is difficult to establish because of the corrosion current (Fig. 101).

NbC is more resistant to corrosion than the metal; anodic current is observed only above + 600 mv. Reduction of oxygen is observed below this potential; as with the other carbides studied, two waves are present (Fig. 102).

f. Ta, TaN, TaC. Tantalum is essentially inert over the potential range studied. The nitride, on the other hand, shows substantial corrosion at potentials more positive than 0 mv. A small amount of oxygen activity is observed below + 100 mv (Fig. 103). Corrosion is observed for TaC above + 630 mv and O_2 reduction activity is observed below + 630 mv (Fig. 104).

g. Cr, Cr_2N, Cr_3C_2. Chromium shows little activity for O_2 reduction and corrodes to soluble chromate above + 900 mv. The behavior of Cr_2N is essentially identical (Fig. 105). The corrosion behavior of Cr_3C_2 is apparently more complex; anodic current is observed above + 350 mv. Net O_2 reduction activity is observed below + 600 mv (Fig. 106)

h. Mo, Mo_2C. Substantial corrosion current is observed for both materials (Fig. 107).

i. W, WC, 94 WC - 6 Co, 80 WC - 20 Co. The corrosion behavior of W and WC are essentially identical. This behavior appears to be somewhat suppressed by alloying with cobalt. Anodic current peaks are observed rather than continuous corrosion (Figs. 108-110).

j. Fe, Fe_2C. The performances of these materials are shown in Figs. 111 and 112. Fe_2C is somewhat more active than Fe and cathodic current is observed at more positive potentials. Both limiting currents are low ($\sim$ 0.8 - 0.9 ma/cm^2) indicating incomplete reduction of O_2. The electrical capacitances of the electrodes indicate stable surfaces on both samples.

k. Ni, Ni_3N, Ni_3C. It was difficult to prepare the carbide and nitrides as solid ingots; powder electrodes were therefore used; the preparative technique are described elsewhere. The voltage-current curves are shown in Figs. 113-116; this data is summarized in Table XXVI.

Ni_3N is slightly more active than nickel, and Ni_3C is two orders of magnitude more active than nickel. It is not clear whether this high activity is an inherent property of Ni_3C or due to a high surface area. Furthermore, the sample is not pure Ni_3C; nickel is also present as a major constituent.

TABLE XXVI

Comparison of Ni, Ni_3N, Ni_3C, for O_2 Reduction

Current Density at Selected Potentials

Sample	Current Density (ma/cm^2) Potential: + 850 mv	+ 800	+ 750	+ 700	+ 600	Surface Area (m^2/gm)
Ni	0.8	1	1.3	1.8	2.2	0.33
Ni_3N + Ni	0.2	1.2	3	5.5	16	0.53
Ni_3C + Ni	0.1	12.0	90	185	290	19.3

1. Carbon-Graphite. The performance of graphite is shown in Figs. 117, 118. The activity of carbon depends on the surface area and structure of the electrode. The particular sample has a high surface area (410 $\mu f/cm^2$) compared to the carbides studied, but a low value compared to the "activated" carbons. This material should provide at least an order of magnitude point of reference. Note that the "limiting" current ($\sim$ 0.6 $\mu f/cm^2$) is approximately half of what can be expected for peroxide-decomposing catalysts.

Discussion

The corrosion behavior of these compounds relative to the parent metals is given in Table XXVII. The data are qualitatively displayed in terms of increased or decreased corrosion.

There are no systematic trends in corrosion behavior useful in predicting the behavior of other compounds or in correlating with other pertinent parameters such as O_2 activity. The corrosion rate of VC, VN, NbC, and TiN are lower than they are for the metals. However, Cr_3C_2, TiC, and TaC corrode faster than the parent materials. Apparently either

TABLE XXVII

Relative Corrosion Behavior

Metal	Nitride	Carbide	Corrosion Level (Metal)
Ti	decreased	increased	low
Zr	small increase	small increase	none
Hf	no change	?	none
V	decrease	decrease	high
Nb	no change	decreased	high
Ta	increase	increase	none
Cr	no change	increase	at high potential
Mo	---	no change	high
W	---	no change	high

porous or soluble products are formed since passivation currents are not observed. This effect implies that the composition of the surface oxide film normally present on the metal has been substantially altered by the presence of carbon.

The carbides are all more active than the parent metal for O_2 reduction and some activity is found even when the metal itself is inert, e.g. Zr, Hf, Ta, and Cr. Except for the titanium compounds, the nitrides are less active than the carbides. The apparent limiting currents (at + 150 mv) for Cr_3C_2, Fe_2C, NbC, and TaC were significantly higher than for graphite, implying that the carbides are more effective in reducing HO_2^-.

The highest activities were observed for TiN, VC, Fe_2C, and Ni_3C. The relative activity of TiN may be misleading since the material had a high surface area (540 $\mu f/cm^2$). The use of VC cathodes is impractical because of corrosion at high positive potentials. Fe_2C is apparently stable over the voltage range studied so that its use is not ruled out by corrosion problems.

The most active carbide was Ni_3C. Because it was studied as a high surface area powder, a rigorous comparison with the other materials is not possible. The BET surface area is difficult to interpret since the method also measures the area of the nickel metal present in the sample. Regardless of the source of the activity it is apparent that active electrodes of Ni_3C can be formed.

This material, the most active of the carbides studied, is approximately 150 - 200 mv less active than platinum. Therefore, the application of Ni_3C to practical working electrodes will have to be based on other factors. Perhaps the most obvious possibility is the development of electrodes with very high, stable surface areas. Alternatively, Ni_3C could be used as a support material for noble metals.

TABLE XXVIII

Performances of Nitrides and Carbides

		Current Density (ma/cm^2)		
Electrode	E_I	i(+500 mv)	i(+150 mv)	Capacitance $\mu f/cm^2$
Ti	+ 200	----	0. 24	100
TiN	+ 770	0. 27	1. 13	540
TiC	+ 820	0. 1	0. 26	220
Zr	----	----	----	---
ZrN	----	----	----	435
ZrC	+ 400	----	0. 48	46
Hf	----	----	----	2
HfN	+ 500	----	. 01	---
HfC	+ 500	----	0. 80	17
V	----	corrosion	----	---
VN	+ 180			> 500
VC	+ 820	0. 27	0. 50	61

TABLE XXVIII (Cont.)

Electrode	E_I	Current Density (ma/cm^2) i(+500 mv)	i(+150 mv)	Capacitance $\mu f/cm^2$
Nb	~ 270	corrosion	1.0	---
NbN	~ 270	----	0.4	---
NbC	+ 600	0.29	1.1	169
Ta	inert	----	----	---
TaN	+ 100	corrodes	----	---
TaC	+ 630	0.15	1.0	---
Cr	+ 200	----	.01	22
Cr_2N	+ 400	----	.01	266
Cr_3C_2	+ 600	0.3	1.1	---
Mo	corrosion			
Mo_2C	corrosion			
W	corrosion			
WC	corrosion			
WC-Co	corrosion			
Fe	+ 650	0.14	0.70	52
Fe_2C	+ 770	0.42	0.88	28
Ni				
Ni_3N	See Table XXVI			
Ni_3C				
Carbon (graphite)	+ 820	0.55	0.56	410

2. Silicides, Borides

The silicides and borides studied are listed in Table XXIX, together with comments on their corrosion behavior and O_2 electrode activity. (See also Figs. 119 - 155).

TABLE XXIX

Performances of Silicides and Borides

Electrode	Corrosion Behavior	E_I for O_2 Reduction
TiB_2	corrodes	< + 200
Ti_5Si_3	corrodes	< + 200
$TiSi_2$	corrodes	< + 700 mv
ZrB_2	high corrosion current	----
$ZrSi_2$	high corrosion current	----
VB_2	high corrosion current	----
VSi_2	high corrosion current	----
NbB	high corrosion current	----
NbB_2	high corrosion current	----
$NbSi_2$	corrodes less than NbB, by order of magnitude	----
TaB	high corrosion current	----
TaB_2	high corrosion current	----
Ta_5Si_3	low corrosion current	----
$TaSi_2$	higher corrosion current	----
CrB	Cathodic current above + 300; Anodic current below + 700	----
CrB_2	similar to CrB	----
Cr_5B_3	similar to CrB	+ 500
Cr_2B	low corrosion currents	low O_2 currents

TABLE XXIX

Electrode	Corrosion Behavior	E_I for O_2 Reduction
Cr_3B	similar to Cr_2B	----
Cr_4B	similar to Cr_2B	----
$CrSi_2$	very low corrosion below 1v	----
Cr_3Si	very low corrosion below 1v	
MoB	high corrosion currents above + 200	----
MoB_2	high corrosion currents above + 200	----
$MoSi_2$	high corrosion currents above + 200 (lower than MoB)	----
WB	high corrosion currents above + 100	----
W_2B	high corrosion currents above + 100	----
W_2B_5	high corrosion currents above + 100	----
WSi_2	high corrosion currents above 0	----
$MnSi_2$	high corrosion currents	
$CoSi_2$	corrosion	
Ni_2B	stable	+ 250
Ni_3B	stable	+ 150
Pt_2B	stable	+ 875
B_4C	stable	low, + 200

Discussion - Borides, Silicides

Corrosion currents are observed for the borides and silicides of the refractory metals. Of interest are the high corrosion rates for the borides and silicides of metals which are inert in 2N KOH, e.g. Zr, Hf, and Ta. Evidently, the normally passivating film of insoluble oxide is substantially modified by the nonmetallic constituent, more so than for carbon or nitrogen.

The chromium compounds are the most stable in this group, although a small amount of corrosion current is observed for the high boron-content compounds, i.e. CrB, CrB_2, and Cr_5B_3. The first two of these materials also show cathodic currents. It is tempting to assign this current to reduction of soluble chromate. However, the stirring in these experiments should remove from the surface chromate produced at high potentials.

Because of these high corrosion currents, the refractory metal borides and silicides cannot be considered as possible oxygen electrodes.

The group VIII borides studied (Ni_2B, Ni_3B, Pt_2B) were relatively resistant to corrosion although even in the case of Pt_2B, anodic current was observed at high potentials (Fig. 154). The measurement of O_2 activity indicated no enhancement due to the presence of boron.

D. Dispersed Electrodes

The floating electrode assembly was employed to evaluate catalysts which were in the form of powders rather than ingots. The design principles and operational techniques were described elsewhere in this report.

1. Calibration

The performance and reproducibility of the floating electrode assembly was determined by replicate runs on a commercially available platinum black (9 mg/cm^2) Teflon electrode material. Four samples were cut from the same sheet of material; samples 2 and 3 were run in duplicate. The current-voltage curves indicate variations of

$\pm$ 10 mv, at a current density of approximately 100 ma/cm^2. It was determined that these variations were due to random fluctuations of the partial pressure of water in the H_2 reference electrode compartment employed to calibrate the Dynamic Hydrogen Electrode. Presaturation of the dry hydrogen substantially decreased this scatter in data.

The performance of commercial electrodes operated in this test system are compared (Table XXX) to an "in-house" electrode prepared from Engelhard platinum black. All electrodes had approximately the same catalyst loading (9 mg/cm^2) bonded to metal screen with TFE.

TABLE XXX

Voltage-Current Performances of Pt Black Electrodes

Commercial Electrodes: A, B, C, 9 mg Pt/cm^2

In House Electrode: D, 10 mg Pt/cm^2

Voltage (IR Free) (mv vs RHE)	Current (ma/cm^2) A	B	C	D
975	6	8	9	25
950	22	25	32	48
925	52	68	86	104
900	140	242	254	256

2. Materials Testing

The materials listed in Table XXXI were studied as dispersed electrodes. The purpose was twofold: (a) to determine the inherent activity of the materials and (b) to determine the applicability of the structure to O_2 electrode catalysts other than platinum.

TABLE XXXI

Materials Studied as Dispersed Electrodes

	Fe_2C - Fe_3C
Pt-Au (60%)	Ni_3C
Pt-Au (40%)	NiO - Co_2O_3 spinel
PdAu (60%)	Ni_3N
PdAu (40%)	

These screening tests were performed without the presaturator assembly described above. As a result the data, although self consistent, cannot be compared directly to the performance figures given in Table XXXII.

"Alloys" of platinum-gold and palladium-gold were prepared by co-precipitation with $NaBH_4$. The performance of these materials as oxygen electrodes are summarized in Table XXXII; data for a platinum black electrode operated under identical conditions is also included. The BET surface areas of these materials were essentially 25 m^2/gm.

Porous silver electrodes were prepared by mixing Ag_2O powder and Teflon, spreading the mixture onto nickel screen, and sintering. The Teflon content was varied between 20% (Electrode A) and 15% (Electrode B); sintering temperatures of 250° (Electrodes A, B) and 350°C (Electrode C) were used. The Teflon content of electrode C was 15%. The performance data are summarized in Table XXXIII.

A low Teflon content and a high sintering temperature are obviously detrimental to electrode performance. Note that at high potentials, the silver electrodes are comparable to the commercial platinum electrodes.

TABLE XXXII

Voltage-Current Performances of Experimental Electrodes

Catalyst: Pt-Au (60%) Electrode A (29 mg/cm^2)
Pt-Au (40%) Electrode B (20 mg/cm^2)
Pd-Au (60%) Electrode C (20 mg/cm^2)
Pd-Au (40%) Electrode D (20 mg/cm^2)
Pt black Electrode E (29 mg/cm^2)

	Current (ma/cm^2)				
Voltage	A	B	C	D	E
975	20	14	15	14	20
950	45	40	30	30	45
925	90	90	75	65	90
900	160	180	140	130	160

TABLE XXXIII

Voltage-Current Performance of Experimental Electrodes
Catalyst: Silver (19 mg/cm^2)

	Current (ma/cm^2)		
Voltage	A	B	C
975	45	30	10
950	65	45	20
925	105	60	25
900	150	80	35
850	250	125	60

A number of iron carbides were prepared according to the techniques described previously. The electrodes prepared from these powders had high ohmic resistances, possibly due to oxidation of the iron. It is possible, of course, to correct the measurements for the IR drop; however, it is not possible to alter the effect of IR drop on the discharge kinetics of the porous electrode. In effect then, a high IR drop will limit the utilization of the catalyst and provide a higher activation polarization for a given current density. Thus the data resulting from this configuration represented lower limits to the activity of the materials studied.

Fe_2C - Fe_3C (prep. #4). This material shows some activity for O_2 reduction (80 ma/cm^2 at 745 mv) but also exhibits a high ohmic resistance.

Fe_3C (prep. #6). Some activity was also observed (80 ma/cm^2 at 670 mv); this electrode also involves a high IR drop.

Fe_3C (prep. #7). This material shows approximately no O_2 activity ($\sim$ 2 ma/cm^2 at 650 mv) and appears to dissolve in KOH.

The voltage-current curves obtained for iron carbide in these experiments compare well, in form, to the data obtained with the rotating disc assembly.

Ni_3N and Ni_3C were also studied; their performance was discussed elsewhere in this report. Ni_3C was the most active of the carbides tested, e.g. generating 185 ma/cm^2 at +700 mv. The IR drop was comparable to that observed for metal electrodes.

As indicated, it was possible to form the spinel $NiO \cdot Co_2O_3$. An electrode was constructed from 3 parts spinel powder and 1 part nickel powder. The performance of this material was low (1 ma/cm^2 at 700 mv), being approximately equivalent to that of nickel powder.

Discussion

It is apparent from the data (a) that the floating electrode system will yield reproducible results for testing O_2 electrodes and (b) that platinum black electrodes can be constructed "in house" which are equal in performance to commercial electrodes.

Electrodes prepared from co-precipitated Pt-Au alloys are essentially equal in performance to platinum black electrodes. Both palladium-gold alloys, although active, are inferior to platinum and platinum-gold.

Active silver electrodes were also prepared. The data in Table XXXIII, judged in terms of the rotating disc work described elsewhere in this report, emphasizes the importance of the proper electrode configuration. The initial activity observed with the porous structure was comparable to platinum electrodes, although a somewhat higher silver loading was used.

Electrodes prepared from iron and nickel carbides were substantially less active than those prepared from platinum. The data for the iron carbides do not represent a true evaluation of the material because of the high ohmic resistance.

Little activity was observed for the nickel-cobalt spinel. This result is anomalous, since the results of others indicate that this material should be an active catalyst.

E. Continuum vs. Atomic Factors

The experiments carried out in this screening program were concerned almost entirely with the influence of alloy or compound formation on the intrinsic catalytic activity for the electrochemical reduction of oxygen. Structural effects, such as the preferential development or stabilization of a high surface area, were generally not considered.

From the data assembled it is not possible to assign O_2 electrode activity to a particular crystal structure or stoichiometry. In this sense then we have not demonstrated the validity of the continuum approach. However, a number of alloys and interstitials showed properties which were substantially different from those of the pure metals. For example, niobium in PtNb does not behave as pure niobium; TiN shows more activity for O_2 reduction than Ti; other examples are given in Section I of this report. These results suggest that a "continuum approach" is probably appropriate; i.e. activity for O_2 reduction must be considered as a property of the alloy and not of either of the constituents.

VI. REFERENCES

1. For an excellent summary, see D. J. G. Ives in "Reference Electrodes", Ed. by D. J. G. Ives and G. J. Janz, Academic Press, New York, 1961, p. 360. Other references include: M. L. B. Rao, A. Damjanovic, and J. O' M. Bockris, J. Phys. Chem. 67, 2508 (1963); J. P. Hoare, J. Electroch. Soc. 111, 232 (1964); A. Krause, J. Slawck, Z. Winowski, Z. Physik. Chem. 40, 261 (1964).
2. See ref. (1); also: E. Yaeger, P. Krause, K. V. Rao, U. S. Comm. Dept. 409, 121 (1963).
3. M. Stern, A. C. Makrides, J. Electroch. Soc. 107, 782 (1960).
4. J. Giner, J. Electroch. Soc. 111, 377 (1964).
5. J. Giner, S. Smith, in press.
6. J. F. Schultz, L. J. H. Hofer, E. M. Cohn, K. C. Stein and R. B. Anderson, Bureau of Mines Bulletin No. 578.
7. J. F. Schultz, L. J. H. Hofer, K. C. Stein, and R. B. Anderson, Bureau of Mines Bulletin No. 612.
8. K. J. Jack, Proc. Roy. Soc. (London) A195, 34 (1948); ibid A195, 41 (1948), and ibid A195, 56 (1948).
9. R. Juza, W. Sachze, Z. Inorg. Chemie, 251, 201 (1943).
10. G. Rienacker, K. Hohl, ibid. 333, 291 (1964).
11. J. Leicester, M. Redmen, J. Appl. Chem., 12, 357 (1962).
12. M. Bahr, T. Bahr, Berichte, 63, 99 (1930).
13. J. Freel, A. K. Galway, Nature 208, 183 (1965).
14. A. K. Galway, J. Chem. Soc. 88, 87 (1966).
15. M. Bahr, V. Jessen, Ber. 63, 2226 (1930).
16. L. J. Hofer, W. Peebles, J. Am. Chem. Soc. 69, 893 (1947).
17. J. Clarke, K. Jack, Chem. & Ind., 1004 (1951).
18. R. Parsons, Trans. Far. Soc. 47, 1332 (1951).
19. M. Pourbaix, "Atlas D' Equilibres E' lectrochimiques" Gauthier-Villars, Paris (1963).

APPENDIX A

PERFORMANCE CURVES

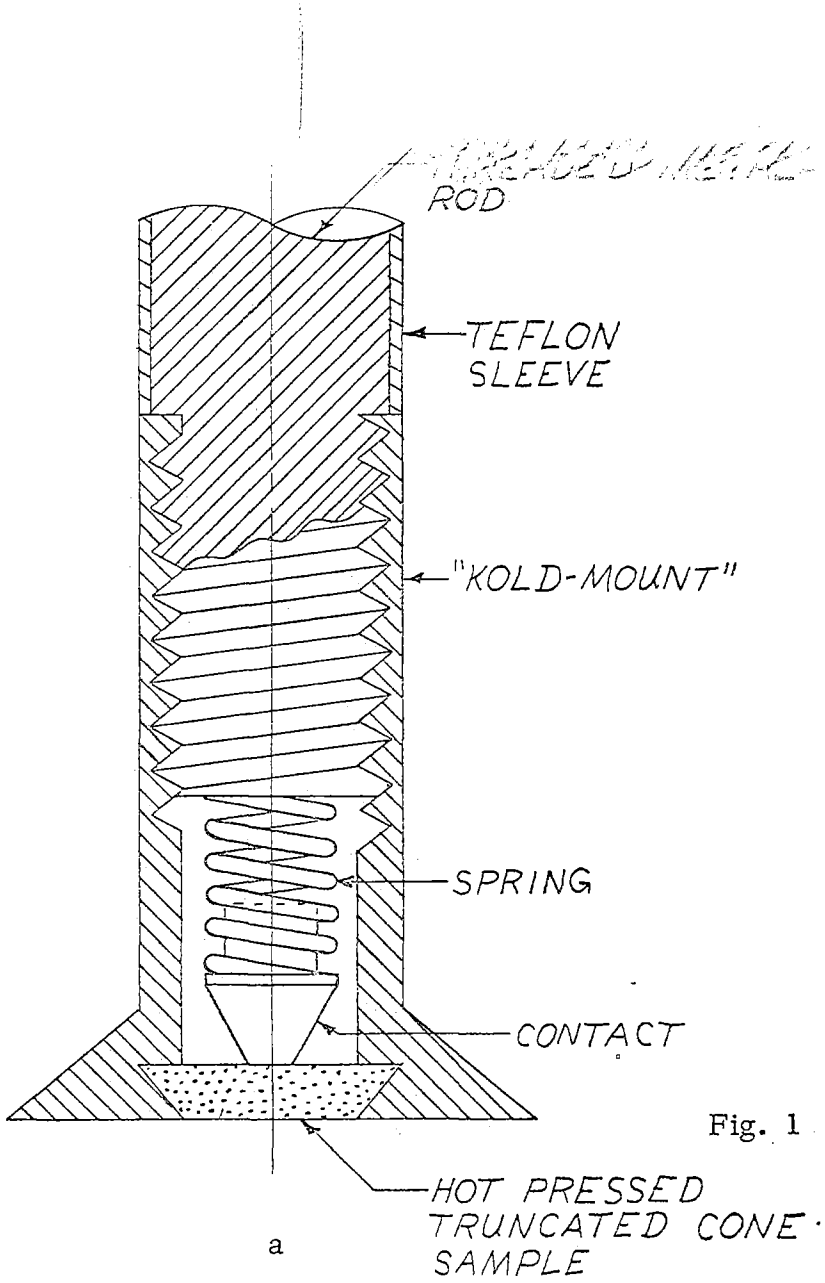
ROD
TEFLON SLEEVE
"KOLD-MOUNT"
SPRING
CONTACT
HOT PRESSED TRUNCATED CONE SAMPLE

a

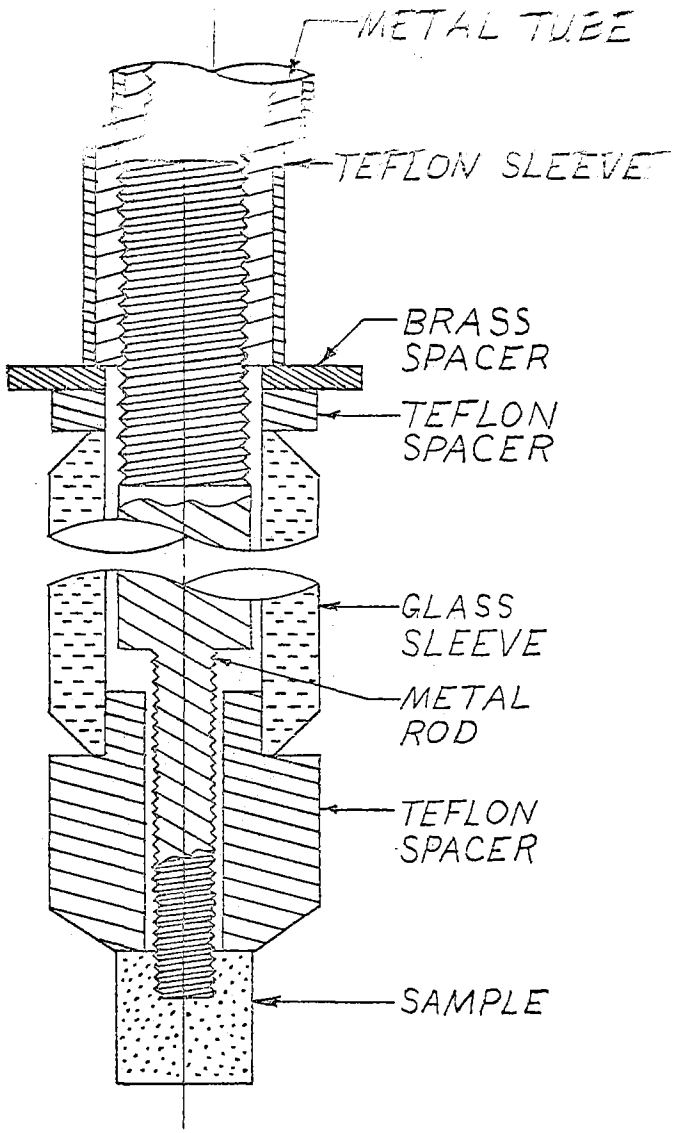
METAL TUBE
TEFLON SLEEVE
BRASS SPACER
TEFLON SPACER
GLASS SLEEVE
METAL ROD
TEFLON SPACER
SAMPLE

b

Fig. 1

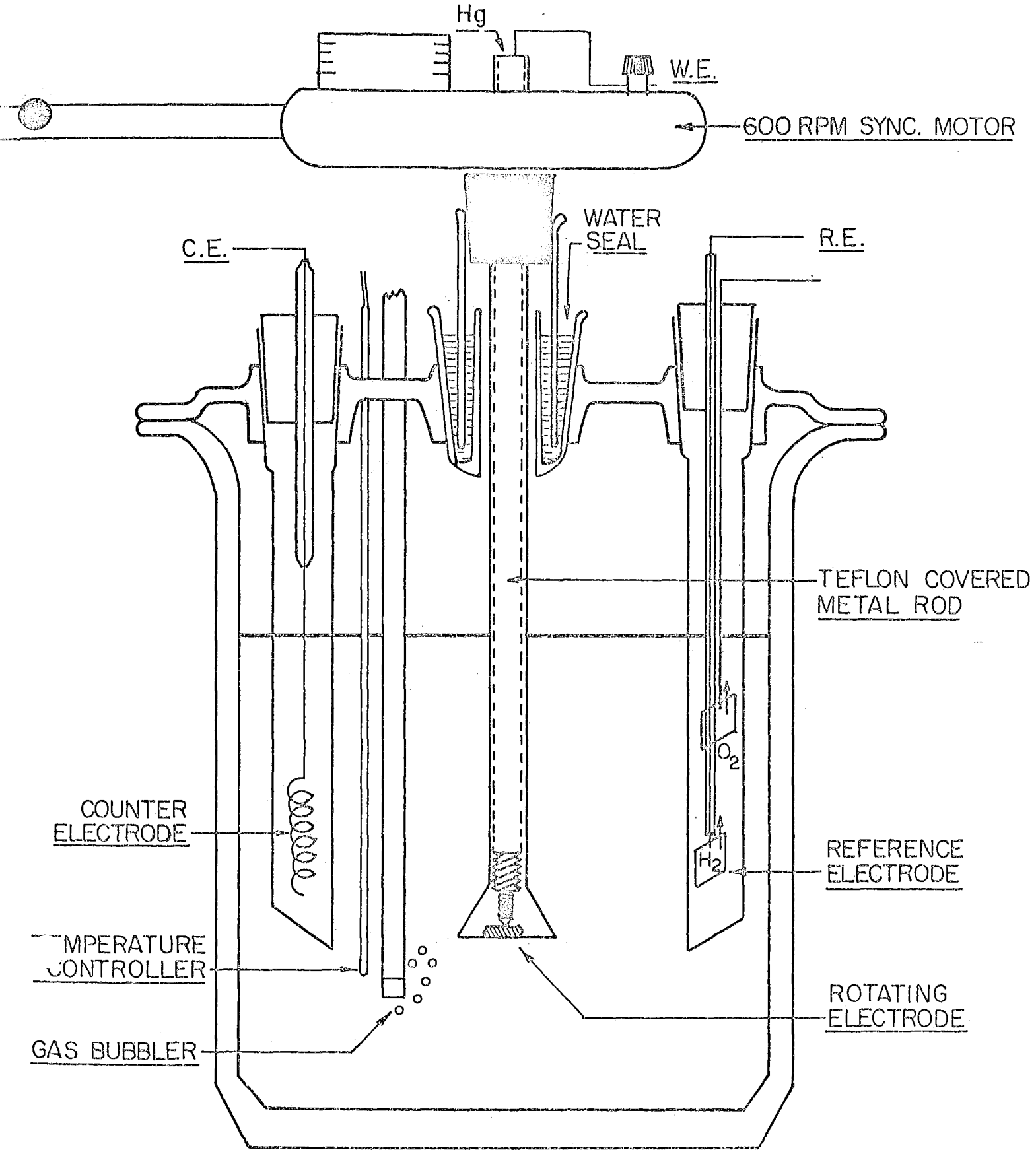

ROTATING ELECTRODE CELL

Fig. 2

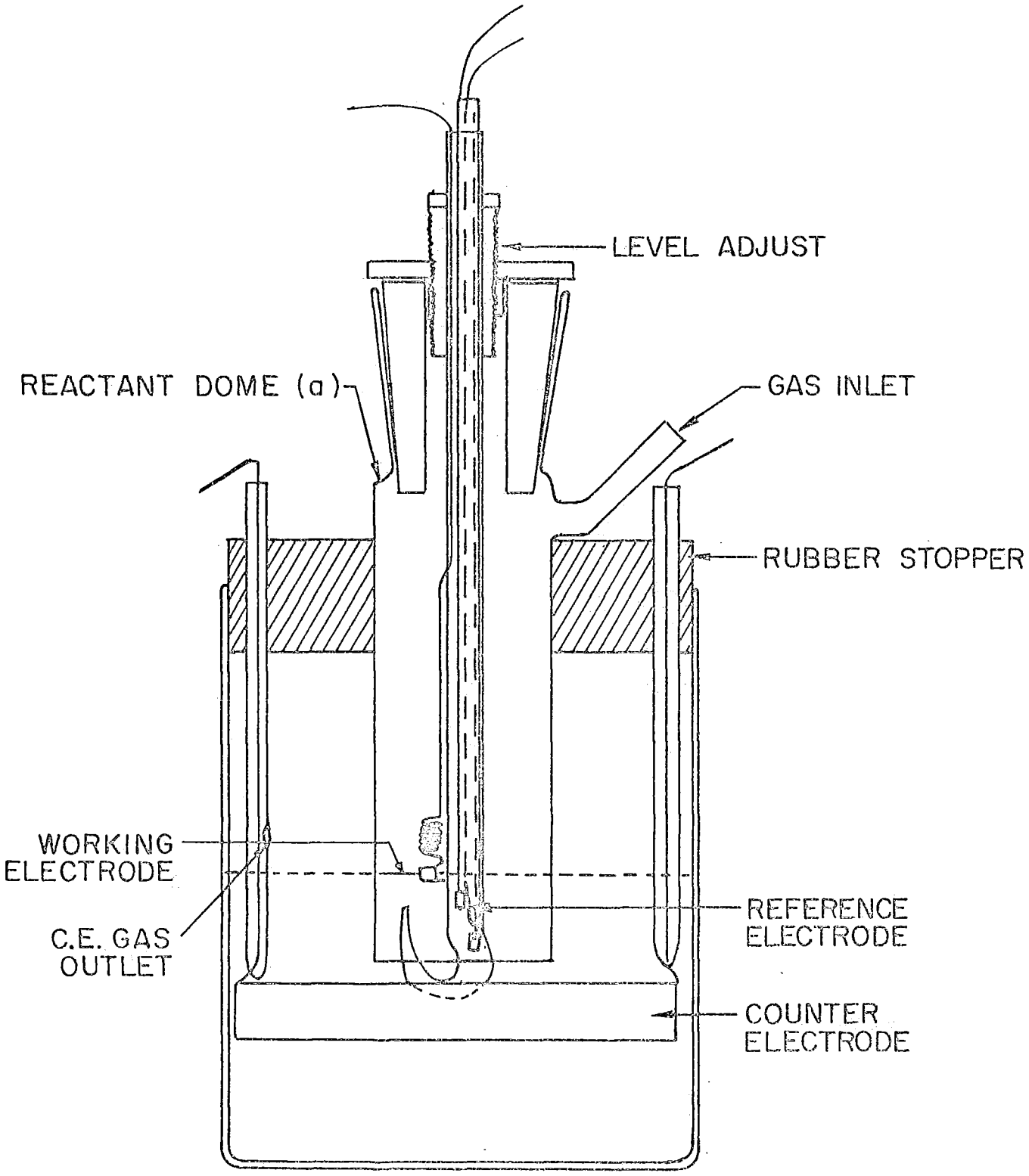

FLOATING ELECTRODE CELL FOR THE MEASUREMENT OF ACTIVITY OF HYDROPHOBIC POROUS ELECTRODES

Fig. 3

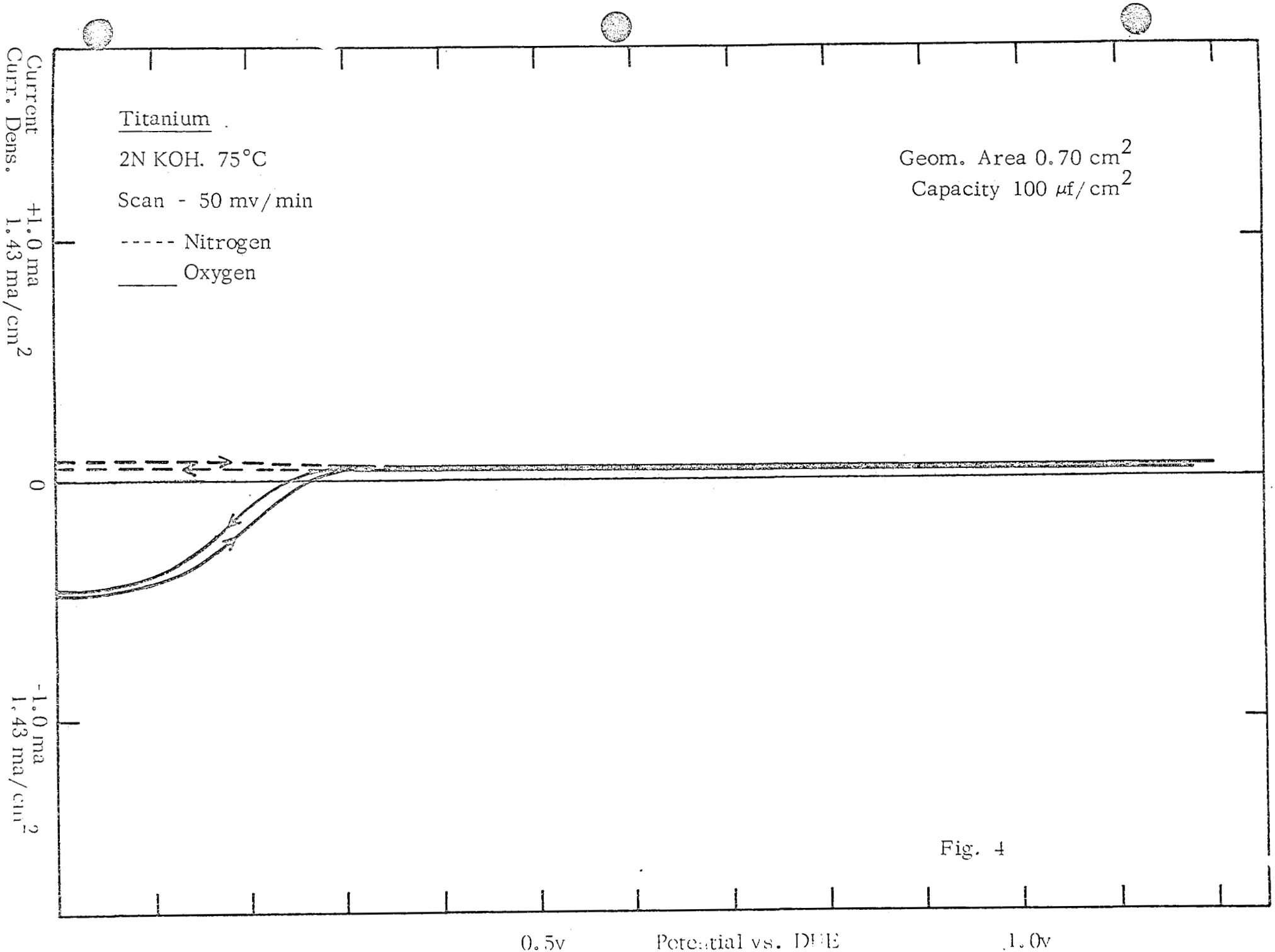
Titanium
2N KOH. 75°C
Scan - 50 mv/min
----- Nitrogen
_____ Oxygen
Geom. Area 0.70 cm2
Capacity 100 μf/cm2
Current
Curr. Dens.
+1.0 ma
1.43 ma/cm2
0
-1.0 ma
1.43 ma/cm2
0.5v
Potential vs. DHE
1.0v

Fig. 4

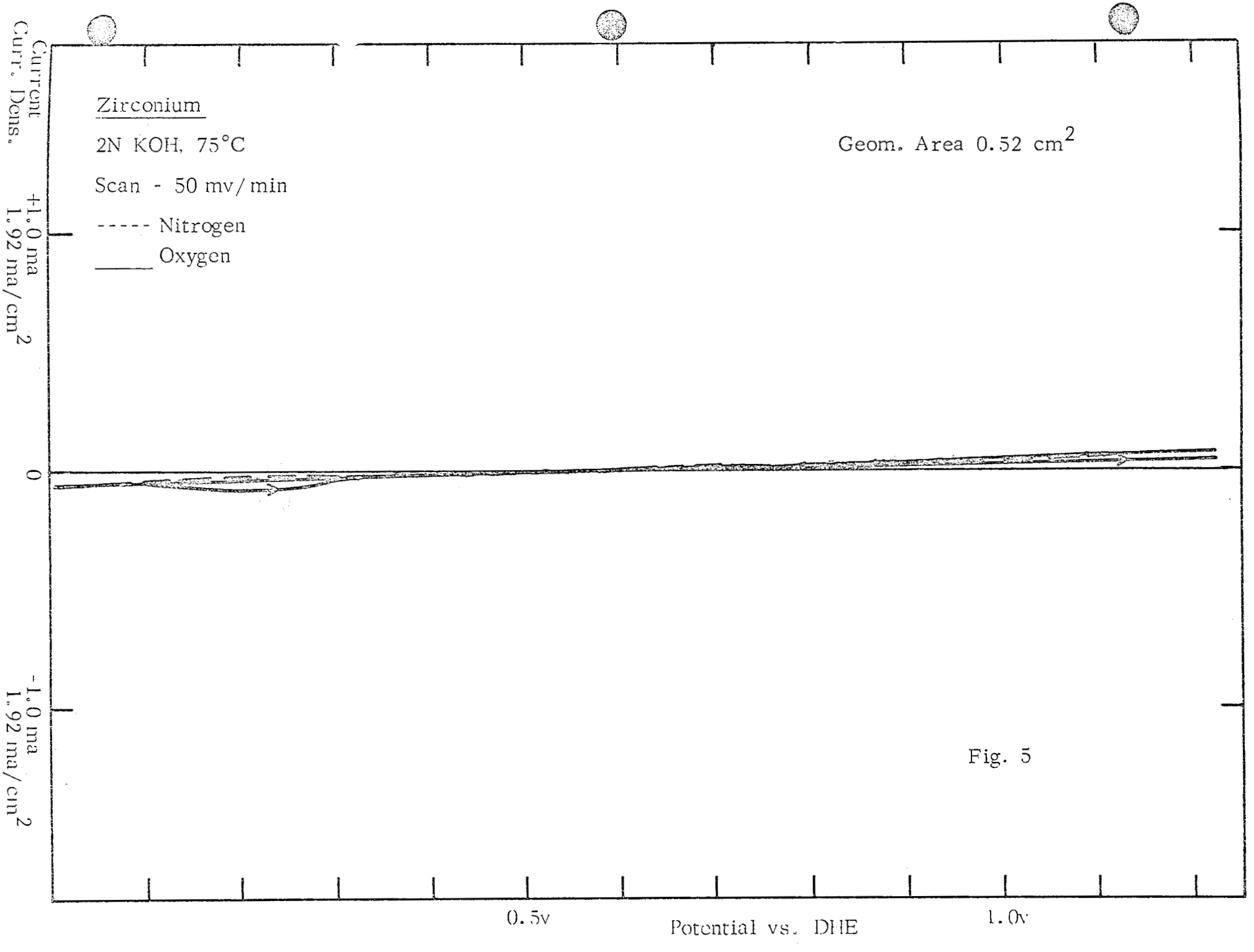
Zirconium
2N KOH, 75°C
Scan - 50 mv/min
----- Nitrogen
_____ Oxygen
Geom. Area 0.52 cm2
Current
Curr. Dens.
+1.0 ma
1.92 ma/cm2
0
-1.0 ma
1.92 ma/cm2
0.5v
1.0v
Potential vs. DHE

Fig. 5

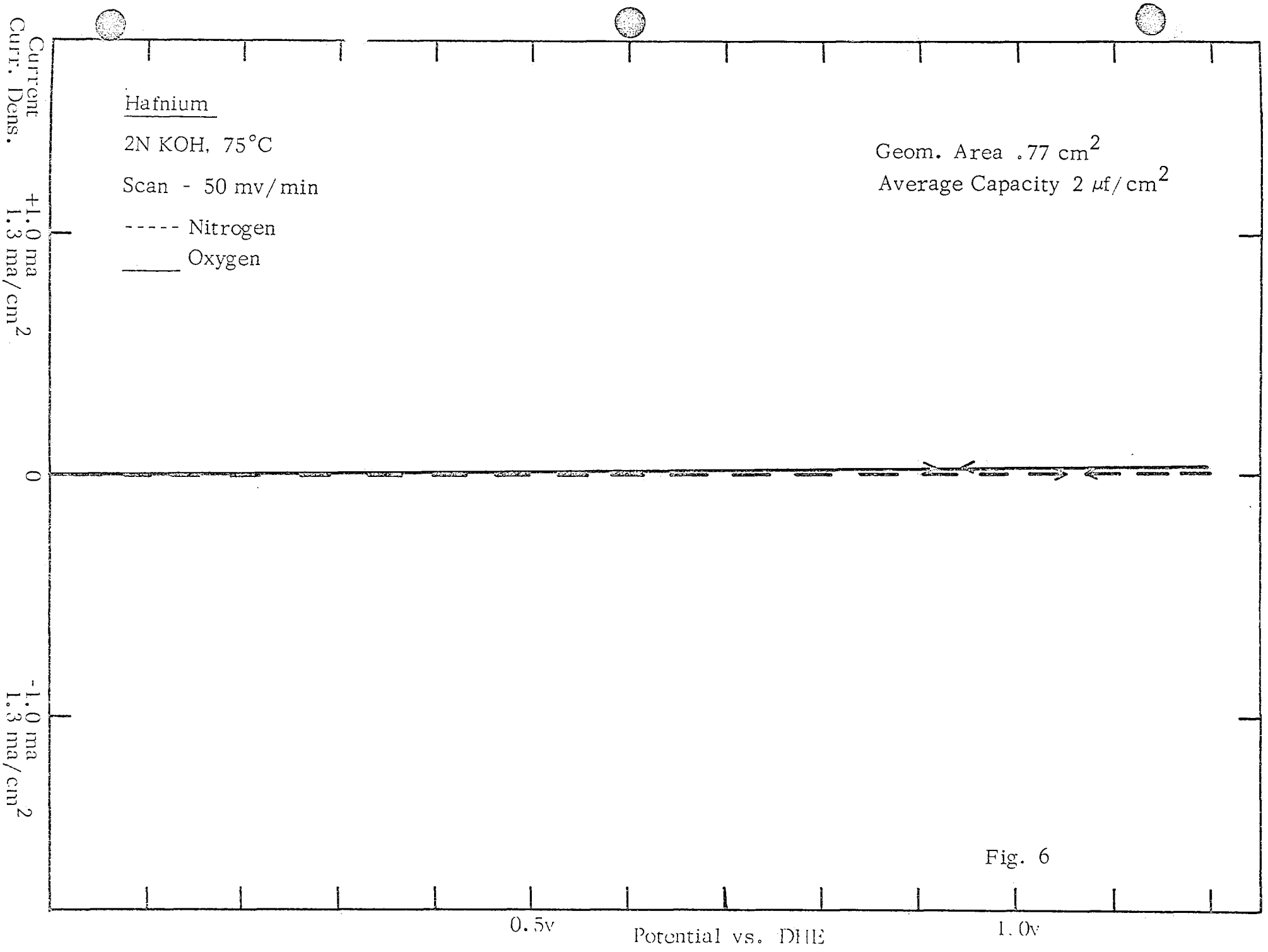
Hafnium
2N KOH, 75°C
Scan - 50 mv/min
----- Nitrogen
_____ Oxygen
Geom. Area .77 cm2
Average Capacity 2 μf/cm2
Current Curr. Dens.
+1.0 ma 1.3 ma/cm2
0
-1.0 ma 1.3 ma/cm2
0.5v
Potential vs. DHE
1.0v

Fig. 6

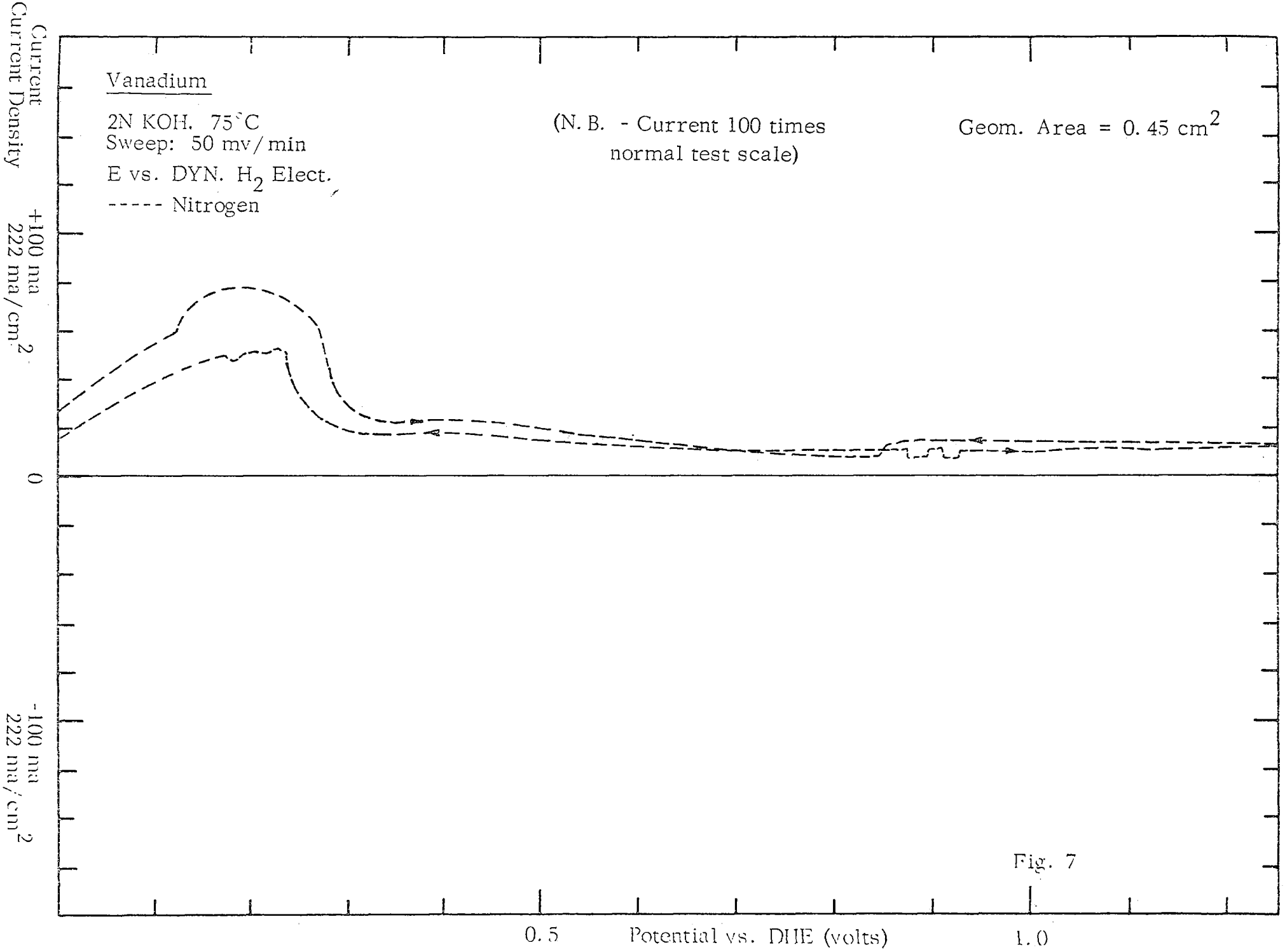
Vanadium
2N KOH. 75°C
Sweep: 50 mv/min
E vs. DYN. H_2 Elect.
----- Nitrogen
(N. B. - Current 100 times normal test scale)
Geom. Area = 0.45 cm^2
Current Density
+100 ma
222 ma/cm^2
0
-100 ma
222 ma/cm^2
0.5
Potential vs. DHE (volts)
1.0

Fig. 7

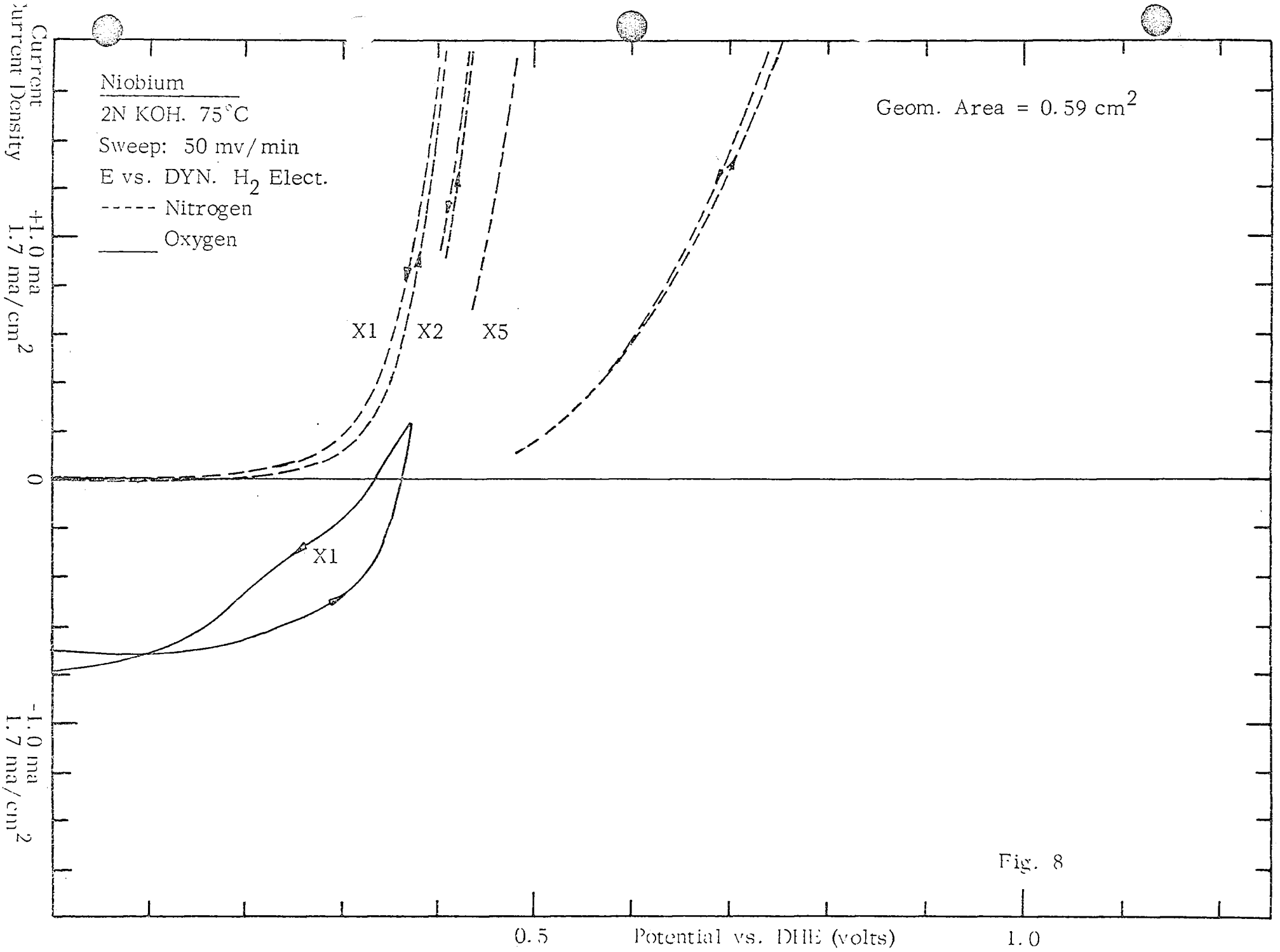
Niobium
2N KOH. 75°C
Sweep: 50 mv/min
E vs. DYN. H_2 Elect.
----- Nitrogen
_____ Oxygen
Geom. Area = 0.59 cm^2
X1
X2
X5
X1
Current Density
+1.0 ma
1.7 ma/cm^2
0
-1.0 ma
1.7 ma/cm^2
0.5
Potential vs. DHE (volts)
1.0

Fig. 8

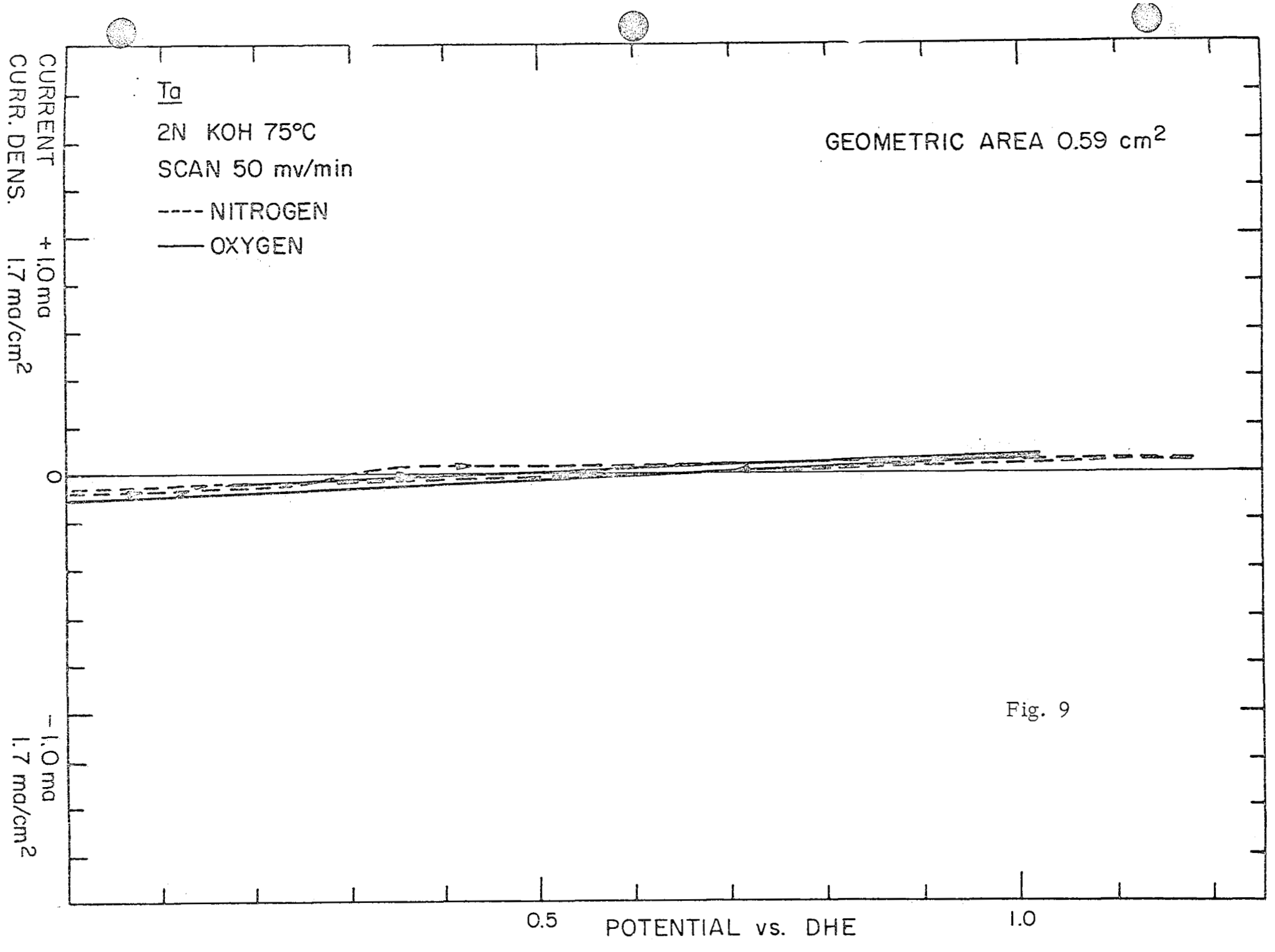
Ta
2N KOH 75°C
SCAN 50 mv/min
---- NITROGEN
—— OXYGEN
GEOMETRIC AREA 0.59 cm2
CURRENT
CURR. DENS.
+1.0 ma
1.7 ma/cm2
0
-1.0 ma
1.7 ma/cm2
0.5
POTENTIAL vs. DHE
1.0

Fig. 9

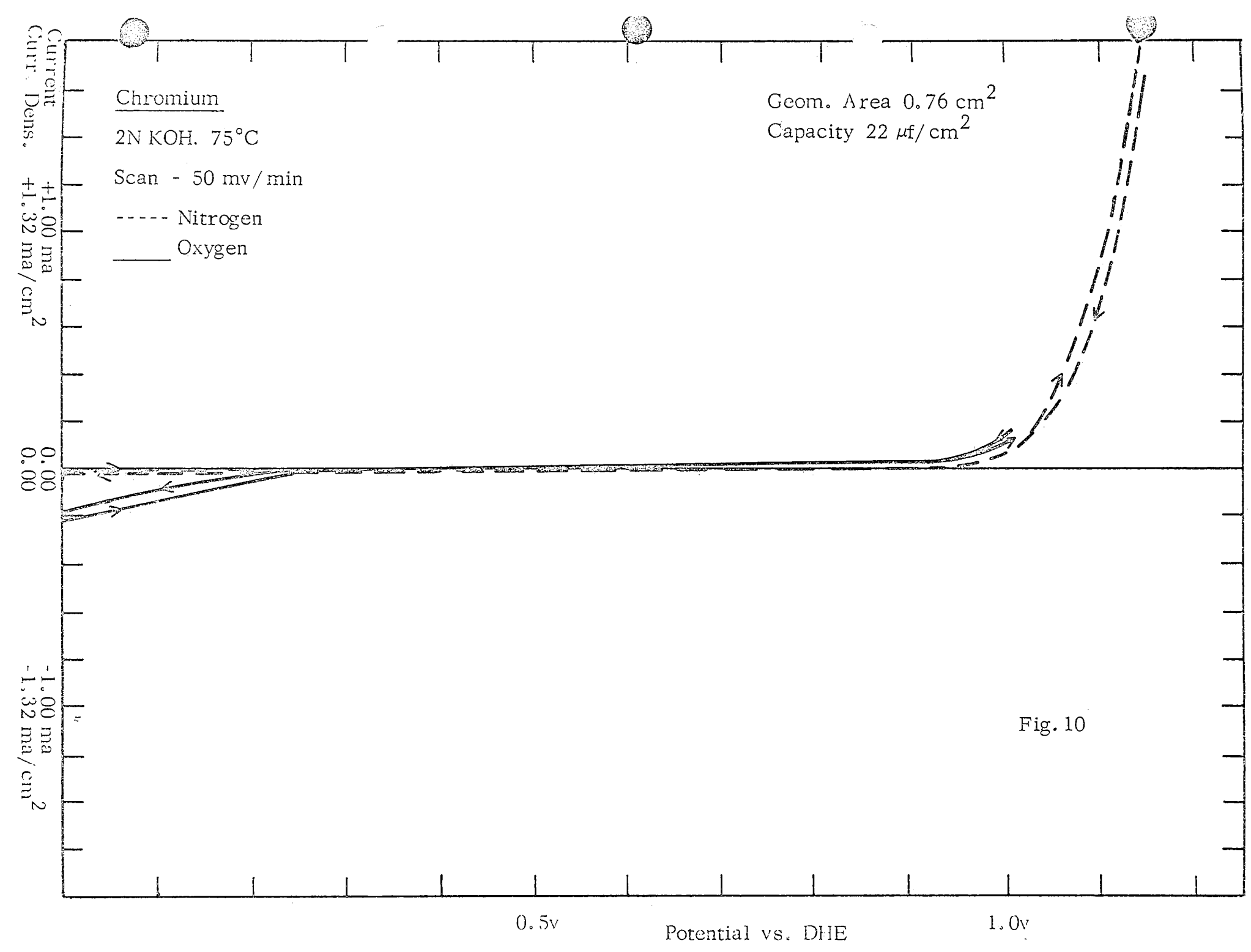
Chromium
2N KOH. 75°C
Scan - 50 mv/min
----- Nitrogen
_____ Oxygen
Geom. Area 0.76 cm²
Capacity 22 μf/cm²
Current
Curr. Dens.
+1.00 ma
+1.32 ma/cm²
0.00
0.00
-1.00 ma
-1.32 ma/cm²
0.5v
Potential vs. DHE
1.0v

Fig. 10

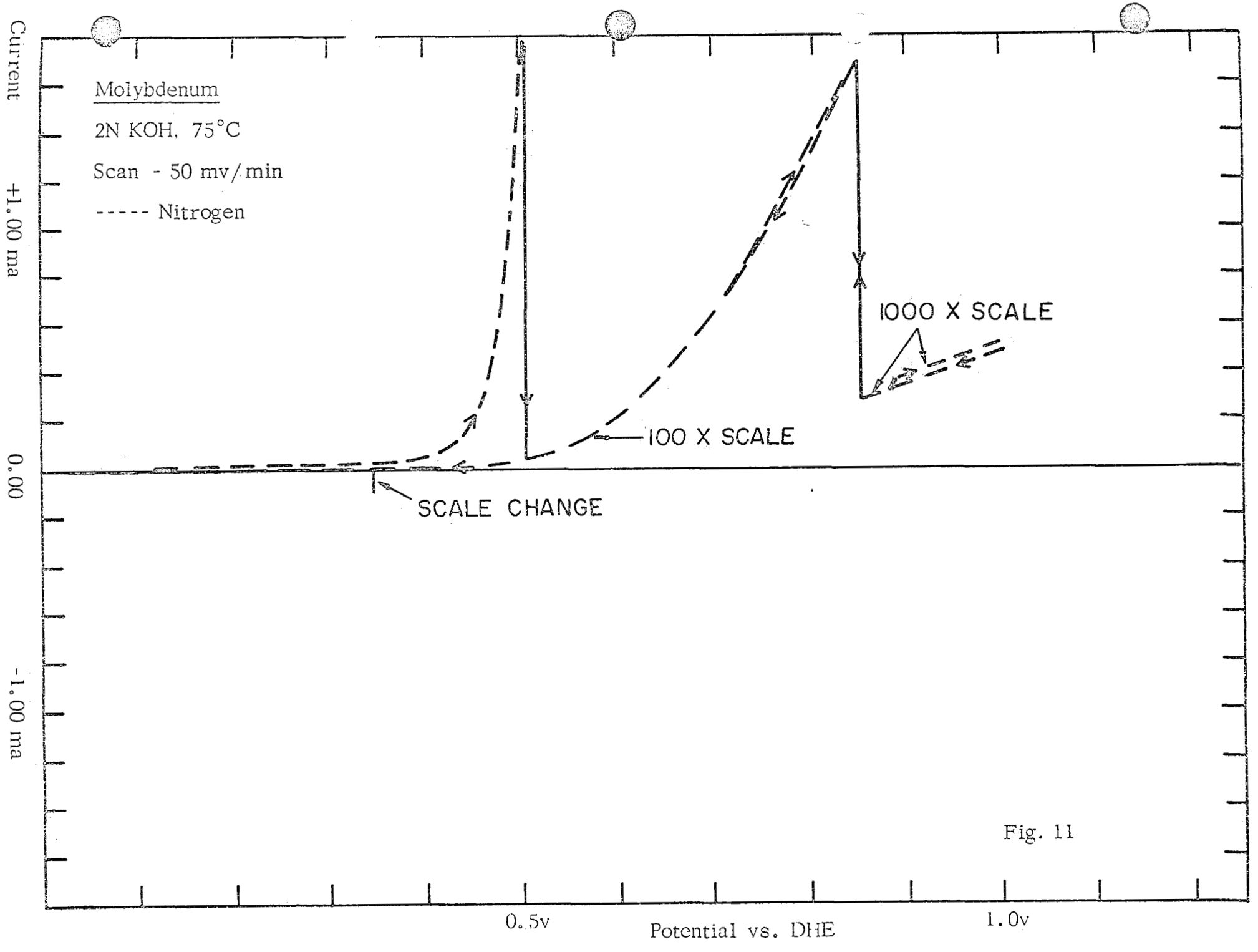
Molybdenum
2N KOH, 75°C
Scan - 50 mv/min
----- Nitrogen
1000 X SCALE
100 X SCALE
SCALE CHANGE
Current
+1.00 ma
0.00
-1.00 ma
0.5v
Potential vs. DHE
1.0v

Fig. 11

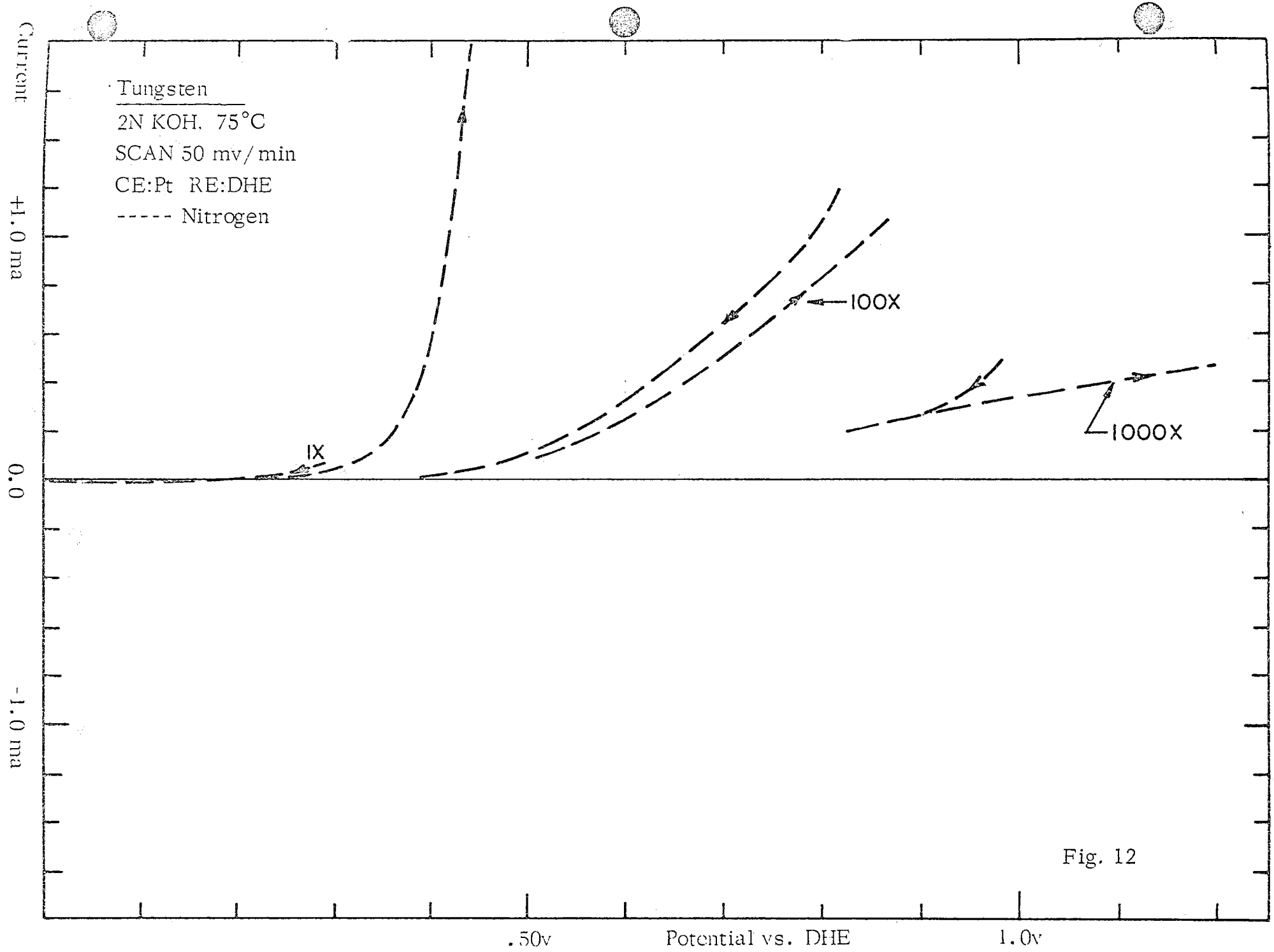
Tungsten
2N KOH. 75°C
SCAN 50 mv/min
CE:Pt RE:DHE
----- Nitrogen
1X
100X
1000X
Current
+1.0 ma
0.0
-1.0 ma
.50v
Potential vs. DHE
1.0v

Fig. 12

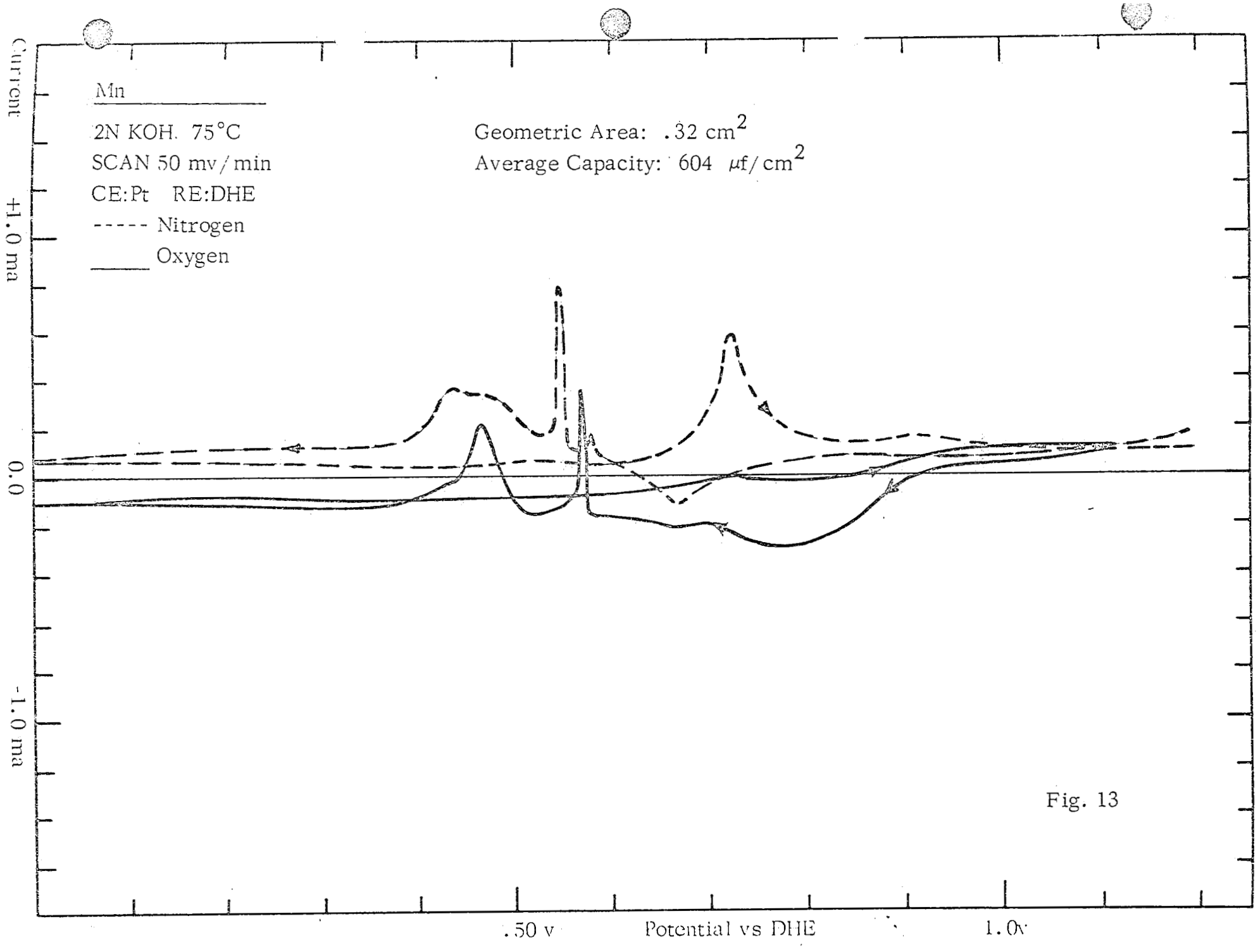
Mn
2N KOH. 75°C
SCAN 50 mv/min
CE:Pt RE:DHE
----- Nitrogen
_____ Oxygen
Geometric Area: .32 cm2
Average Capacity: 604 μf/cm2
Current
+1.0 ma
0.0
-1.0 ma
.50 v
Potential vs DHE
1.0v

Fig. 13

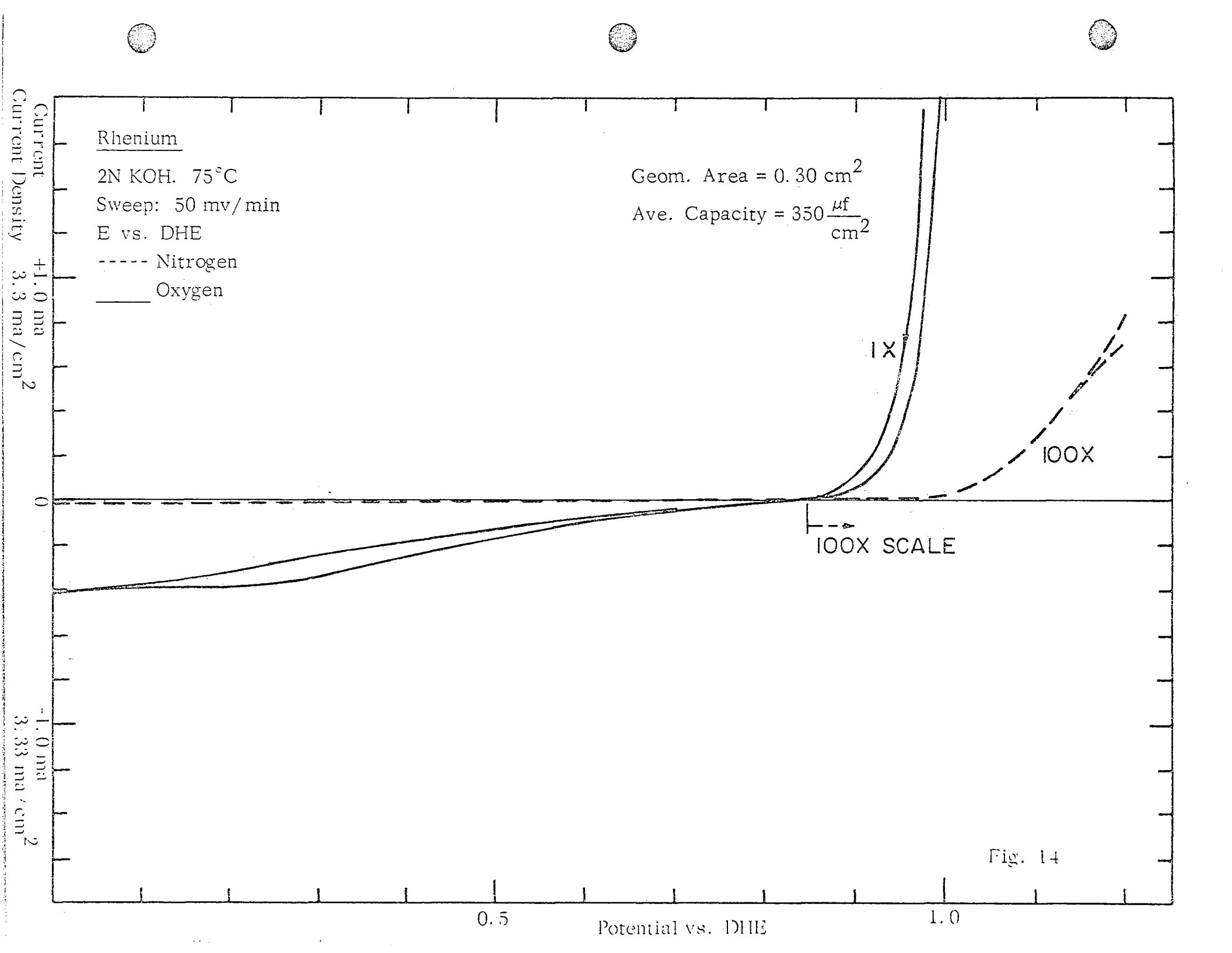
Rhenium
2N KOH. 75°C
Sweep: 50 mv/min
E vs. DHE
----- Nitrogen
_____ Oxygen
Geom. Area = 0.30 cm²
Ave. Capacity = 350 μf/cm²
1X
100X
100X SCALE
Current Density
+1.0 ma
3.3 ma/cm²
0
-1.0 ma
3.33 ma/cm²
0.5
1.0
Potential vs. DHE

Fig. 14

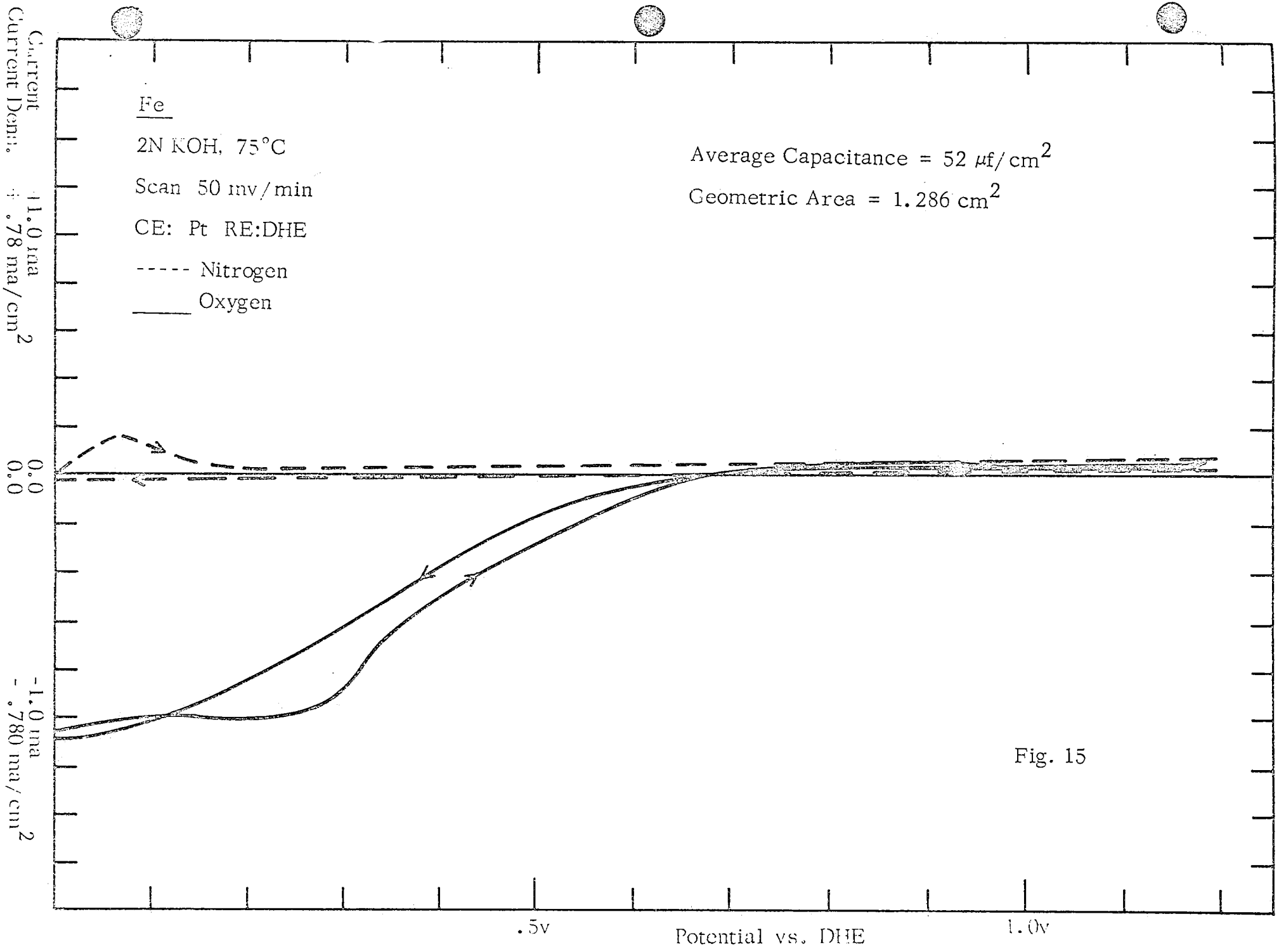
Fe
2N KOH, 75°C
Scan 50 mv/min
CE: Pt RE:DHE
----- Nitrogen
_____ Oxygen
Average Capacitance = 52 μf/cm²
Geometric Area = 1.286 cm²
Current Density
+1.0 ma
+ .78 ma/cm²
0.0
0.0
-1.0 ma
- .780 ma/cm²
.5v
Potential vs. DHE
1.0v

Fig. 15

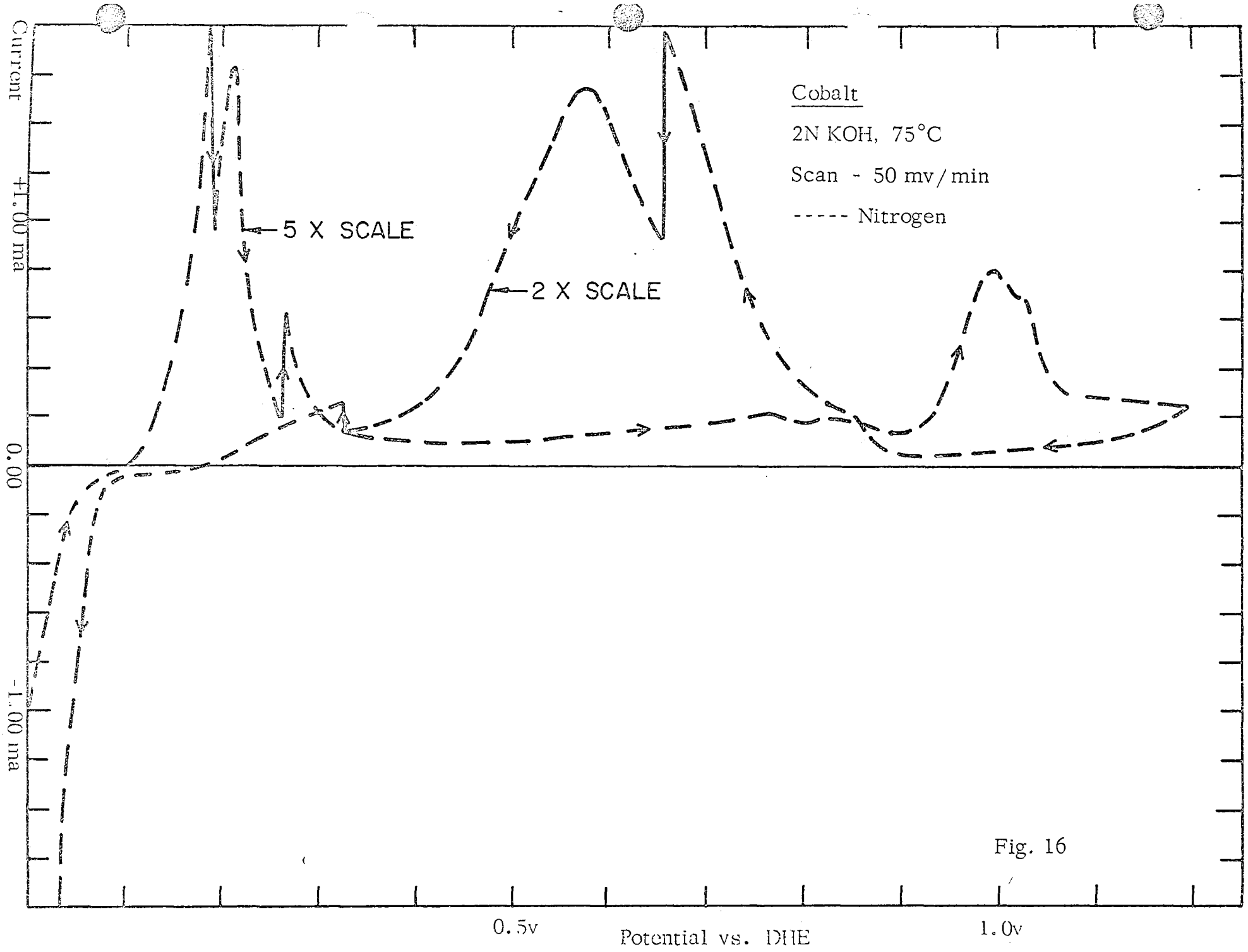
Current
+1.00 ma
0.00
-1.00 ma
5 X SCALE
2 X SCALE
Cobalt
2N KOH, 75°C
Scan - 50 mv/min
----- Nitrogen
0.5v
1.0v
Potential vs. DHE

Fig. 16

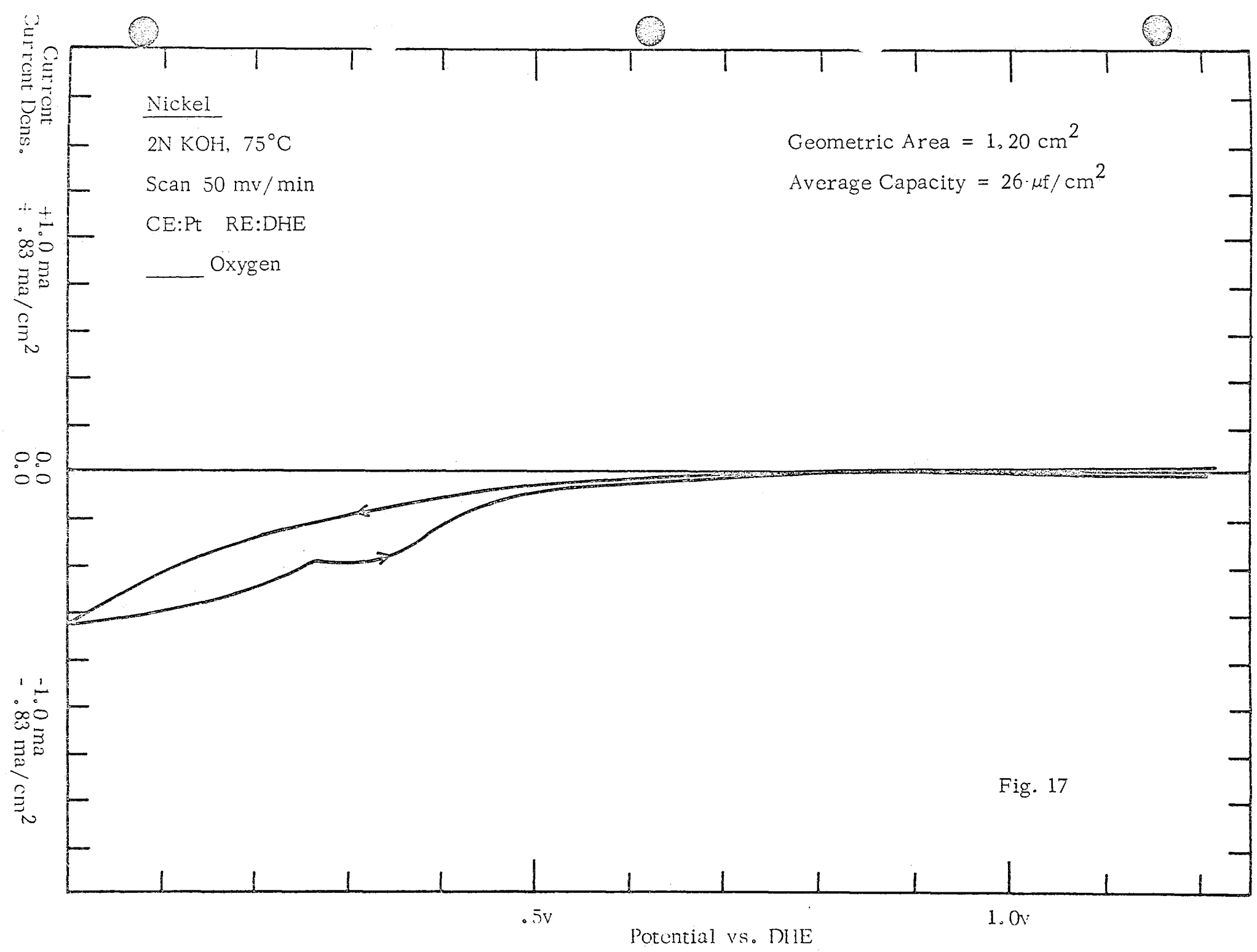
Nickel
2N KOH, 75°C
Scan 50 mv/min
CE:Pt RE:DHE
Oxygen
Geometric Area = 1.20 cm²
Average Capacity = 26 μf/cm²
Current Dens.
+1.0 ma
+ .83 ma/cm²
0.0
0.0
-1.0 ma
- .83 ma/cm²
.5v
1.0v
Potential vs. DHE

Fig. 17

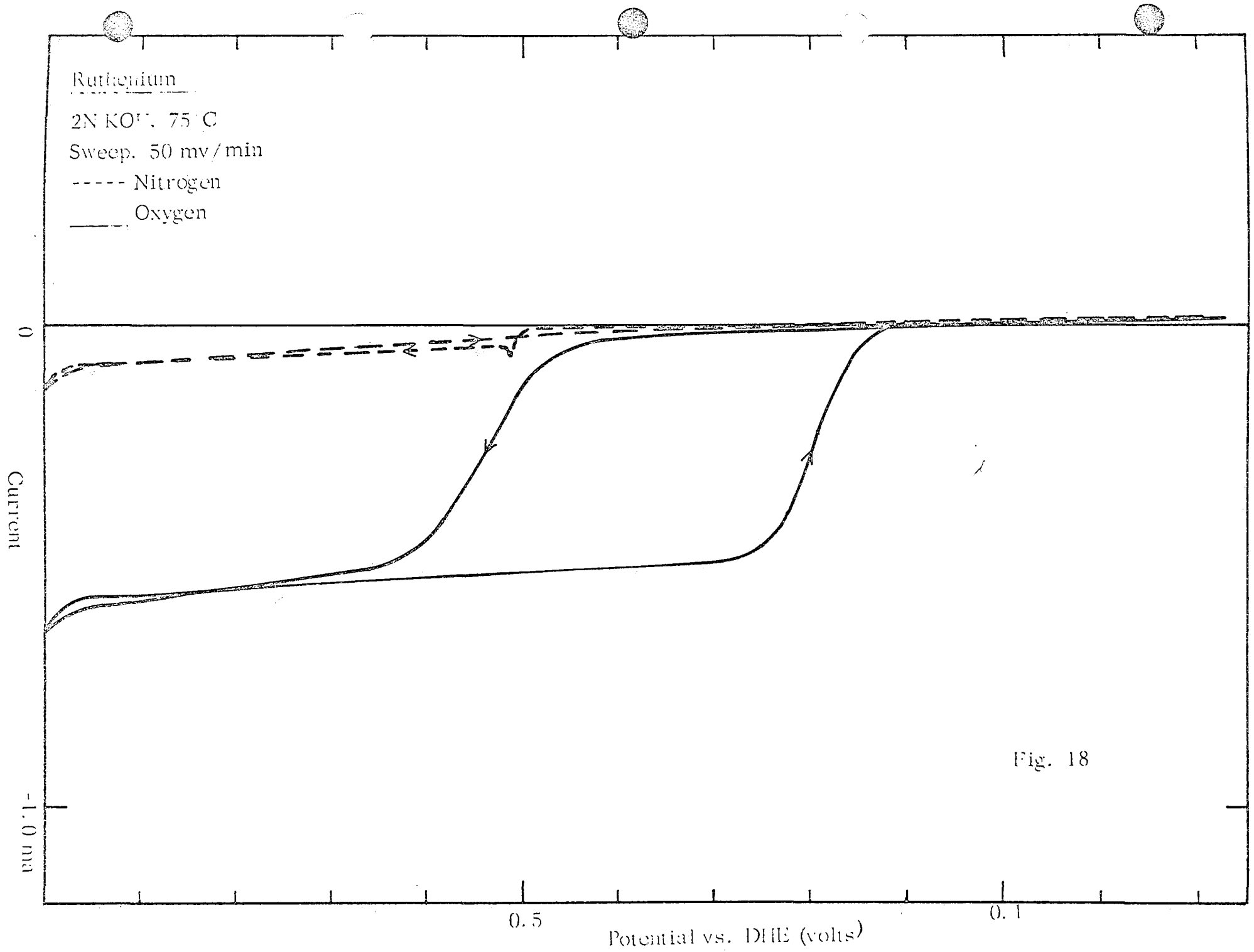
Ruthenium
2N KOH, 75° C
Sweep. 50 mv/min
----- Nitrogen
_____ Oxygen
0
Current
-1.0 ma
0.5
0.1
Potential vs. DHE (volts)

Fig. 18

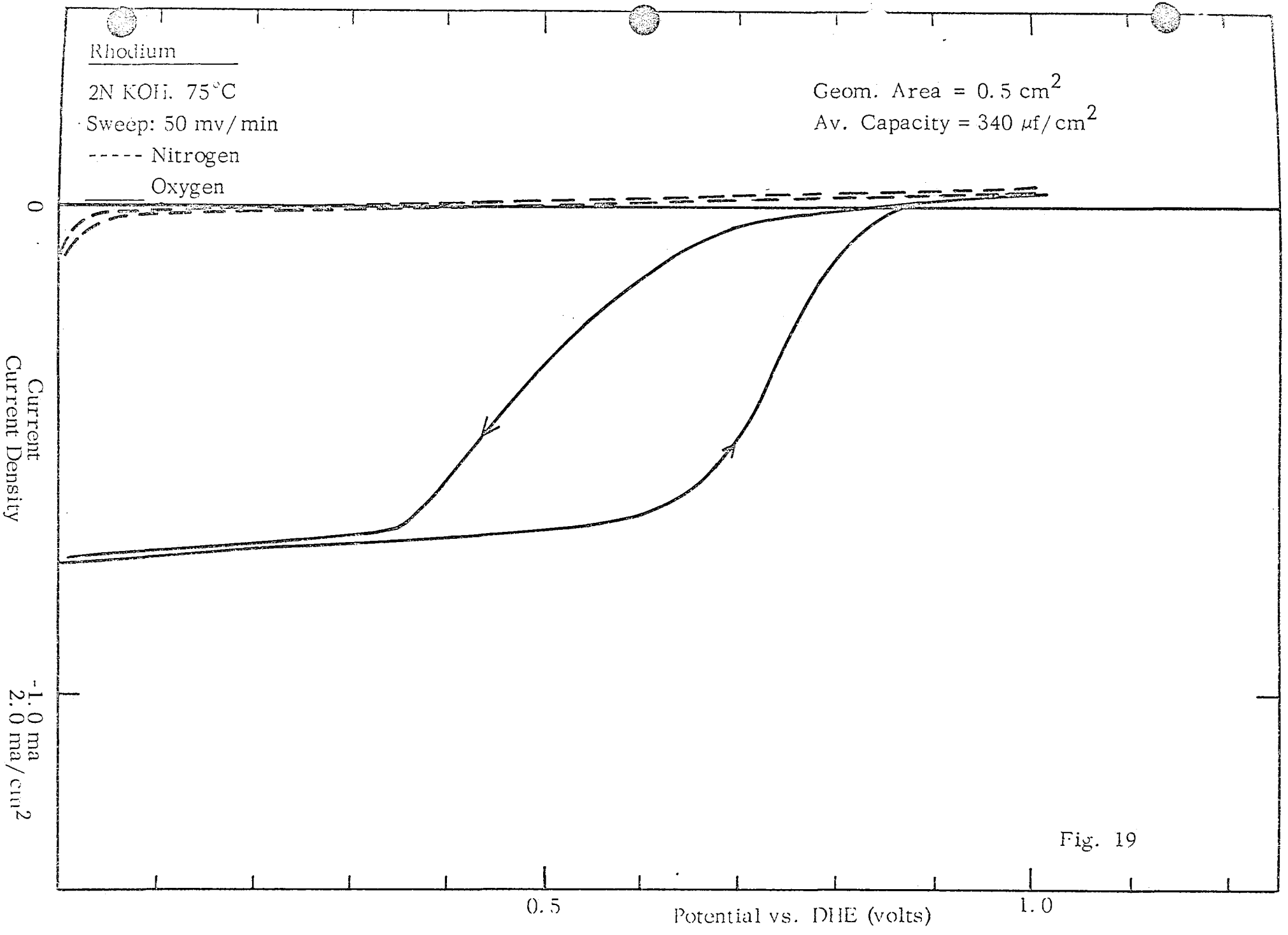
Rhodium
2N KOH. 75°C
Sweep: 50 mv/min
----- Nitrogen
Oxygen
Geom. Area = 0.5 cm²
Av. Capacity = 340 μf/cm²
0
Current
Current Density
-1.0 ma
2.0 ma/cm²
0.5
1.0
Potential vs. DHE (volts)

Fig. 19

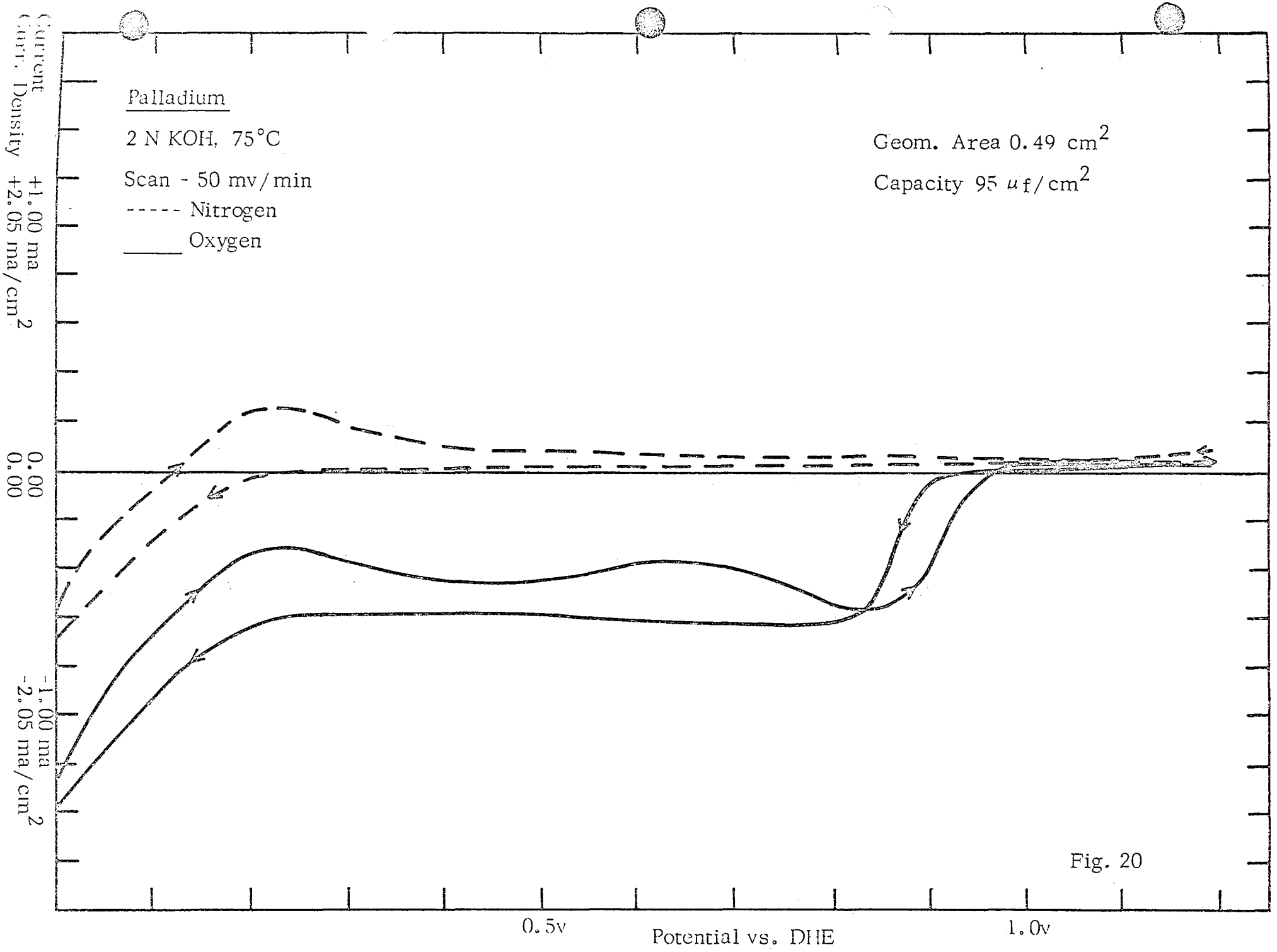
Palladium
2 N KOH, 75°C
Scan - 50 mv/min
----- Nitrogen
_____ Oxygen
Geom. Area 0.49 cm2
Capacity 95 μf/cm2
Current Density
+1.00 ma
+2.05 ma/cm2
0.00
0.00
-1.00 ma
-2.05 ma/cm2
0.5v
Potential vs. DHE
1.0v

Fig. 20

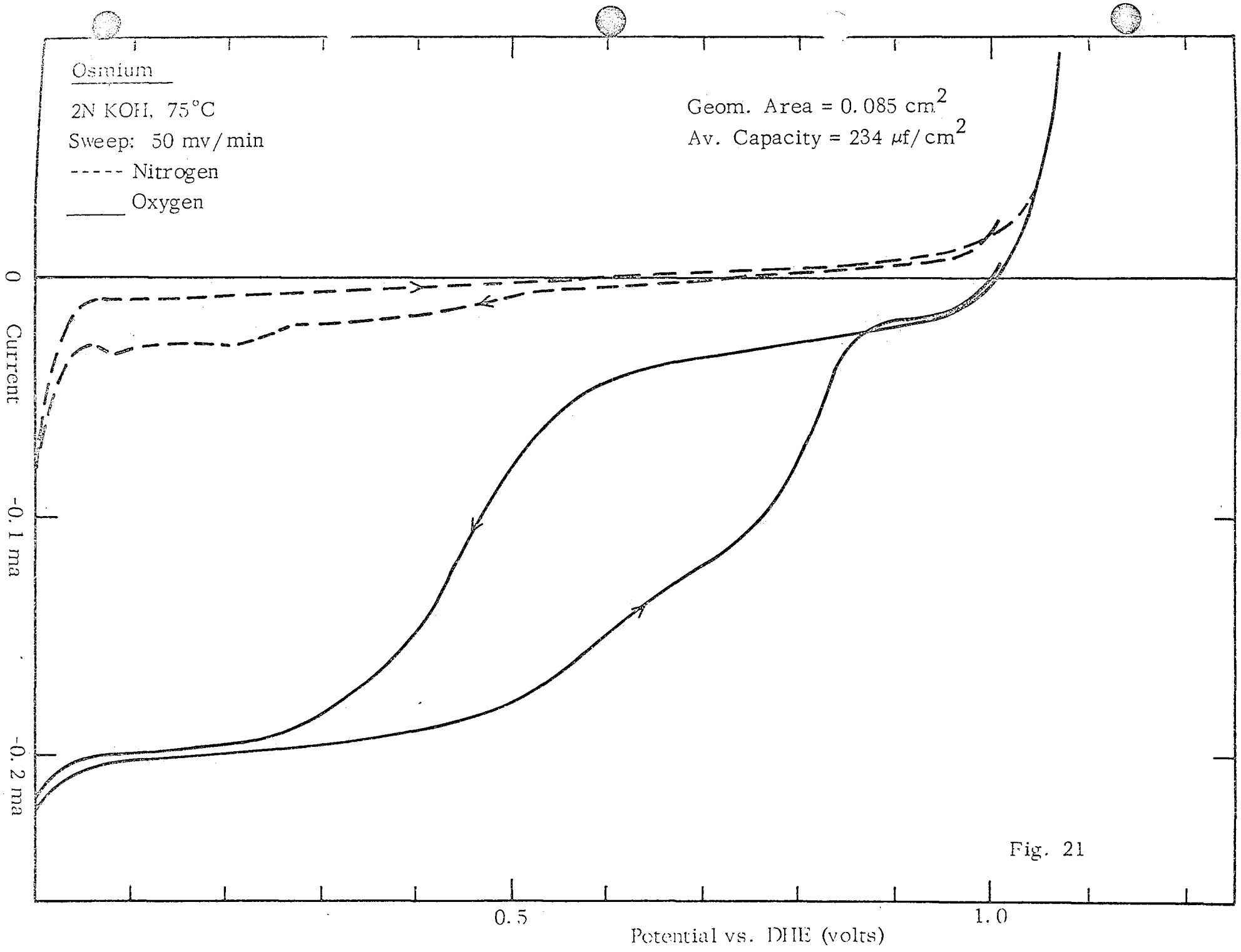
Osmium
2N KOH, 75°C
Sweep: 50 mv/min
----- Nitrogen
_____ Oxygen
Geom. Area = 0.085 cm²
Av. Capacity = 234 μf/cm²
0
Current
-0.1 ma
-0.2 ma
0.5
1.0
Potential vs. DHE (volts)

Fig. 21

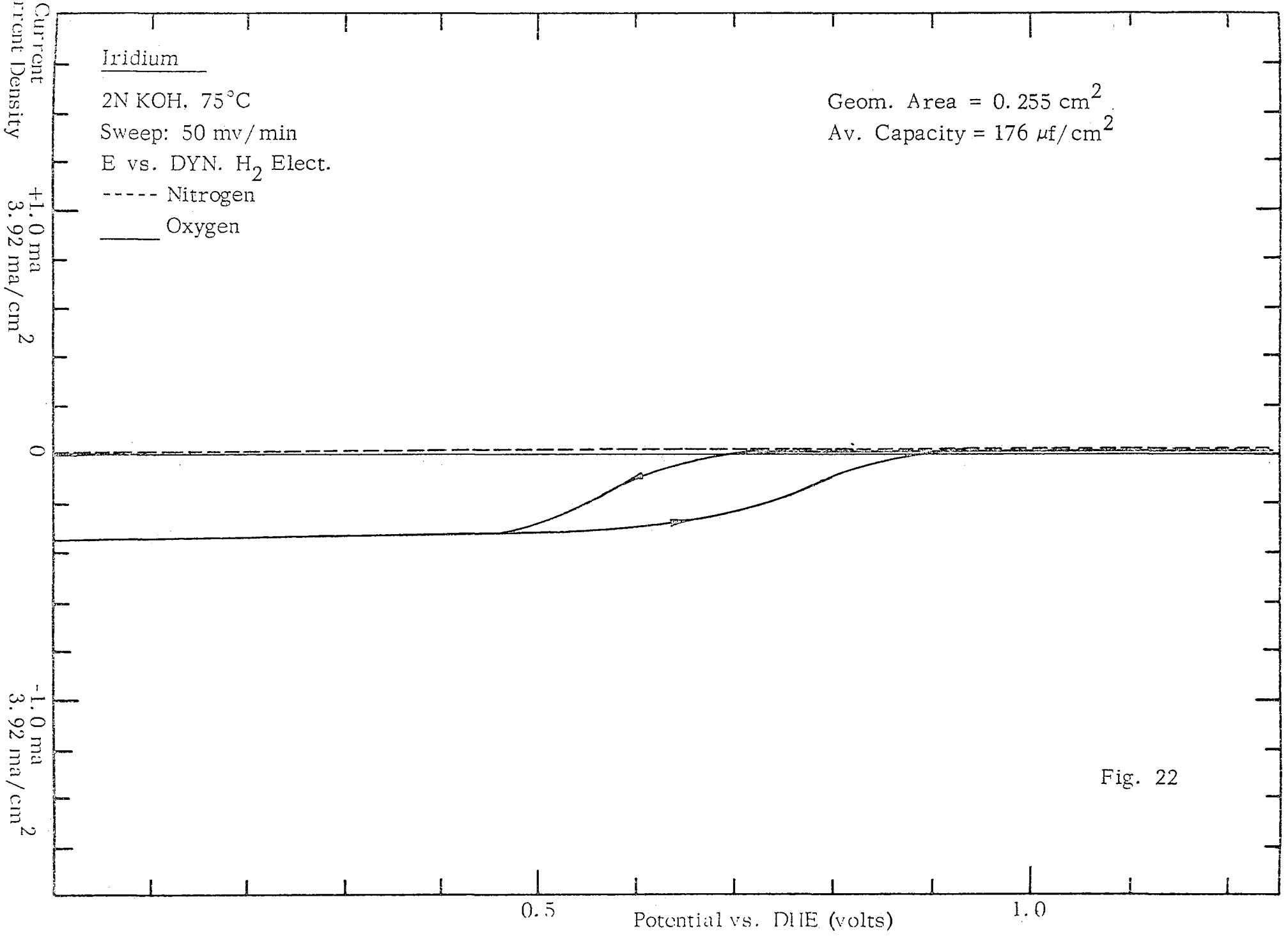
Iridium
2N KOH, 75°C
Sweep: 50 mv/min
E vs. DYN. H_2 Elect.
----- Nitrogen
_____ Oxygen
Geom. Area = 0.255 cm^2
Av. Capacity = 176 $\mu f/cm^2$
Current Density
+1.0 ma
3.92 ma/cm^2
0
-1.0 ma
3.92 ma/cm^2
0.5
1.0
Potential vs. DHE (volts)

Fig. 22

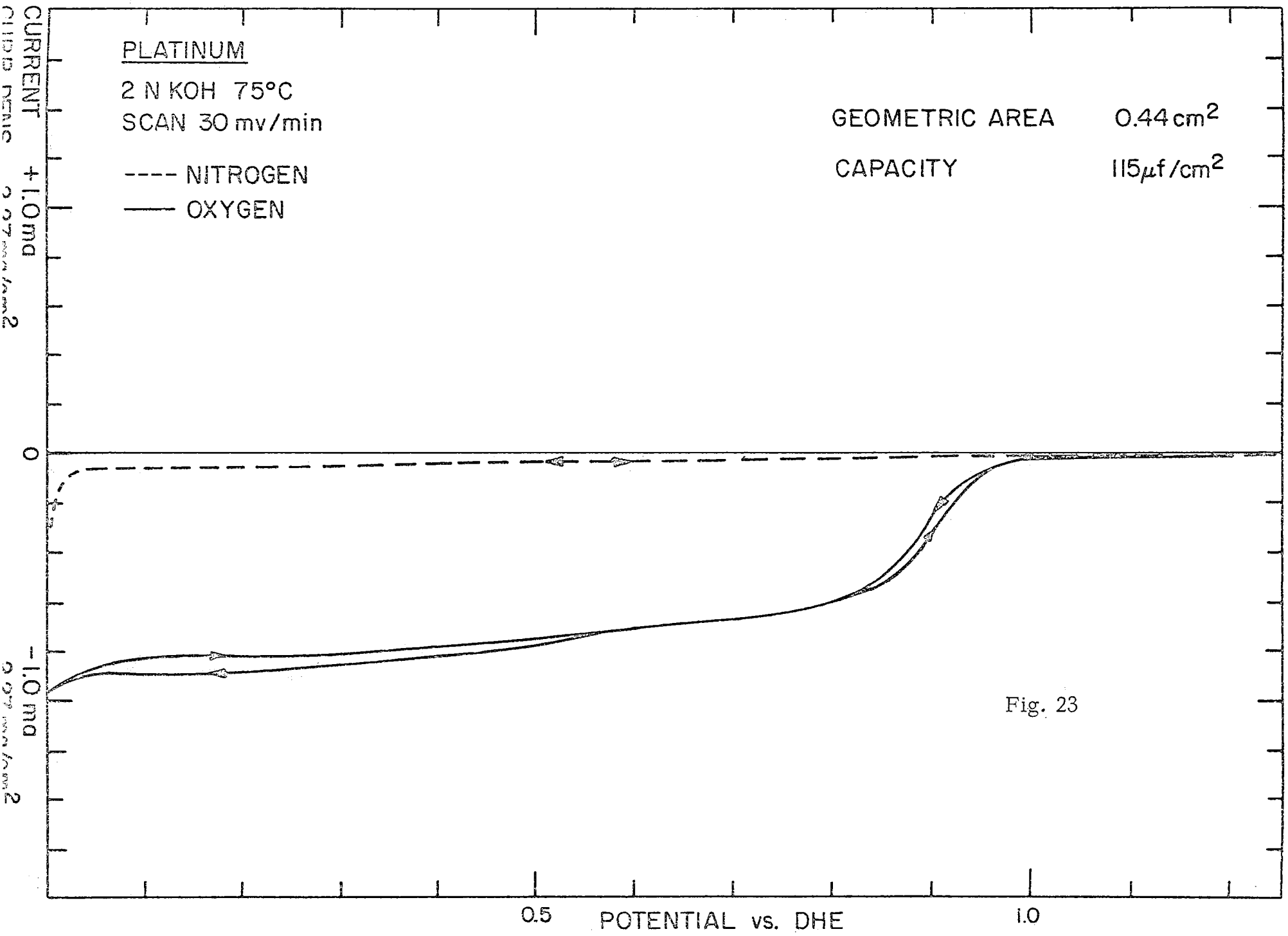
PLATINUM
2 N KOH 75°C
SCAN 30 mv/min
---- NITROGEN
—— OXYGEN
GEOMETRIC AREA 0.44 cm²
CAPACITY 115 μf/cm²
CURRENT
+1.0 ma
0
-1.0 ma
0.5
POTENTIAL vs. DHE
1.0

Fig. 23

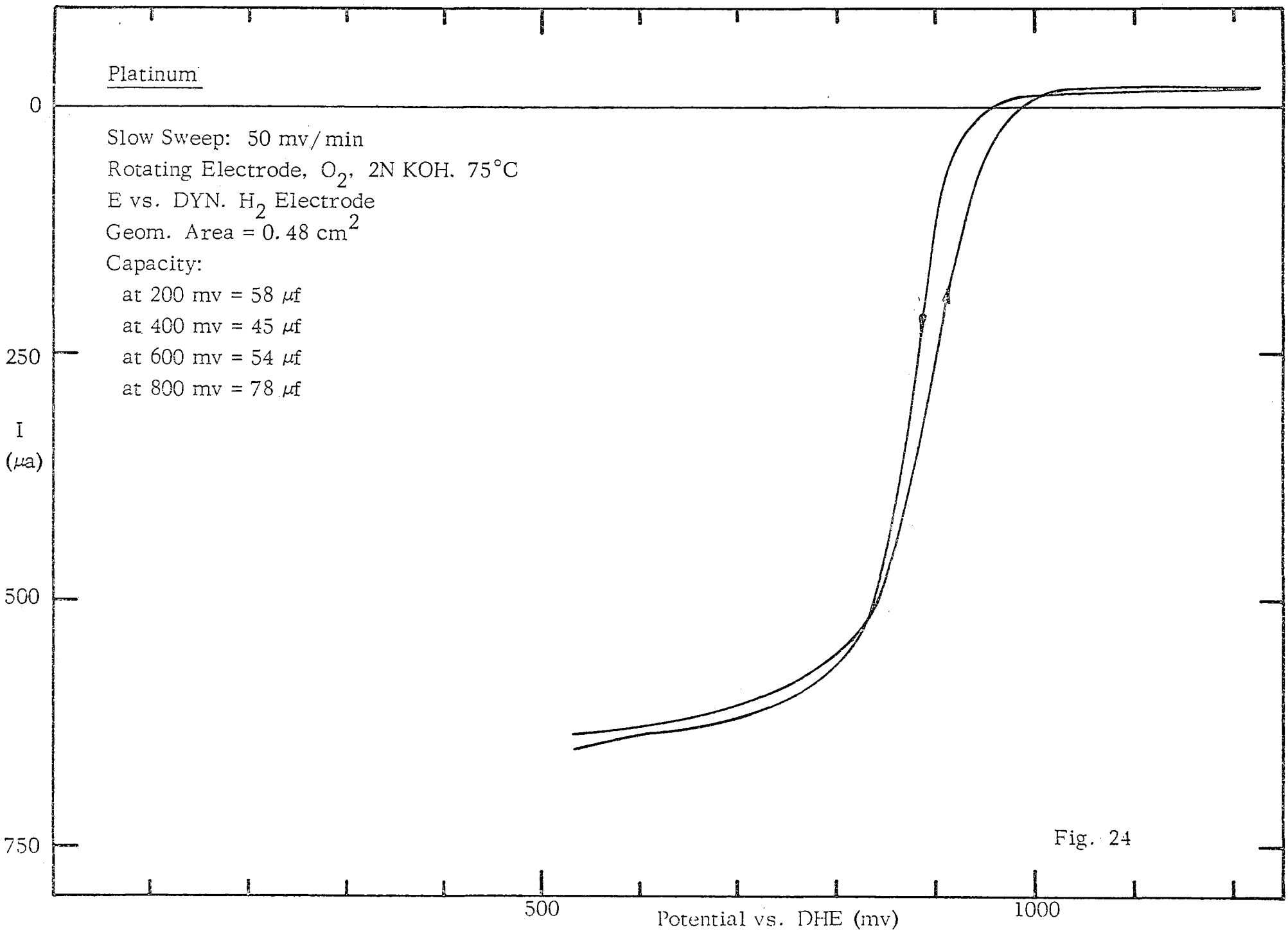
Platinum
Slow Sweep: 50 mv/min
Rotating Electrode, O_2, 2N KOH. 75°C
E vs. DYN. H_2 Electrode
Geom. Area = 0.48 cm^2
Capacity:
at 200 mv = 58 μf
at 400 mv = 45 μf
at 600 mv = 54 μf
at 800 mv = 78 μf
0
250
500
750
I
(μa)
500
1000
Potential vs. DHE (mv)

Fig. 24

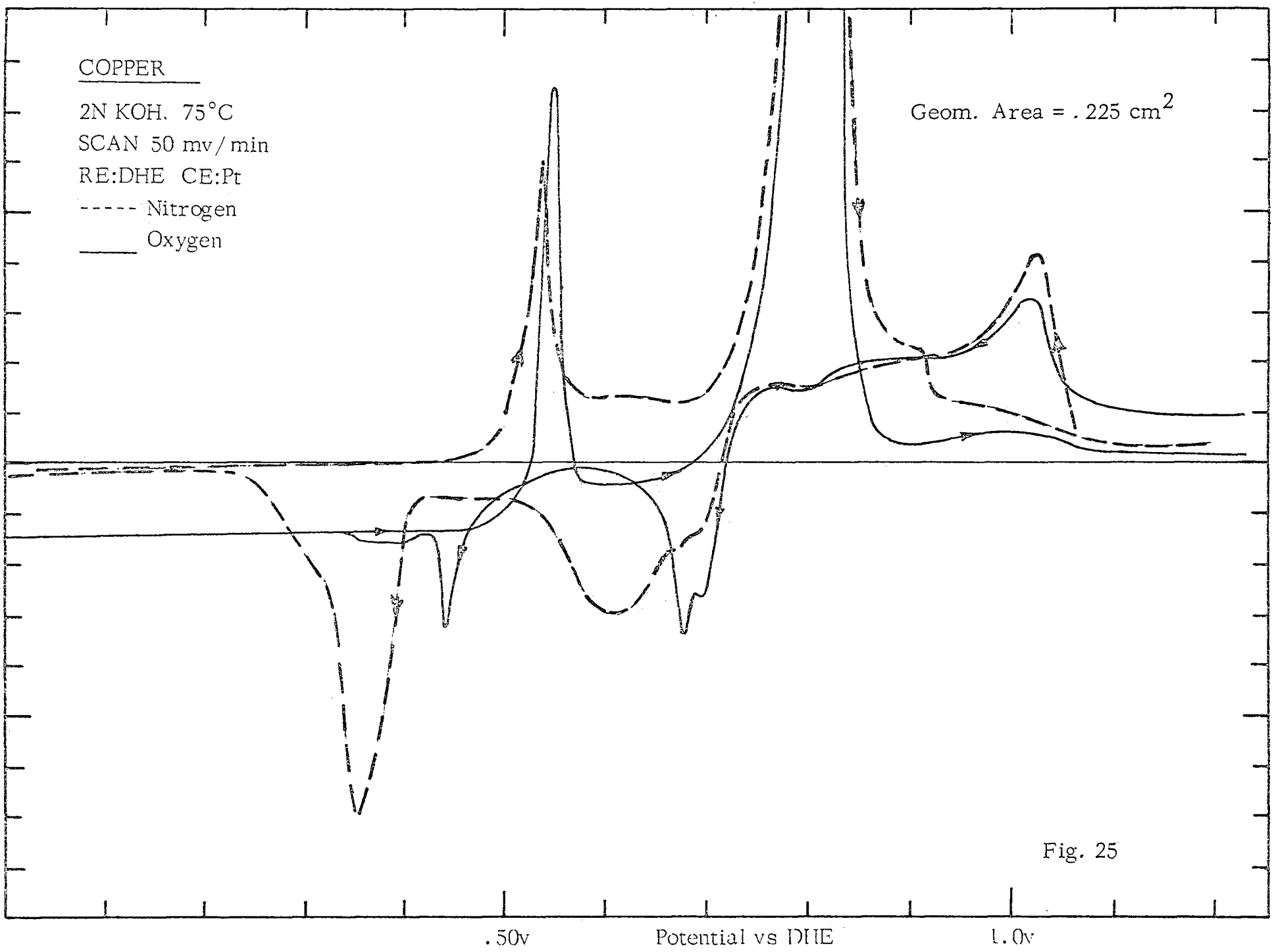
COPPER
2N KOH. 75°C
SCAN 50 mv/min
RE:DHE CE:Pt
----- Nitrogen
_____ Oxygen
Geom. Area = .225 cm2
Current
+1.0 ma
0.0
-1.0 ma
.50v
Potential vs DHE
1.0v

Fig. 25

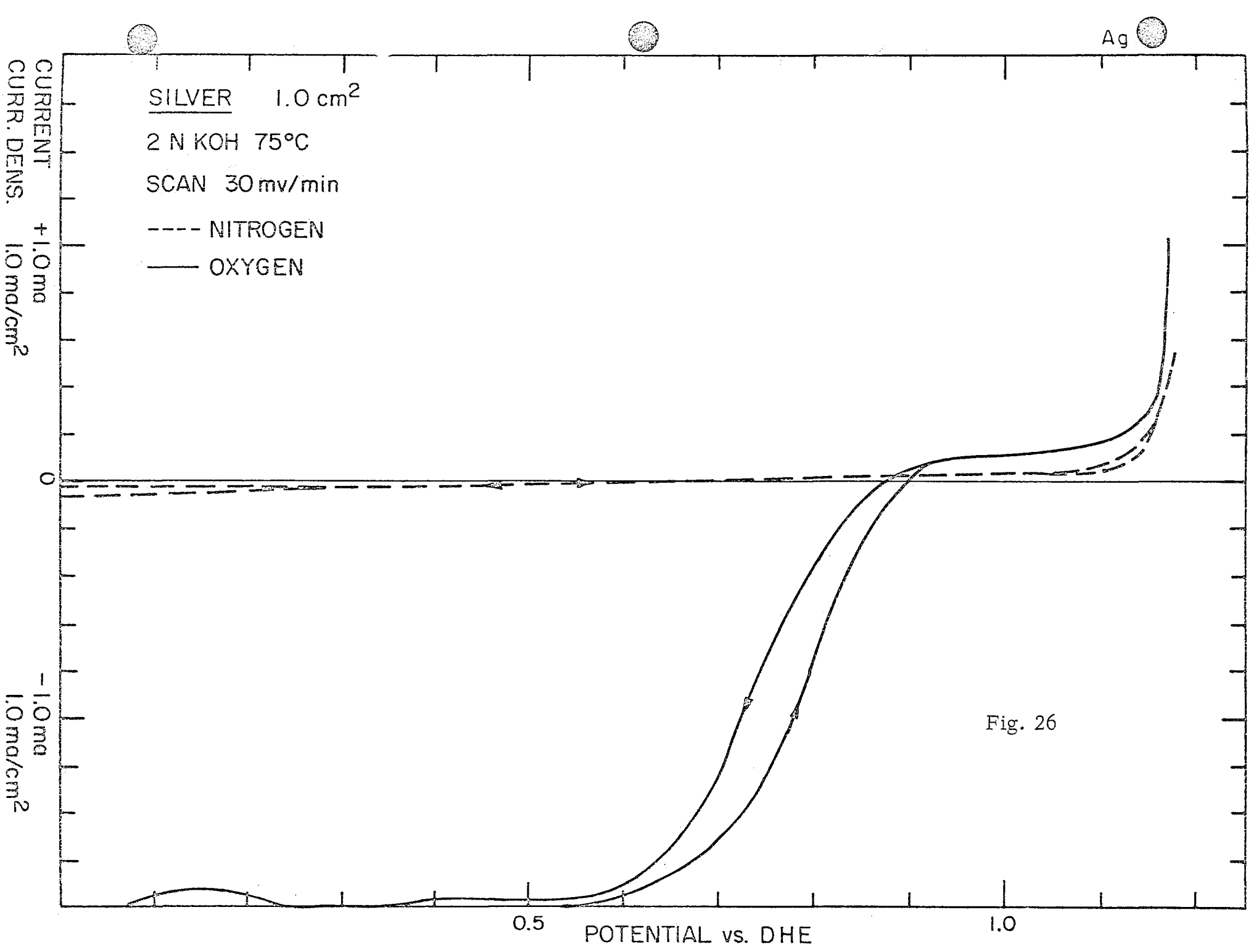
Ag
SILVER 1.0 cm²
2 N KOH 75°C
SCAN 30 mv/min
---- NITROGEN
—— OXYGEN
CURRENT
CURR. DENS.
+1.0 ma
1.0 ma/cm²
0
-1.0 ma
1.0 ma/cm²
0.5
POTENTIAL vs. DHE
1.0

Fig. 26

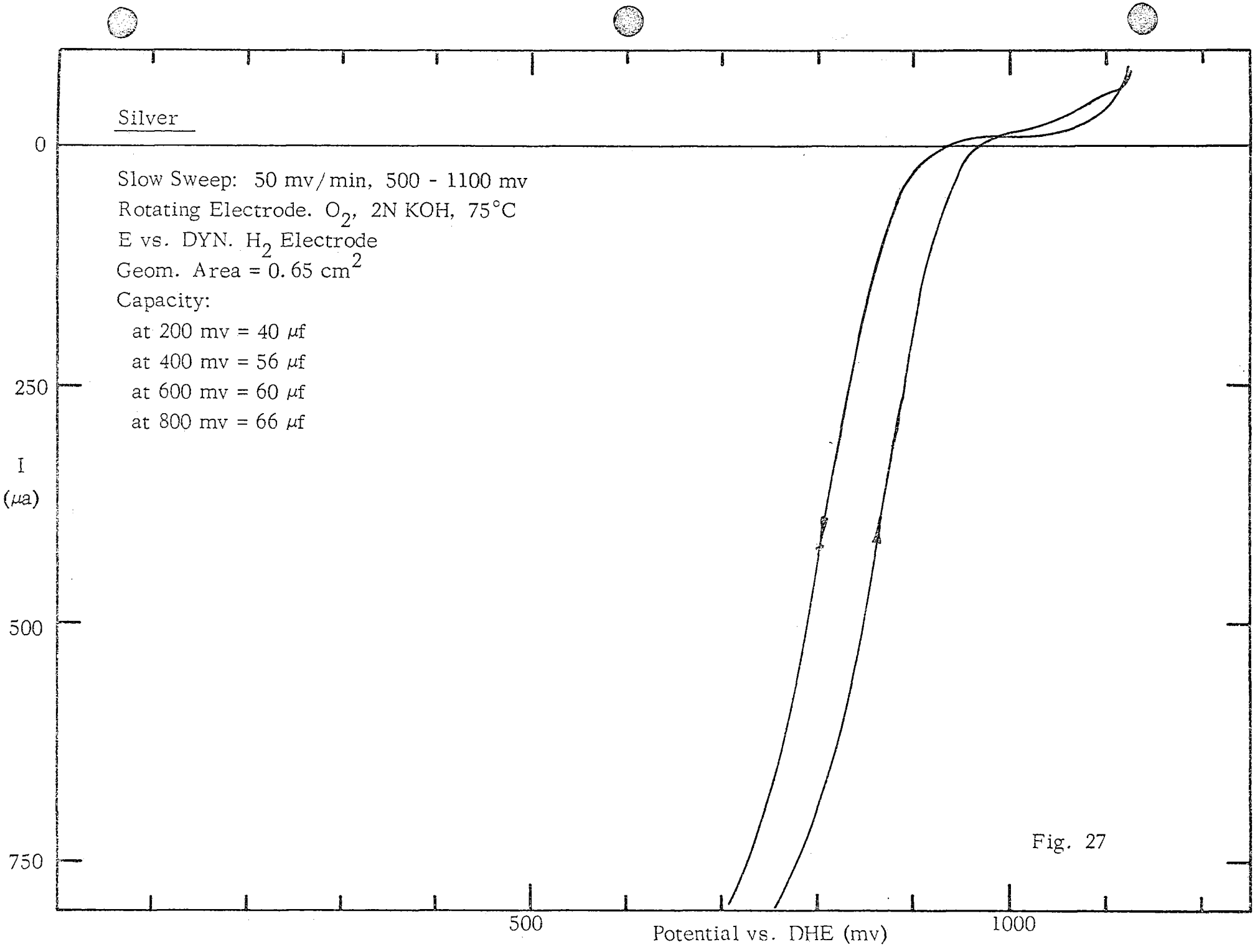
Silver
0
Slow Sweep: 50 mv/min, 500 - 1100 mv
Rotating Electrode. O_2, 2N KOH, 75°C
E vs. DYN. H_2 Electrode
Geom. Area = 0.65 cm^2
Capacity:
at 200 mv = 40 μf
at 400 mv = 56 μf
at 600 mv = 60 μf
at 800 mv = 66 μf
250
I
(μa)
500
750
500
1000
Potential vs. DHE (mv)

Fig. 27

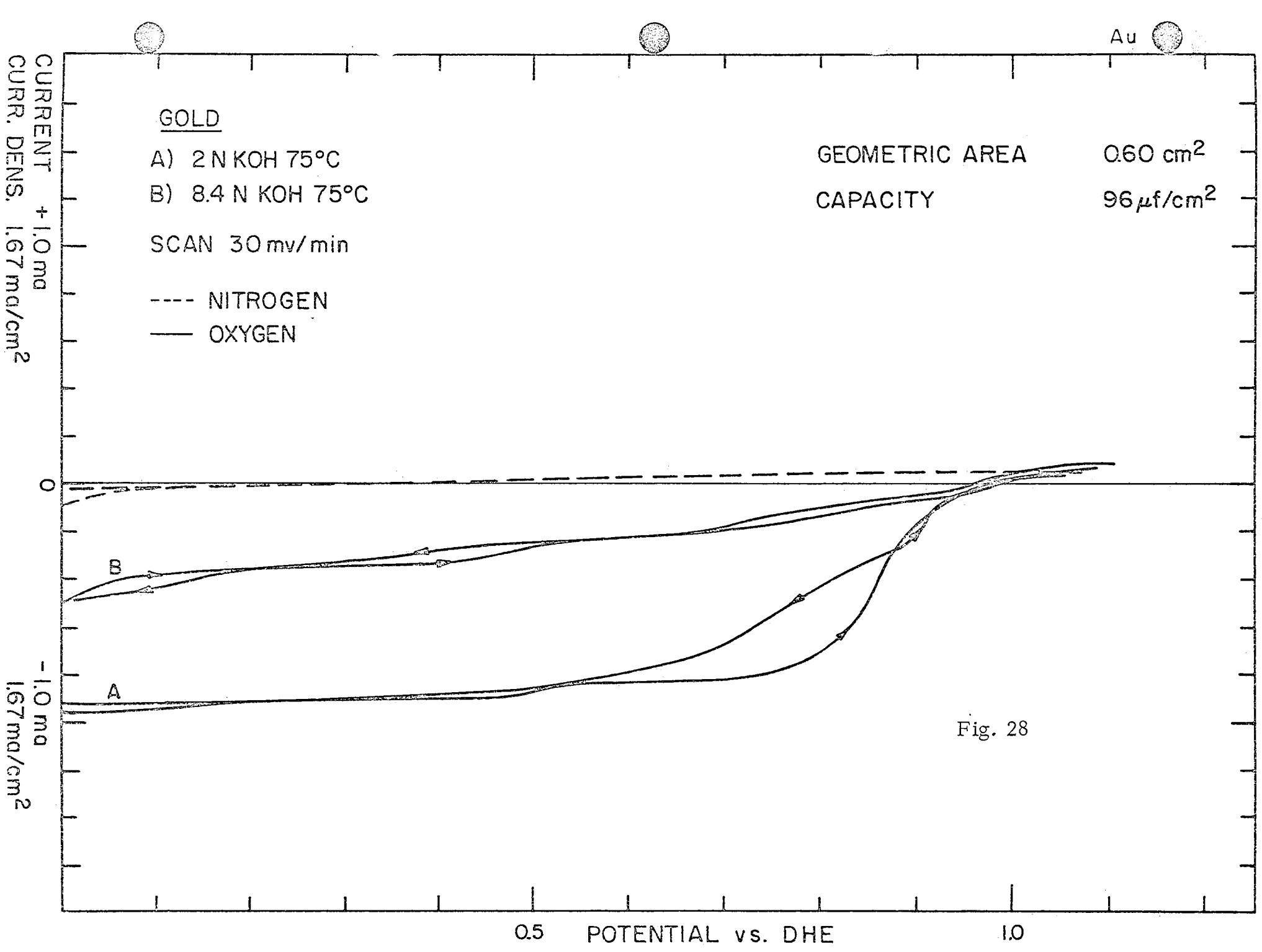
Au
GOLD
A) 2 N KOH 75°C
B) 8.4 N KOH 75°C
SCAN 30 mv/min
---- NITROGEN
—— OXYGEN
GEOMETRIC AREA 0.60 cm²
CAPACITY 96 μf/cm²
CURRENT +1.0 ma
CURR. DENS. 1.67 ma/cm²
0
-1.0 ma
1.67 ma/cm²
B
A
0.5
POTENTIAL vs. DHE
1.0

Fig. 28

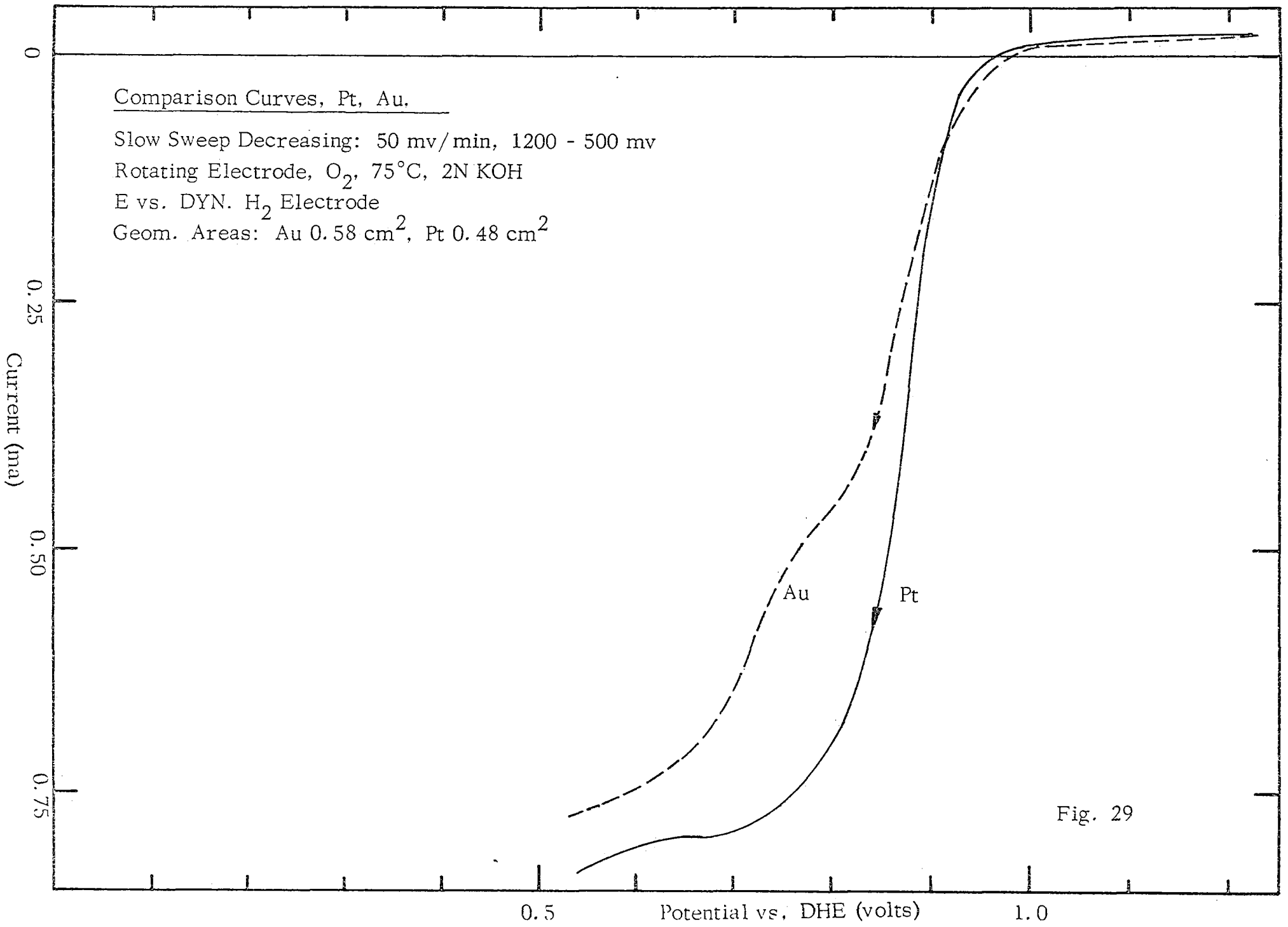
Comparison Curves, Pt, Au.
Slow Sweep Decreasing: 50 mv/min, 1200 - 500 mv
Rotating Electrode, O_2, 75°C, 2N KOH
E vs. DYN. H_2 Electrode
Geom. Areas: Au 0.58 cm^2, Pt 0.48 cm^2
0
0.25
0.50
0.75
Current (ma)
Au
Pt
0.5
Potential vs. DHE (volts)
1.0

Fig. 29

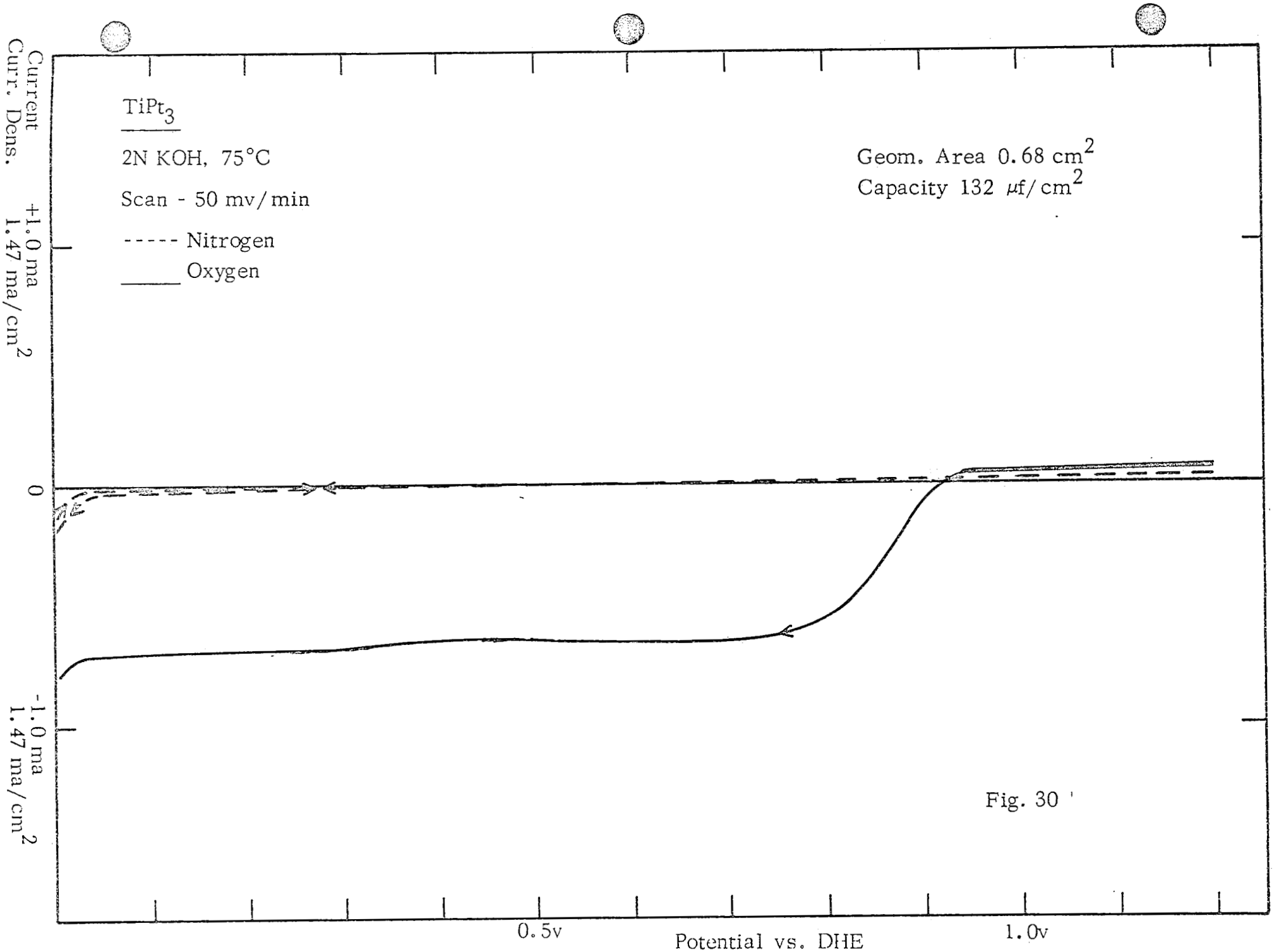
TiPt3
2N KOH, 75°C
Scan - 50 mv/min
----- Nitrogen
_____ Oxygen
Geom. Area 0.68 cm2
Capacity 132 μf/cm2
Current
Curr. Dens.
+1.0 ma
1.47 ma/cm2
0
-1.0 ma
1.47 ma/cm2
0.5v
Potential vs. DHE
1.0v

Fig. 30

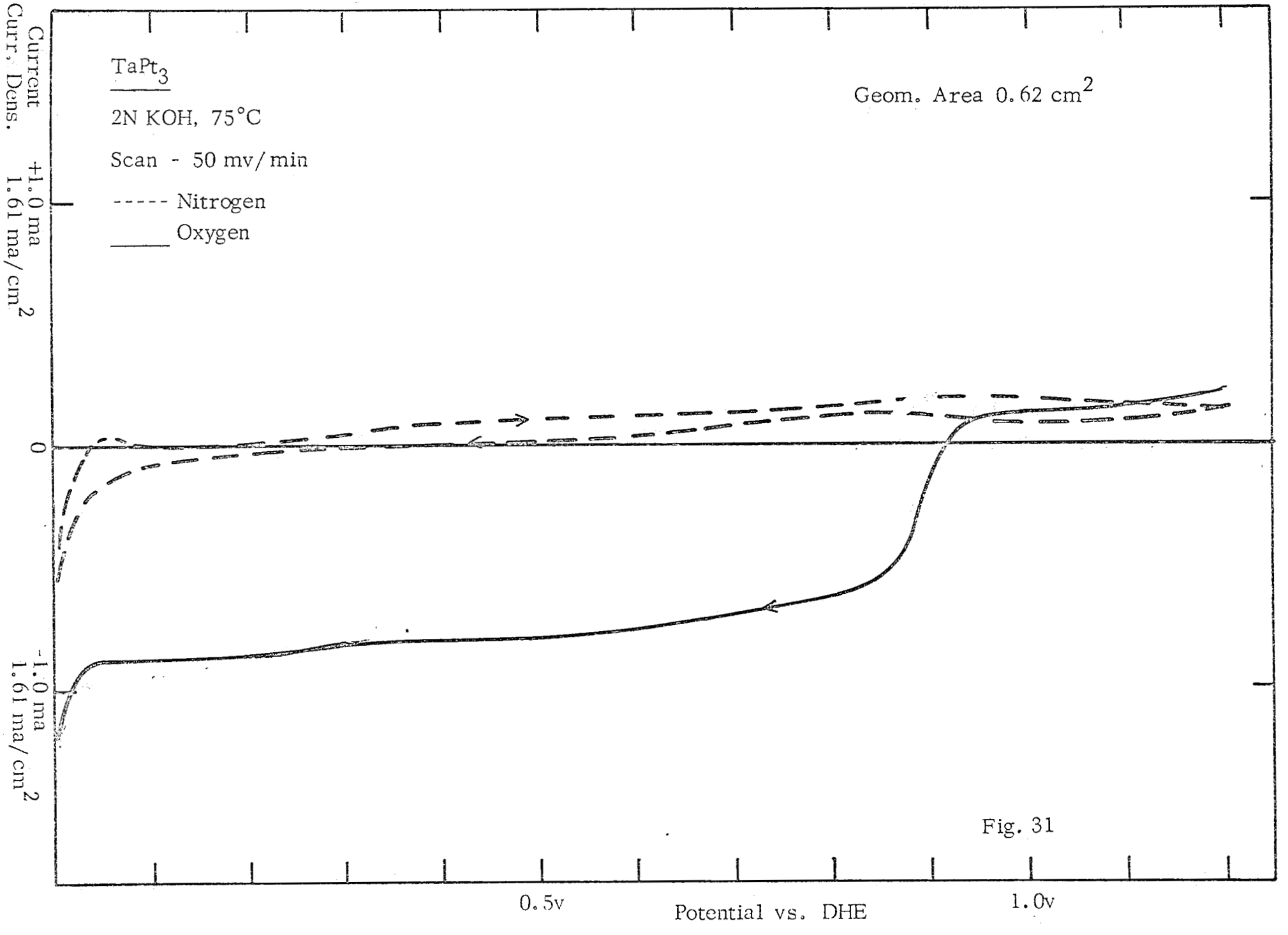
$TaPt_3$
2N KOH, 75°C
Scan - 50 mv/min
----- Nitrogen
_____ Oxygen
Geom. Area 0.62 cm^2
Current
Curr. Dens.
+1.0 ma
1.61 ma/cm^2
0
-1.0 ma
1.61 ma/cm^2
0.5v
Potential vs. DHE
1.0v

Fig. 31

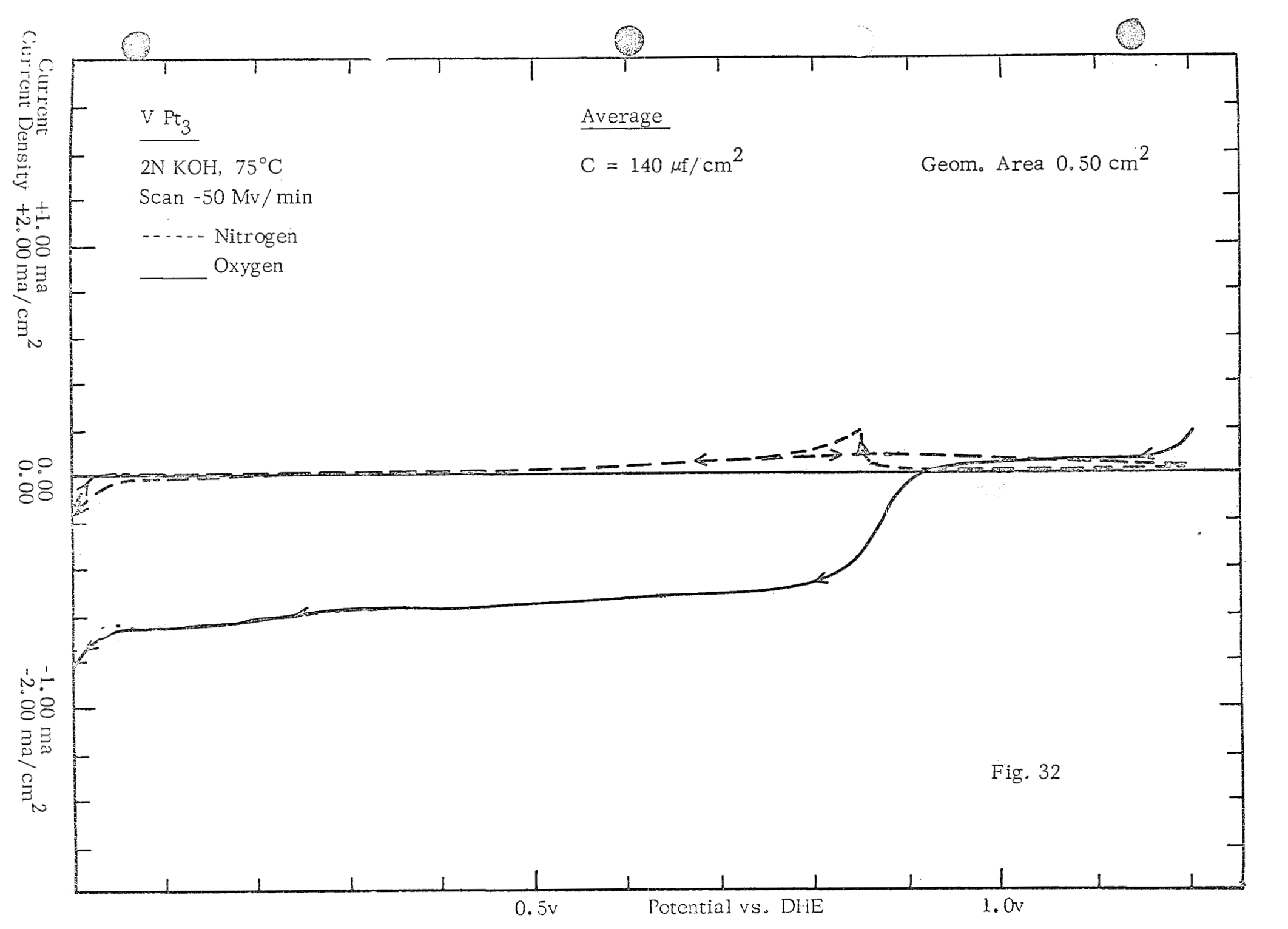
V Pt_3
Average
2N KOH, 75°C
Scan -50 Mv/min
C = 140 μf/cm^2
Geom. Area 0.50 cm^2
------ Nitrogen
_____ Oxygen
Current Density
+1.00 ma
+2.00 ma/cm^2
0.00
0.00
-1.00 ma
-2.00 ma/cm^2
0.5v
Potential vs. DHE
1.0v

Fig. 32

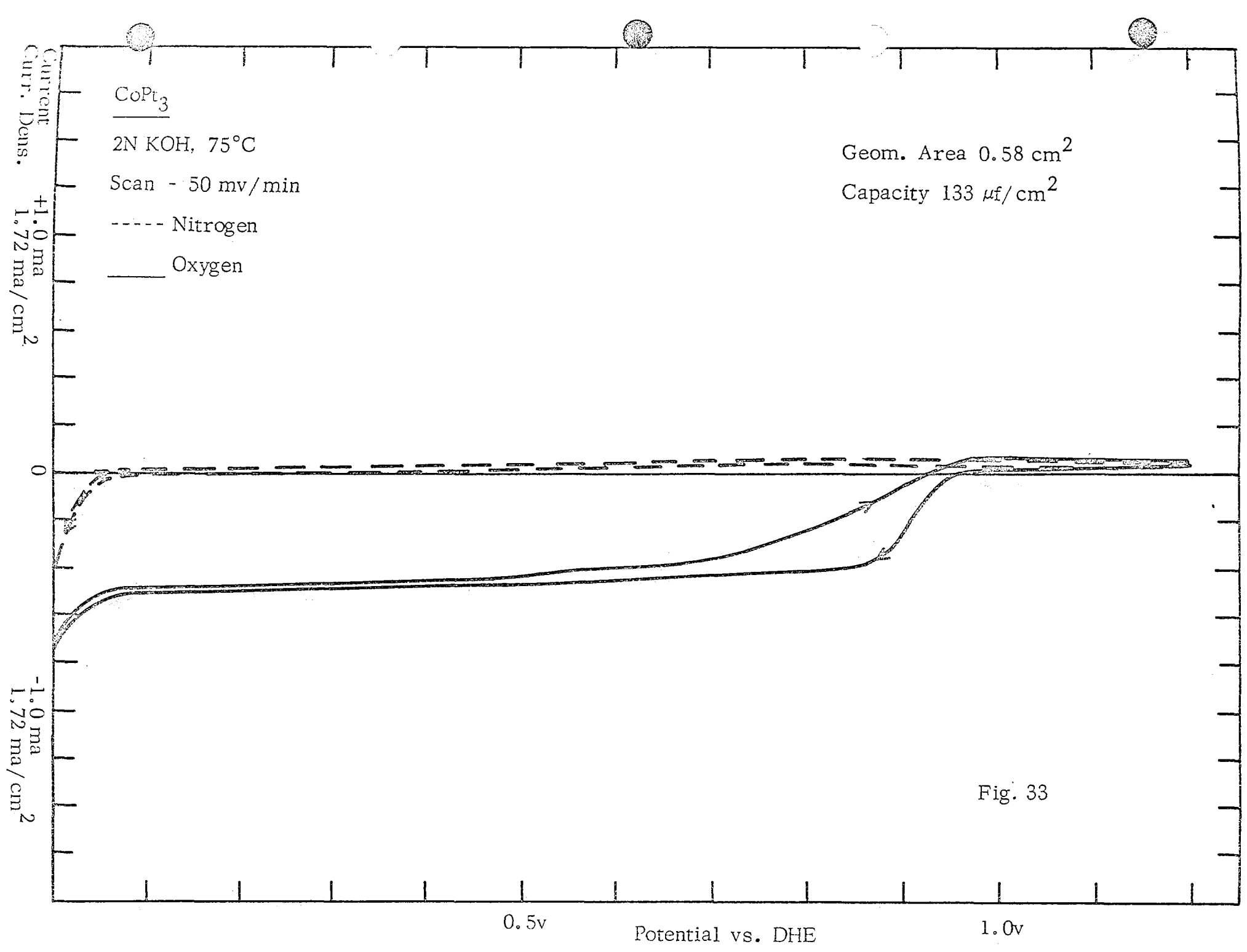
$CoPt_3$
2N KOH, 75°C
Scan - 50 mv/min
----- Nitrogen
_____ Oxygen
Geom. Area 0.58 cm^2
Capacity 133 $\mu f/cm^2$
Current
Curr. Dens.
+1.0 ma
1,72 ma/cm^2
0
-1.0 ma
1,72 ma/cm^2
0.5v
Potential vs. DHE
1.0v

Fig. 33

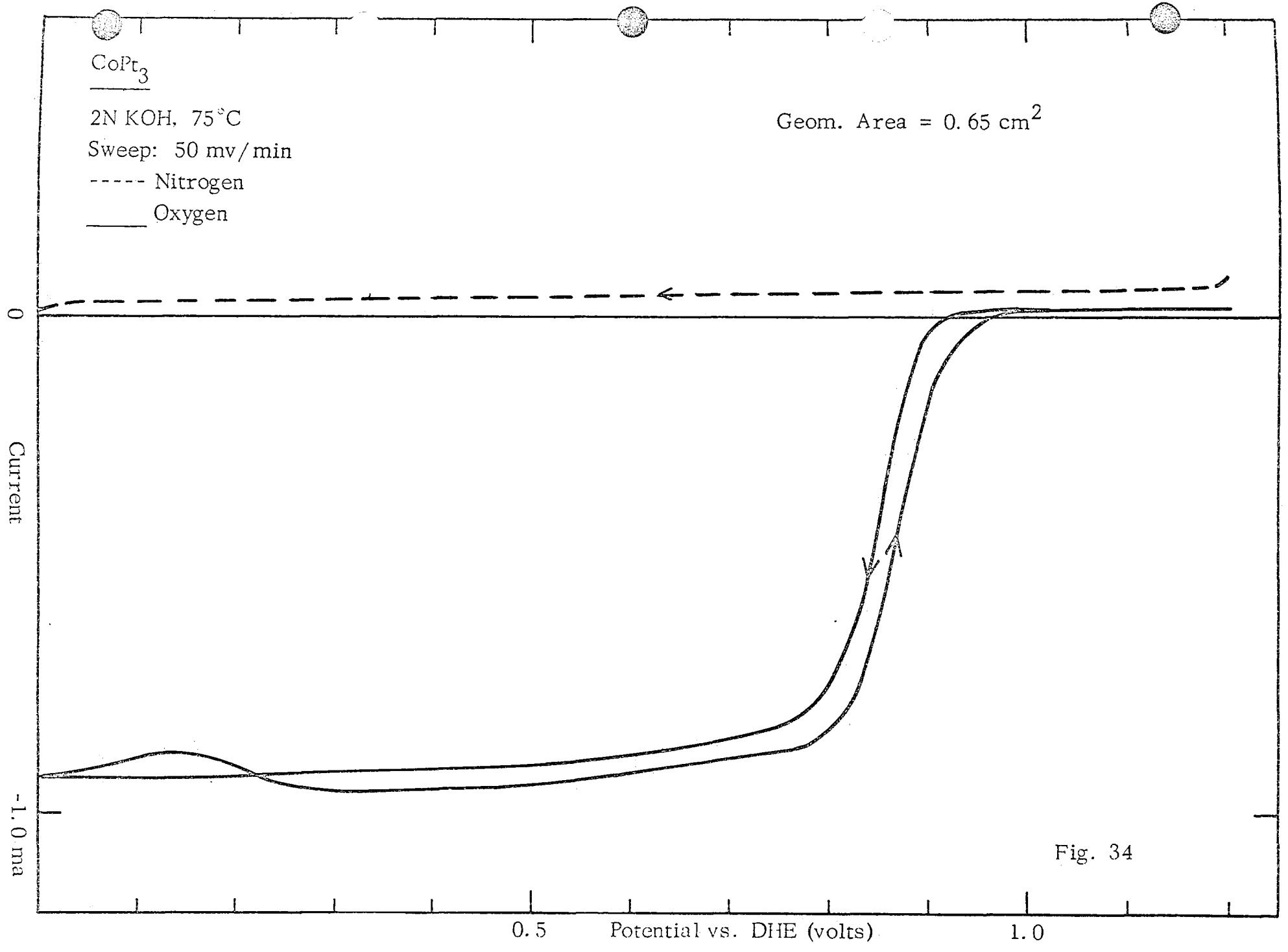
$CoPt_3$
2N KOH, 75°C
Sweep: 50 mv/min
----- Nitrogen
_____ Oxygen
Geom. Area = 0.65 cm^2
0
Current
-1.0 ma
0.5
Potential vs. DHE (volts)
1.0

Fig. 34

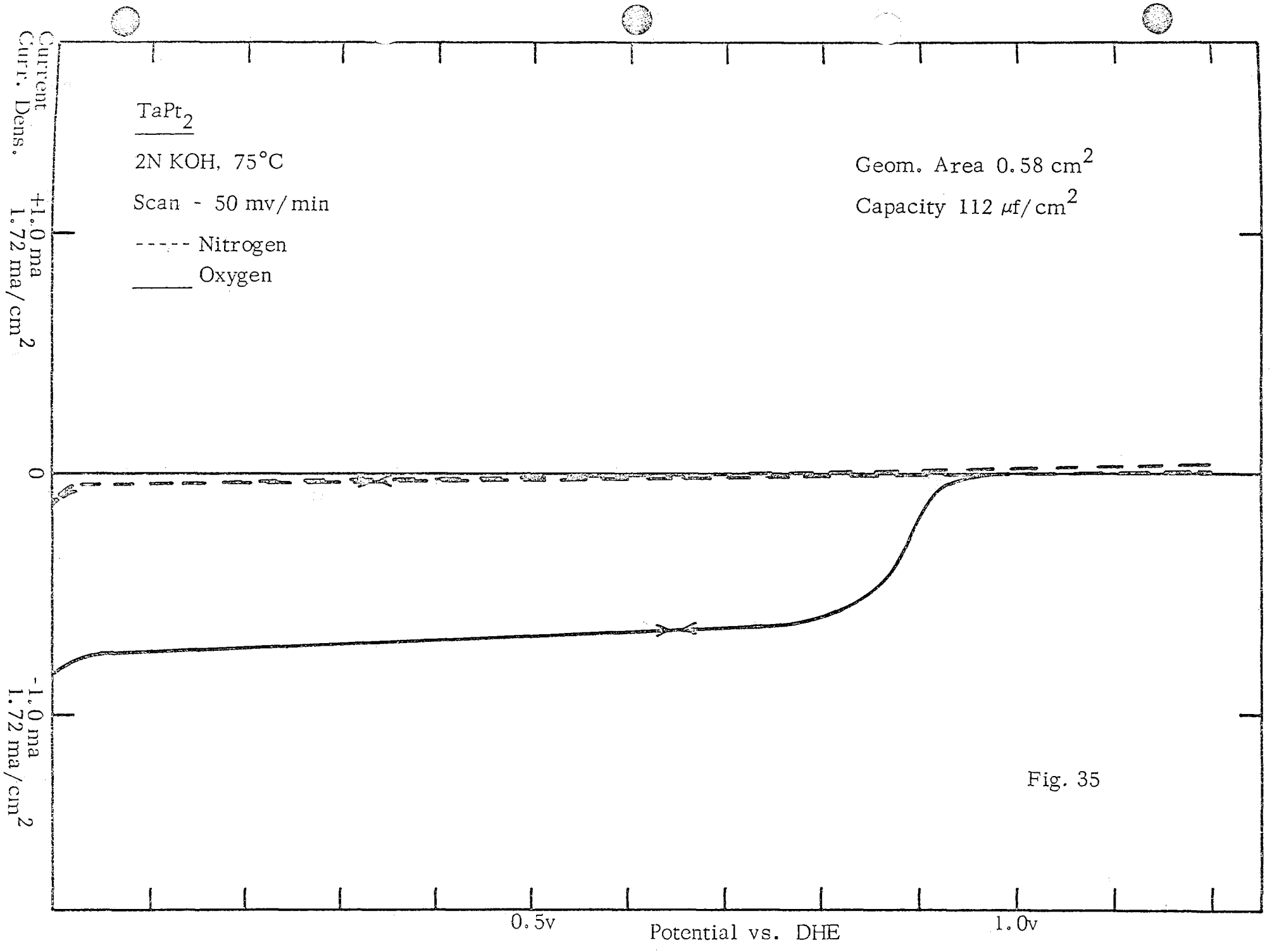
Current
Curr. Dens.
+1.0 ma
1.72 ma/cm2
0
-1.0 ma
1.72 ma/cm2
TaPt2
2N KOH, 75°C
Scan - 50 mv/min
----- Nitrogen
_____ Oxygen
Geom. Area 0.58 cm2
Capacity 112 μf/cm2
0.5v
Potential vs. DHE
1.0v

Fig. 35

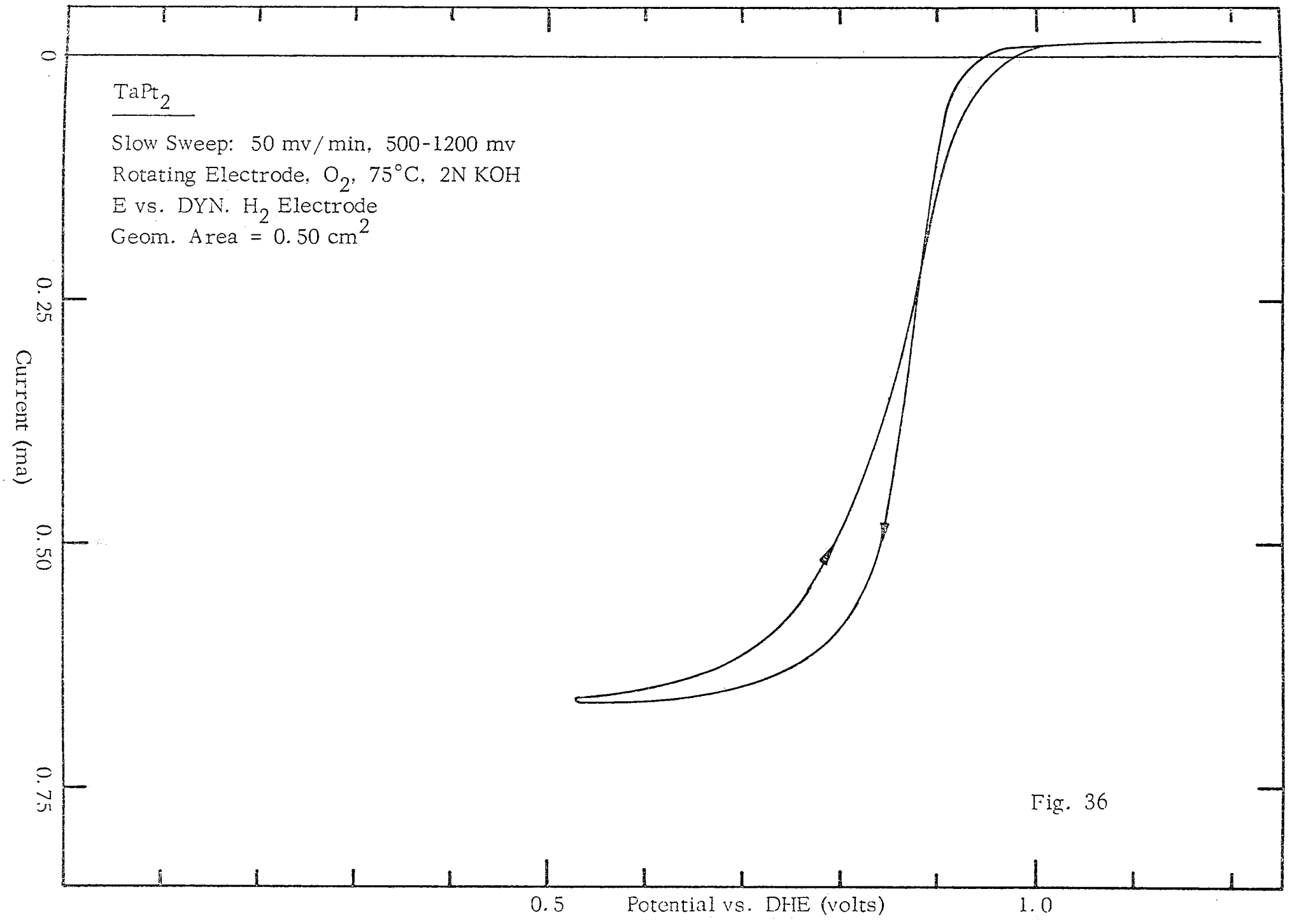
$TaPt_2$
Slow Sweep: 50 mv/min, 500-1200 mv
Rotating Electrode, O_2, 75°C, 2N KOH
E vs. DYN. H_2 Electrode
Geom. Area = 0.50 cm^2
0
0.25
0.50
0.75
Current (ma)
0.5
Potential vs. DHE (volts)
1.0

Fig. 36

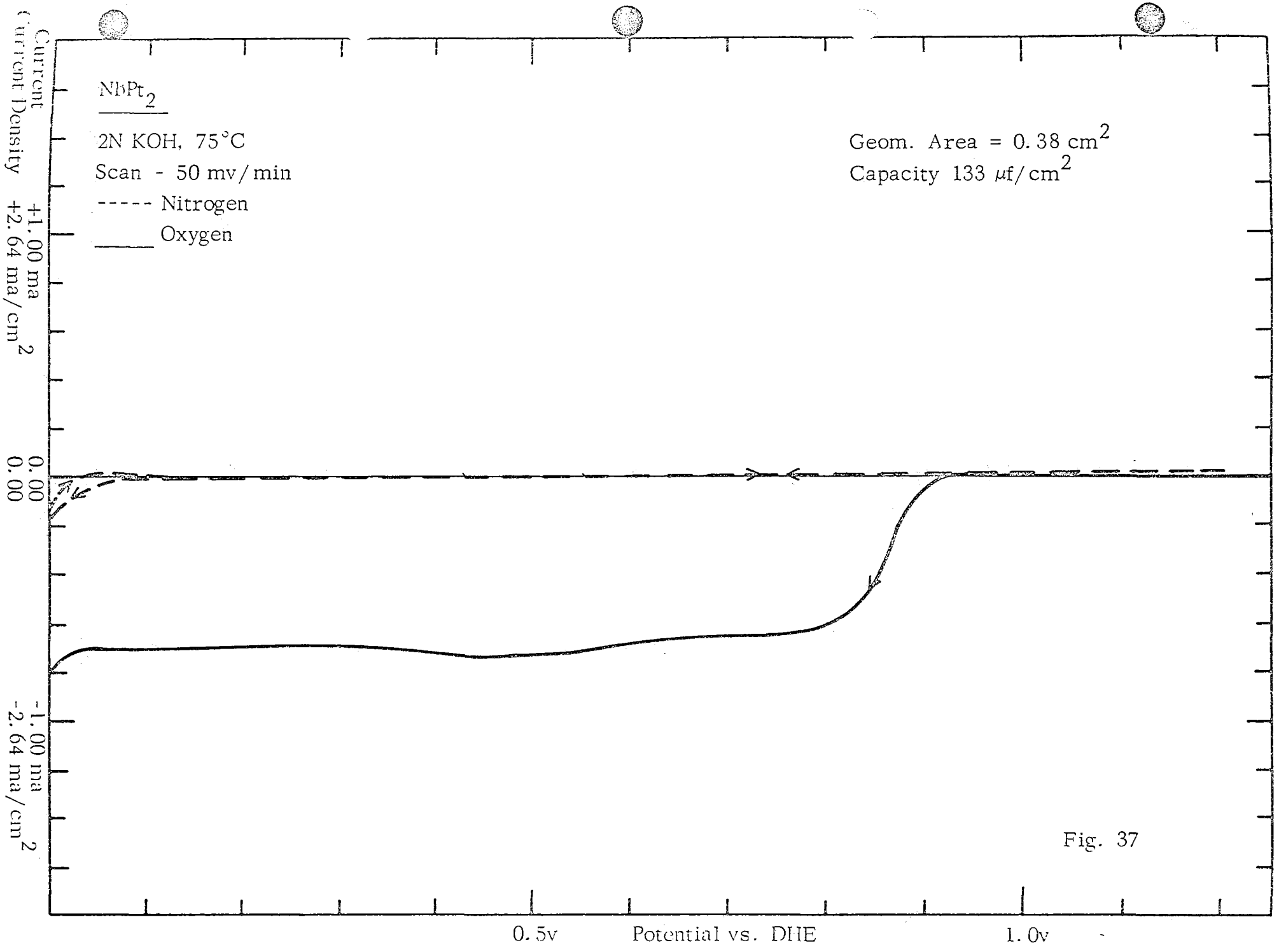
NbPt2
2N KOH, 75°C
Scan - 50 mv/min
----- Nitrogen
_____ Oxygen
Geom. Area = 0.38 cm2
Capacity 133 μf/cm2
Current Density
+1.00 ma
+2.64 ma/cm2
0.00
0.00
-1.00 ma
-2.64 ma/cm2
0.5v
Potential vs. DHE
1.0v

Fig. 37

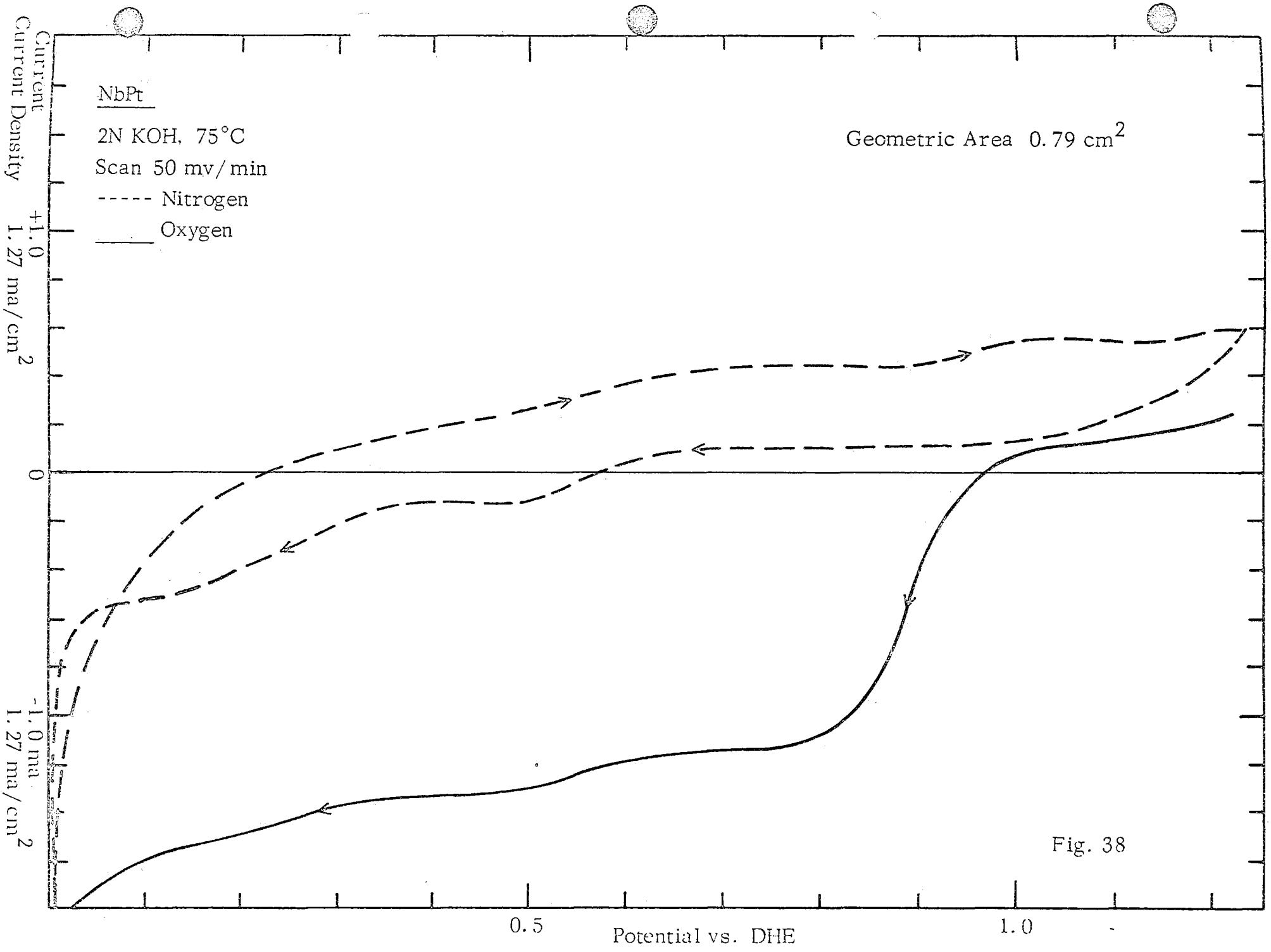
NbPt
2N KOH, 75°C
Scan 50 mv/min
----- Nitrogen
_____ Oxygen
Geometric Area 0.79 cm2
Current Density
+1.0
1.27 ma/cm2
0
-1.0 ma
1.27 ma/cm2
0.5
Potential vs. DHE
1.0

Fig. 38

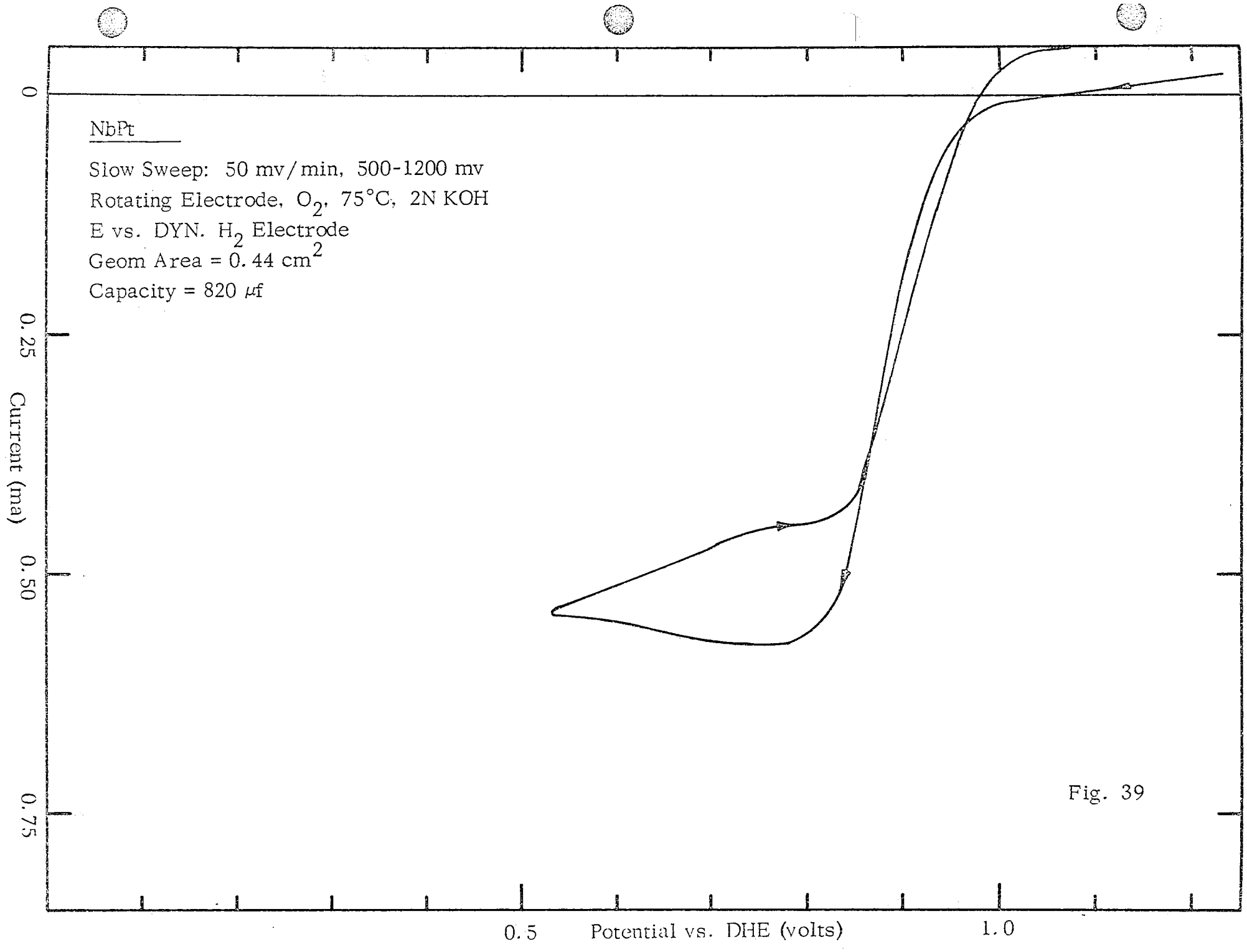
NbPt
Slow Sweep: 50 mv/min, 500-1200 mv
Rotating Electrode, O_2, 75°C, 2N KOH
E vs. DYN. H_2 Electrode
Geom Area = 0.44 cm^2
Capacity = 820 μf
0
0.25
0.50
0.75
Current (ma)
0.5
Potential vs. DHE (volts)
1.0

Fig. 39

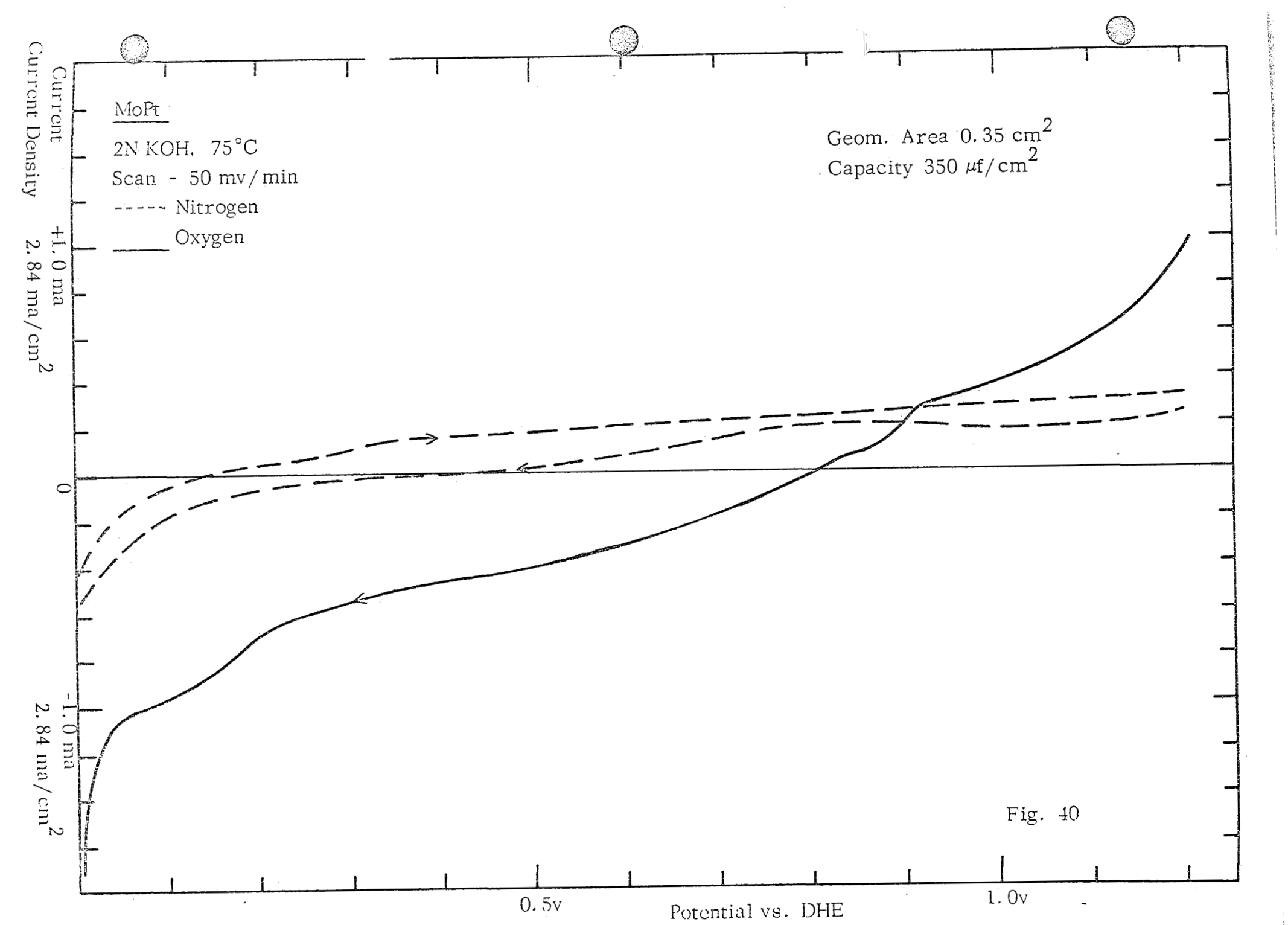
MoPt
2N KOH, 75°C
Scan - 50 mv/min
----- Nitrogen
_____ Oxygen
Geom. Area 0.35 cm²
Capacity 350 μf/cm²
Current
Current Density
+1.0 ma
2.84 ma/cm²
0
-1.0 ma
2.84 ma/cm²
0.5v
1.0v
Potential vs. DHE

Fig. 40

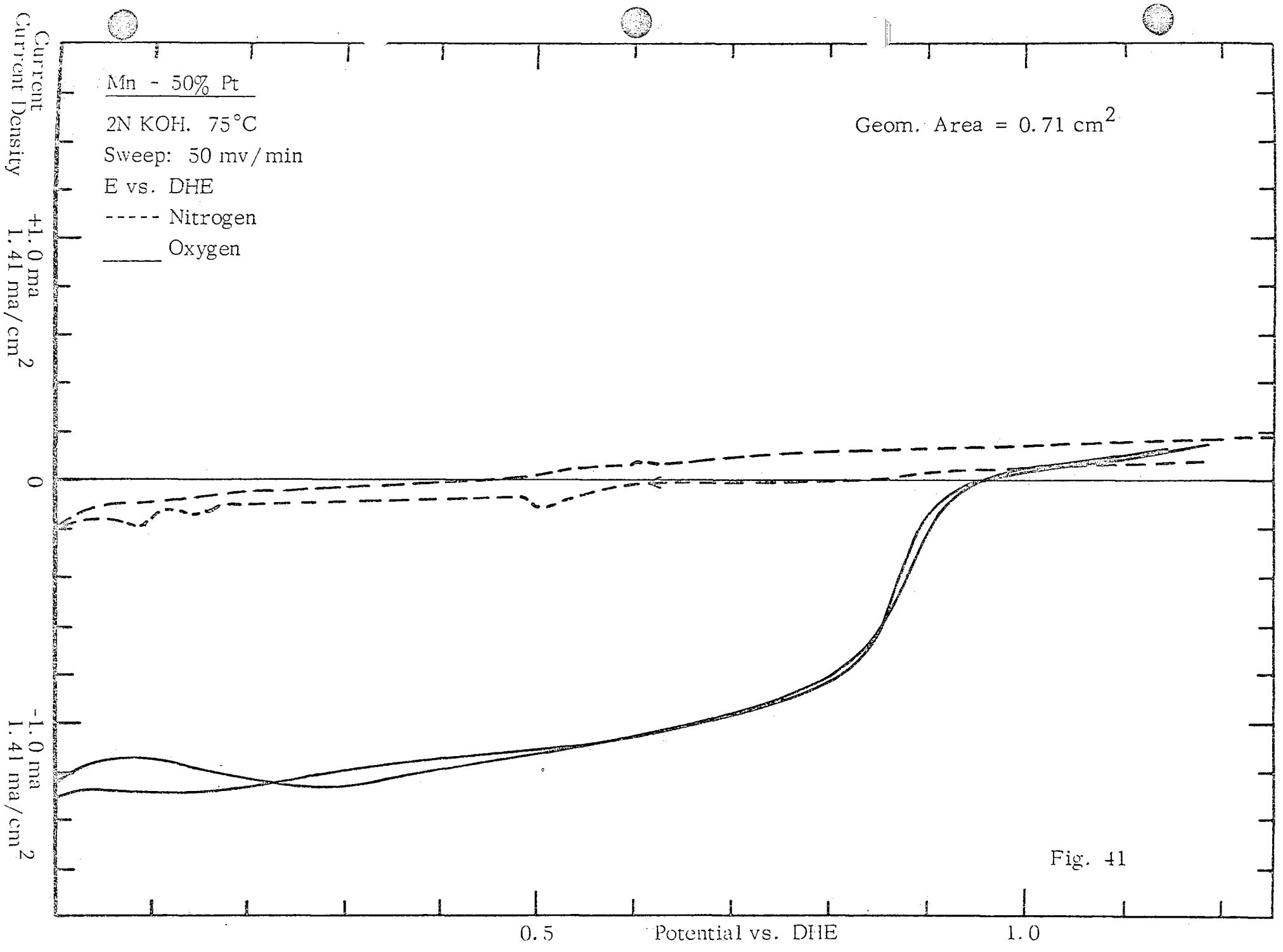
Mn - 50% Pt
2N KOH. 75°C
Sweep: 50 mv/min
E vs. DHE
----- Nitrogen
_____ Oxygen
Geom. Area = 0.71 cm2
Current Density
+1.0 ma
1.41 ma/cm2
0
-1.0 ma
1.41 ma/cm2
0.5
Potential vs. DHE
1.0

Fig. 41

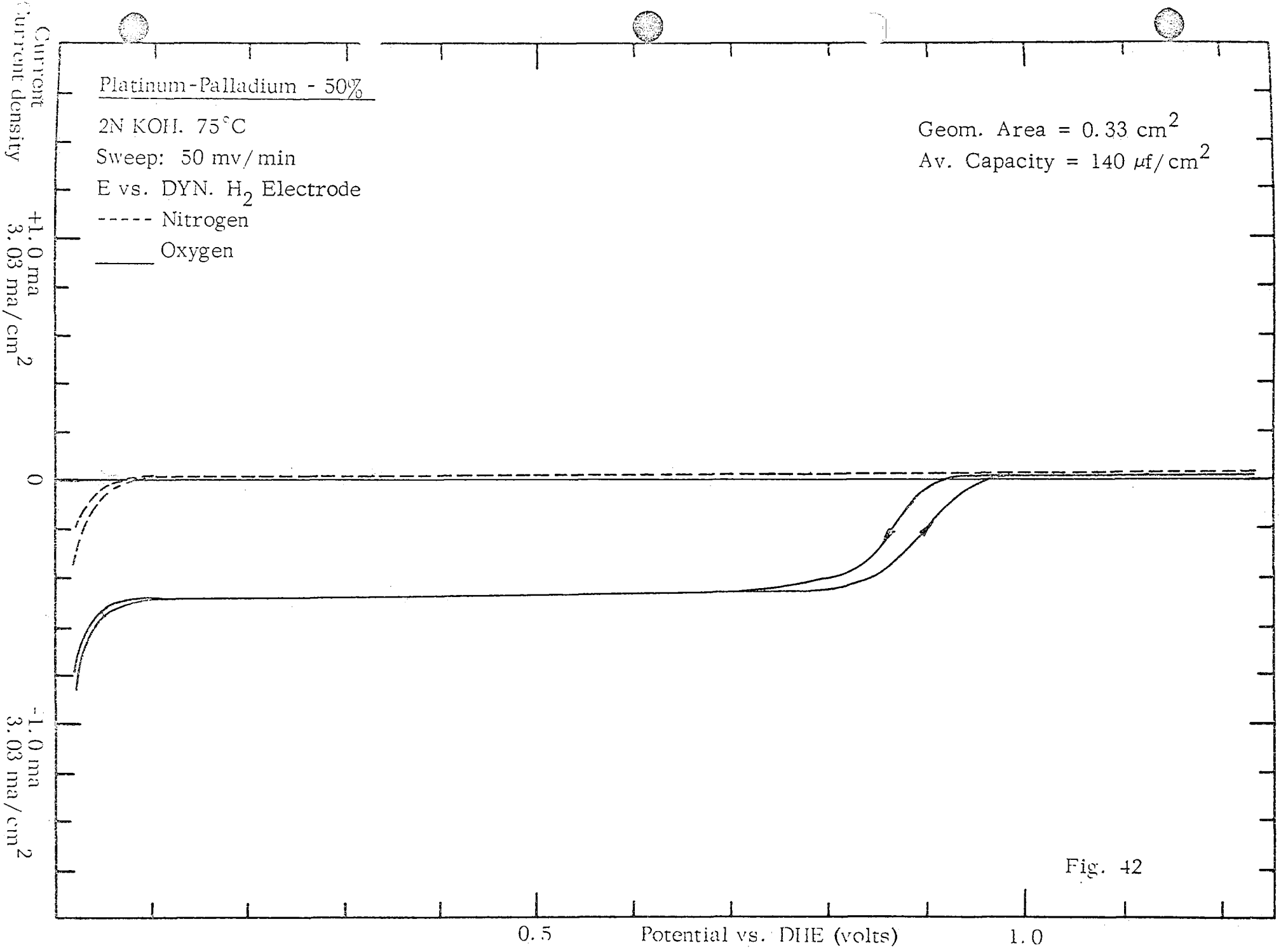
Platinum-Palladium - 50%
2N KOH. 75°C
Sweep: 50 mv/min
E vs. DYN. H_2 Electrode
----- Nitrogen
_____ Oxygen
Geom. Area = 0.33 cm^2
Av. Capacity = 140 $\mu f/cm^2$
Current density
+1.0 ma
3.03 ma/cm^2
0
-1.0 ma
3.03 ma/cm^2
0.5
Potential vs. DHE (volts)
1.0

Fig. 42

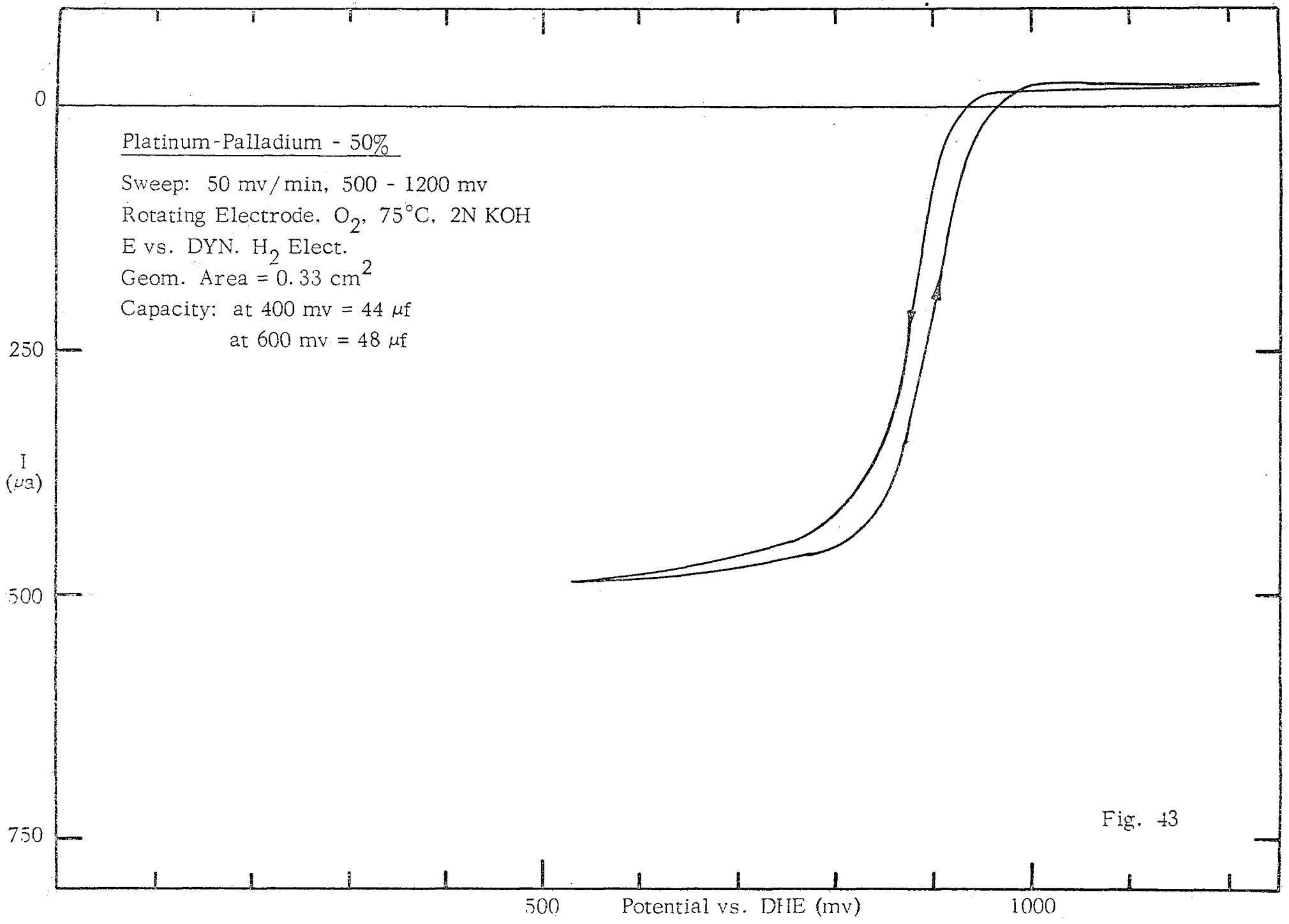
Platinum-Palladium - 50%
Sweep: 50 mv/min, 500 - 1200 mv
Rotating Electrode, O_2, 75°C, 2N KOH
E vs. DYN. H_2 Elect.
Geom. Area = 0.33 cm^2
Capacity: at 400 mv = 44 μf
at 600 mv = 48 μf
0
250
500
750
I (μa)
500
Potential vs. DHE (mv)
1000

Fig. 43

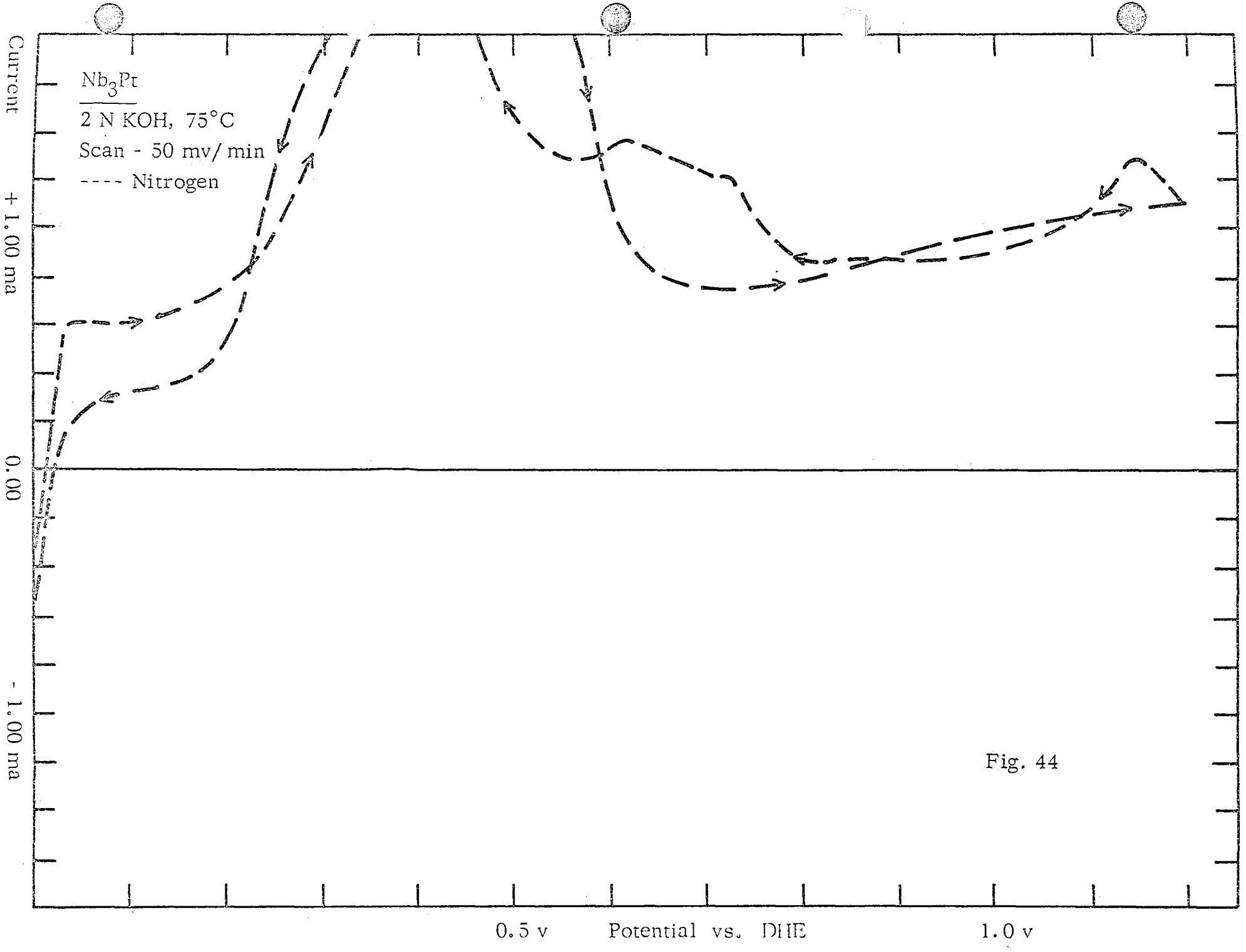
Nb3Pt
2 N KOH, 75°C
Scan - 50 mv/ min
---- Nitrogen
Current
+ 1.00 ma
0.00
- 1.00 ma
0.5 v
Potential vs. DHE
1.0 v

Fig. 44

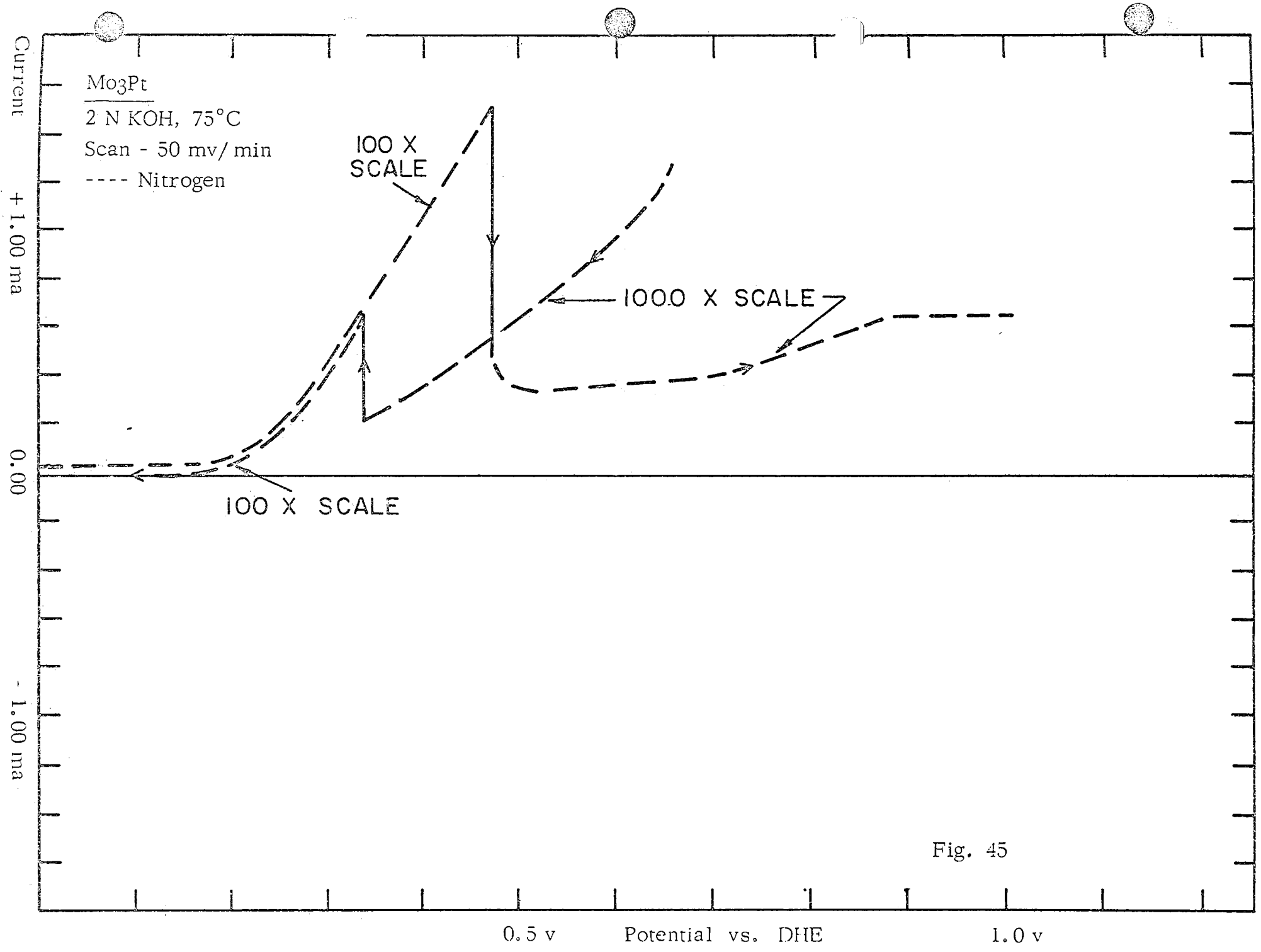
Current
+ 1.00 ma
0.00
- 1.00 ma
Mo3Pt
2 N KOH, 75°C
Scan - 50 mv/ min
---- Nitrogen
100 X SCALE
1000 X SCALE
100 X SCALE
0.5 v
Potential vs. DHE
1.0 v

Fig. 45

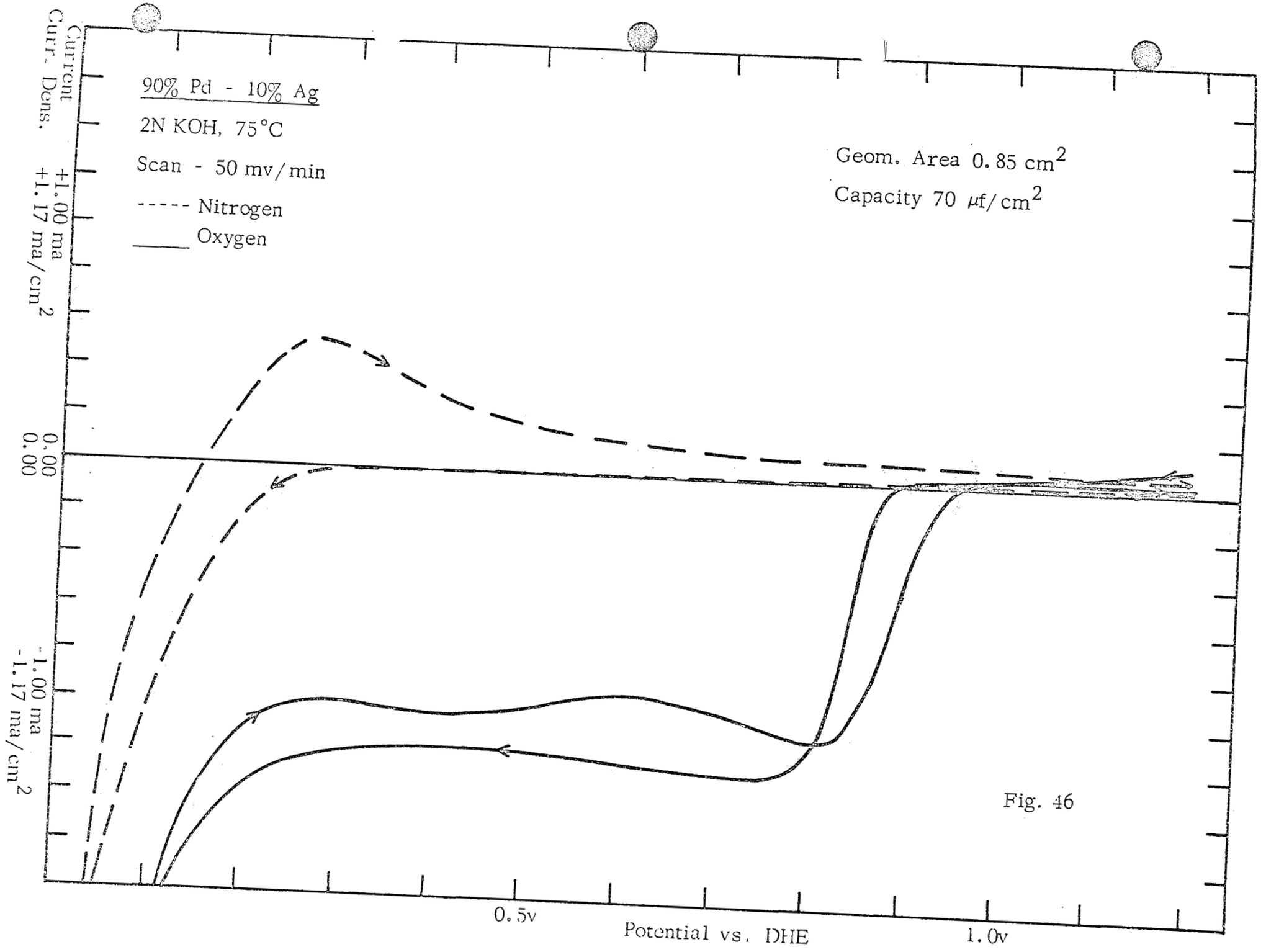
90% Pd - 10% Ag
2N KOH, 75°C
Scan - 50 mv/min
----- Nitrogen
_____ Oxygen
Geom. Area 0.85 cm2
Capacity 70 μf/cm2
Current
Curr. Dens.
+1.00 ma
+1.17 ma/cm2
0.00
0.00
-1.00 ma
-1.17 ma/cm2
0.5v
Potential vs. DHE
1.0v

Fig. 46

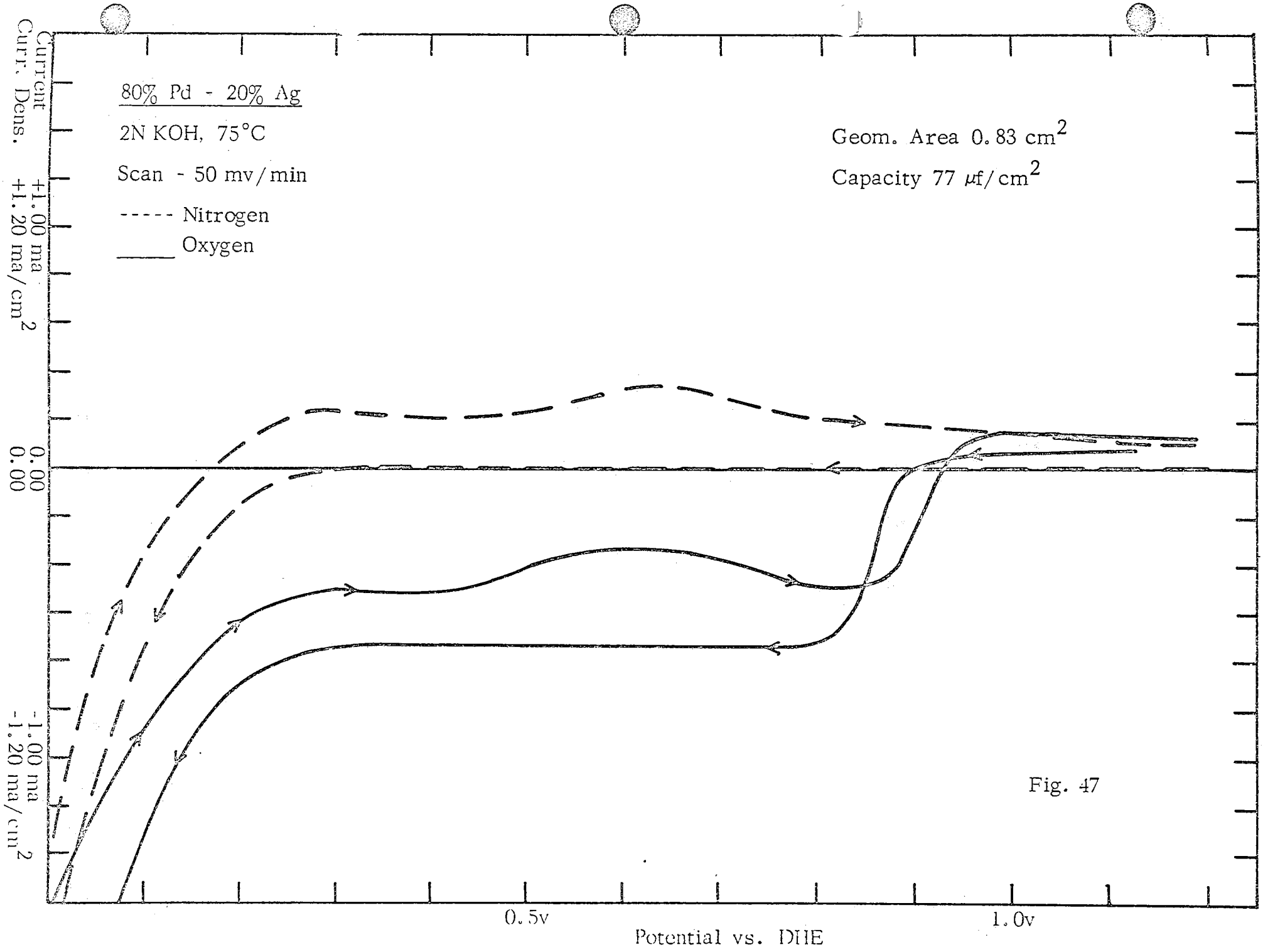
80% Pd - 20% Ag
2N KOH, 75°C
Scan - 50 mv/min
----- Nitrogen
_____ Oxygen
Geom. Area 0.83 cm2
Capacity 77 μf/cm2
Current
Curr. Dens.
+1.00 ma
+1.20 ma/cm2
0.00
0.00
-1.00 ma
-1.20 ma/cm2
0.5v
1.0v
Potential vs. DHE

Fig. 47

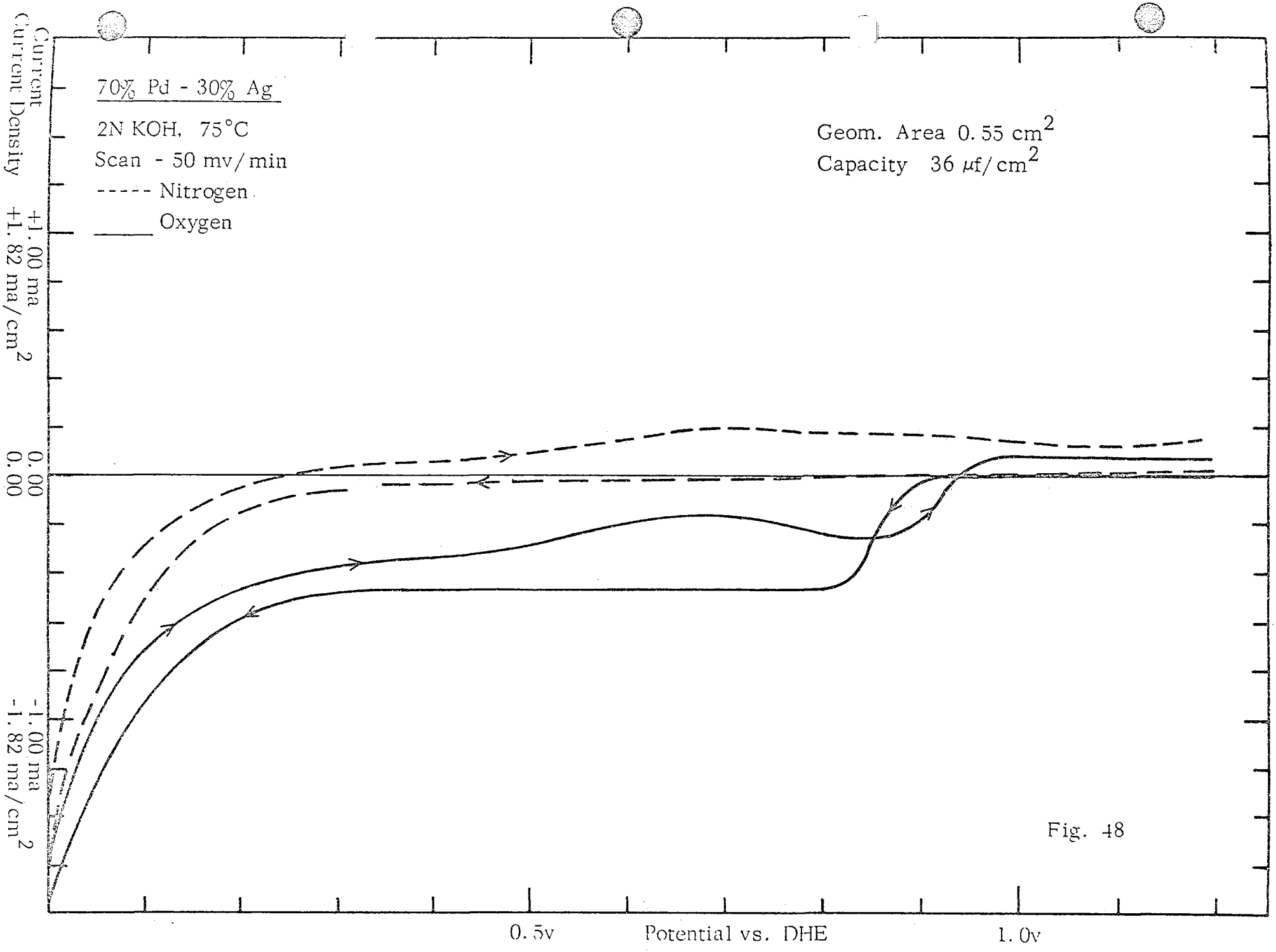
70% Pd - 30% Ag
2N KOH, 75°C
Scan - 50 mv/min
----- Nitrogen
_____ Oxygen
Geom. Area 0.55 cm²
Capacity 36 μf/cm²
Current
Current Density
+1.00 ma
+1.82 ma/cm²
0.00
0.00
-1.00 ma
-1.82 ma/cm²
0.5v
Potential vs. DHE
1.0v

Fig. 48

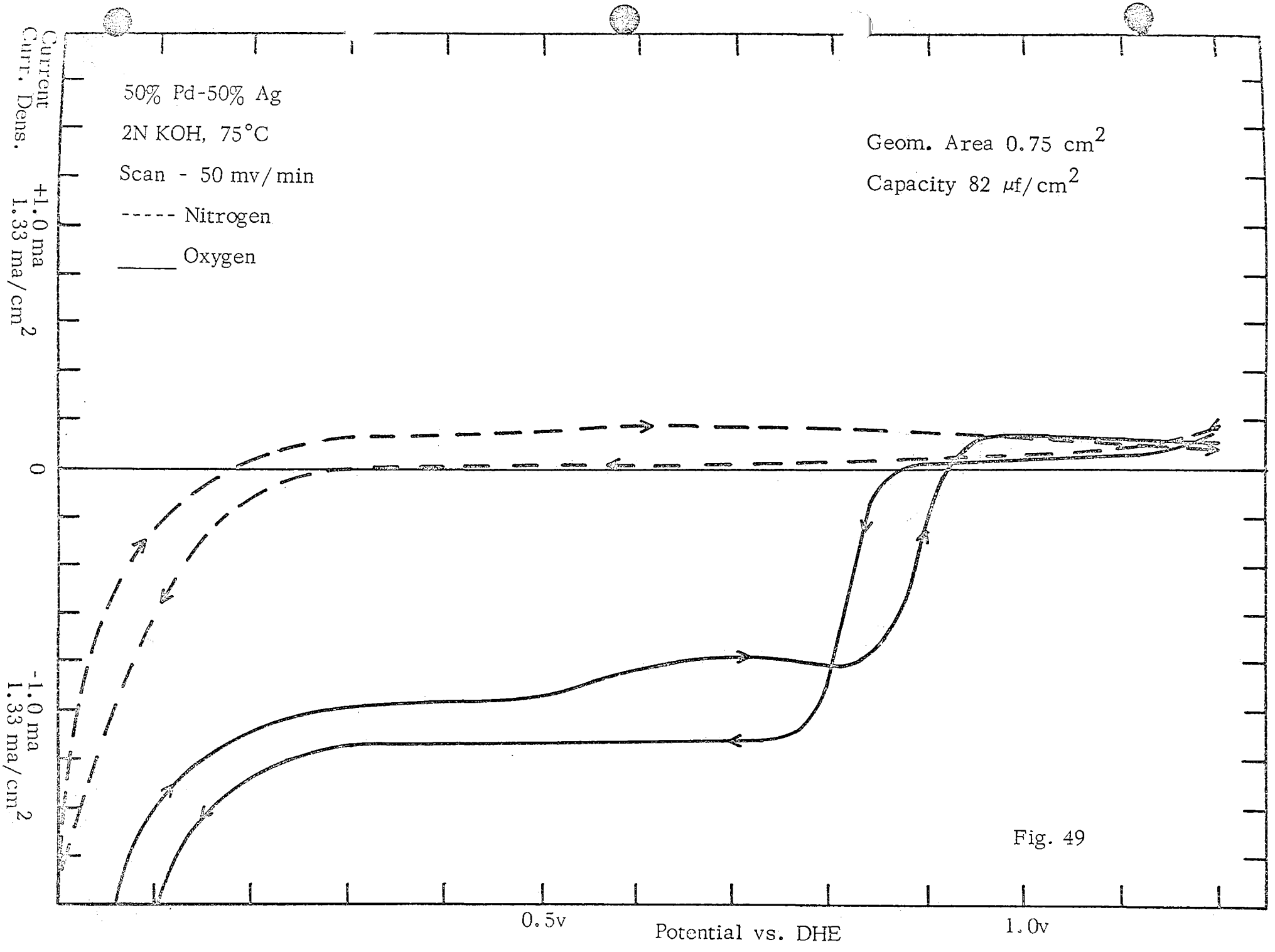
50% Pd-50% Ag
2N KOH, 75°C
Scan - 50 mv/min
----- Nitrogen
_____ Oxygen
Geom. Area 0.75 cm²
Capacity 82 μf/cm²
Current
Curr. Dens.
+1.0 ma
1.33 ma/cm²
0
-1.0 ma
1.33 ma/cm²
0.5v
Potential vs. DHE
1.0v

Fig. 49

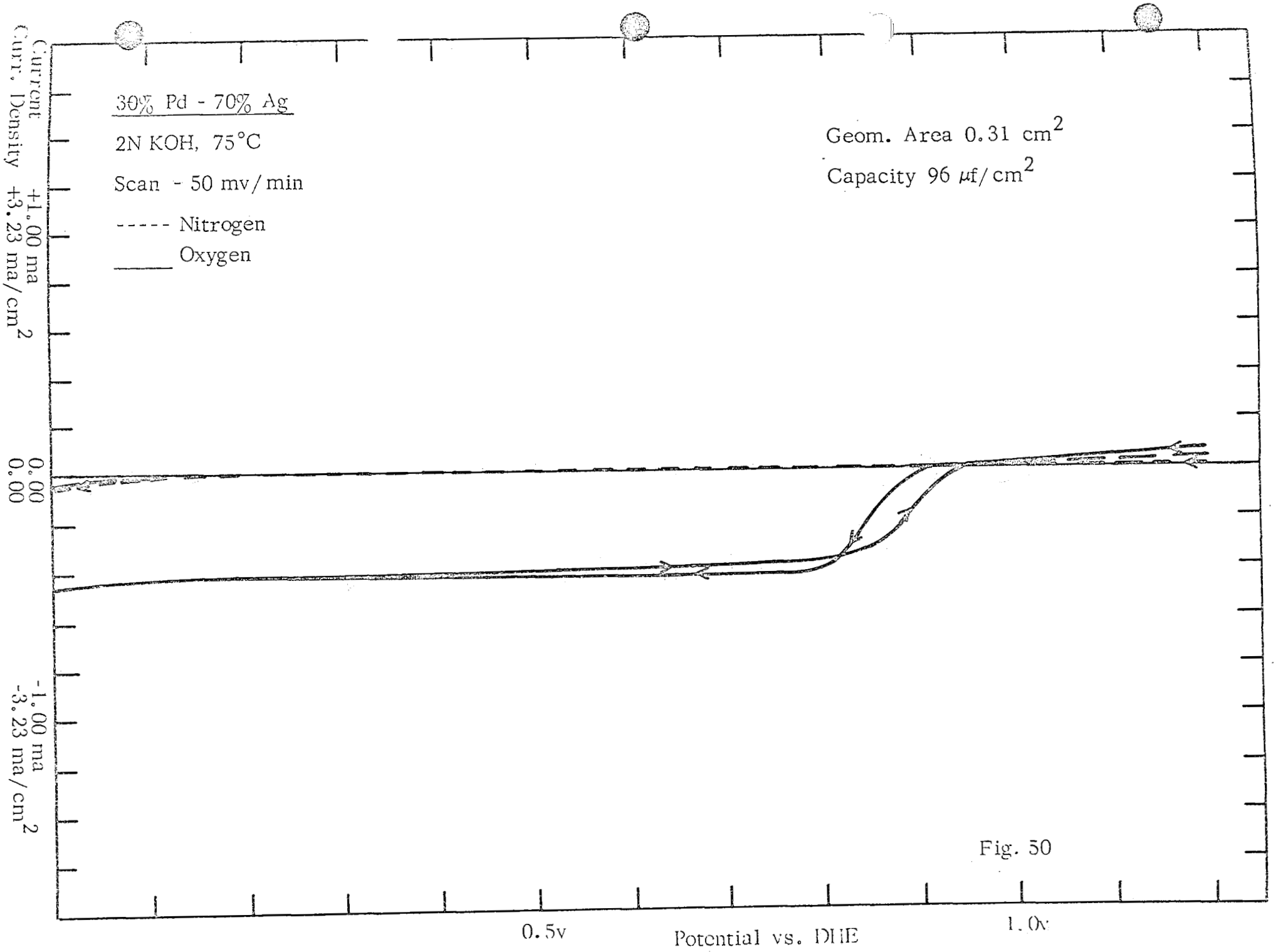
30% Pd - 70% Ag
2N KOH, 75°C
Scan - 50 mv/min
----- Nitrogen
_____ Oxygen
Geom. Area 0.31 cm2
Capacity 96 μf/cm2
Current
Curr. Density
+1.00 ma
+3.23 ma/cm2
0.00
0.00
-1.00 ma
-3.23 ma/cm2
0.5v
Potential vs. DHE
1.0v

Fig. 50

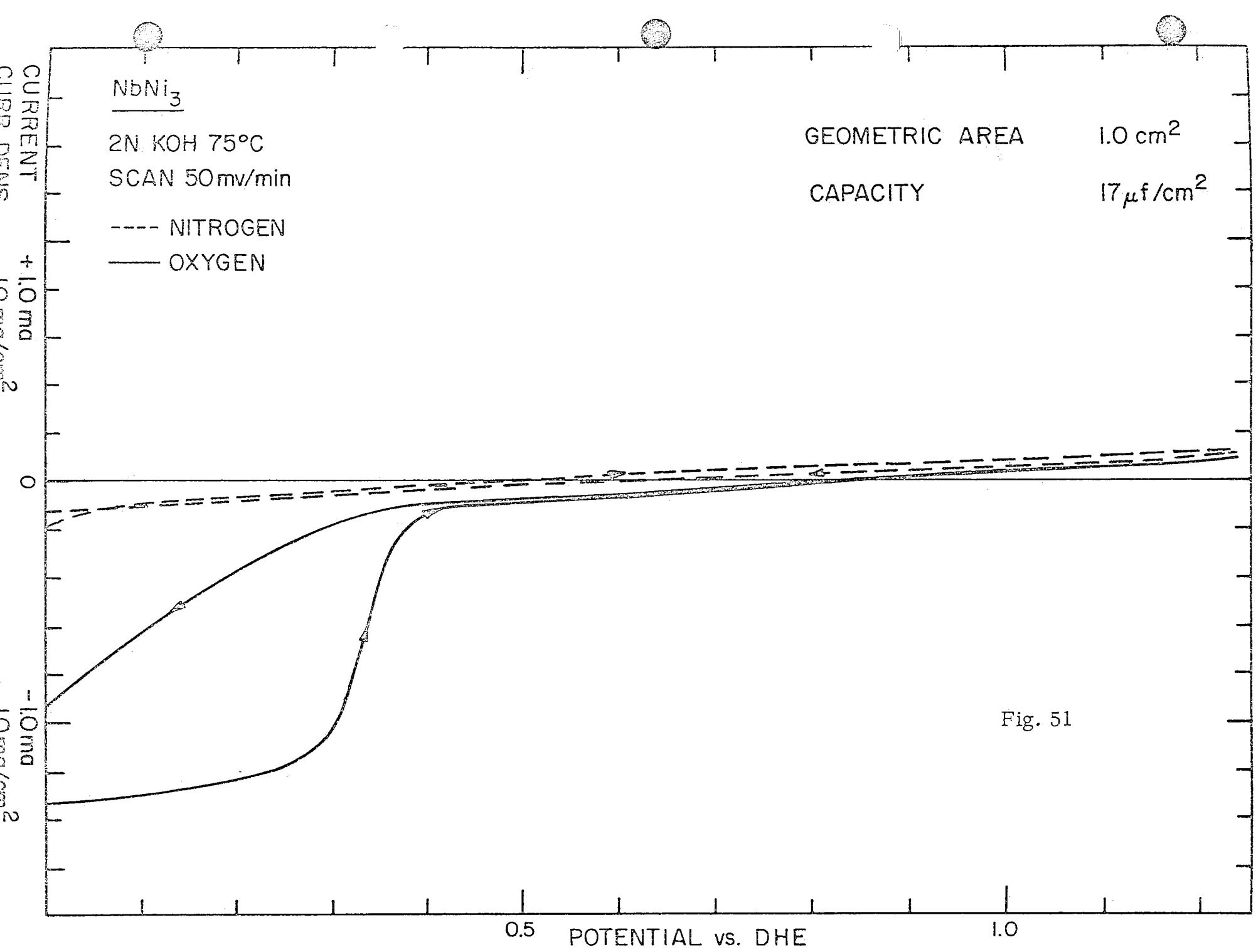
NbNi3
2N KOH 75°C
SCAN 50mv/min
---- NITROGEN
—— OXYGEN
GEOMETRIC AREA 1.0 cm2
CAPACITY 17 μf/cm2
CURRENT
+1.0 ma
0
-1.0 ma
0.5
POTENTIAL vs. DHE
1.0

Fig. 51

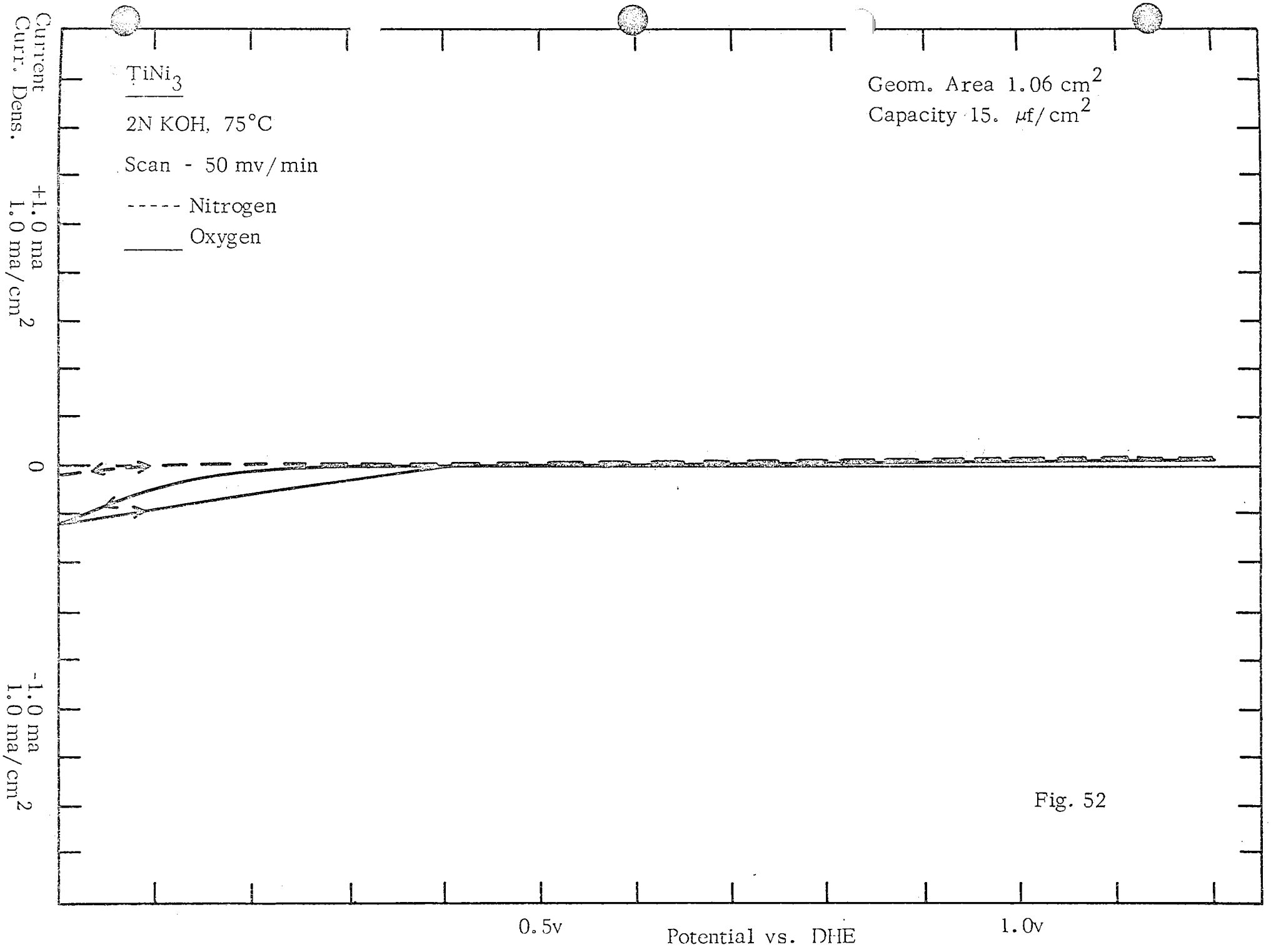
Current
Curr. Dens.
+1.0 ma
1.0 ma/cm²
0
-1.0 ma
1.0 ma/cm²
TiNi3
2N KOH, 75°C
Scan - 50 mv/min
----- Nitrogen
_____ Oxygen
Geom. Area 1.06 cm²
Capacity 15. μf/cm²
0.5v
Potential vs. DHE
1.0v

Fig. 52

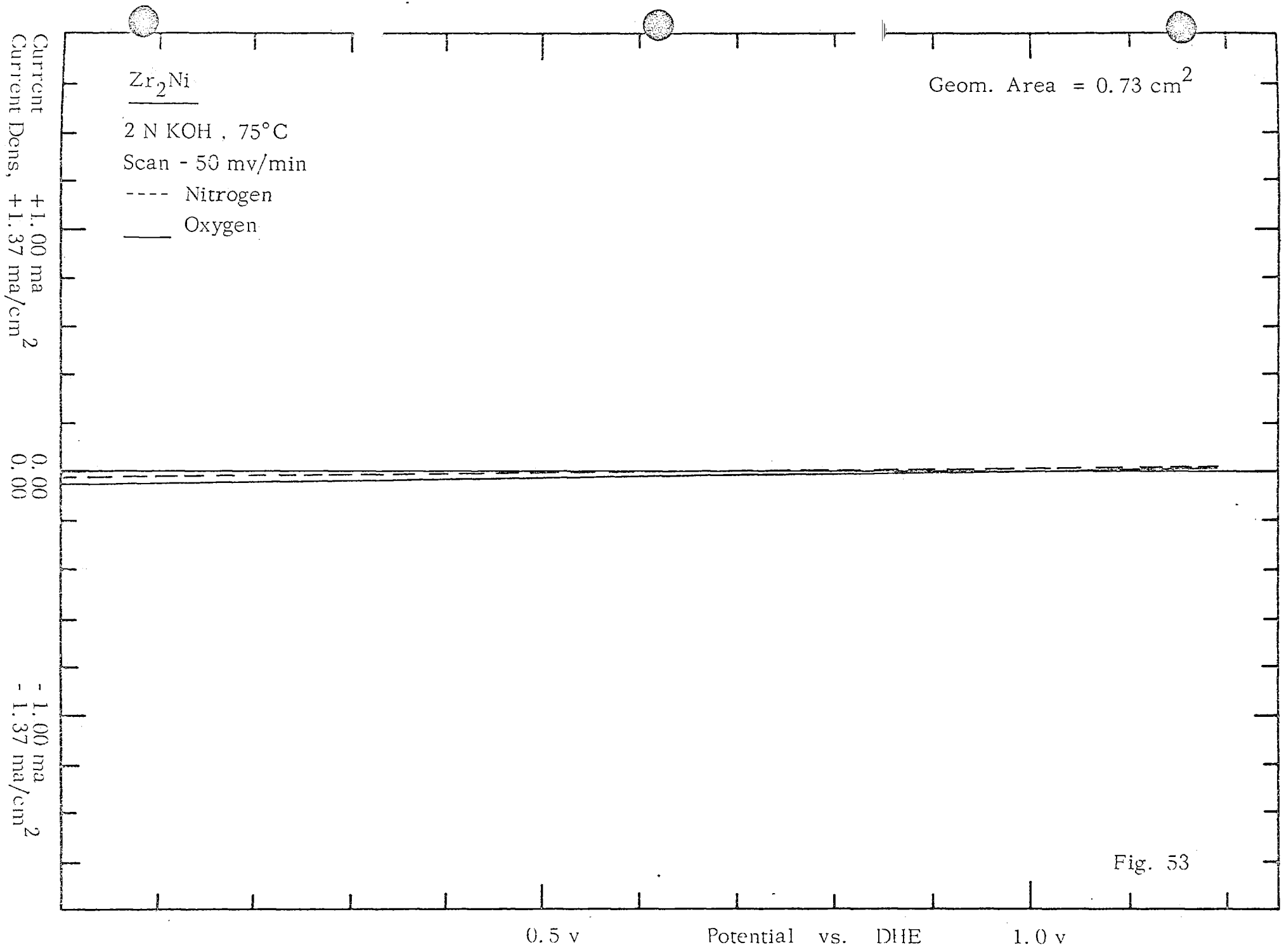
Zr2Ni
2 N KOH , 75°C
Scan - 50 mv/min
---- Nitrogen
____ Oxygen
Geom. Area = 0.73 cm2
Current Dens, +1.37 ma/cm2
+1.00 ma
0.00
0.00
- 1.00 ma
- 1.37 ma/cm2
0.5 v
Potential vs. DHE
1.0 v

Fig. 53

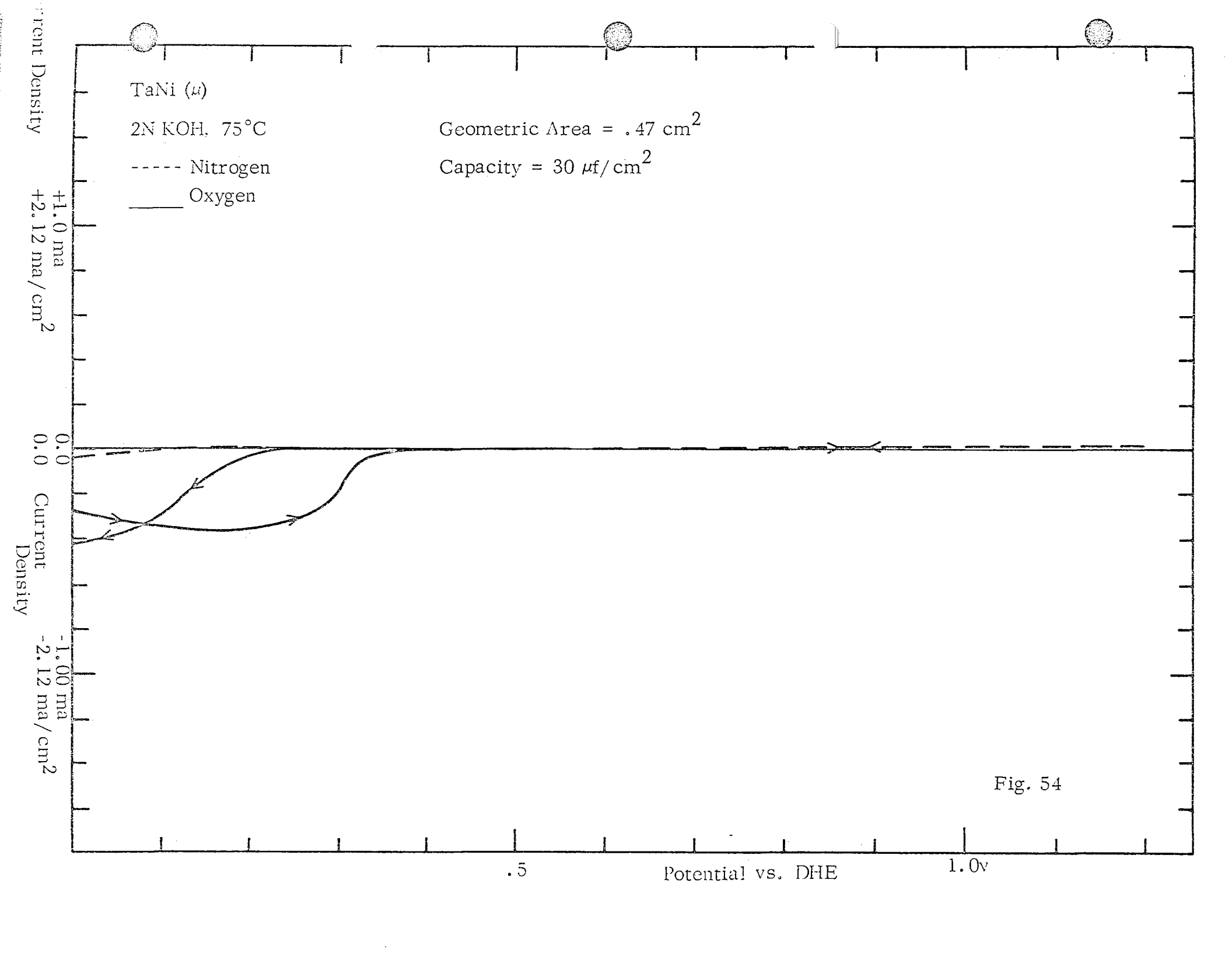
TaNi (μ)
2N KOH, 75°C
Geometric Area = .47 cm²
Capacity = 30 μf/cm²
----- Nitrogen
_____ Oxygen
+1.0 ma
+2.12 ma/cm²
0.0
0.0
Current Density
-1.00 ma
-2.12 ma/cm²
.5
Potential vs. DHE
1.0v

Fig. 54

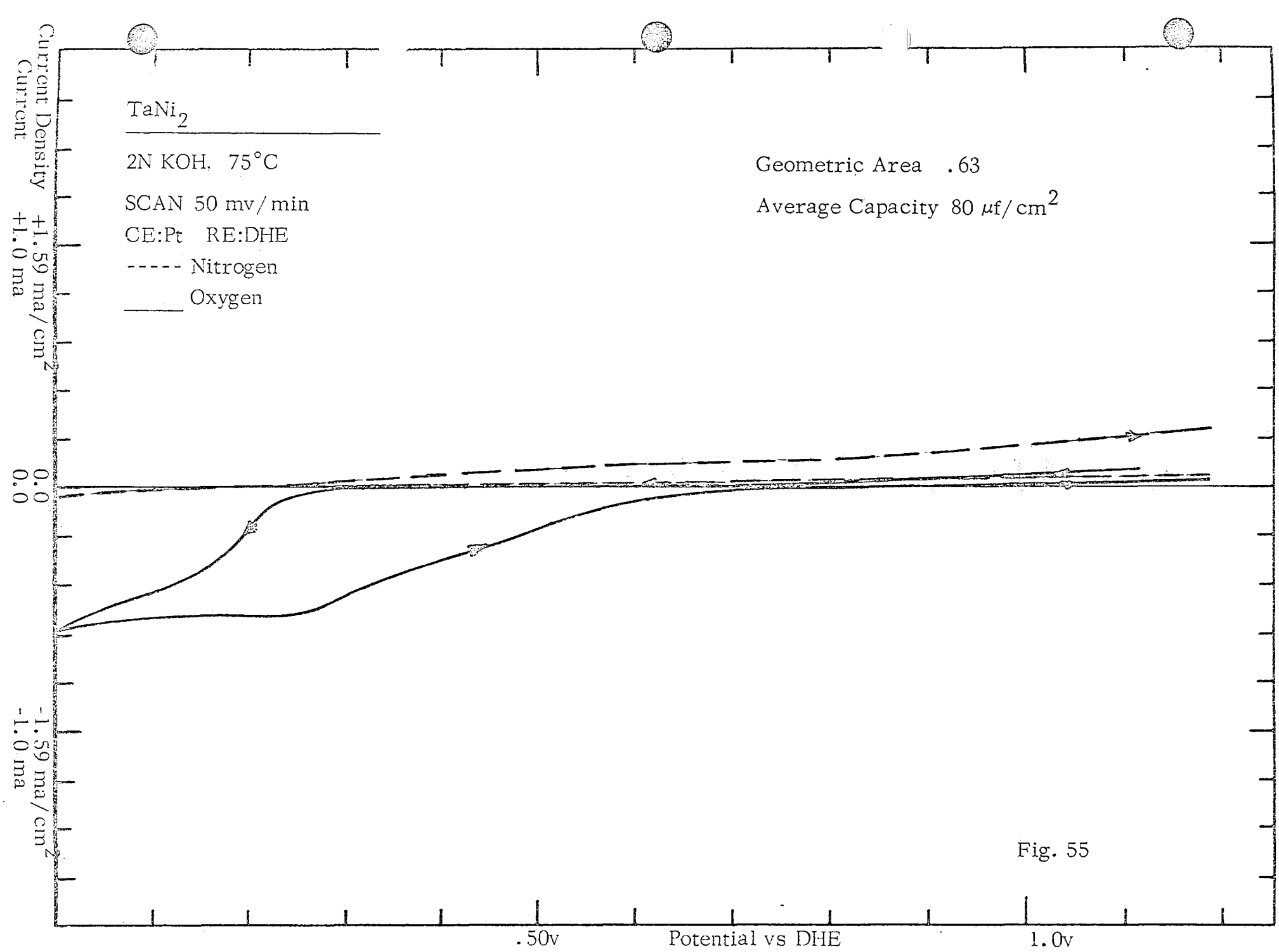
Current Density
Current
+1.59 ma/cm²
+1.0 ma
0.0
0.0
-1.59 ma/cm²
-1.0 ma
TaNi2
2N KOH. 75°C
SCAN 50 mv/min
CE:Pt RE:DHE
----- Nitrogen
_____ Oxygen
Geometric Area .63
Average Capacity 80 μf/cm²
.50v
Potential vs DHE
1.0v

Fig. 55

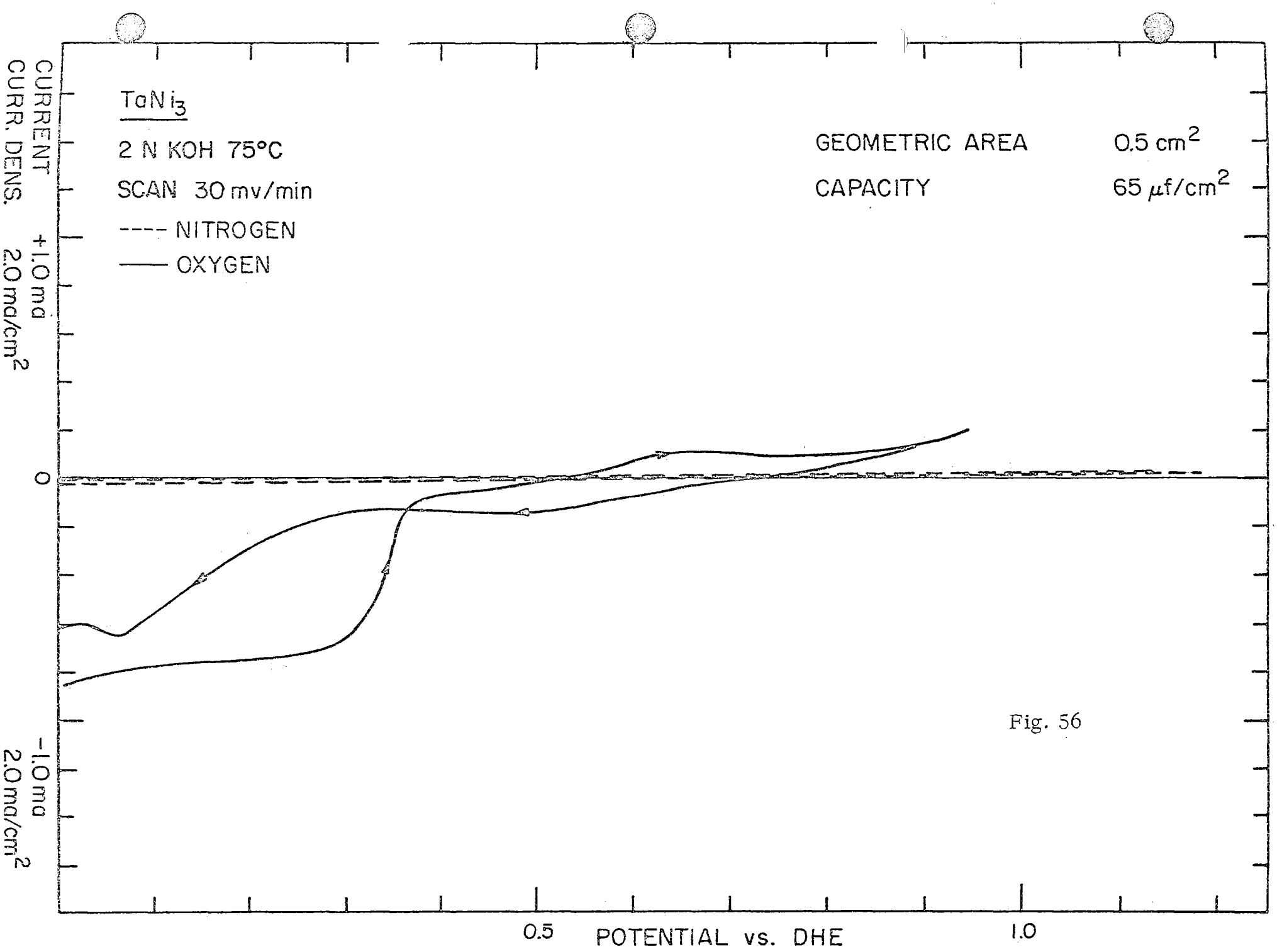
TaNi3
2 N KOH 75°C
SCAN 30 mv/min
---- NITROGEN
—— OXYGEN
GEOMETRIC AREA 0.5 cm2
CAPACITY 65 μf/cm2
CURRENT
CURR. DENS.
+1.0 ma
2.0 ma/cm2
0
-1.0 ma
2.0 ma/cm2
0.5
POTENTIAL vs. DHE
1.0

Fig. 56

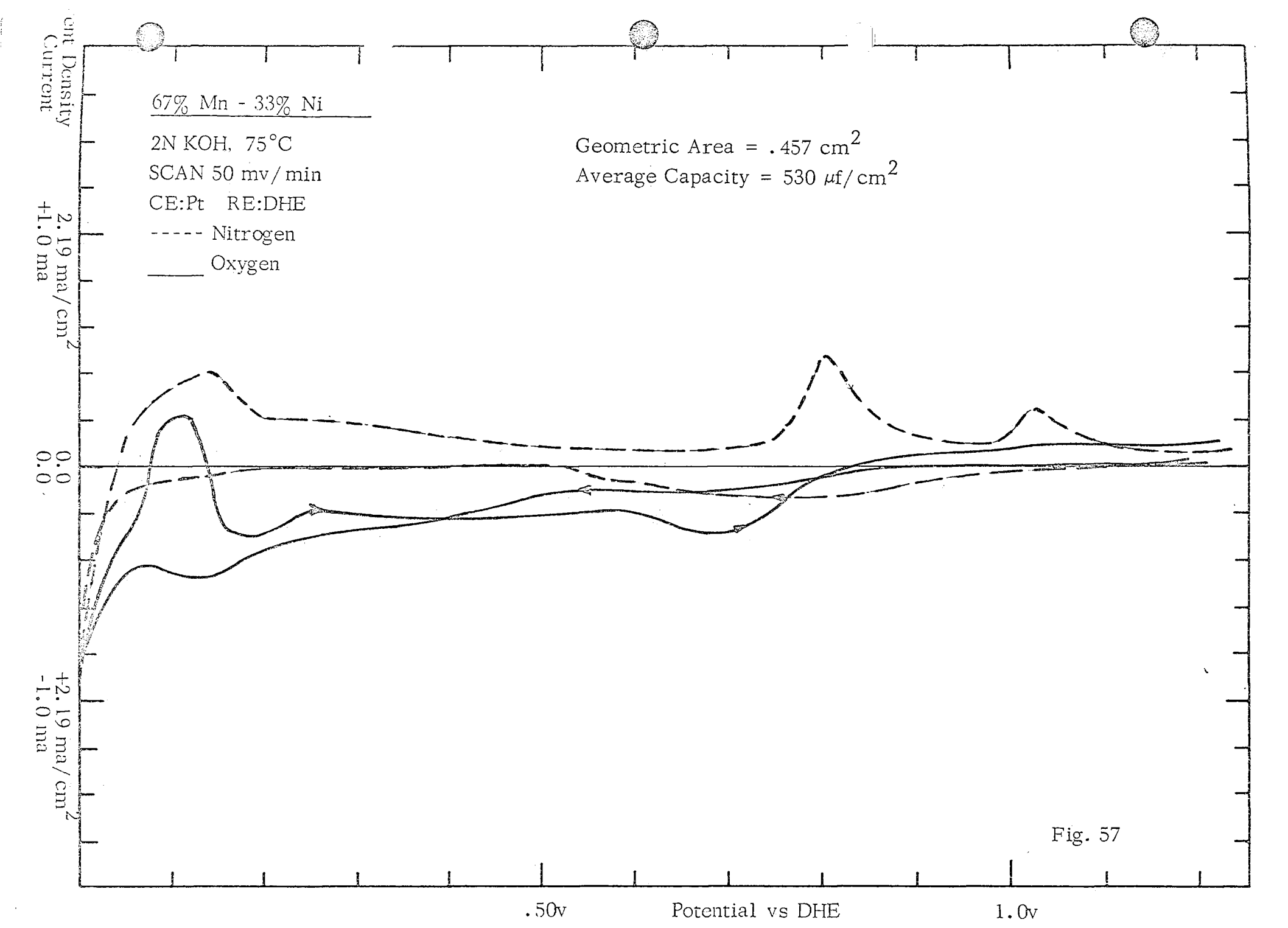
67% Mn - 33% Ni
2N KOH, 75°C
SCAN 50 mv/min
CE:Pt RE:DHE
----- Nitrogen
_____ Oxygen
Geometric Area = .457 cm2
Average Capacity = 530 μf/cm2
Current Density
+1.0 ma
2.19 ma/cm2
0.0
0.0
+2.19 ma/cm2
-1.0 ma
.50v
Potential vs DHE
1.0v

Fig. 57

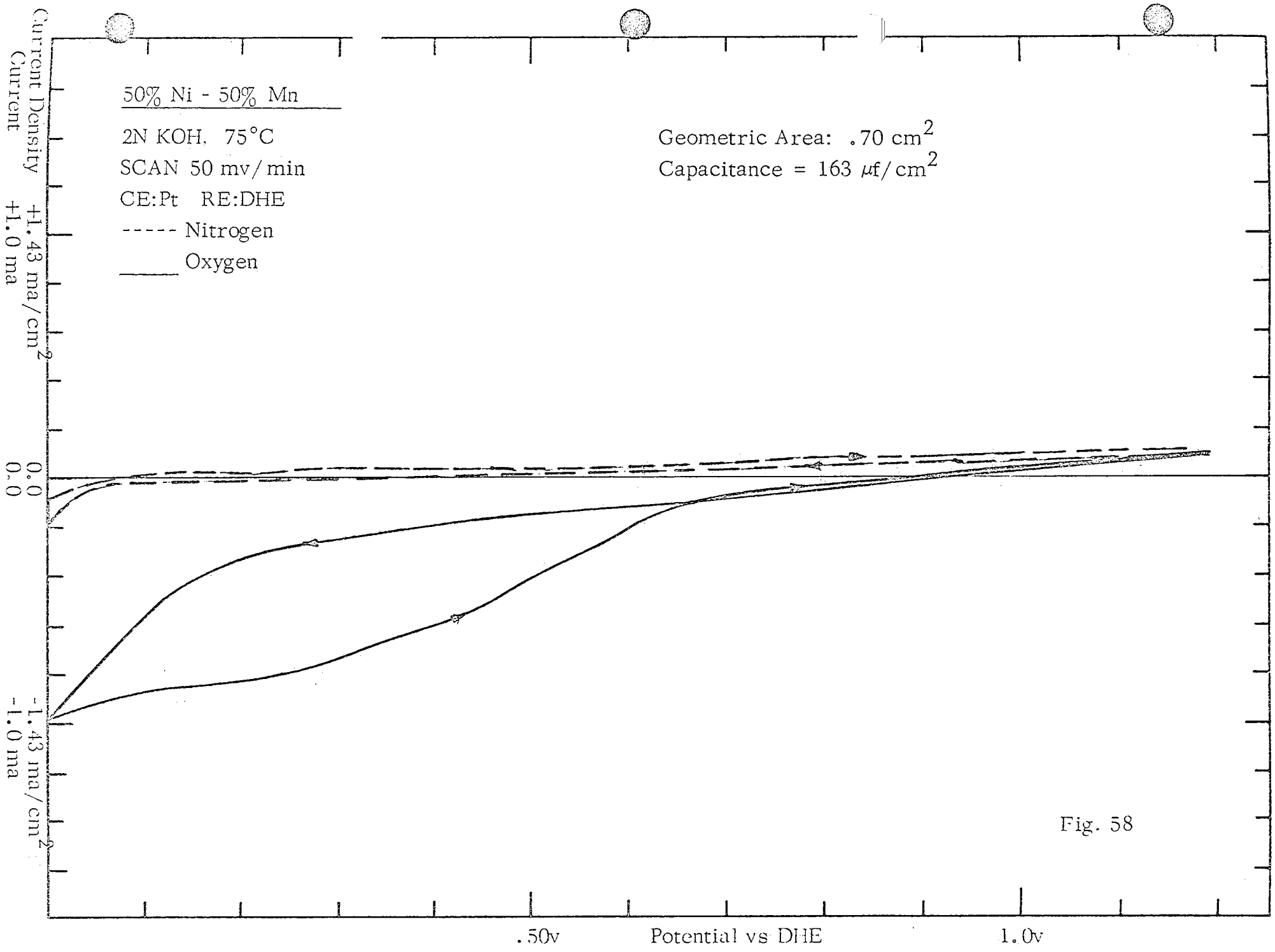
50% Ni - 50% Mn
2N KOH, 75°C
SCAN 50 mv/min
CE:Pt RE:DHE
----- Nitrogen
_____ Oxygen
Geometric Area: .70 cm2
Capacitance = 163 μf/cm2
Current Density
Current
+1.43 ma/cm2
+1.0 ma
0.0
0.0
-1.43 ma/cm2
-1.0 ma
.50v
Potential vs DHE
1.0v

Fig. 58

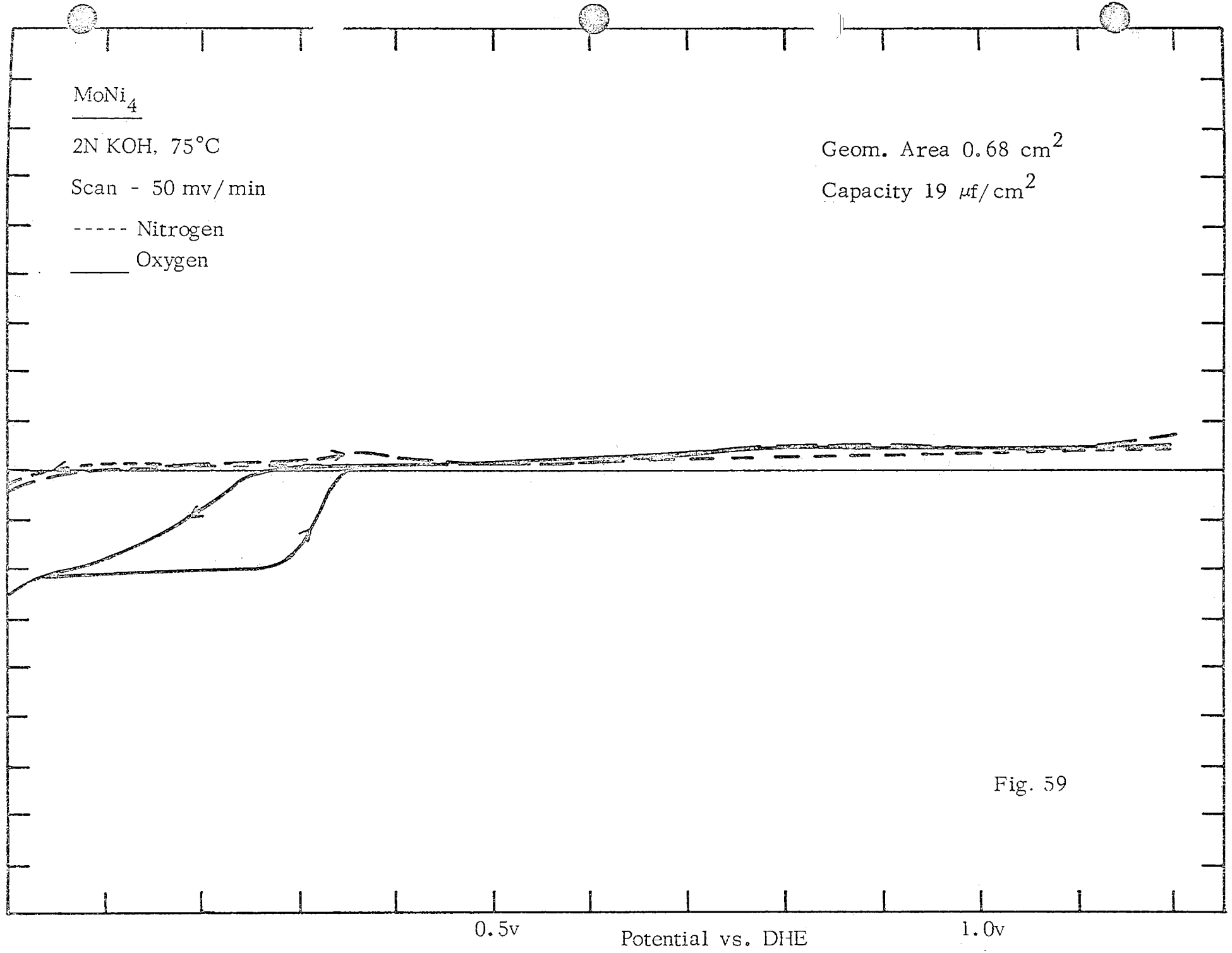
MoNi4
2N KOH, 75°C
Scan - 50 mv/min
----- Nitrogen
_____ Oxygen
Geom. Area 0.68 cm2
Capacity 19 μf/cm2
Current
Curr. Dens.
+1.00 ma
+1.47 ma/cm2
0.00
0.00
-1.00 ma
-1.47 ma/cm2
0.5v
Potential vs. DHE
1.0v

Fig. 59

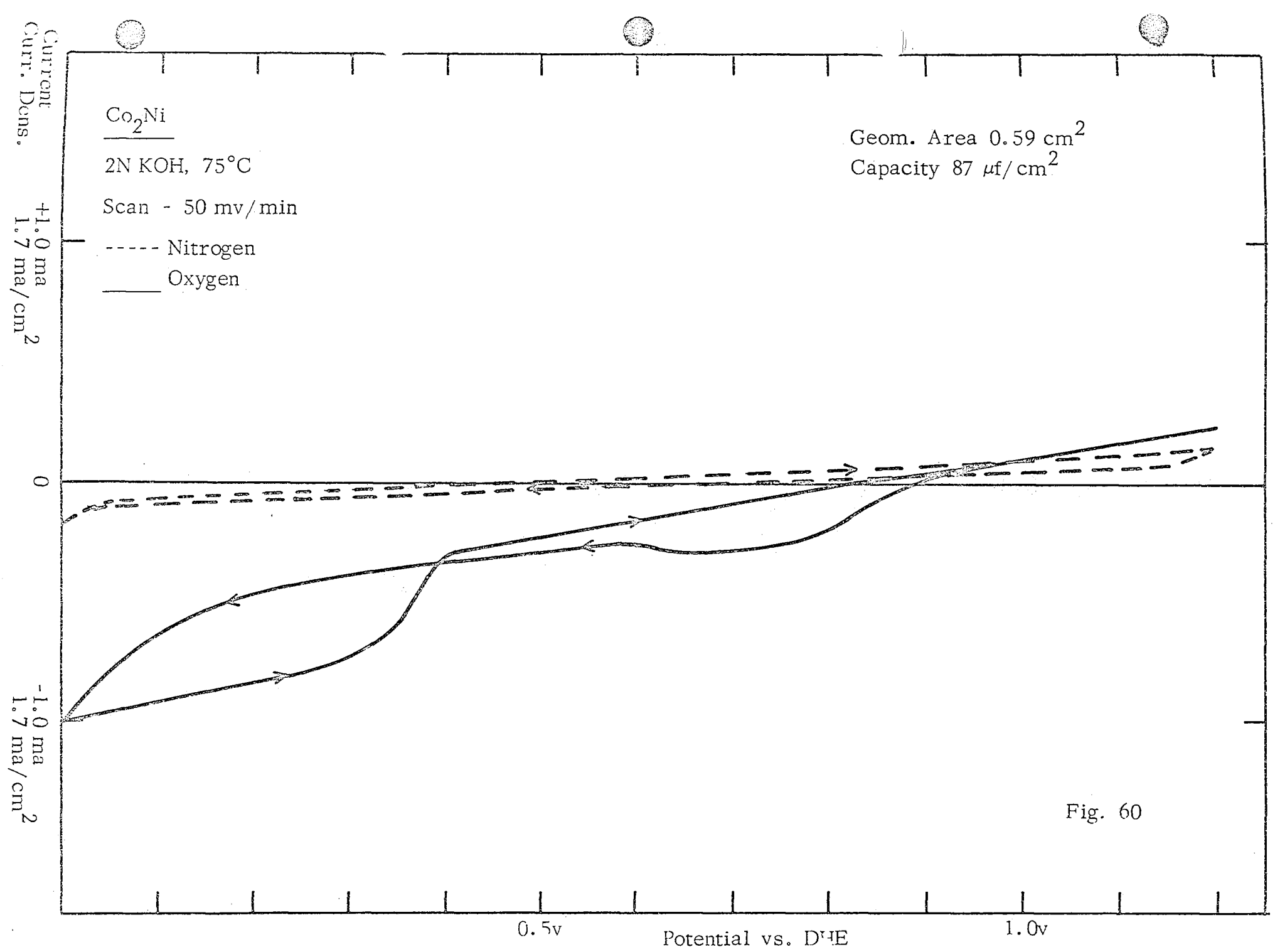
Current
Curr. Dens.
Co_2Ni
2N KOH, 75°C
Scan - 50 mv/min
----- Nitrogen
_____ Oxygen
Geom. Area 0.59 cm^2
Capacity 87 $\mu f/cm^2$
+1.0 ma
1.7 ma/cm^2
0
-1.0 ma
1.7 ma/cm^2
0.5v
Potential vs. DHE
1.0v

Fig. 60

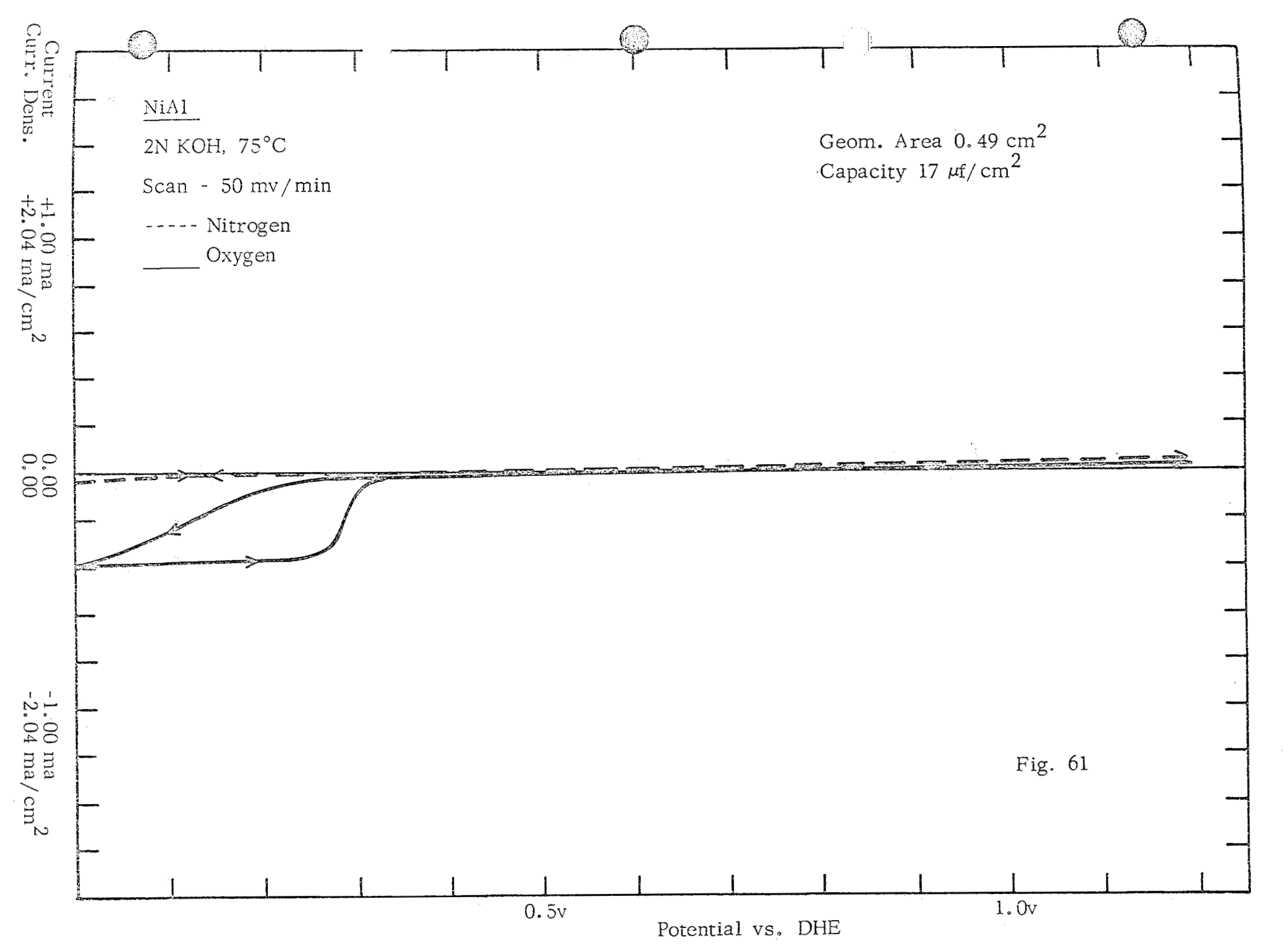
NiAl
2N KOH, 75°C
Scan - 50 mv/min
----- Nitrogen
_____ Oxygen
Geom. Area 0.49 cm2
Capacity 17 μf/cm2
Current
Curr. Dens.
+1.00 ma
+2.04 ma/cm2
0.00
0.00
-1.00 ma
-2.04 ma/cm2
0.5v
1.0v
Potential vs. DHE

Fig. 61

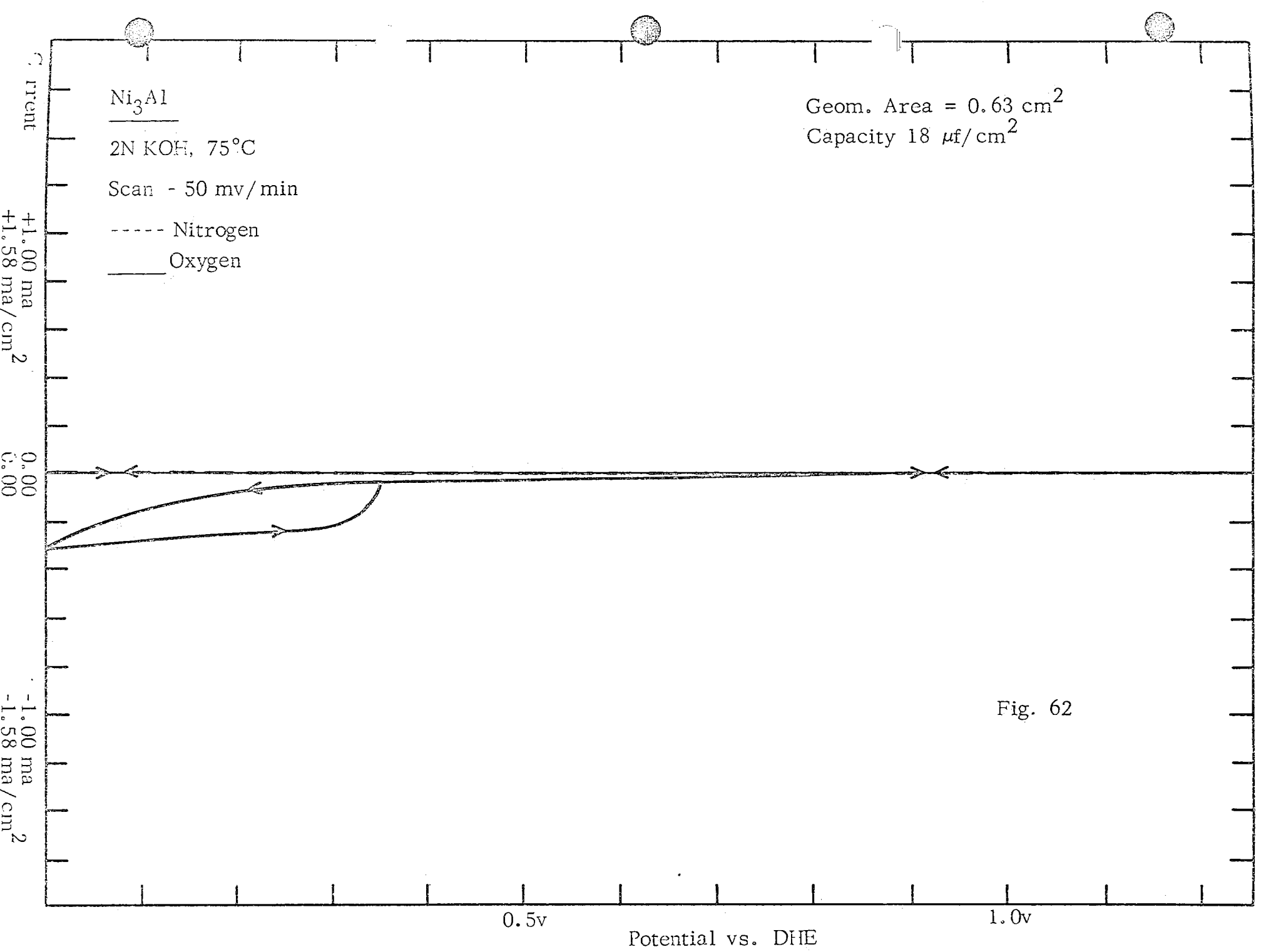
Ni3Al
2N KOH, 75°C
Scan - 50 mv/min
----- Nitrogen
_____ Oxygen
Geom. Area = 0.63 cm2
Capacity 18 μf/cm2
Current
+1.00 ma
+1.58 ma/cm2
0.00
0.00
-1.00 ma
-1.58 ma/cm2
0.5v
1.0v
Potential vs. DHE

Fig. 62

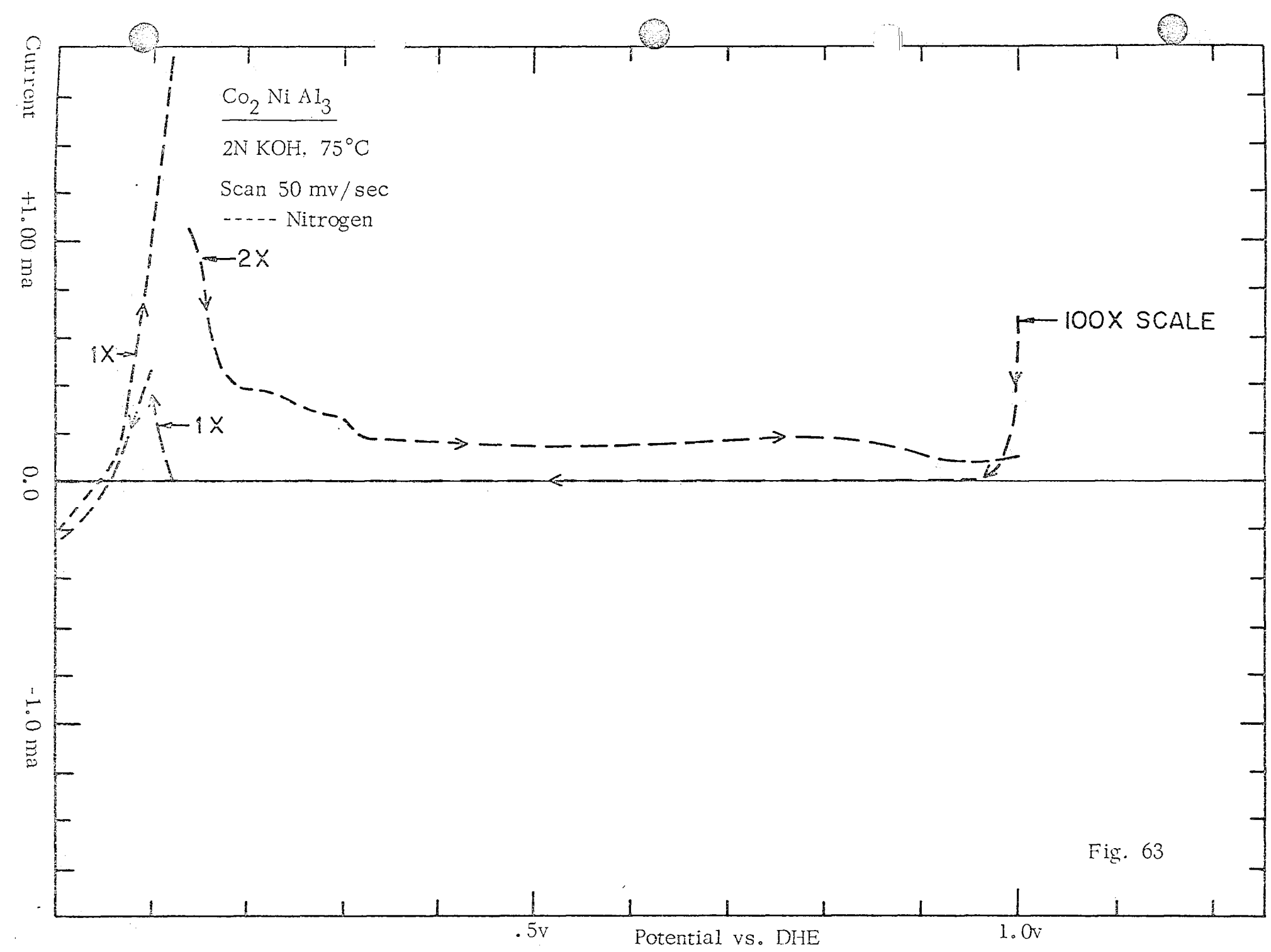
Current
+1.00 ma
0.0
-1.0 ma
$Co_2 Ni Al_3$
2N KOH, 75°C
Scan 50 mv/sec
----- Nitrogen
2X
1X
1X
100X SCALE
.5v
Potential vs. DHE
1.0v

Fig. 63

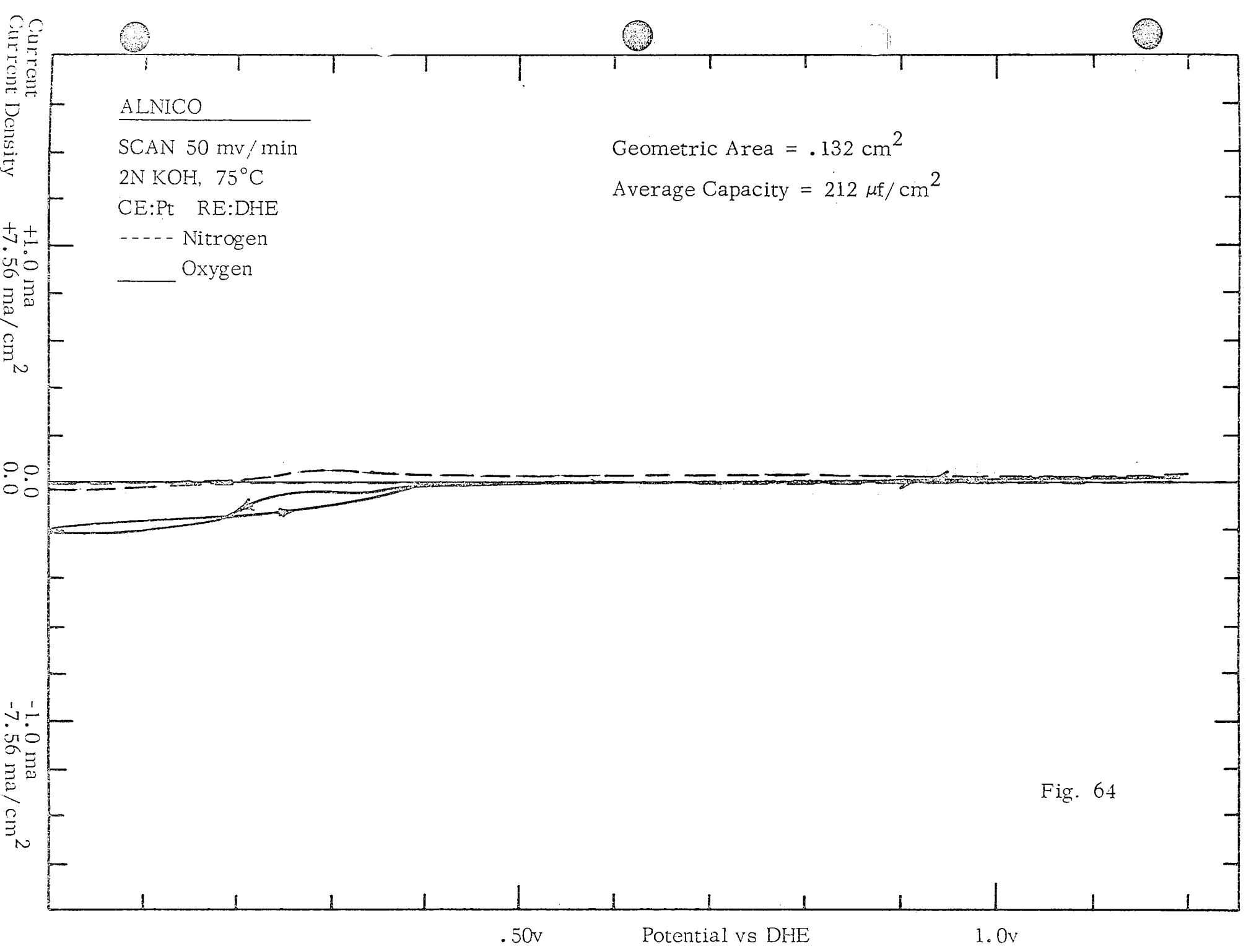
ALNICO
SCAN 50 mv/min
2N KOH, 75°C
CE:Pt RE:DHE
----- Nitrogen
_____ Oxygen
Geometric Area = .132 cm²
Average Capacity = 212 μf/cm²
Current
Current Density
+1.0 ma
+7.56 ma/cm²
0.0
0.0
-1.0 ma
-7.56 ma/cm²
.50v
Potential vs DHE
1.0v

Fig. 64

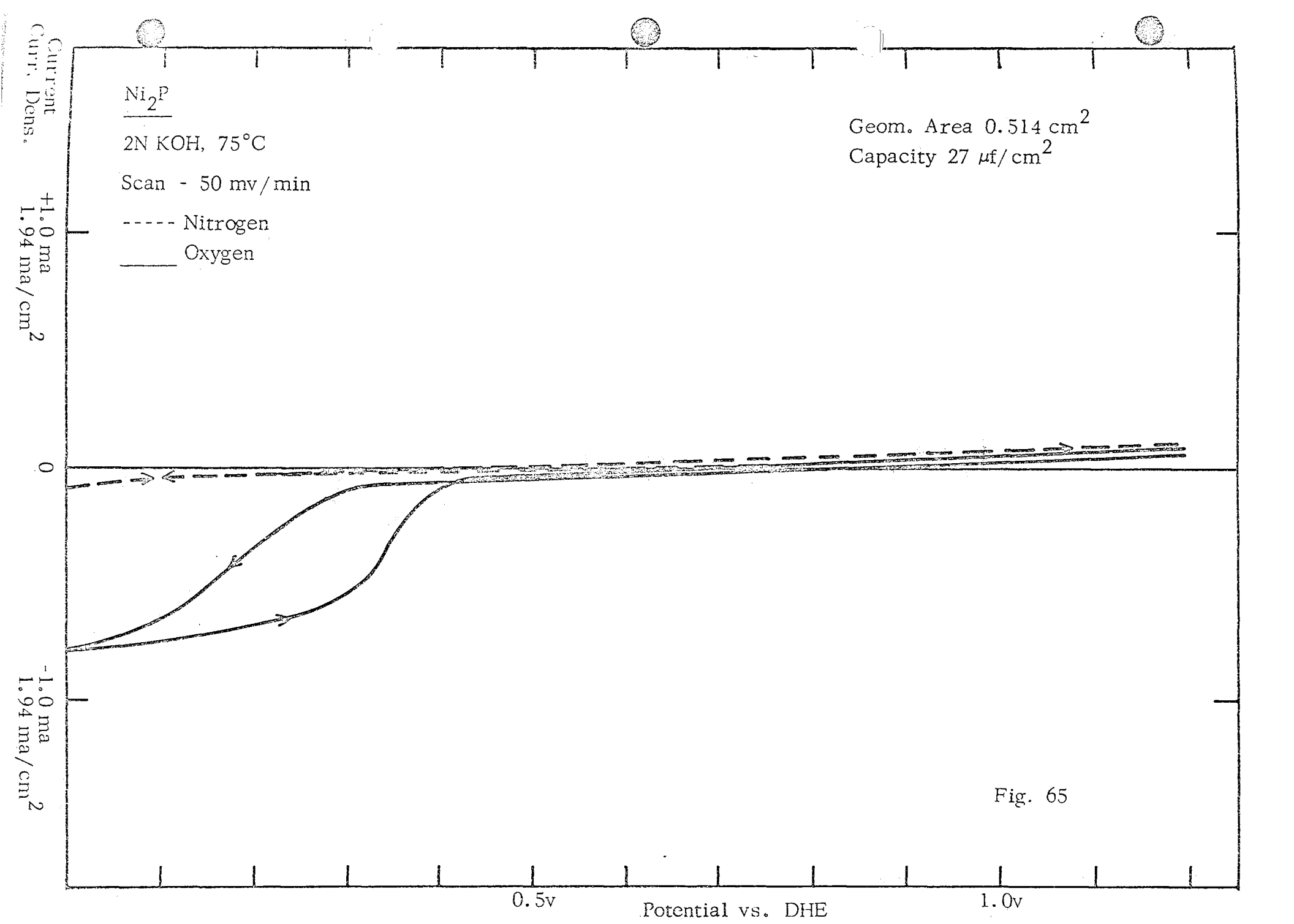
Ni2P
2N KOH, 75°C
Scan - 50 mv/min
----- Nitrogen
_____ Oxygen
Geom. Area 0.514 cm2
Capacity 27 μf/cm2
Current
Curr. Dens.
+1.0 ma
1.94 ma/cm2
0
-1.0 ma
1.94 ma/cm2
0.5v
Potential vs. DHE
1.0v

Fig. 65

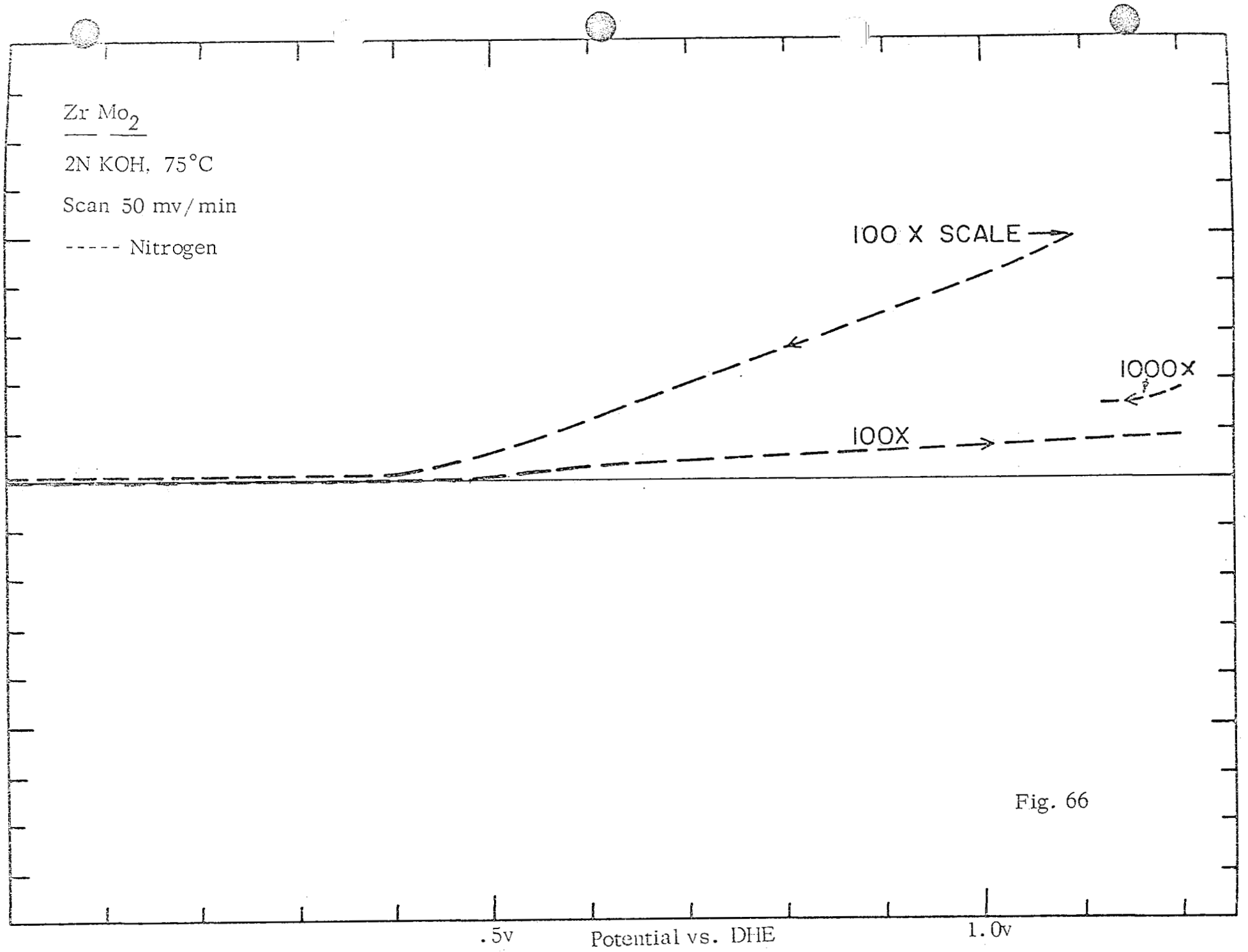
Zr Mo_2
2N KOH, 75°C
Scan 50 mv/min
----- Nitrogen
100 X SCALE
1000X
100X
Current
+1.0 ma
0.0
-1.0 ma
.5v
Potential vs. DHE
1.0v

Fig. 66

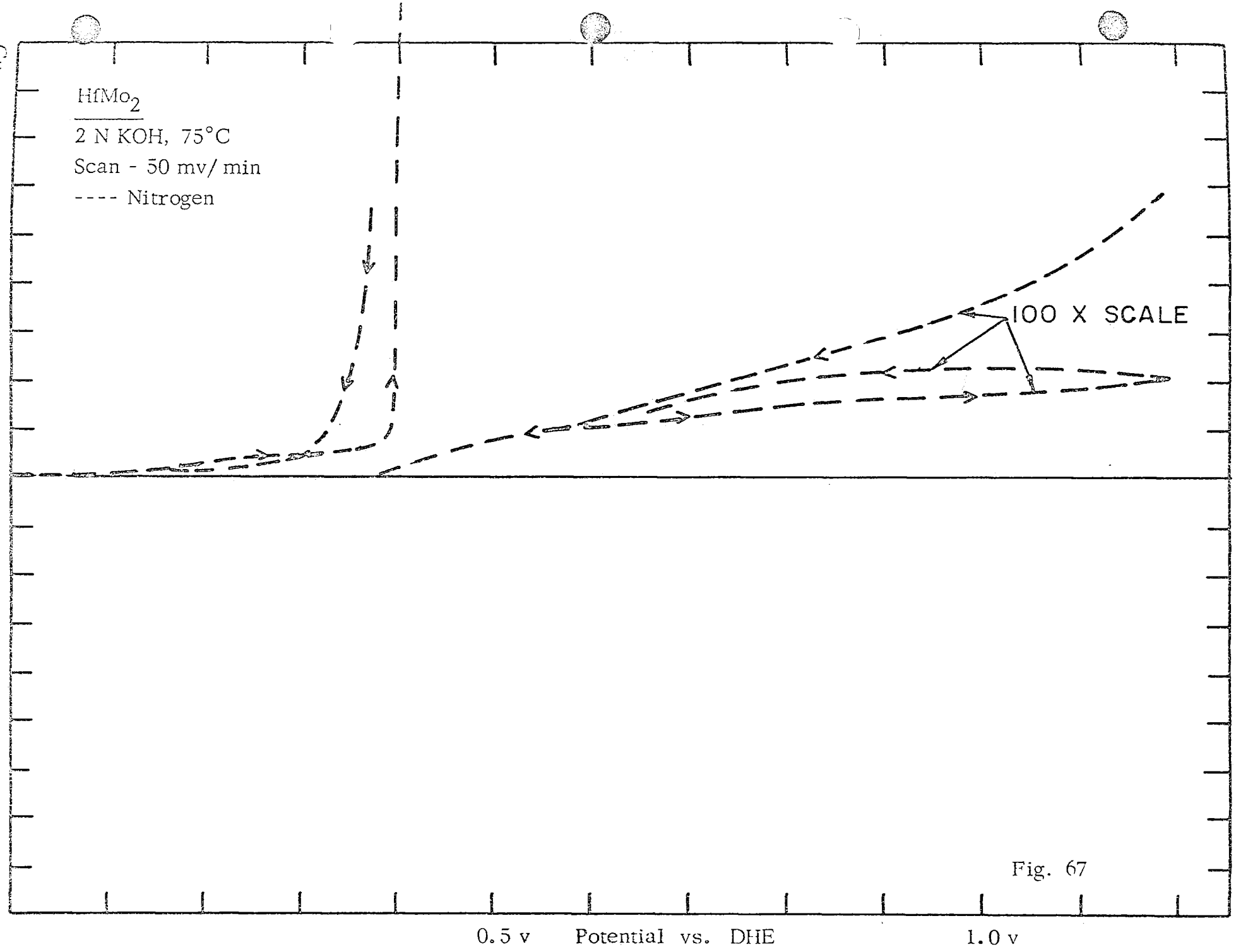
$HfMo_2$
2 N KOH, 75°C
Scan - 50 mv/ min
---- Nitrogen
100 X SCALE
Current
+ 1.00 ma
0.00
- 1.00 ma
0.5 v
Potential vs. DHE
1.0 v

Fig. 67

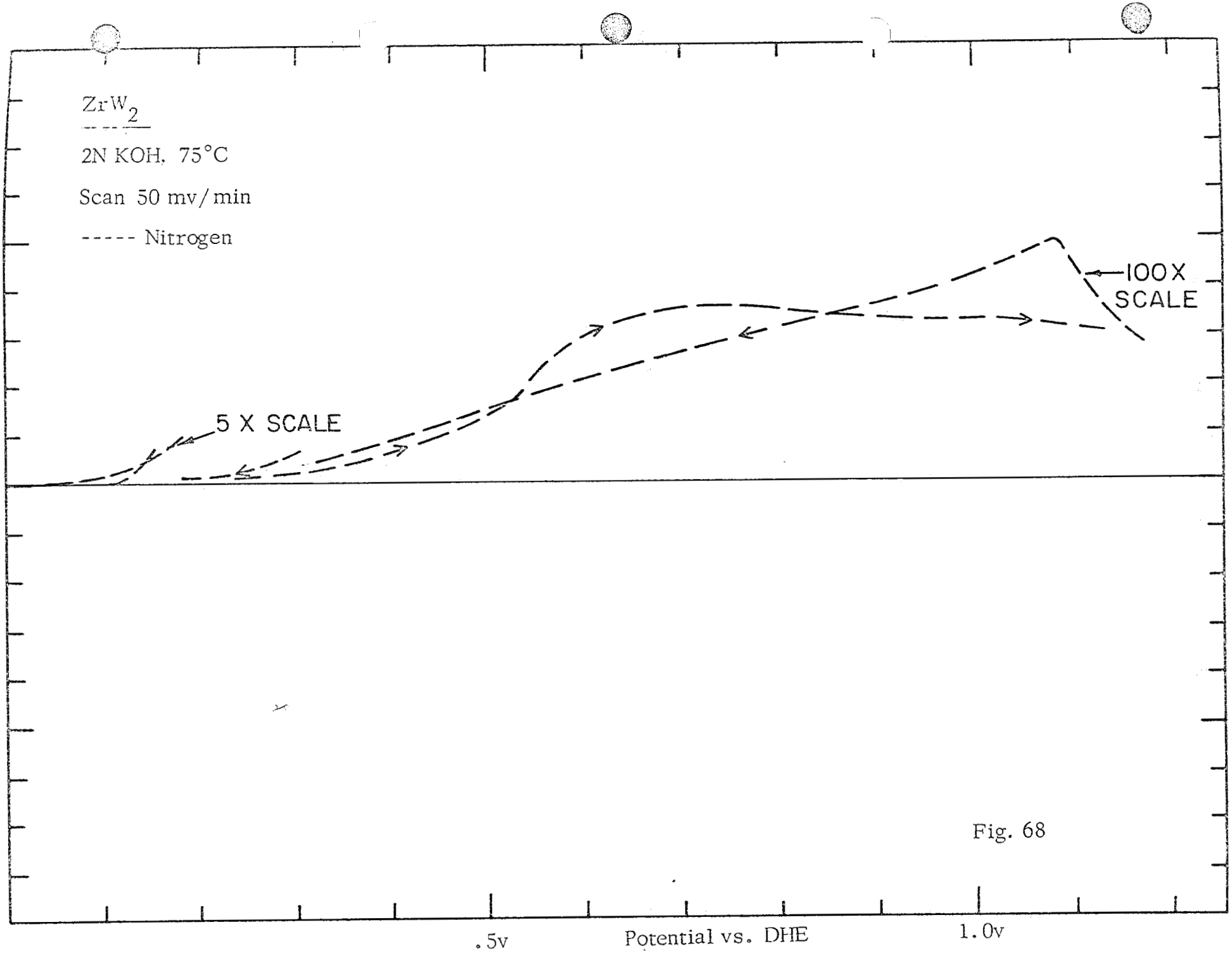
ZrW_2
2N KOH, 75°C
Scan 50 mv/min
----- Nitrogen
100 X SCALE
5 X SCALE
.5v
Potential vs. DHE
1.0v

Fig. 68

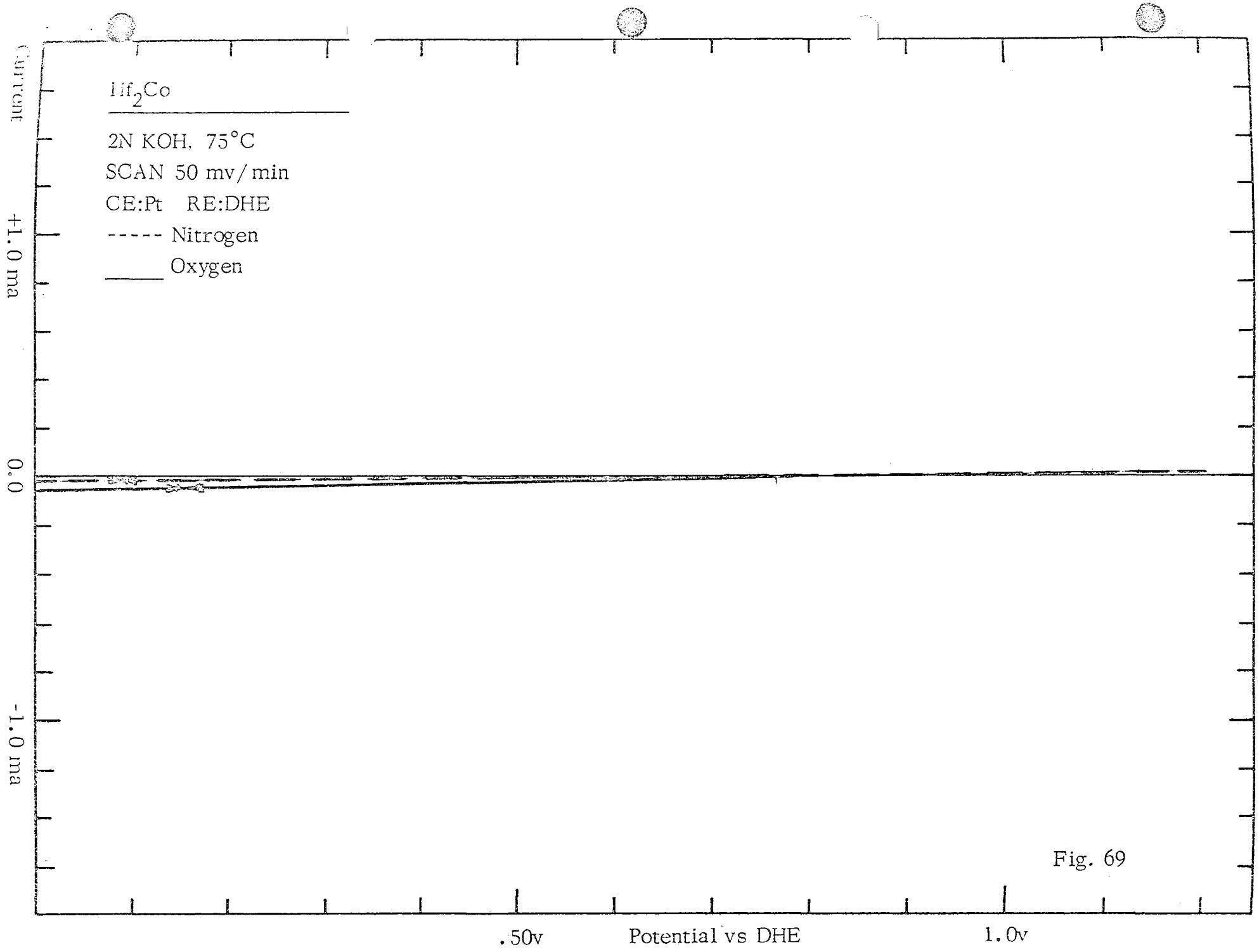
Current
Hf_2Co
2N KOH, 75°C
SCAN 50 mv/min
CE:Pt RE:DHE
----- Nitrogen
_____ Oxygen
+1.0 ma
0.0
-1.0 ma
.50v
Potential vs DHE
1.0v

Fig. 69

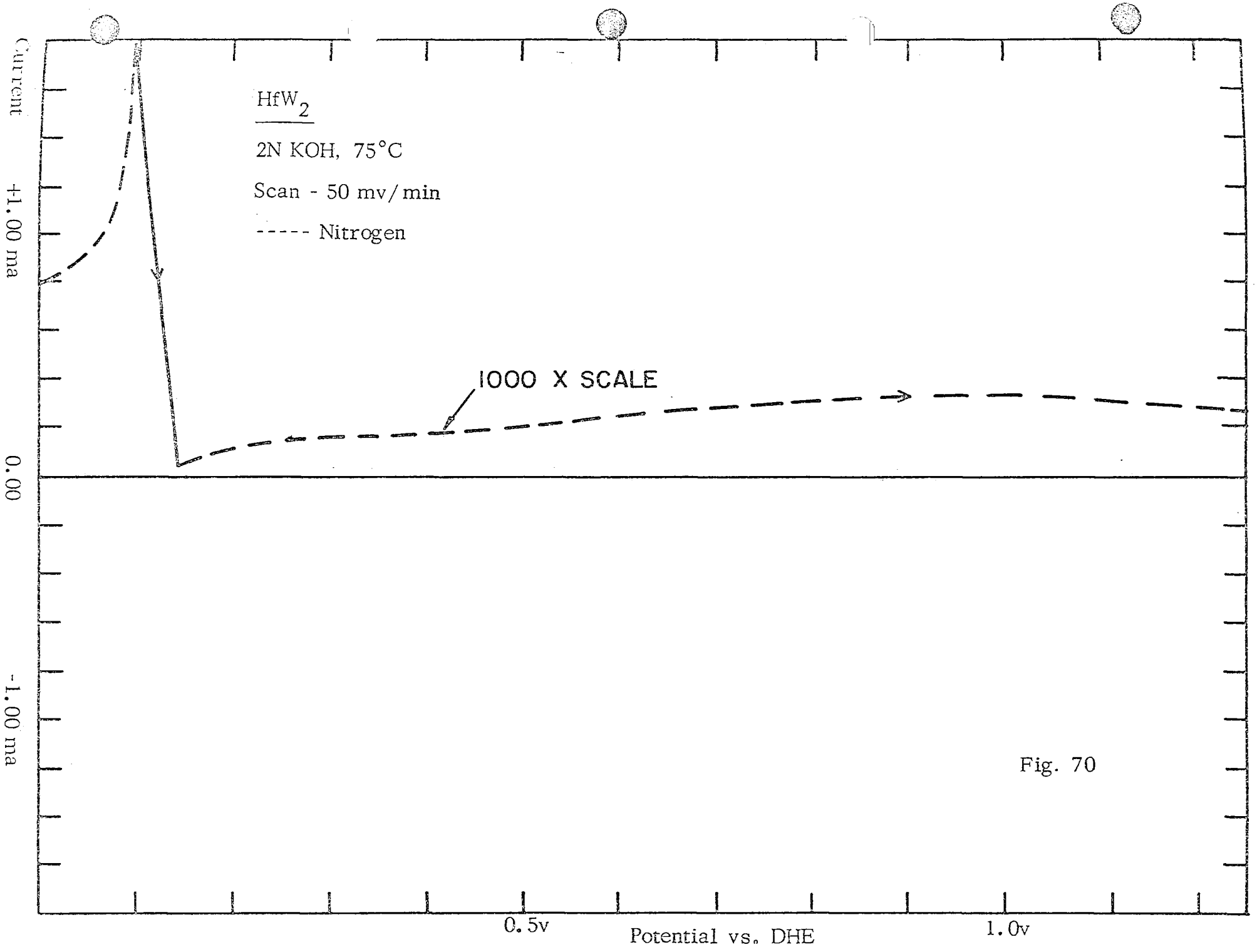
Current
+1.00 ma
0.00
-1.00 ma
HfW2
2N KOH, 75°C
Scan - 50 mv/min
----- Nitrogen
1000 X SCALE
0.5v
Potential vs. DHE
1.0v

Fig. 70

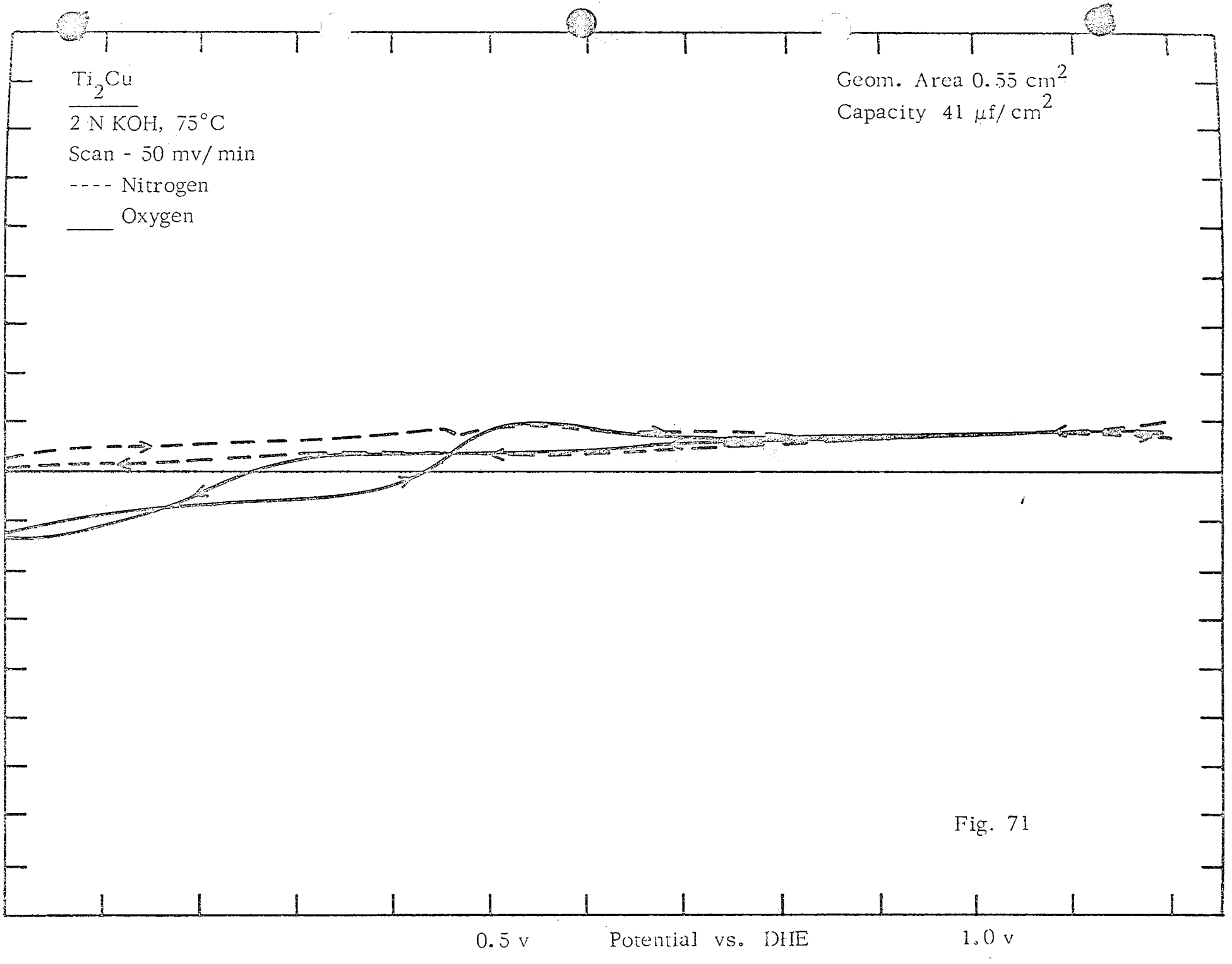
Ti2Cu
2 N KOH, 75°C
Scan - 50 mv/ min
---- Nitrogen
____ Oxygen
Geom. Area 0.55 cm2
Capacity 41 μf/ cm2
Current
Curr. Dens.
+ 1.00 ma
+ 1.82 ma/ cm2
0.00
0.00
- 1.00 ma
- 1.82 ma/ cm2
0.5 v
Potential vs. DHE
1.0 v

Fig. 71

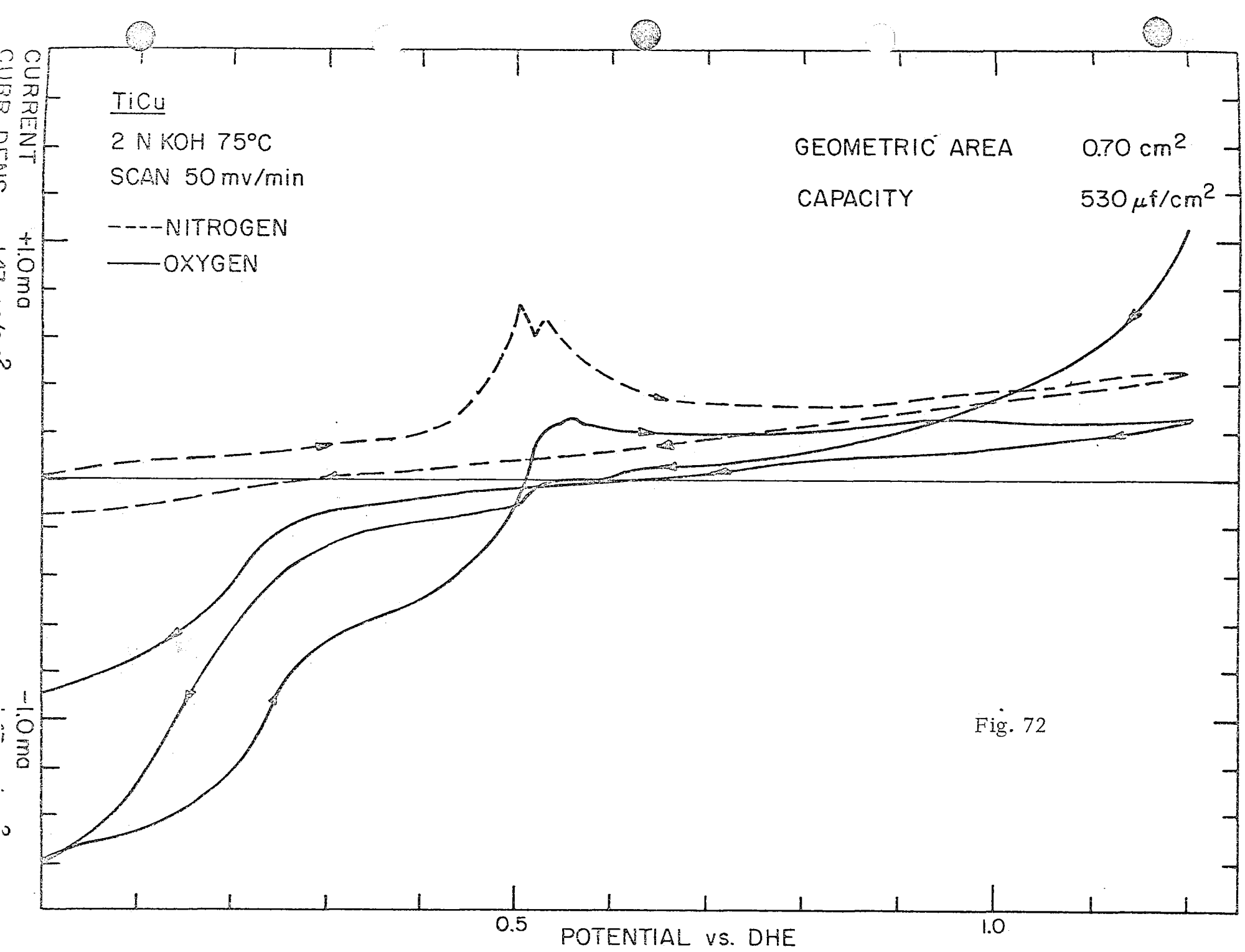
TiCu
2 N KOH 75°C
SCAN 50 mv/min
----NITROGEN
——OXYGEN
GEOMETRIC AREA 0.70 cm²
CAPACITY 530 μf/cm²
CURRENT
+1.0 ma
-1.0 ma
0.5
1.0
POTENTIAL vs. DHE

Fig. 72

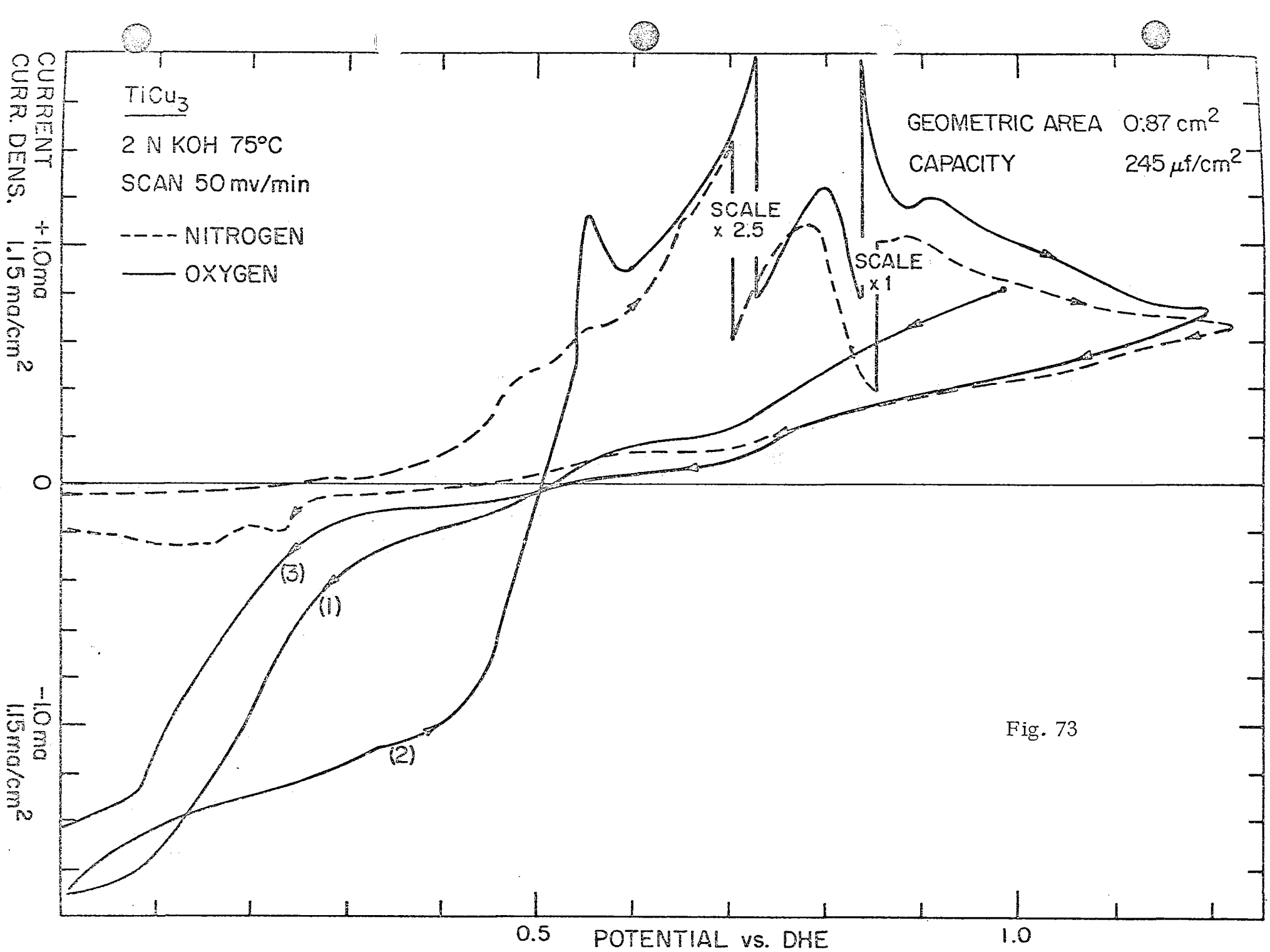
TiCu3
2 N KOH 75°C
SCAN 50 mv/min
---- NITROGEN
—— OXYGEN
GEOMETRIC AREA 0.87 cm2
CAPACITY 245 μf/cm2
SCALE x 2.5
SCALE x 1
CURRENT CURR. DENS. +1.0ma 1.15 ma/cm2
0
-1.0 ma 1.15ma/cm2
(1)
(2)
(3)
0.5
POTENTIAL vs. DHE
1.0

Fig. 73

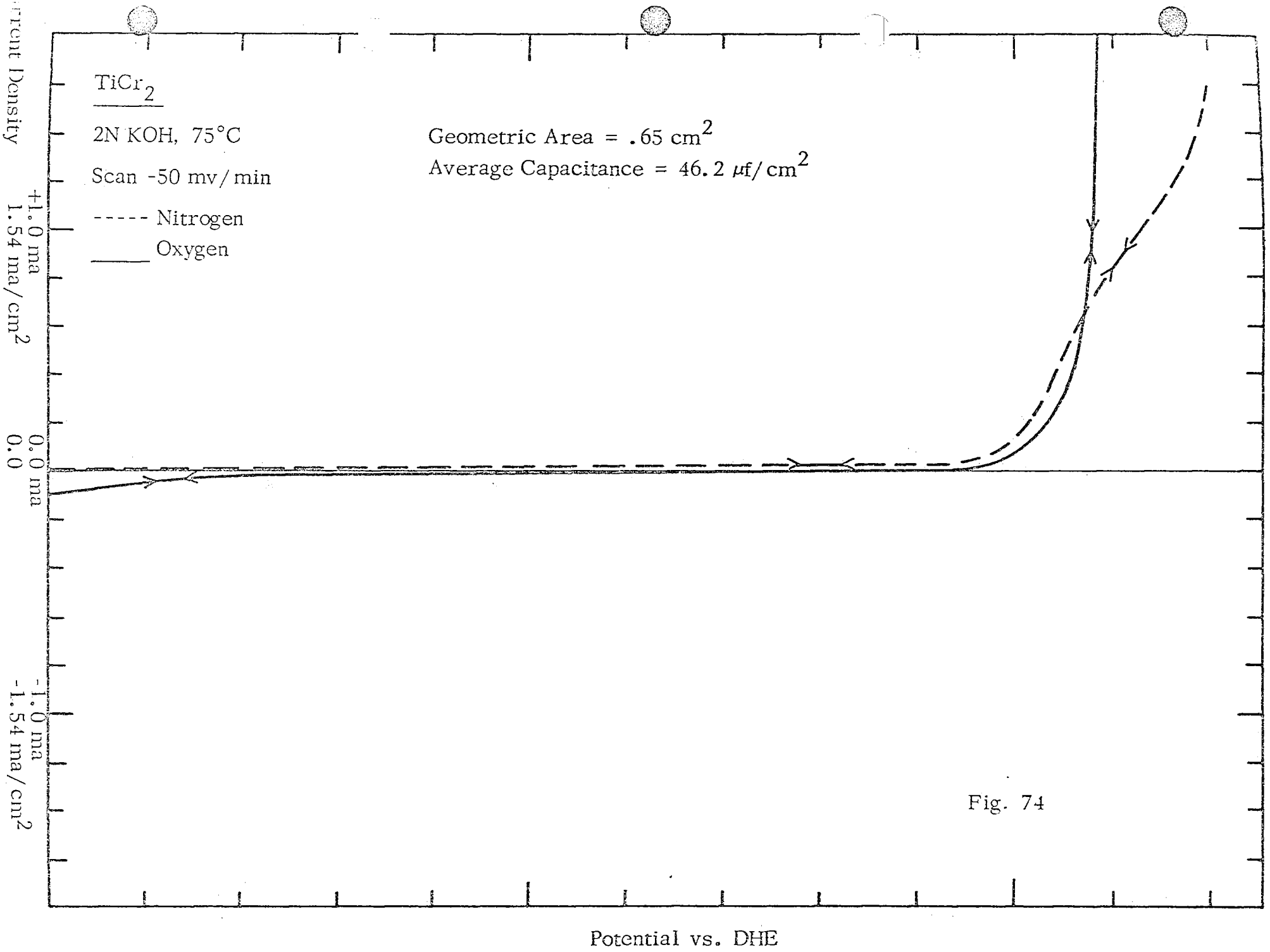
TiCr2
2N KOH, 75°C
Scan -50 mv/min
----- Nitrogen
_____ Oxygen
Geometric Area = .65 cm2
Average Capacitance = 46.2 μf/cm2
Current Density
+1.0 ma
1.54 ma/cm2
0.0 ma
0.0
-1.0 ma
-1.54 ma/cm2
Potential vs. DHE

Fig. 74

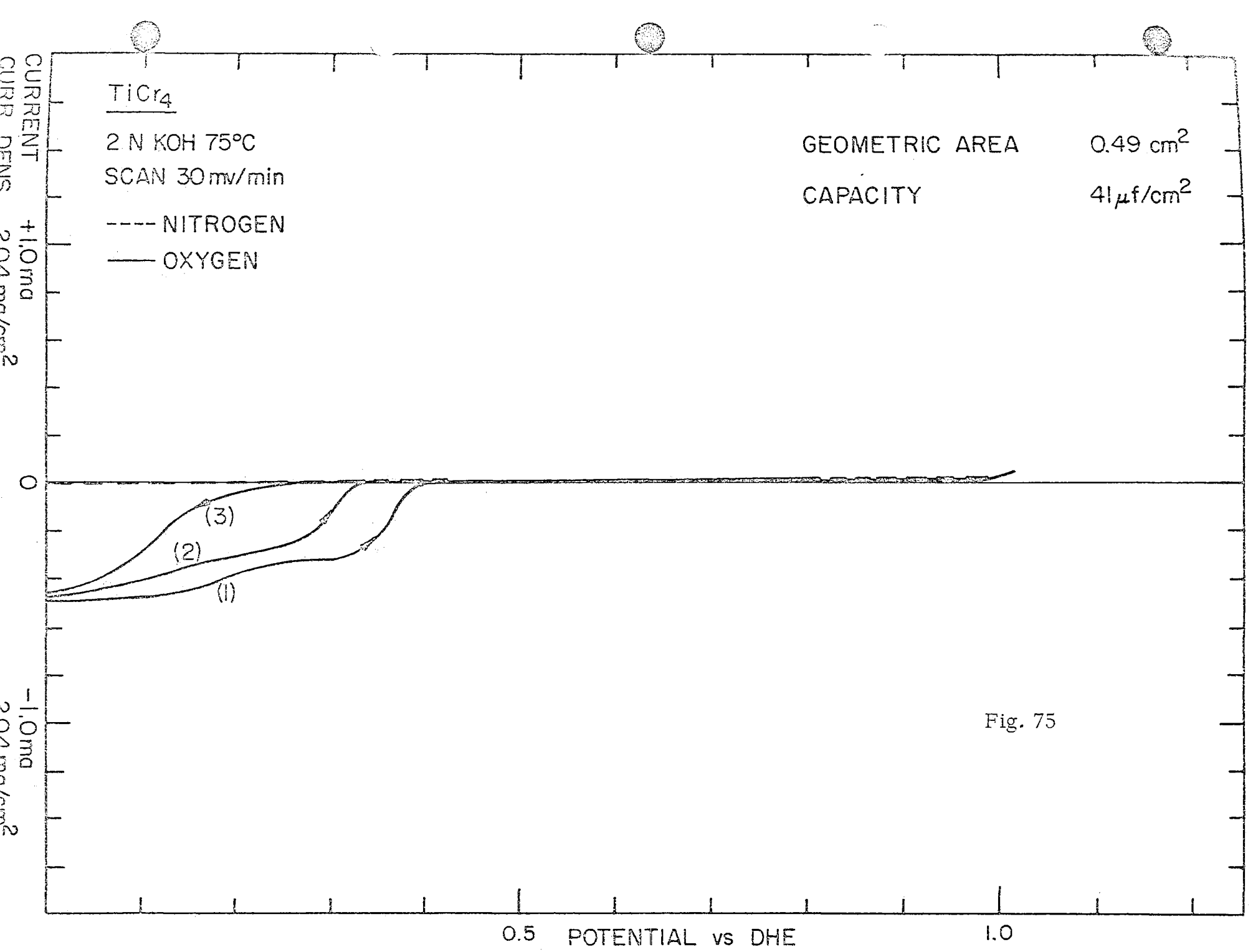
TiCr4
2 N KOH 75°C
SCAN 30 mv/min
---- NITROGEN
—— OXYGEN
GEOMETRIC AREA 0.49 cm2
CAPACITY 41 μf/cm2
CURRENT
CURR. DENS. +1.0 ma
2.04 ma/cm2
0
-1.0 ma
2.04 ma/cm2
(3)
(2)
(1)
0.5
POTENTIAL vs DHE
1.0

Fig. 75

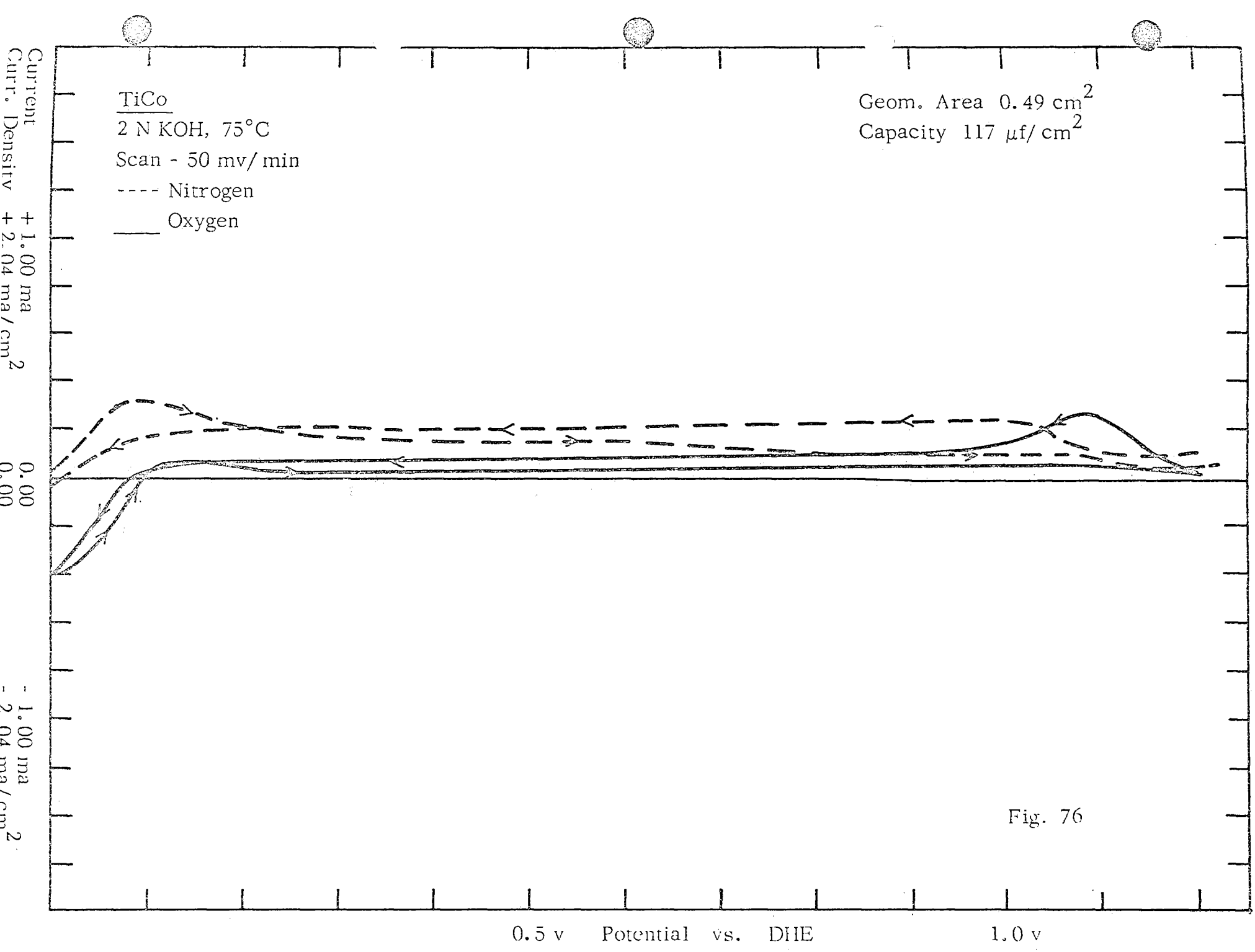
TiCo
2 N KOH, 75°C
Scan - 50 mv/ min
---- Nitrogen
____ Oxygen
Geom. Area 0.49 cm2
Capacity 117 μf/ cm2
Current
Curr. Density
+ 1.00 ma
+ 2.04 ma/ cm2
0.00
0.00
- 1.00 ma
- 2.04 ma/ cm2
0.5 v
Potential vs. DHE
1.0 v

Fig. 76

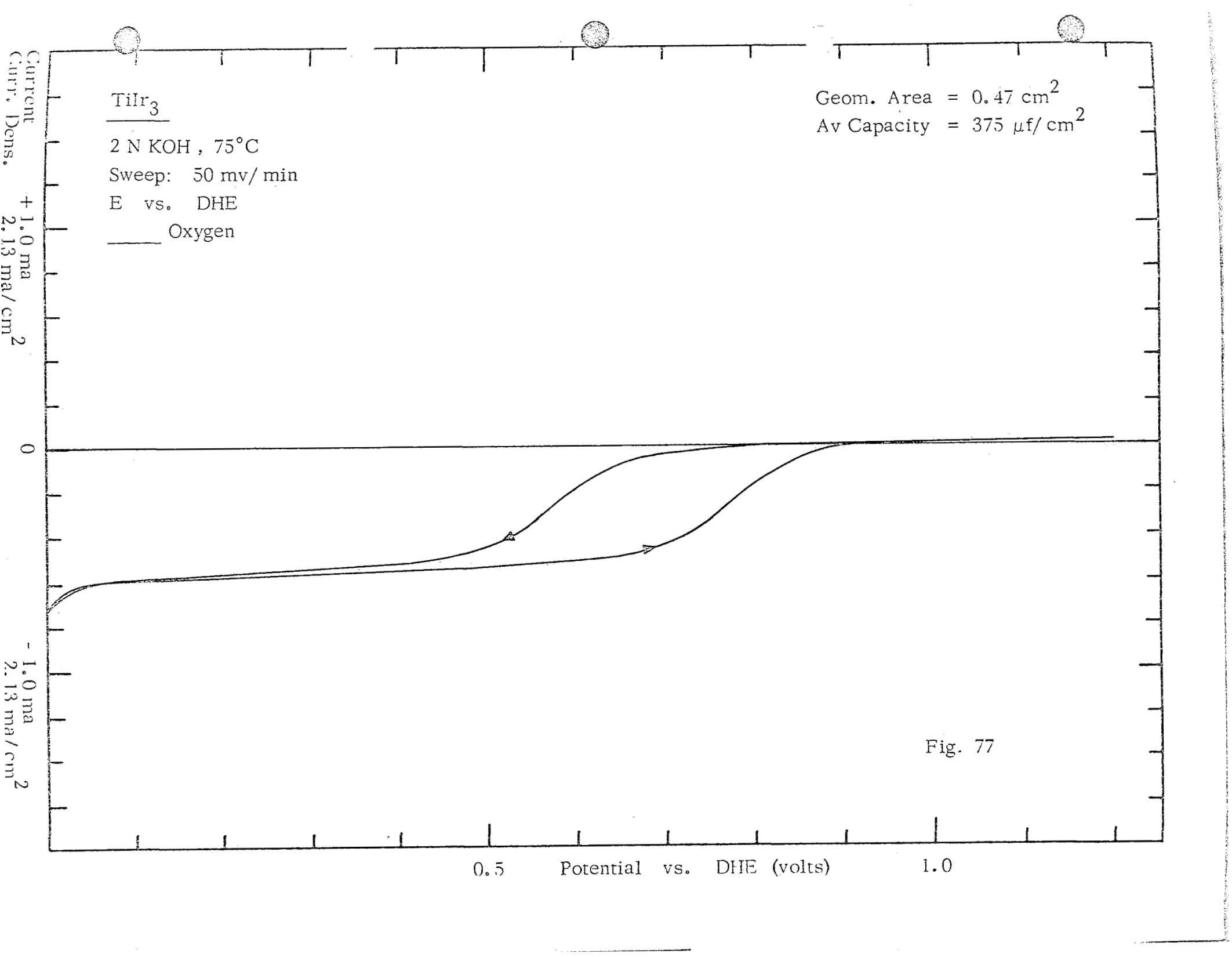
TiIr3
2 N KOH , 75°C
Sweep: 50 mv/ min
E vs. DHE
Oxygen
Geom. Area = 0.47 cm2
Av Capacity = 375 μf/ cm2
Current
Curr. Dens.
+ 1.0 ma
2.13 ma/ cm2
0
- 1.0 ma
2.13 ma/ cm2
0.5
Potential vs. DHE (volts)
1.0

Fig. 77

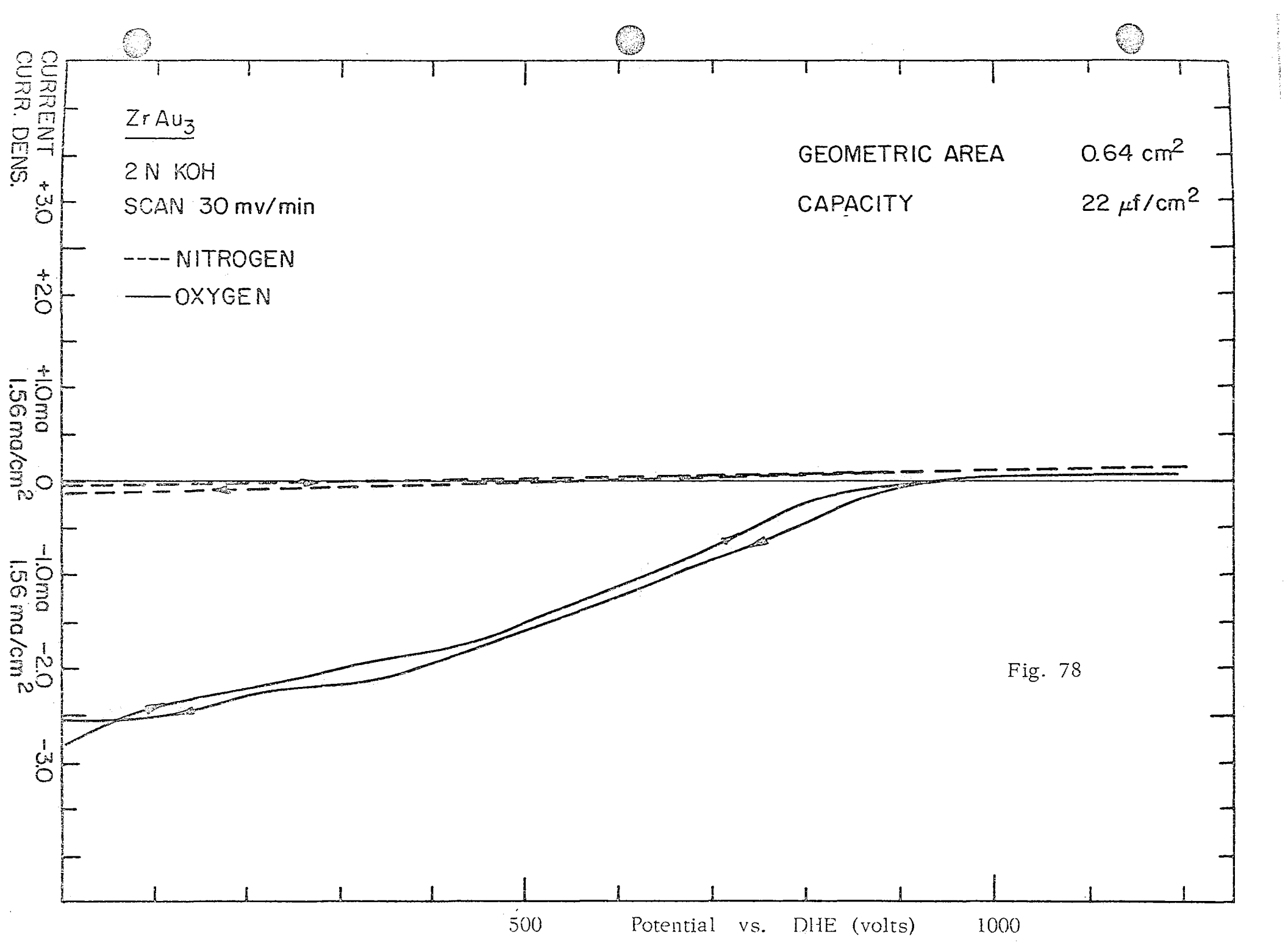
ZrAu3
2 N KOH
SCAN 30 mv/min
---- NITROGEN
—— OXYGEN
GEOMETRIC AREA 0.64 cm2
CAPACITY 22 μf/cm2
CURRENT
CURR. DENS.
+3.0
+2.0
+1.0ma
1.56 ma/cm2
0
-1.0ma
1.56 ma/cm2
-2.0
-3.0
500
Potential vs. DHE (volts)
1000

Fig. 78

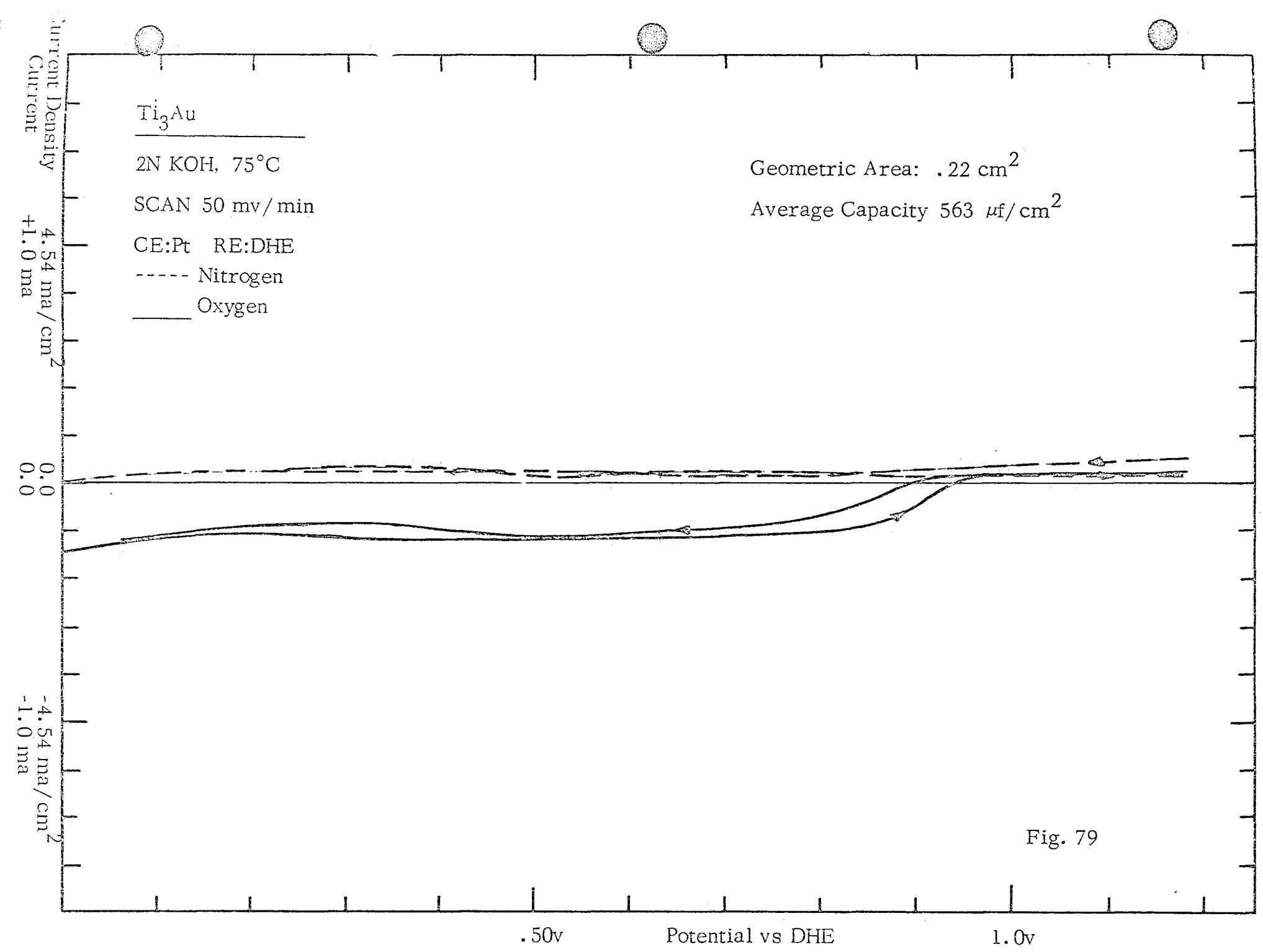
Current Density
Current
Ti_3Au
2N KOH, 75°C
SCAN 50 mv/min
CE:Pt RE:DHE
----- Nitrogen
_____ Oxygen
Geometric Area: .22 cm^2
Average Capacity 563 $\mu f/cm^2$
+4.54 ma/cm^2
+1.0 ma
0.0
0.0
-4.54 ma/cm^2
-1.0 ma
.50v
Potential vs DHE
1.0v

Fig. 79

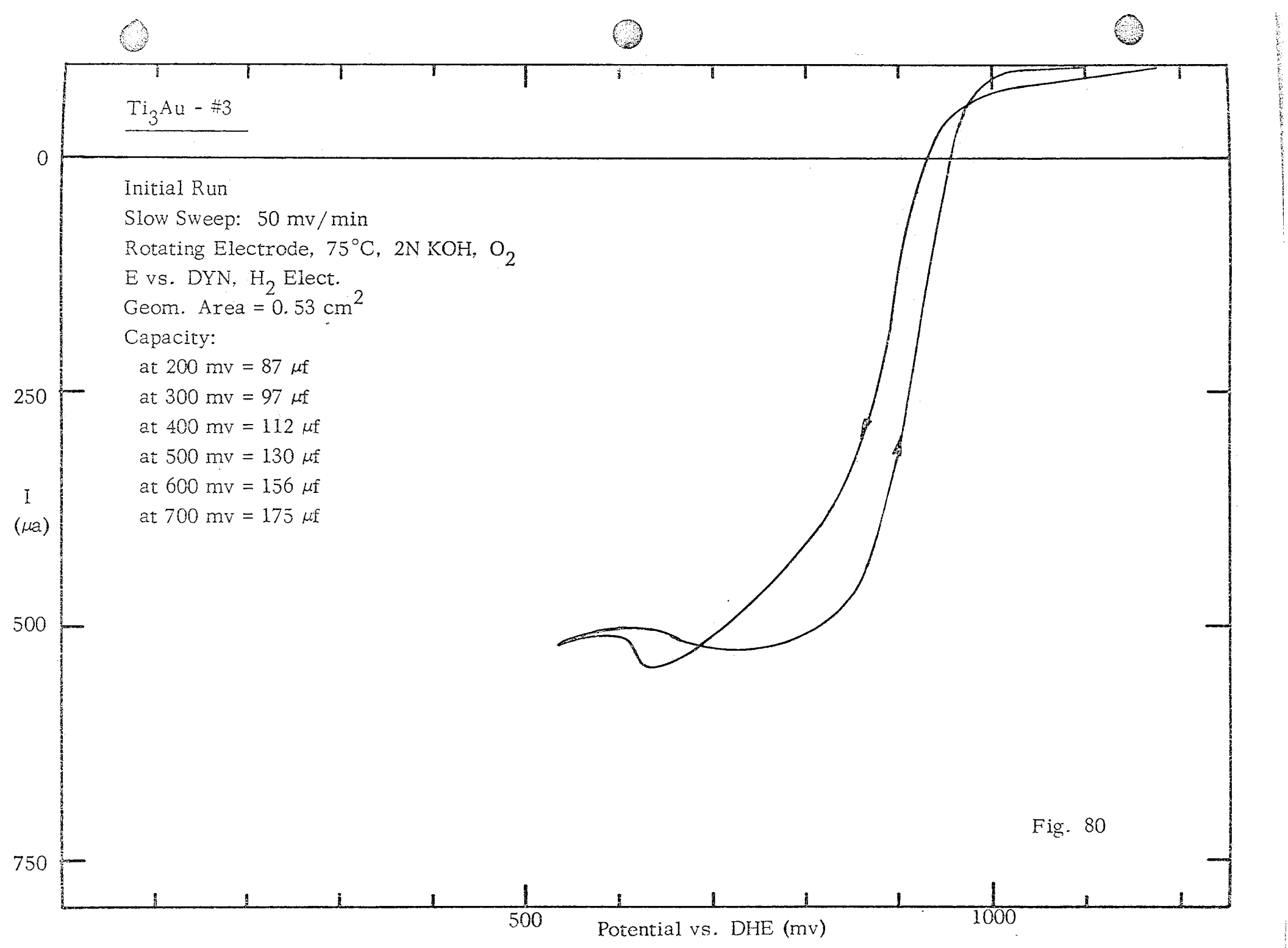
Ti_3Au - #3
Initial Run
Slow Sweep: 50 mv/min
Rotating Electrode, 75°C, 2N KOH, O_2
E vs. DYN, H_2 Elect.
Geom. Area = 0.53 cm^2
Capacity:
at 200 mv = 87 μf
at 300 mv = 97 μf
at 400 mv = 112 μf
at 500 mv = 130 μf
at 600 mv = 156 μf
at 700 mv = 175 μf
0
250
500
750
I (μa)
500
1000
Potential vs. DHE (mv)

Fig. 80

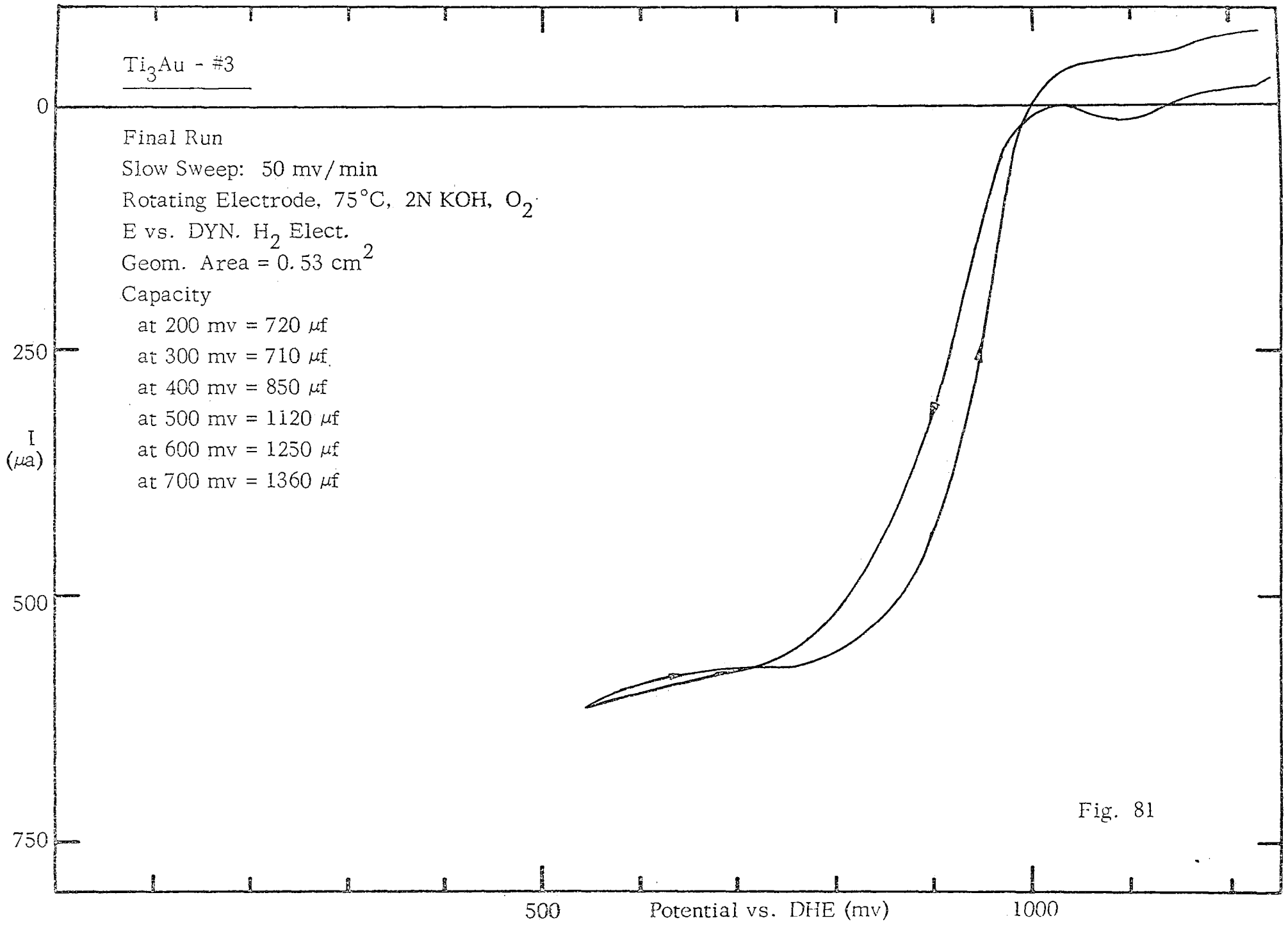
Ti_3Au - #3
Final Run
Slow Sweep: 50 mv/min
Rotating Electrode, 75°C, 2N KOH, O_2
E vs. DYN. H_2 Elect.
Geom. Area = 0.53 cm^2
Capacity
at 200 mv = 720 μf
at 300 mv = 710 μf
at 400 mv = 850 μf
at 500 mv = 1120 μf
at 600 mv = 1250 μf
at 700 mv = 1360 μf
0
250
500
750
I (μa)
500
Potential vs. DHE (mv)
1000

Fig. 81

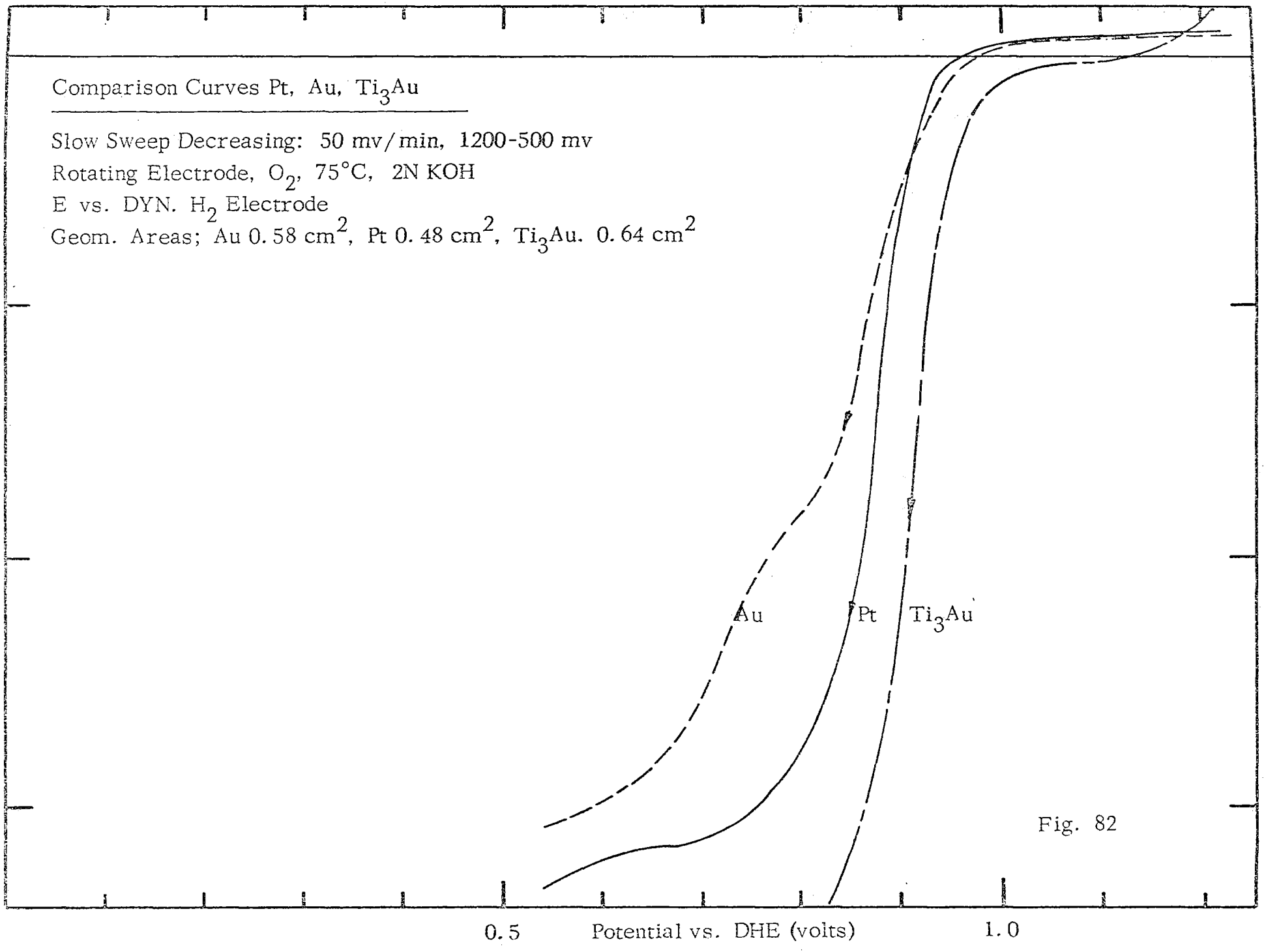
Comparison Curves Pt, Au, Ti_3Au
Slow Sweep Decreasing: 50 mv/min, 1200-500 mv
Rotating Electrode, O_2, 75°C, 2N KOH
E vs. DYN. H_2 Electrode
Geom. Areas; Au 0.58 cm^2, Pt 0.48 cm^2, Ti_3Au. 0.64 cm^2
0
0.25
0.50
0.75
Current (ma)
Au
Pt
Ti_3Au
0.5
Potential vs. DHE (volts)
1.0

Fig. 82

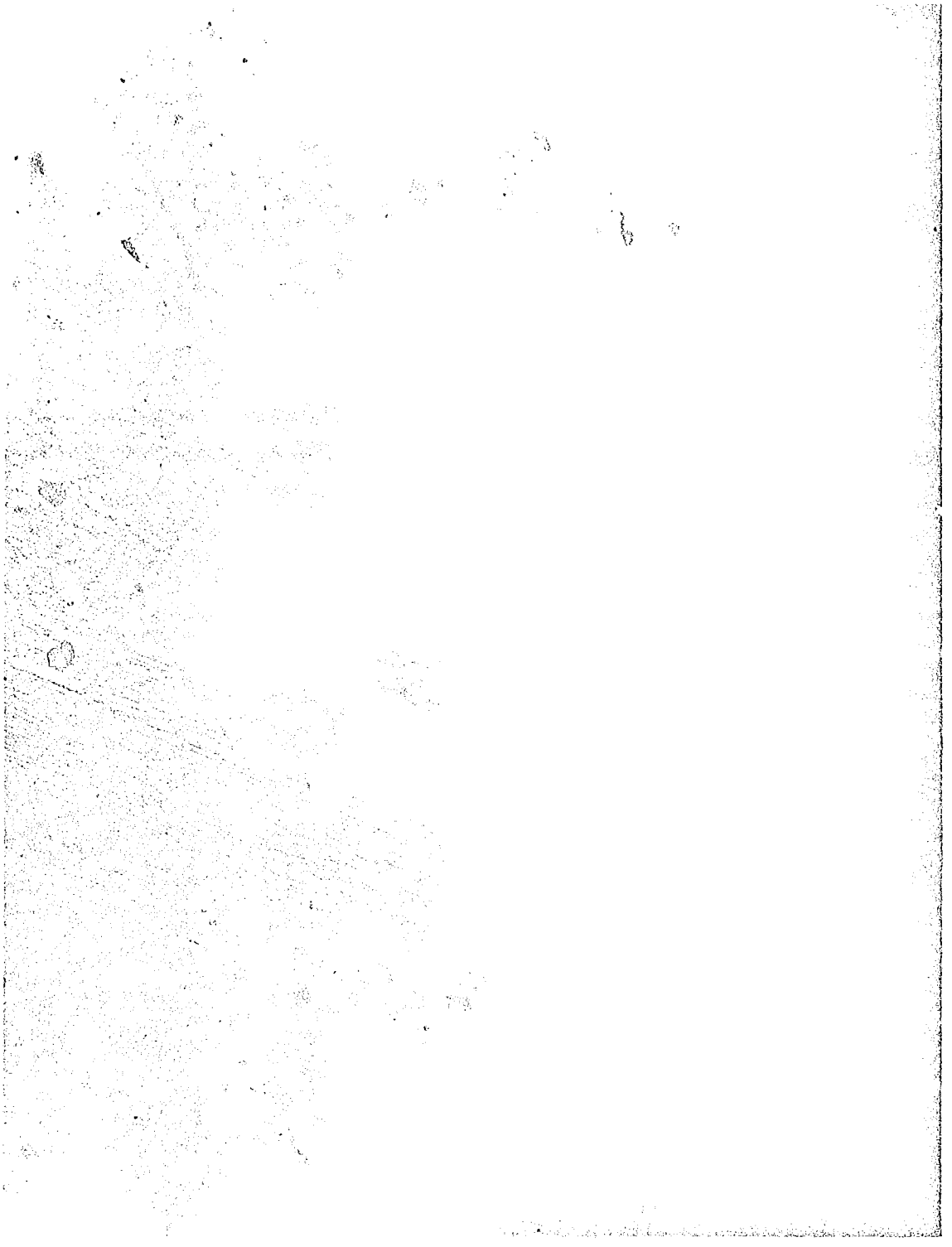

Fig. 83 An electron micrograph of freshly polished Ti_3Au (X 15, 000)

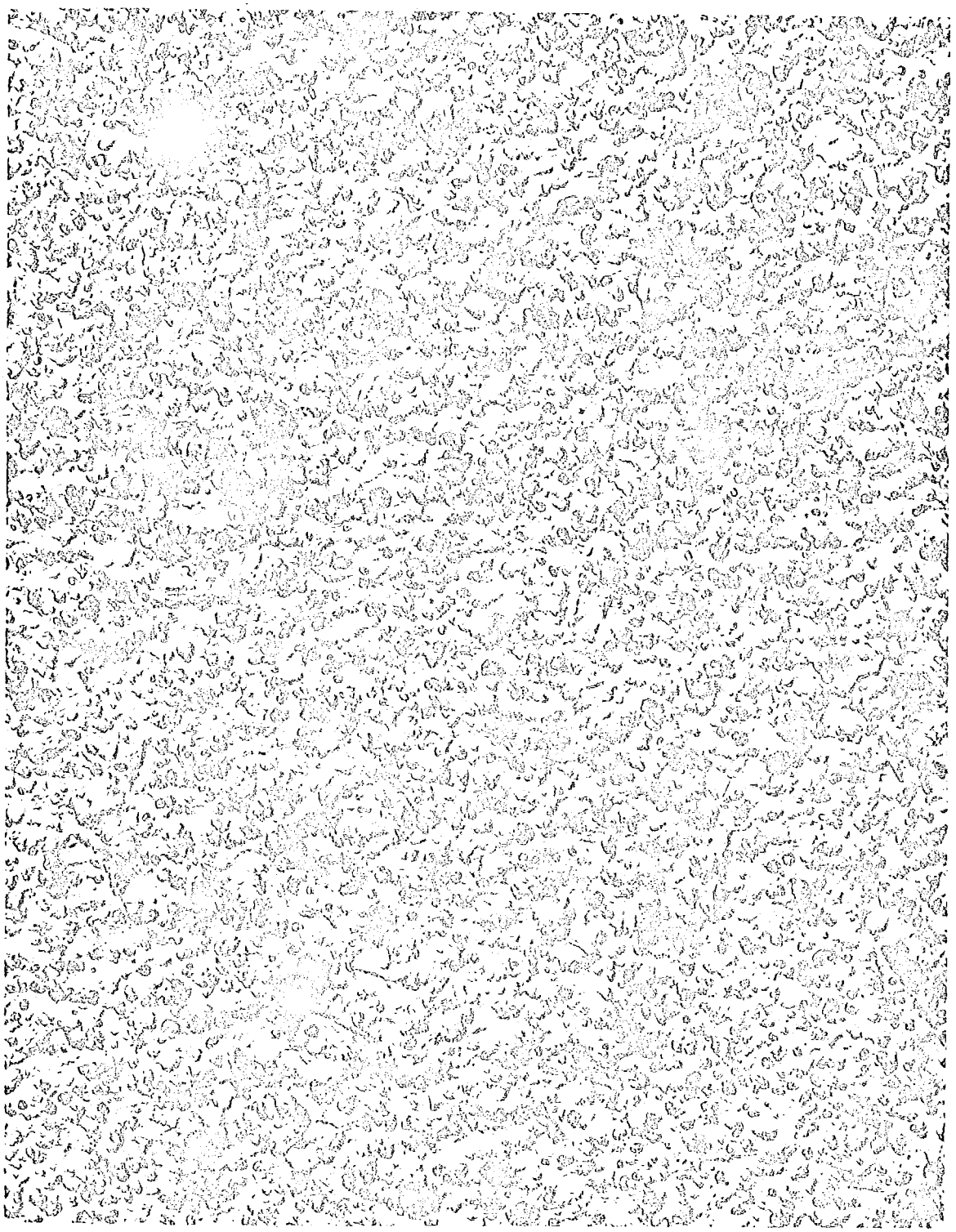

Fig. 84 An electron micrograph of Ti_3Au held at + 1200 mv for 24 hrs (X 15, 000)

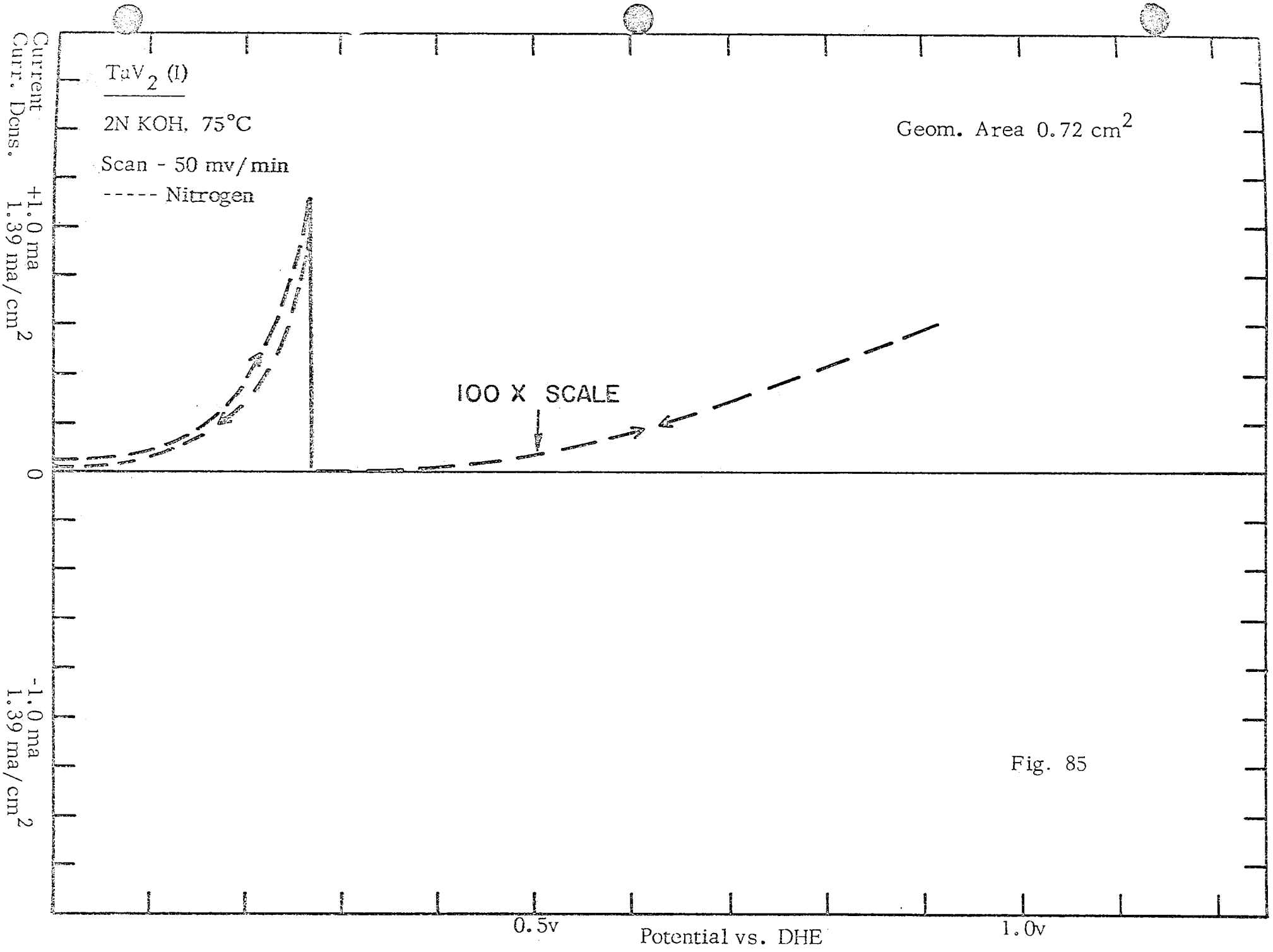
TaV_2 (I)
2N KOH, 75°C
Scan - 50 mv/min
----- Nitrogen
Geom. Area 0.72 cm^2
100 X SCALE
Current
Curr. Dens.
+1.0 ma
1.39 ma/cm^2
0
-1.0 ma
1.39 ma/cm^2
0.5v
Potential vs. DHE
1.0v

Fig. 85

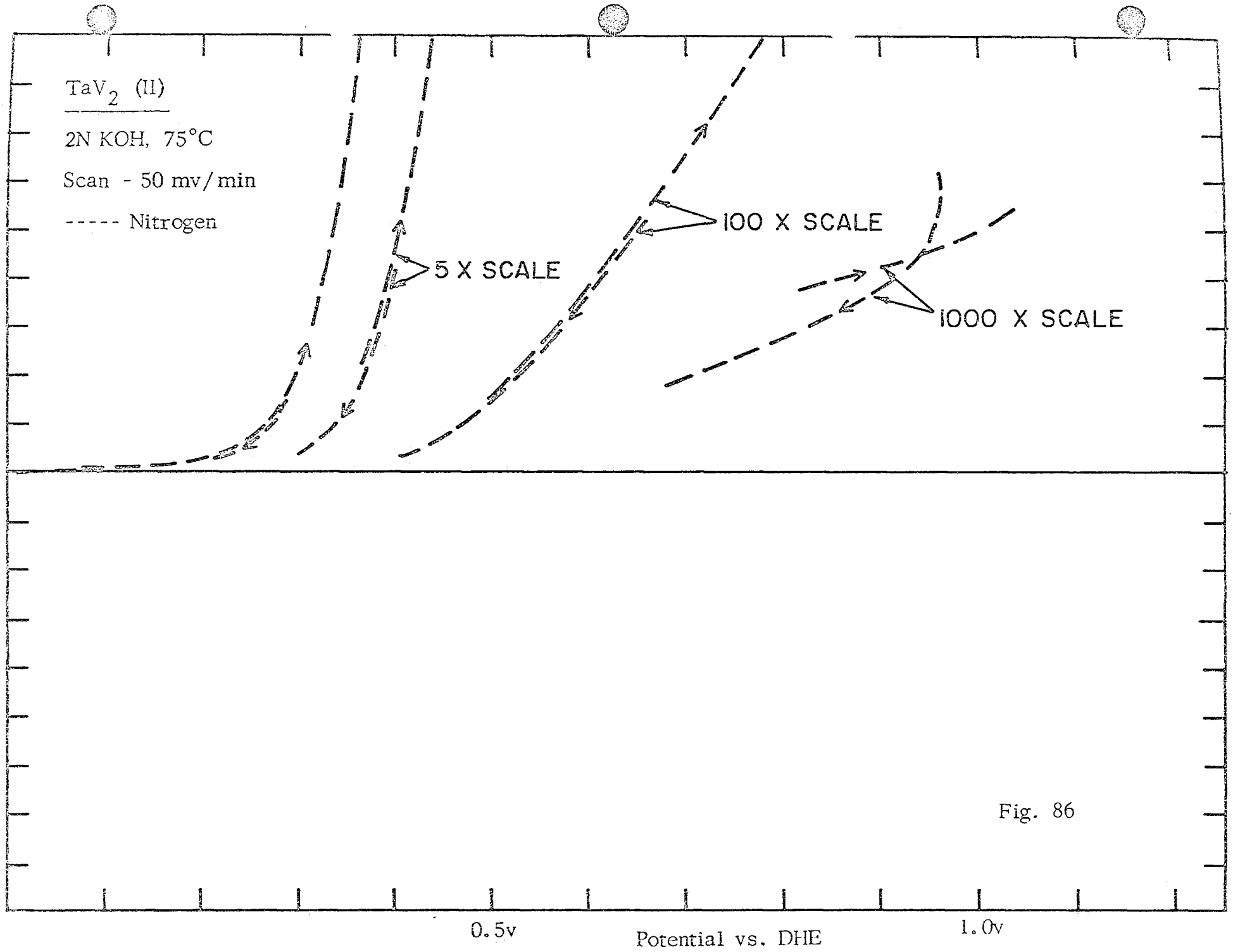
TaV2 (II)
2N KOH, 75°C
Scan - 50 mv/min
----- Nitrogen
5 X SCALE
100 X SCALE
1000 X SCALE
Current
+1.00 ma
0.00
-1.0 ma
0.5v
Potential vs. DHE
1.0v

Fig. 86

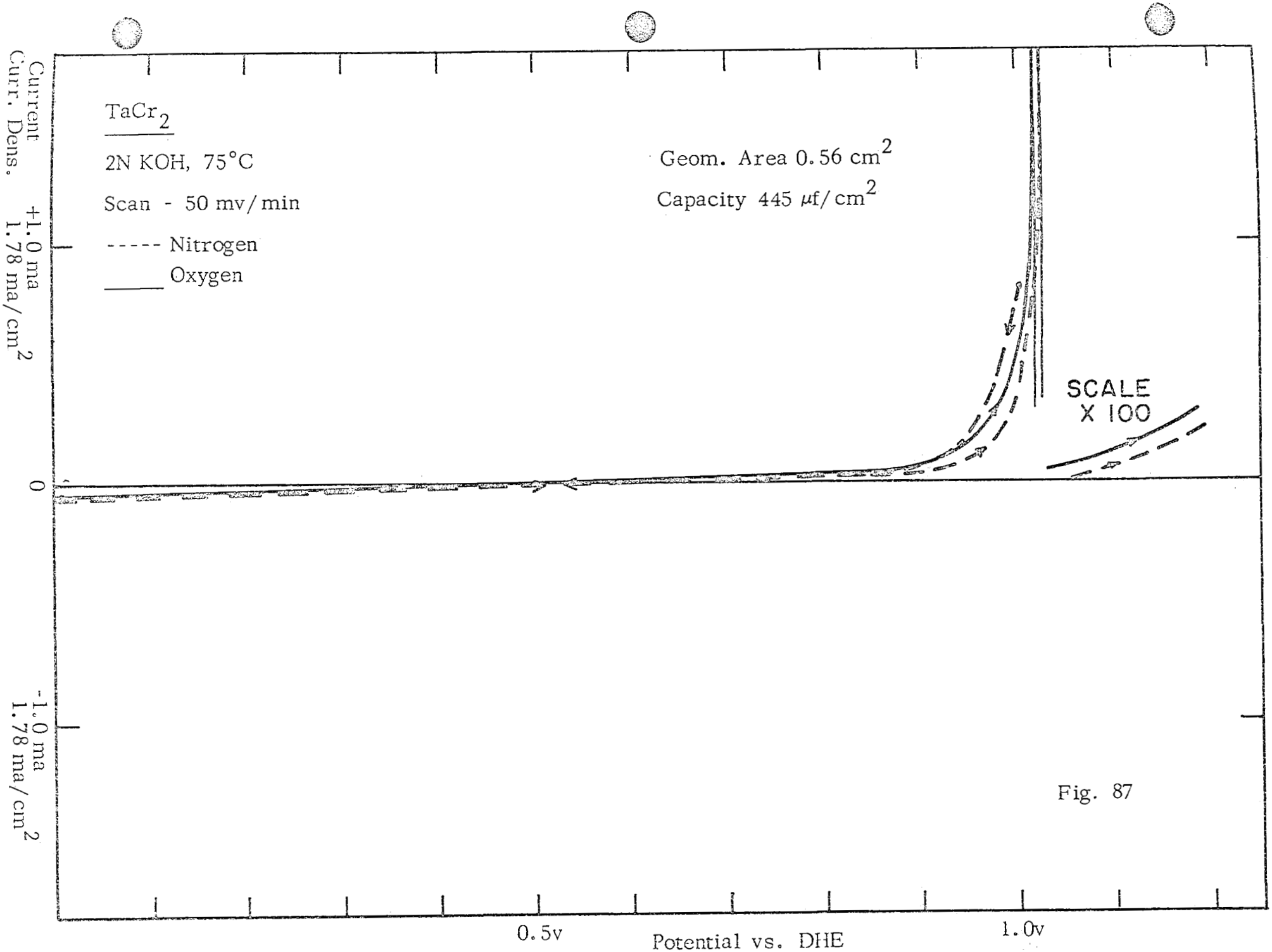
TaCr2
2N KOH, 75°C
Scan - 50 mv/min
----- Nitrogen
_____ Oxygen
Geom. Area 0.56 cm2
Capacity 445 μf/cm2
SCALE X 100
Current Curr. Dens.
+1.0 ma 1.78 ma/cm2
0
-1.0 ma 1.78 ma/cm2
0.5v
Potential vs. DHE
1.0v

Fig. 87

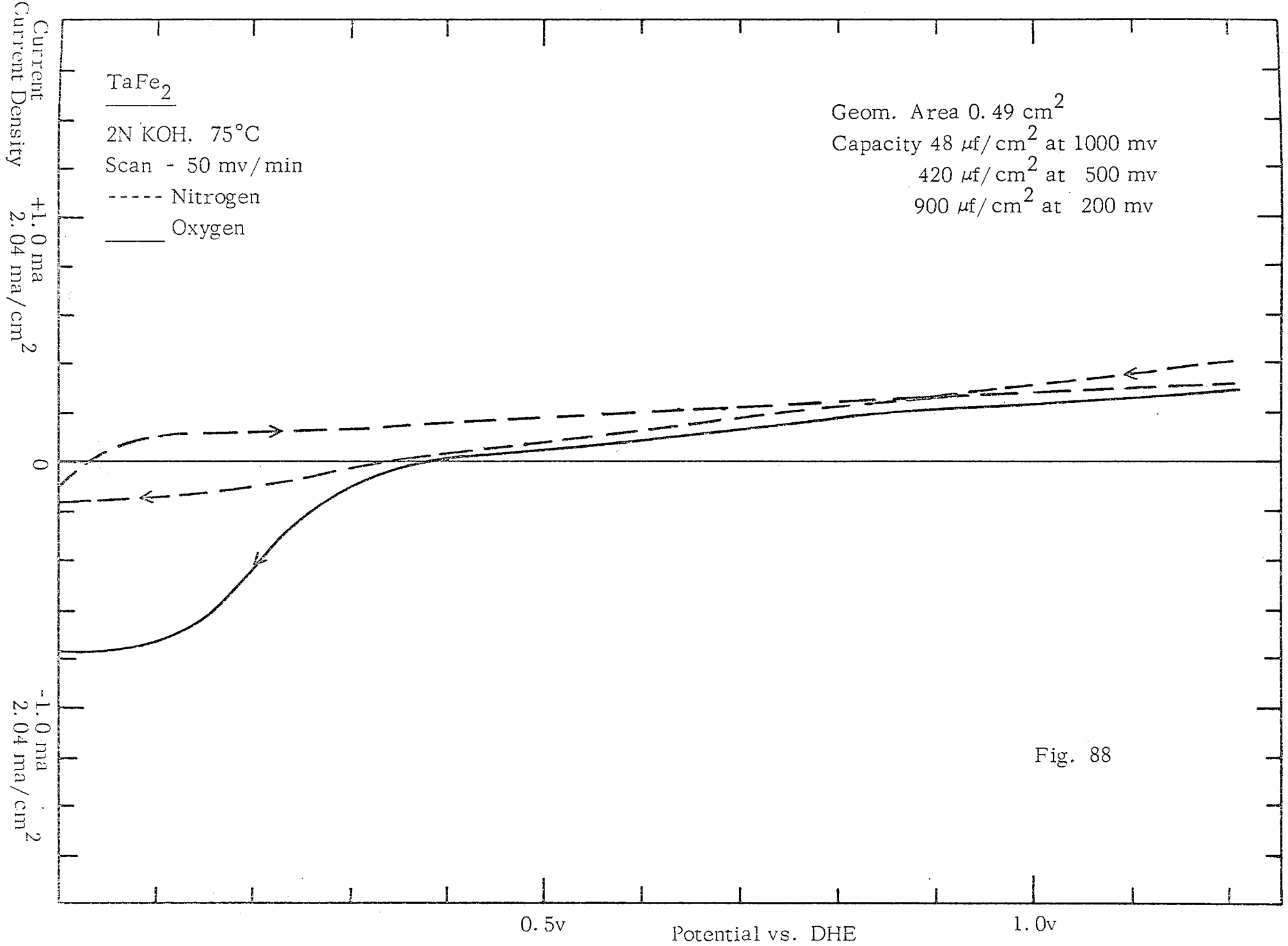
TaFe2
2N KOH. 75°C
Scan - 50 mv/min
----- Nitrogen
_____ Oxygen
Geom. Area 0.49 cm2
Capacity 48 μf/cm2 at 1000 mv
420 μf/cm2 at 500 mv
900 μf/cm2 at 200 mv
Current Density
+1.0 ma
2.04 ma/cm2
0
-1.0 ma
2.04 ma/cm2
0.5v
Potential vs. DHE
1.0v

Fig. 88

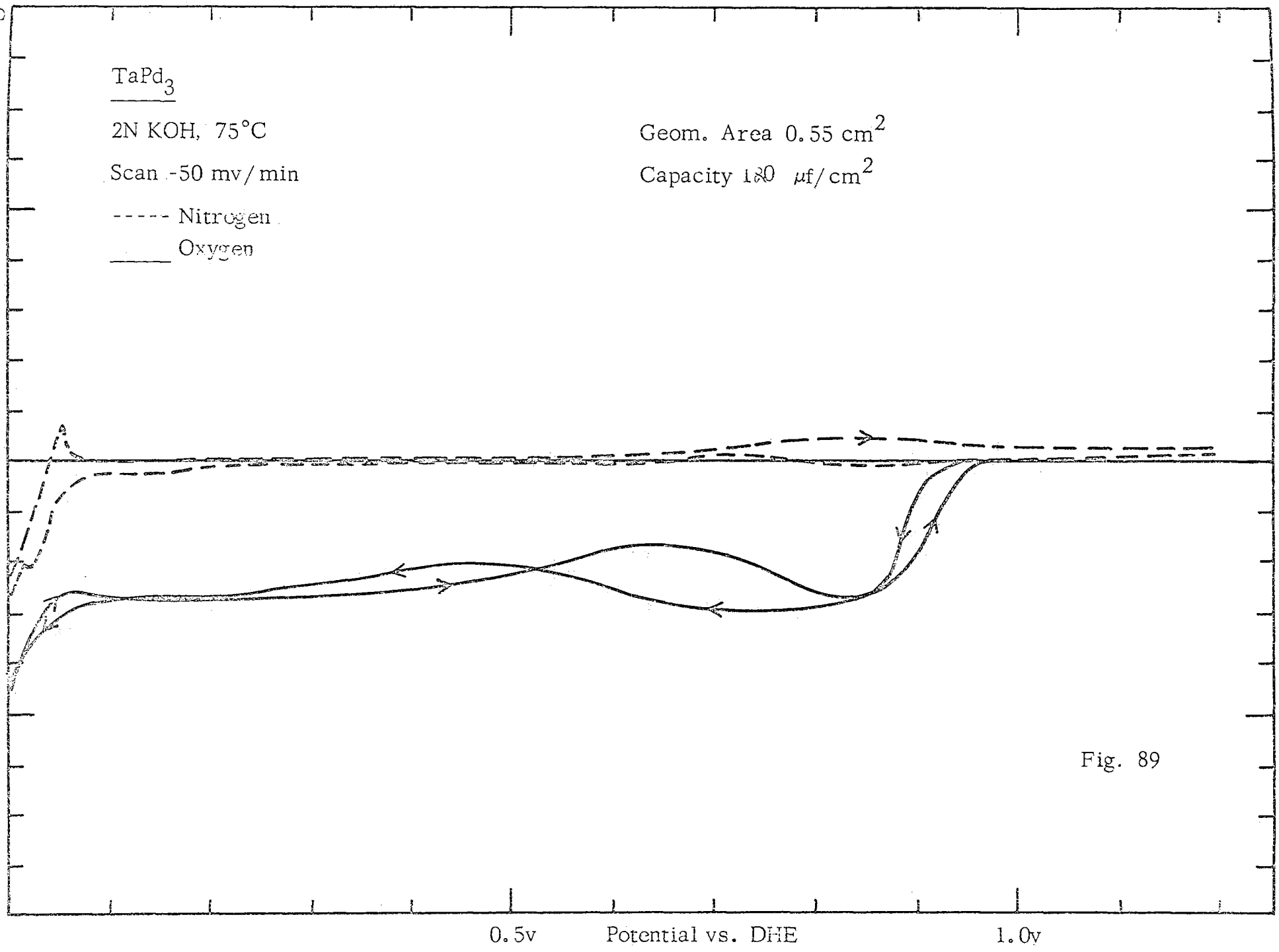
TaPd3
2N KOH, 75°C
Scan -50 mv/min
----- Nitrogen
_____ Oxygen
Geom. Area 0.55 cm2
Capacity 180 μf/cm2
Current Density
+1.00 ma
+1.82 ma/cm2
0.00
0.00
-1.00 ma
-1.82 ma/cm2
0.5v
Potential vs. DHE
1.0v

Fig. 89

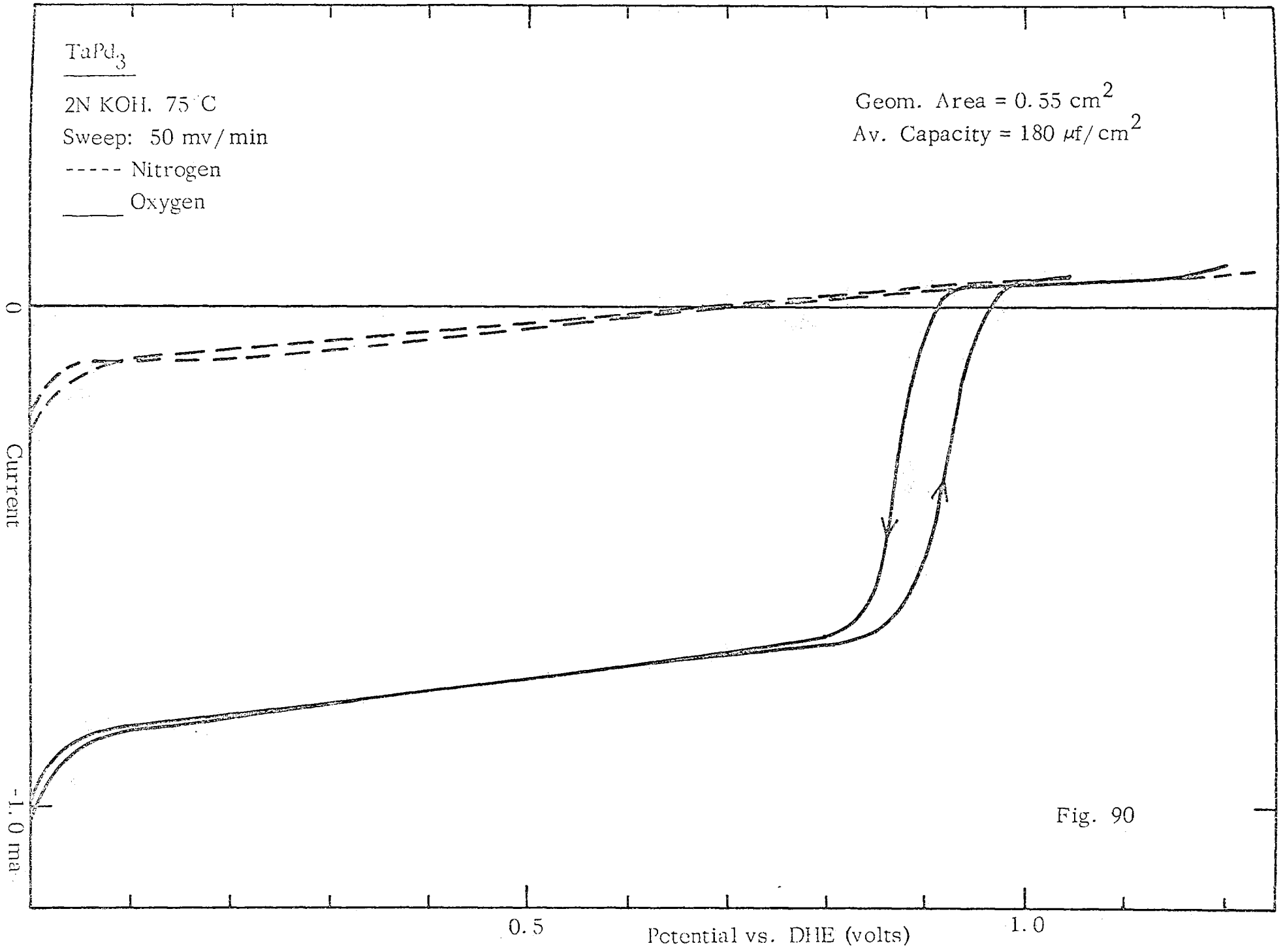
TaPd3
2N KOH. 75 °C
Sweep: 50 mv/min
----- Nitrogen
_____ Oxygen
Geom. Area = 0.55 cm2
Av. Capacity = 180 μf/cm2
0
Current
-1.0 ma
0.5
Potential vs. DHE (volts)
1.0

Fig. 90

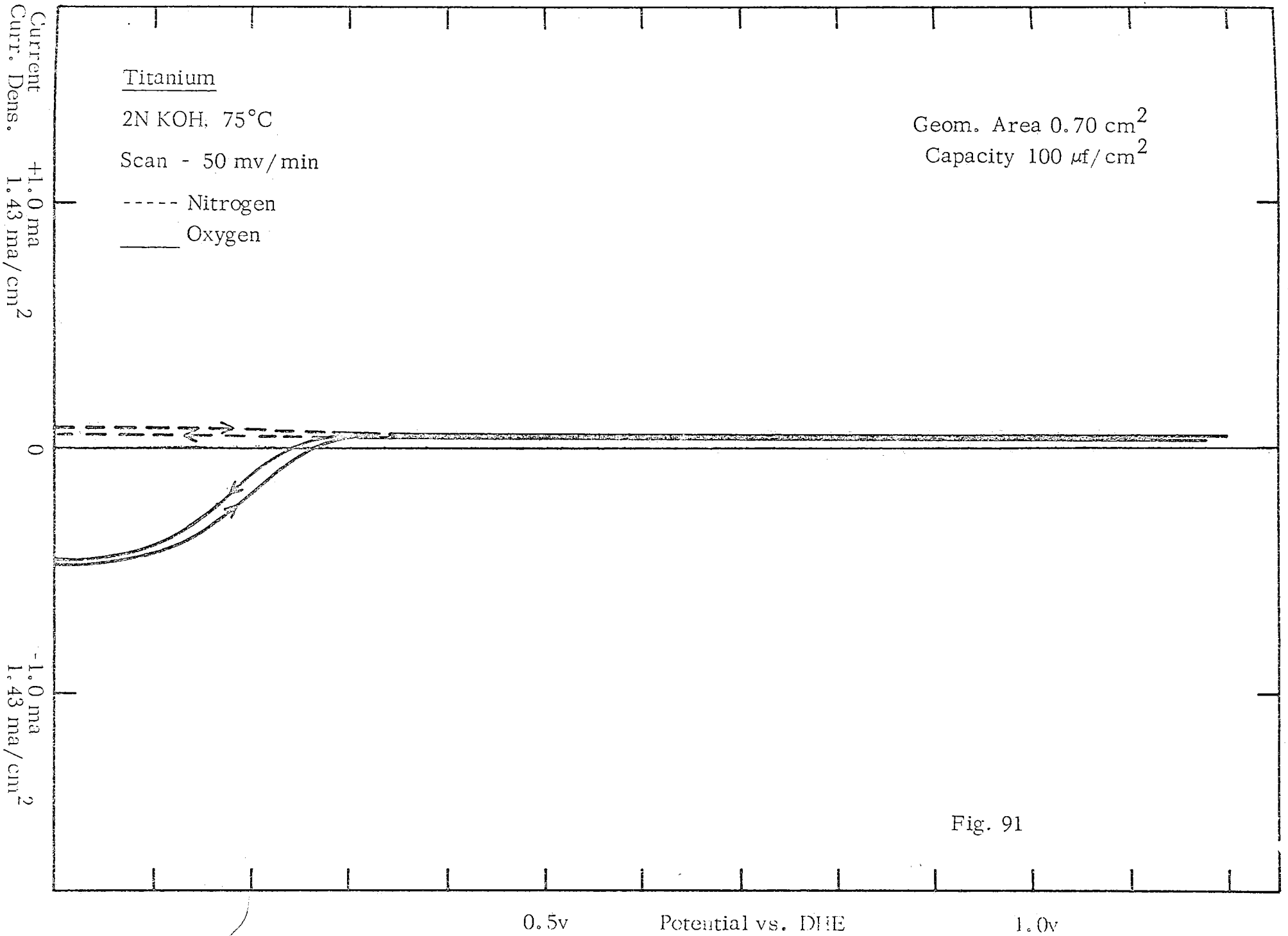
Titanium
2N KOH, 75°C
Scan - 50 mv/min
----- Nitrogen
_____ Oxygen
Geom. Area 0.70 cm2
Capacity 100 μf/cm2
Current
Curr. Dens.
+1.0 ma
1.43 ma/cm2
0
-1.0 ma
1.43 ma/cm2
0.5v
Potential vs. DHE
1.0v

Fig. 91

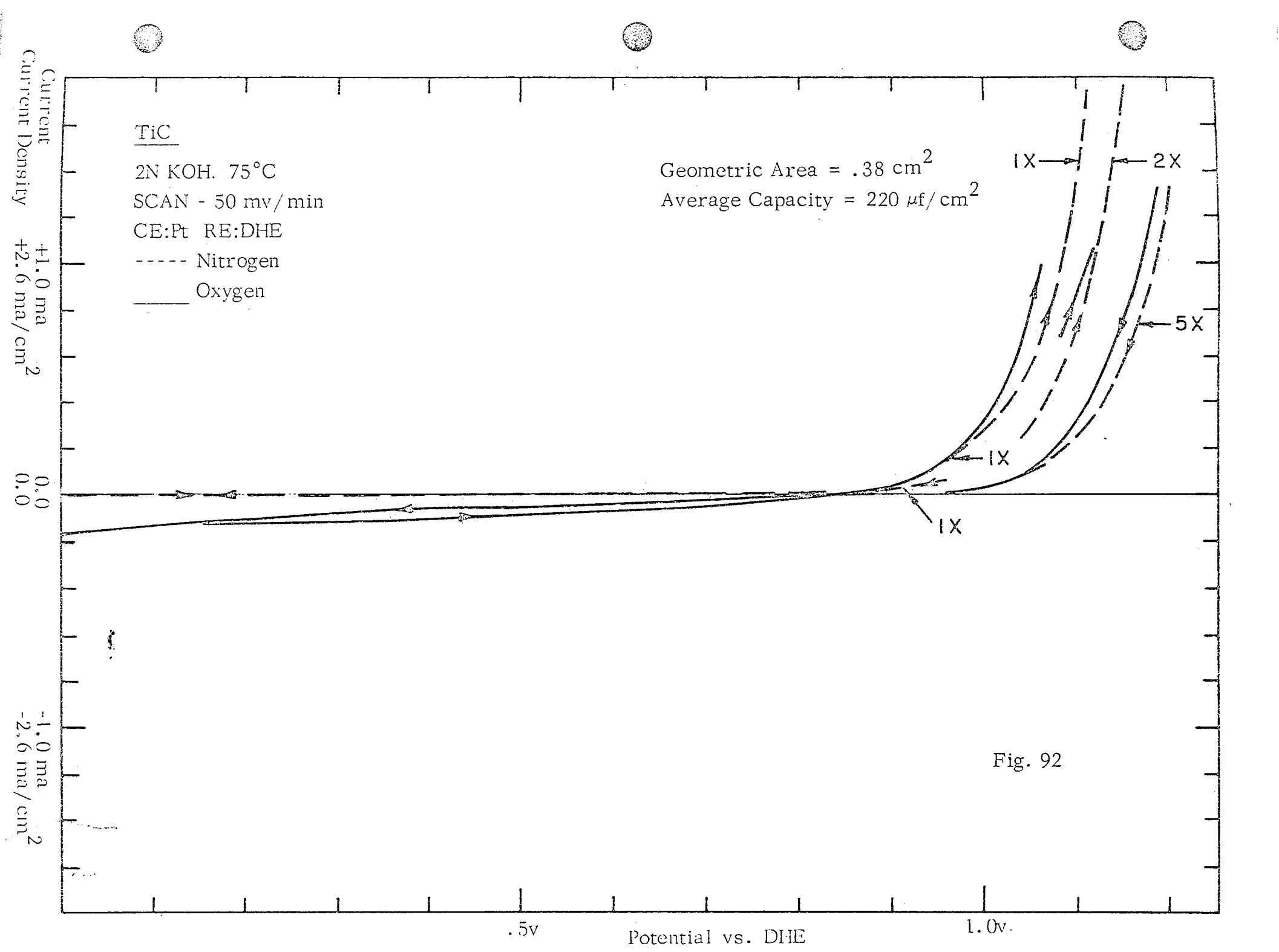
TiC
2N KOH. 75°C
SCAN - 50 mv/min
CE:Pt RE:DHE
----- Nitrogen
_____ Oxygen
Geometric Area = .38 cm²
Average Capacity = 220 μf/cm²
1X
2X
5X
1X
1X
Current Density
+1.0 ma
+2.6 ma/cm²
0.0
0.0
-1.0 ma
-2.6 ma/cm²
.5v
Potential vs. DHE
1.0v.

Fig. 92

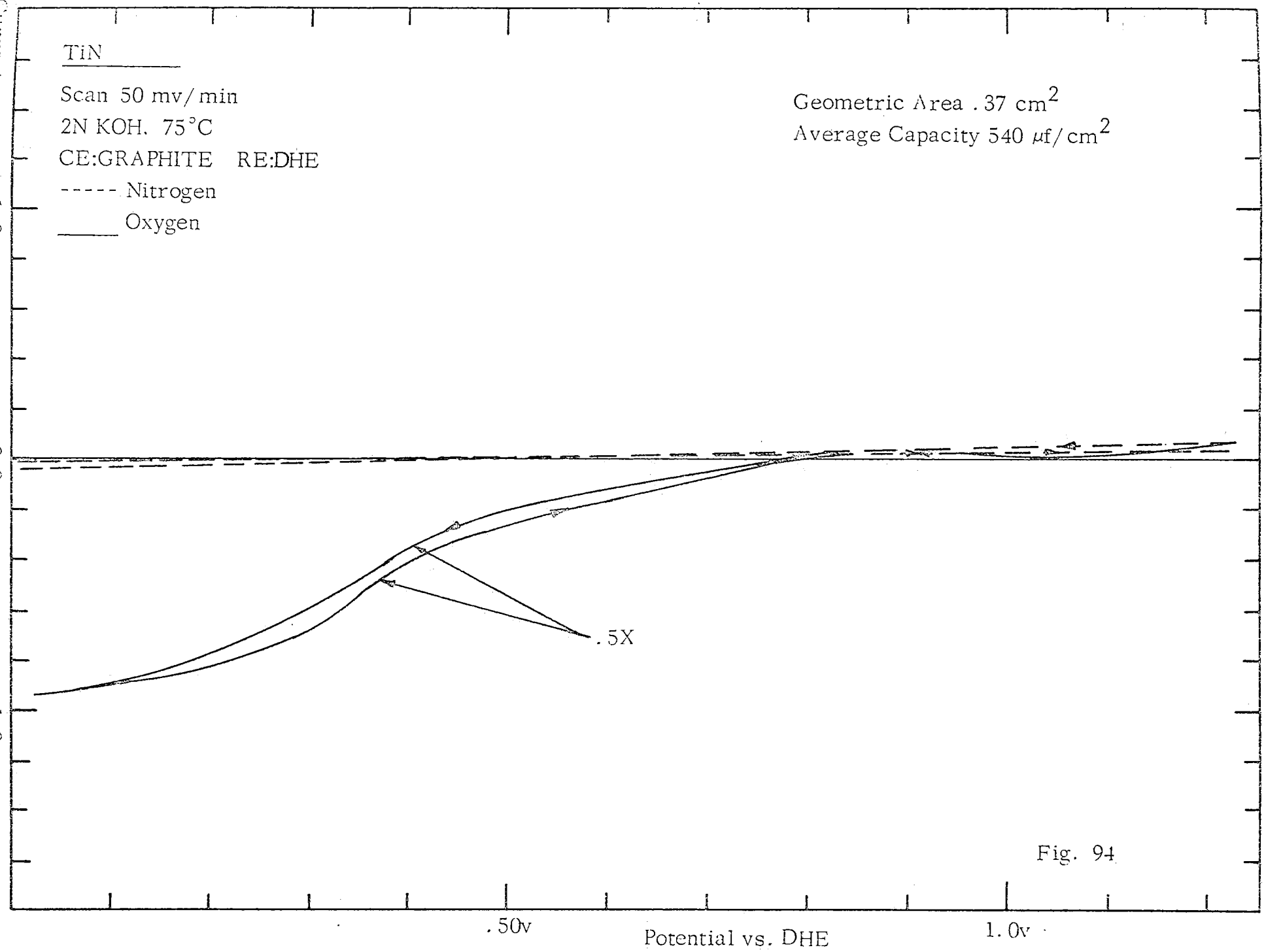
TiN
Scan 50 mv/min
2N KOH. 75°C
CE:GRAPHITE RE:DHE
----- Nitrogen
_____ Oxygen
Geometric Area .37 cm2
Average Capacity 540 μf/cm2
Current density
+1.0 ma
+2.7 ma/cm2
0.0
0.0
-1.0 ma
-2.7 ma/cm2
.5X
.50v
Potential vs. DHE
1.0v

Fig. 94

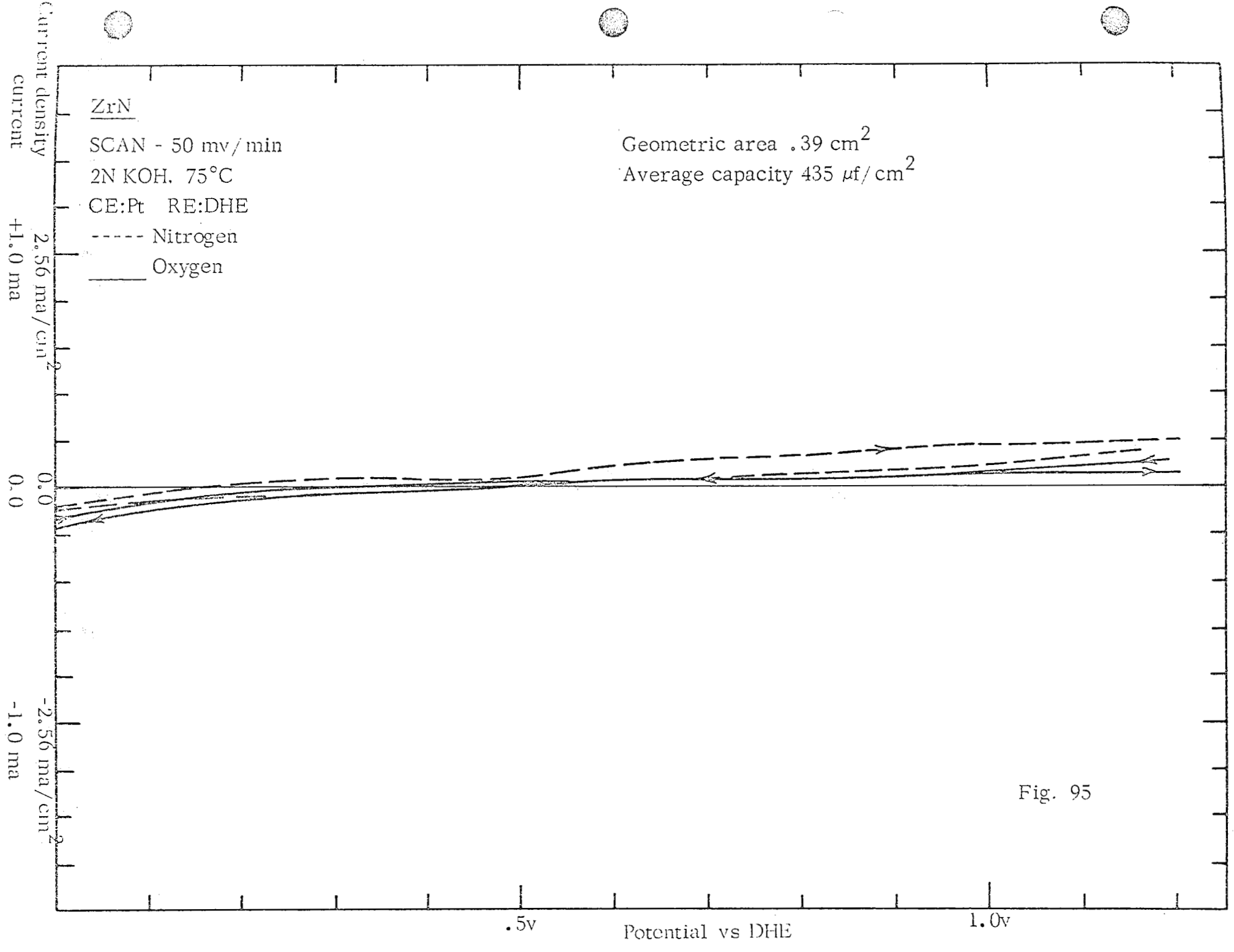
ZrN
SCAN - 50 mv/min
2N KOH. 75°C
CE:Pt RE:DHE
----- Nitrogen
_____ Oxygen
Geometric area .39 cm2
Average capacity 435 μf/cm2
Current density
current
+1.0 ma
2.56 ma/cm2
0.0
0.0
-2.56 ma/cm2
-1.0 ma
.5v
Potential vs DHE
1.0v

Fig. 95

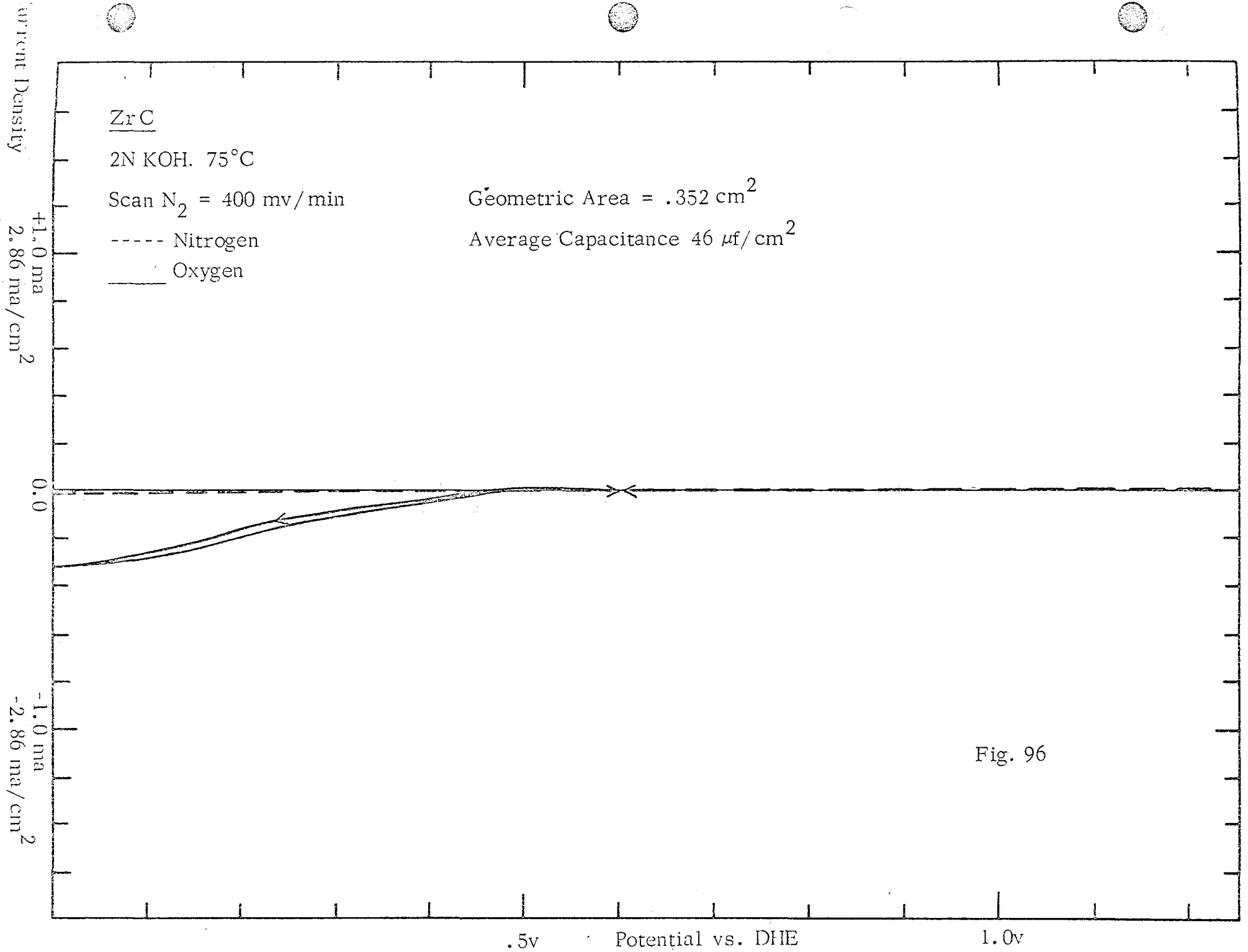
Current Density
+1.0 ma
2.86 ma/cm2
0.0
-1.0 ma
-2.86 ma/cm2
ZrC
2N KOH. 75°C
Scan N2 = 400 mv/min
----- Nitrogen
_____ Oxygen
Geometric Area = .352 cm2
Average Capacitance 46 μf/cm2
.5v
Potential vs. DHE
1.0v

Fig. 96

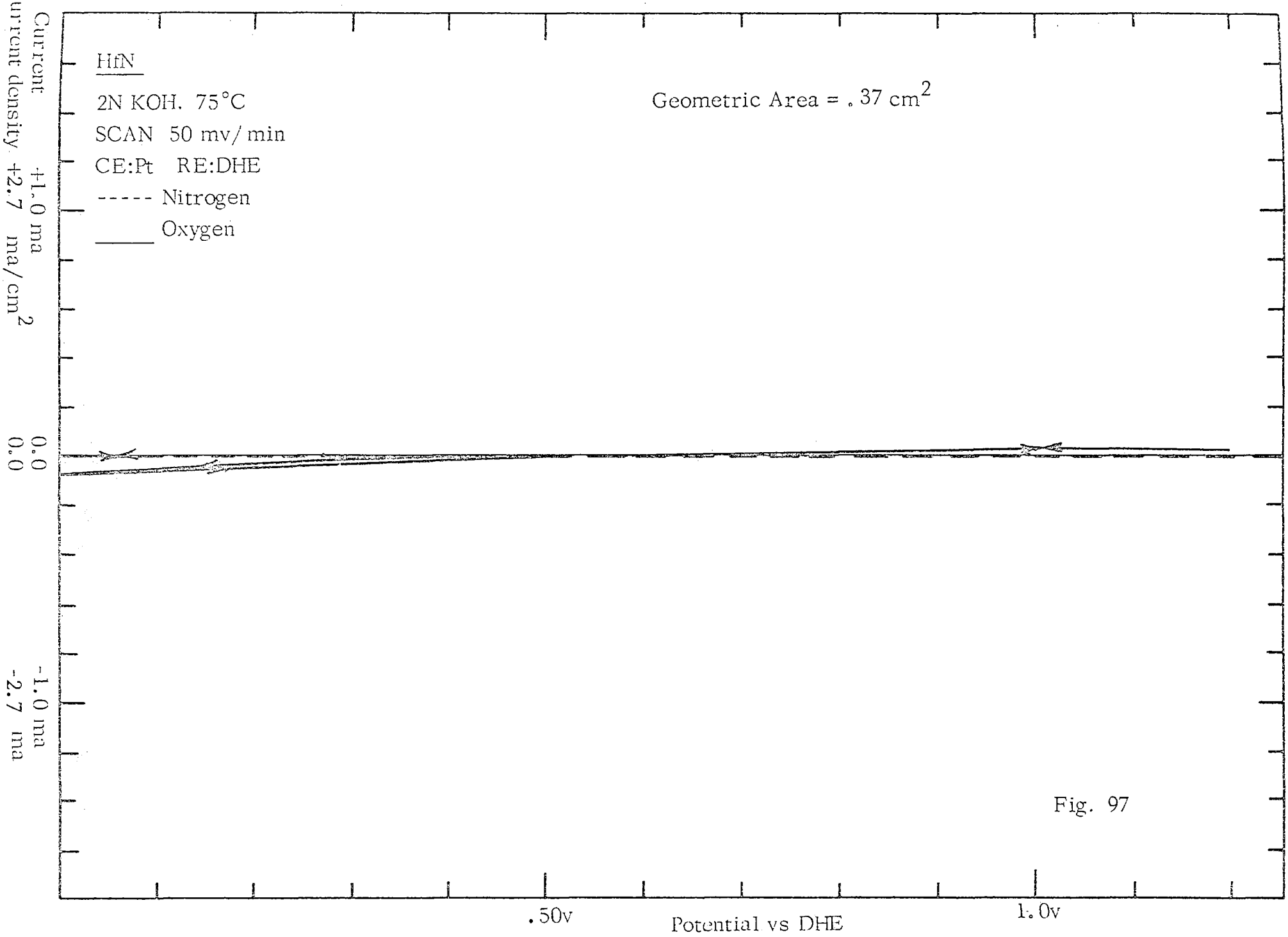
HfN
2N KOH. 75°C
SCAN 50 mv/ min
CE:Pt RE:DHE
----- Nitrogen
_____ Oxygen
Geometric Area = .37 cm2
Current
Current density +2.7 ma/cm2
+1.0 ma
0.0
0.0
-1.0 ma
-2.7 ma
.50v
Potential vs DHE
1.0v

Fig. 97

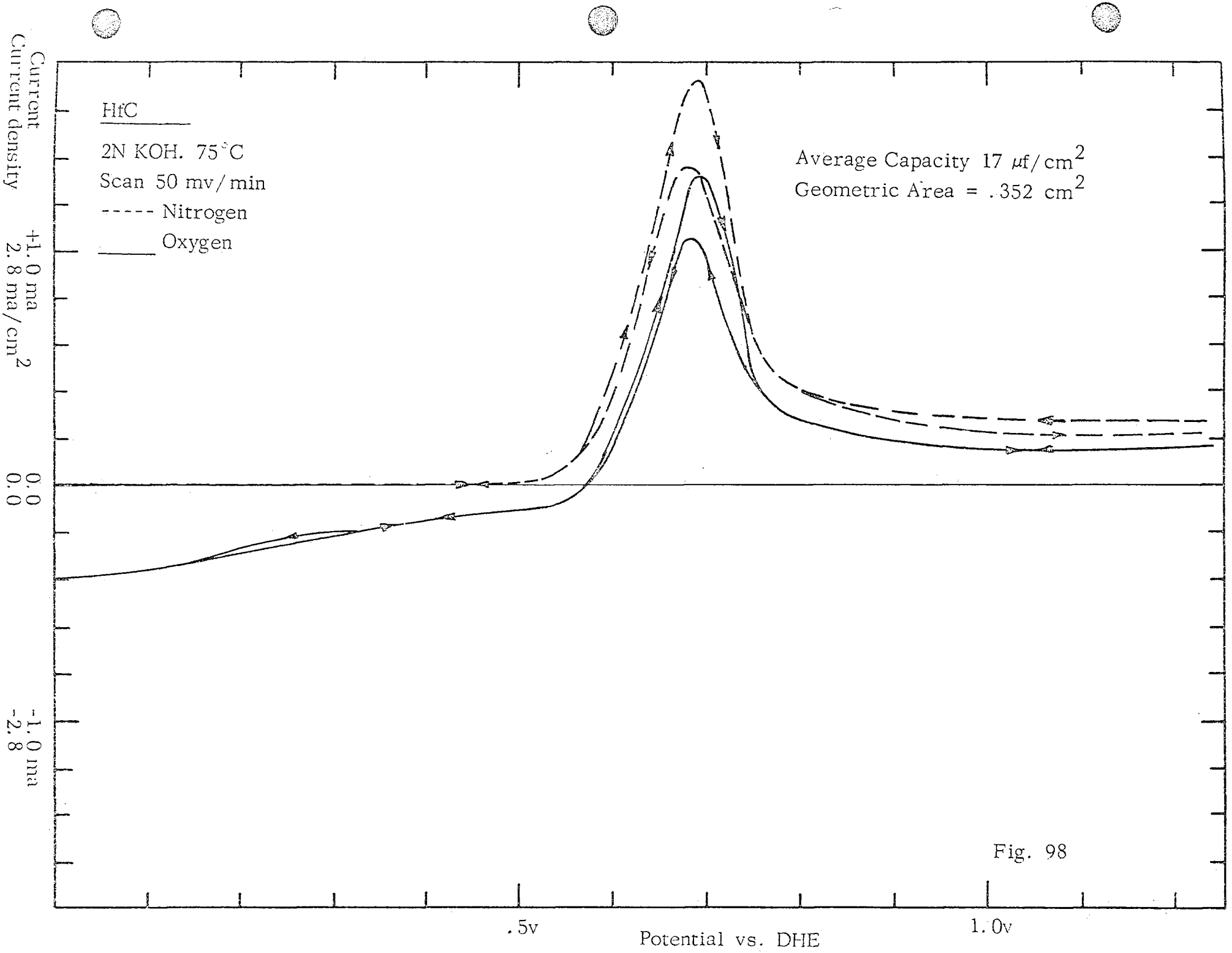
HfC
2N KOH. 75°C
Scan 50 mv/min
----- Nitrogen
_____ Oxygen
Average Capacity 17 μf/cm²
Geometric Area = .352 cm²
Current
Current density
+1.0 ma
2.8 ma/cm²
0.0
0.0
-1.0 ma
-2.8
.5v
1.0v
Potential vs. DHE

Fig. 98

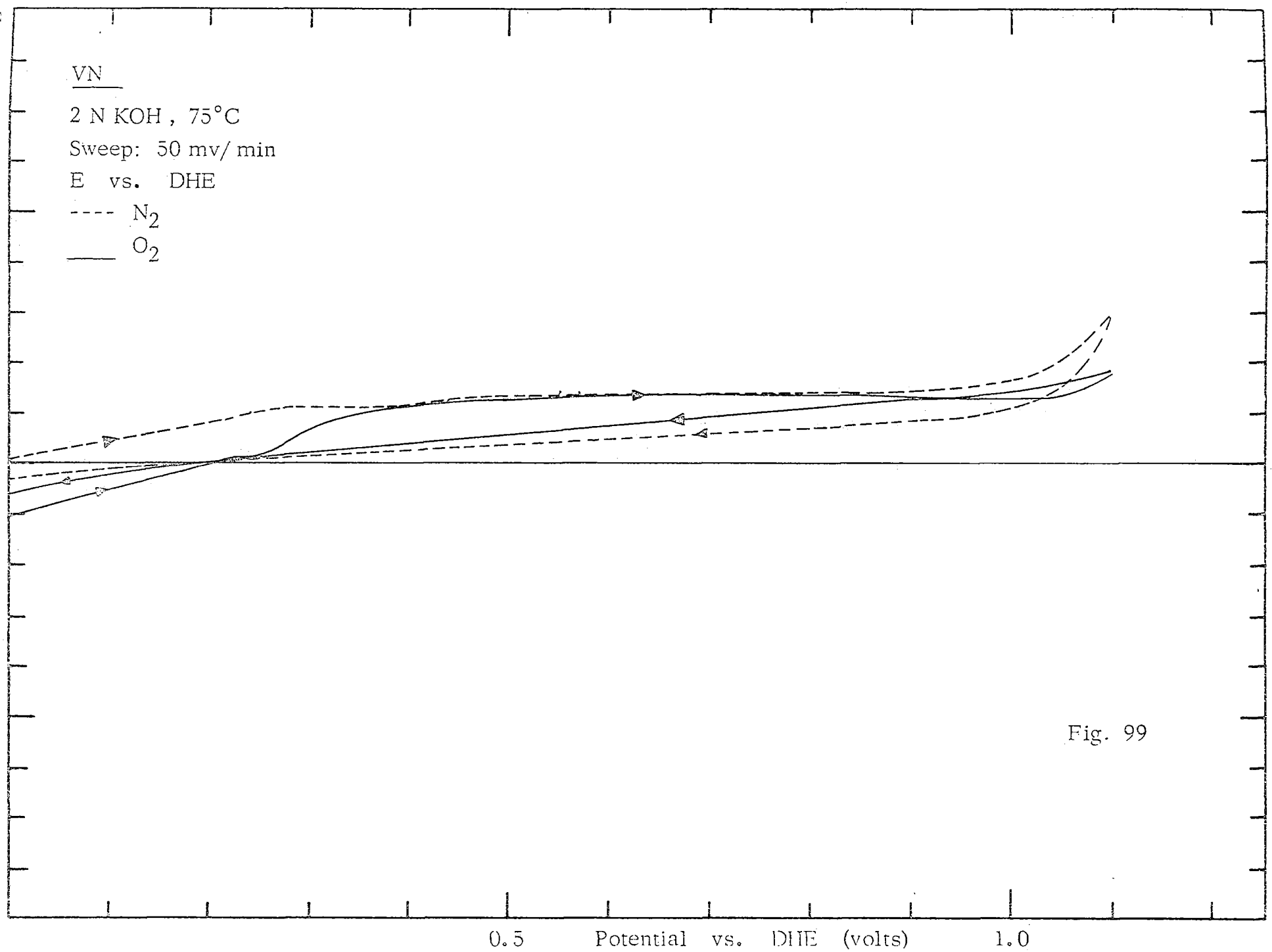
VN
2 N KOH , 75°C
Sweep: 50 mv/ min
E vs. DHE
---- N_2
—— O_2
Current
Curr. Density + 1.0 ma
2.6 ma/ cm^2
0
- 1.0 ma
2.6 ma/ cm^2
0.5
Potential vs. DHE (volts)
1.0

Fig. 99

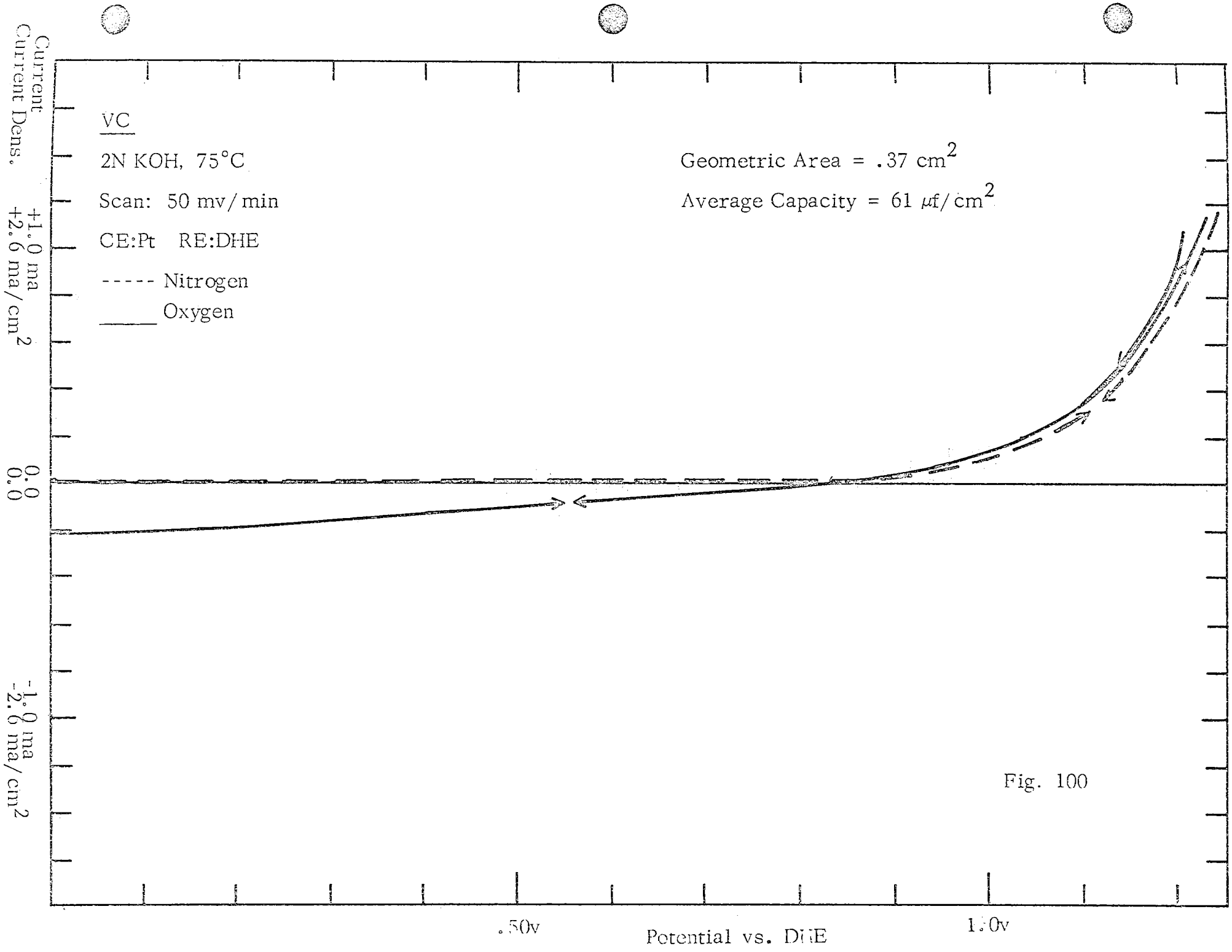
Current Dens.
+1.0 ma
+2.6 ma/cm2
0.0
0.0
-1.0 ma
-2.6 ma/cm2
VC
2N KOH, 75°C
Scan: 50 mv/min
CE:Pt RE:DHE
----- Nitrogen
_____ Oxygen
Geometric Area = .37 cm2
Average Capacity = 61 μf/cm2
.50v
1.0v
Potential vs. DHE

Fig. 100

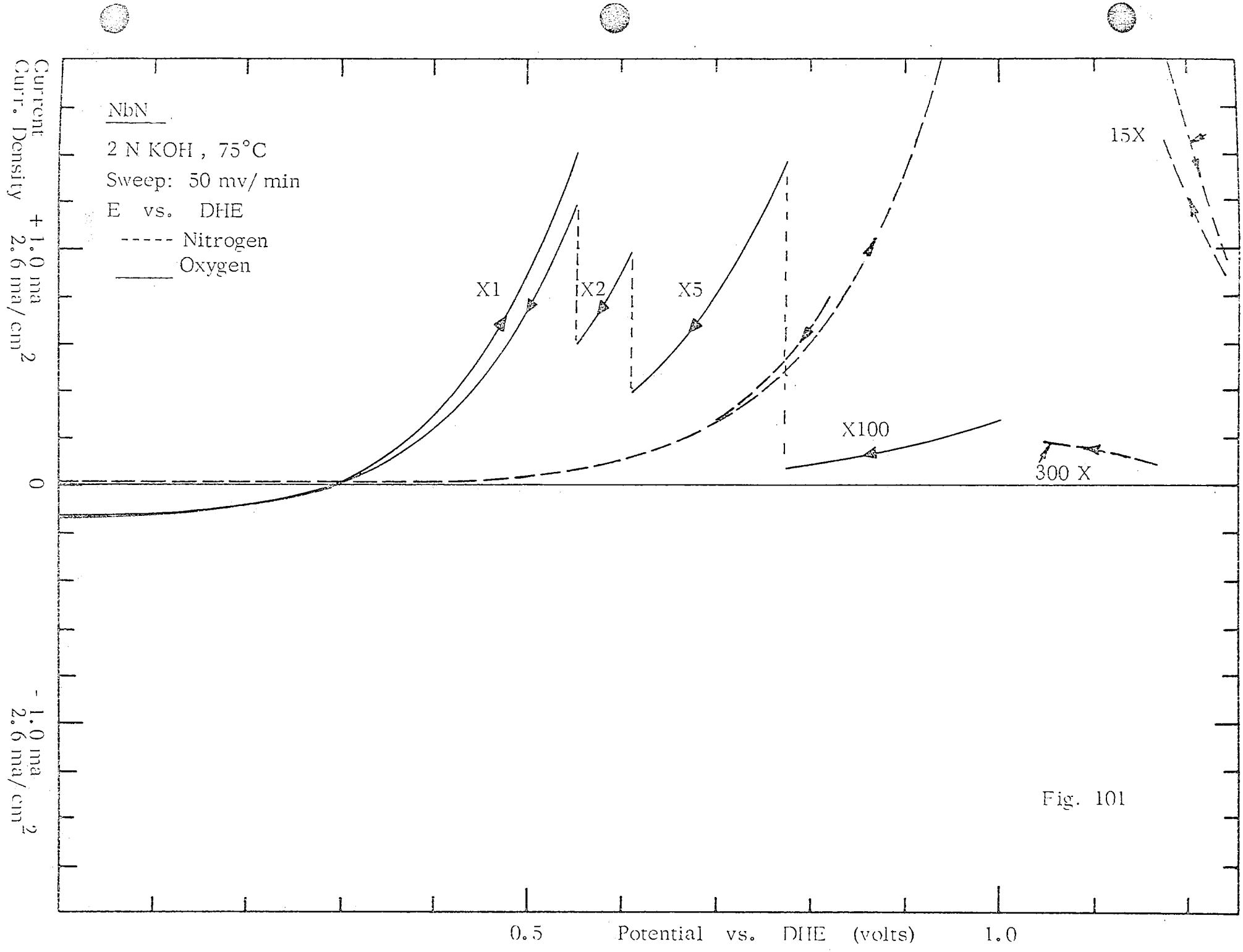
NbN
2 N KOH , 75°C
Sweep: 50 mv/ min
E vs. DHE
----- Nitrogen
_____ Oxygen
X1
X2
X5
X100
15X
300 X
Current
Curr. Density
+ 1.0 ma
2.6 ma/cm2
0
- 1.0 ma
2.6 ma/cm2
0.5
Potential vs. DHE (volts)
1.0

Fig. 101

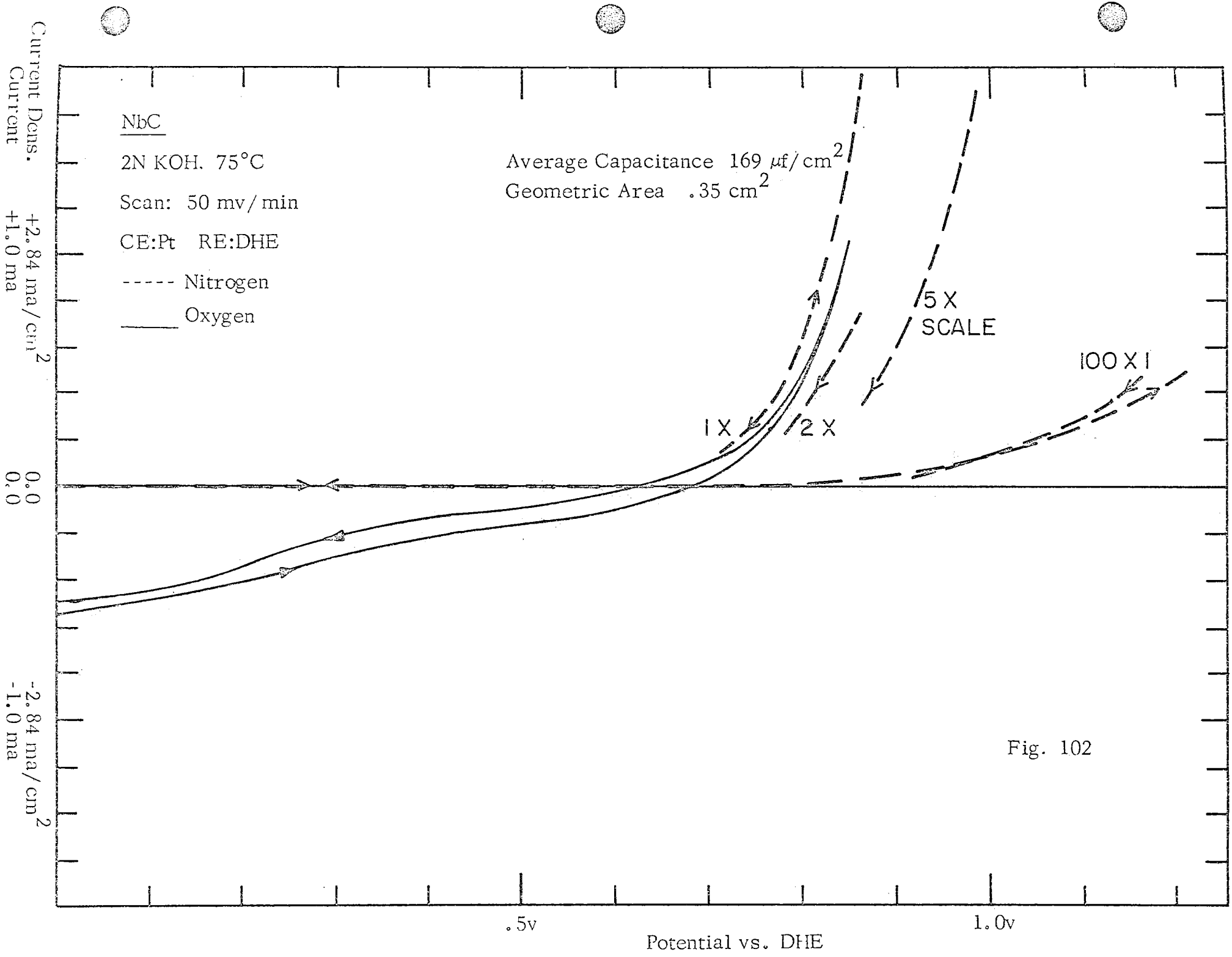
NbC
2N KOH. 75°C
Scan: 50 mv/min
CE:Pt RE:DHE
----- Nitrogen
_____ Oxygen
Average Capacitance 169 μf/cm²
Geometric Area .35 cm²
5 X SCALE
100 X 1
1 X
2 X
Current Dens.
Current
+2.84 ma/cm²
+1.0 ma
0.0
0.0
-2.84 ma/cm²
-1.0 ma
.5v
1.0v
Potential vs. DHE

Fig. 102

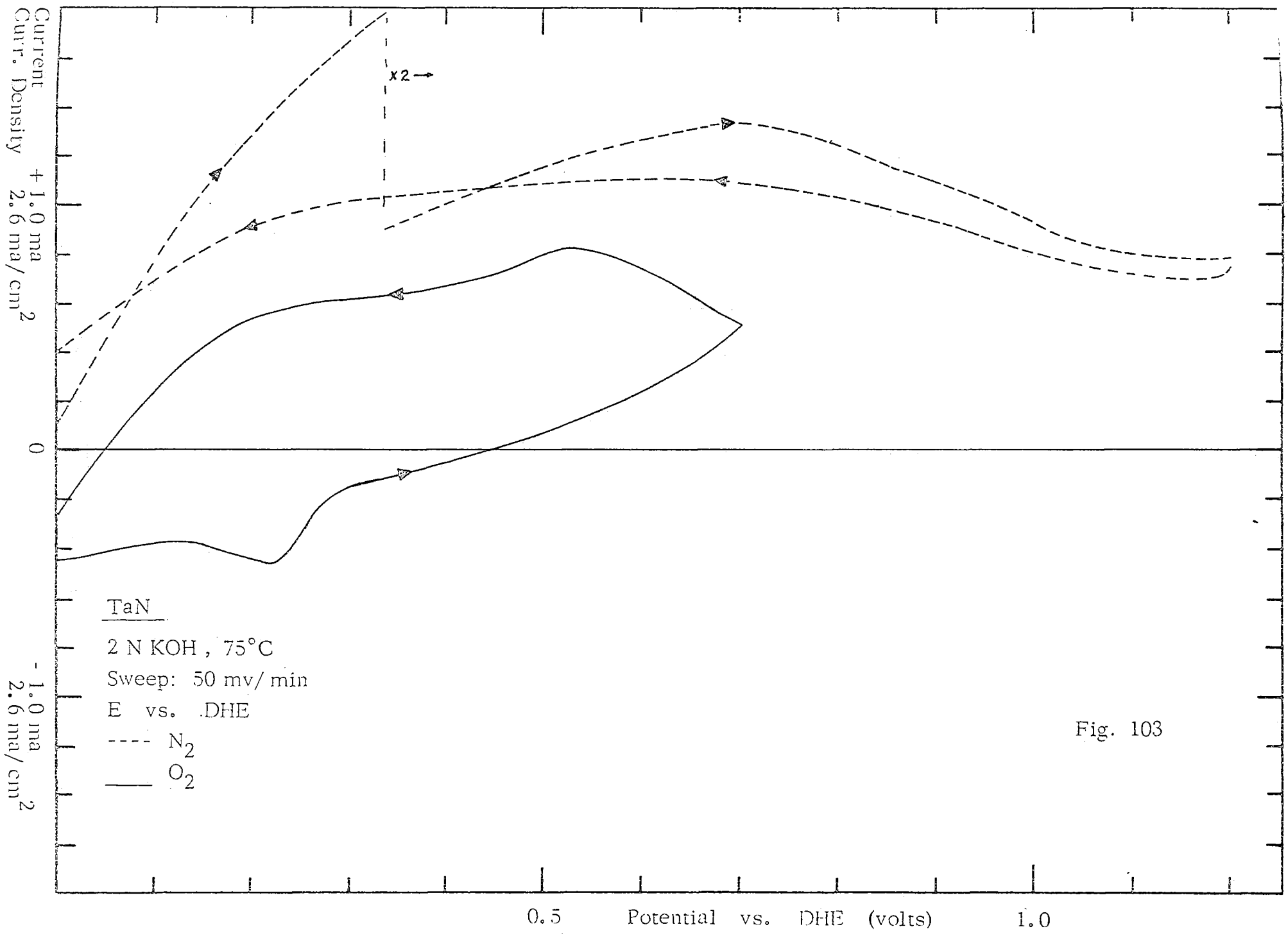
Current
Curr. Density
+1.0 ma
2.6 ma/cm2
0
-1.0 ma
2.6 ma/cm2
x2
TaN
2 N KOH , 75°C
Sweep: 50 mv/ min
E vs. DHE
---- N2
—— O2
0.5
Potential vs. DHE (volts)
1.0

Fig. 103

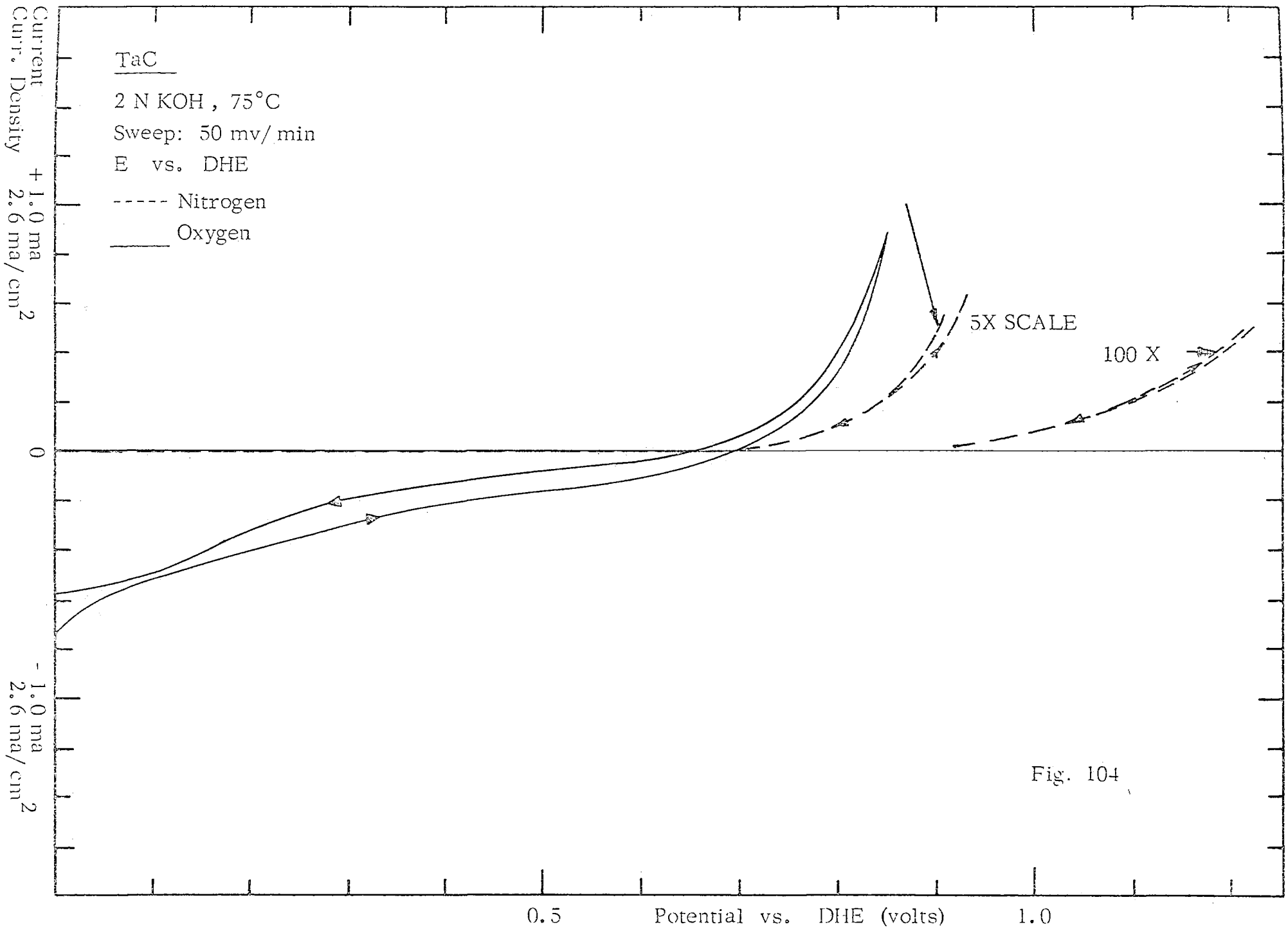
TaC
2 N KOH , 75°C
Sweep: 50 mv/ min
E vs. DHE
----- Nitrogen
_____ Oxygen
5X SCALE
100 X
Current
Curr. Density
+ 1.0 ma
2.6 ma/cm2
0
- 1.0 ma
2.6 ma/cm2
0.5
Potential vs. DHE (volts)
1.0

Fig. 104

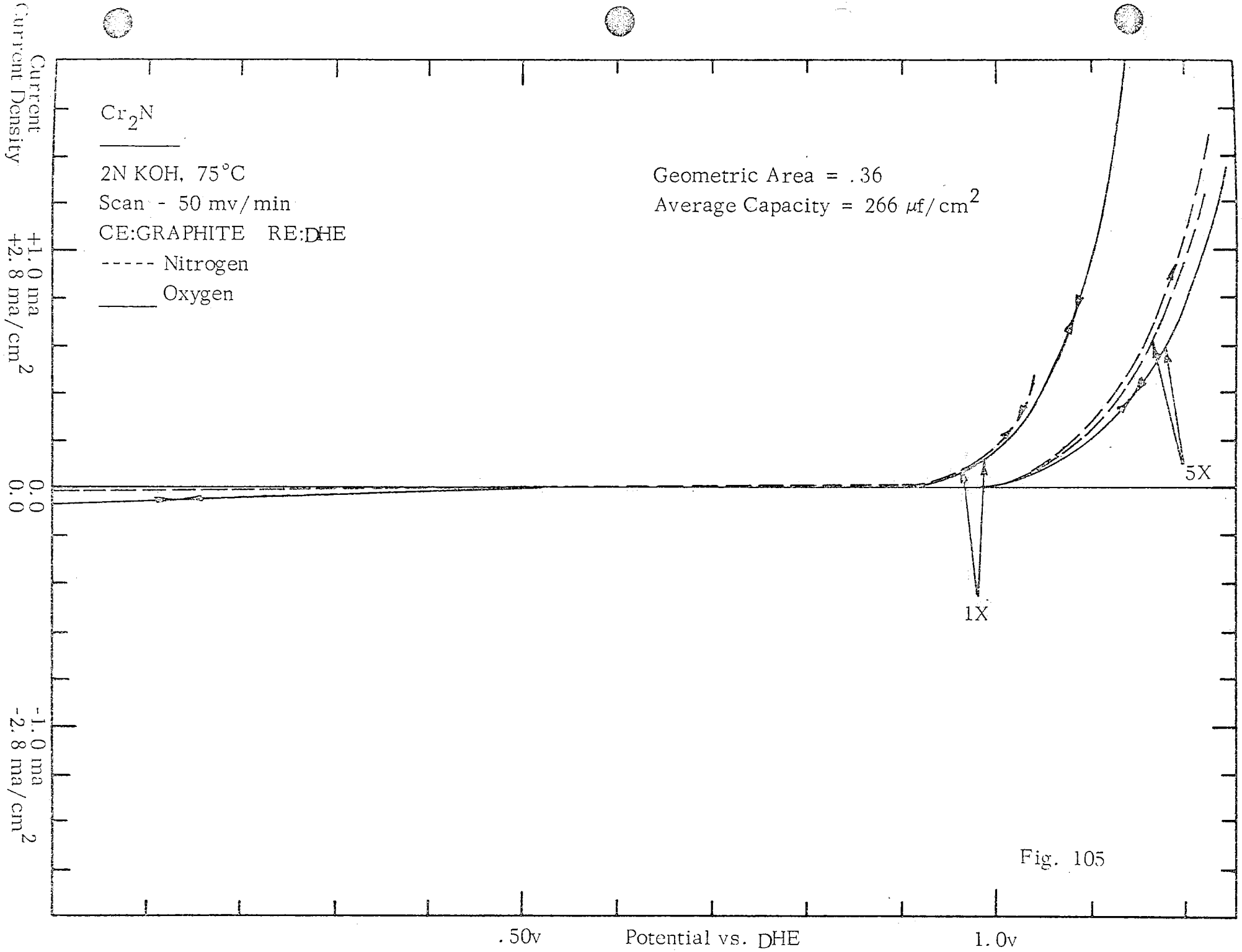
Current Density
+1.0 ma
+2.8 ma/cm2
0.0
0.0
-1.0 ma
-2.8 ma/cm2
Cr2N
2N KOH, 75°C
Scan - 50 mv/min
CE:GRAPHITE RE:DHE
----- Nitrogen
_____ Oxygen
Geometric Area = .36
Average Capacity = 266 μf/cm2
5X
1X
.50v
Potential vs. DHE
1.0v

Fig. 105

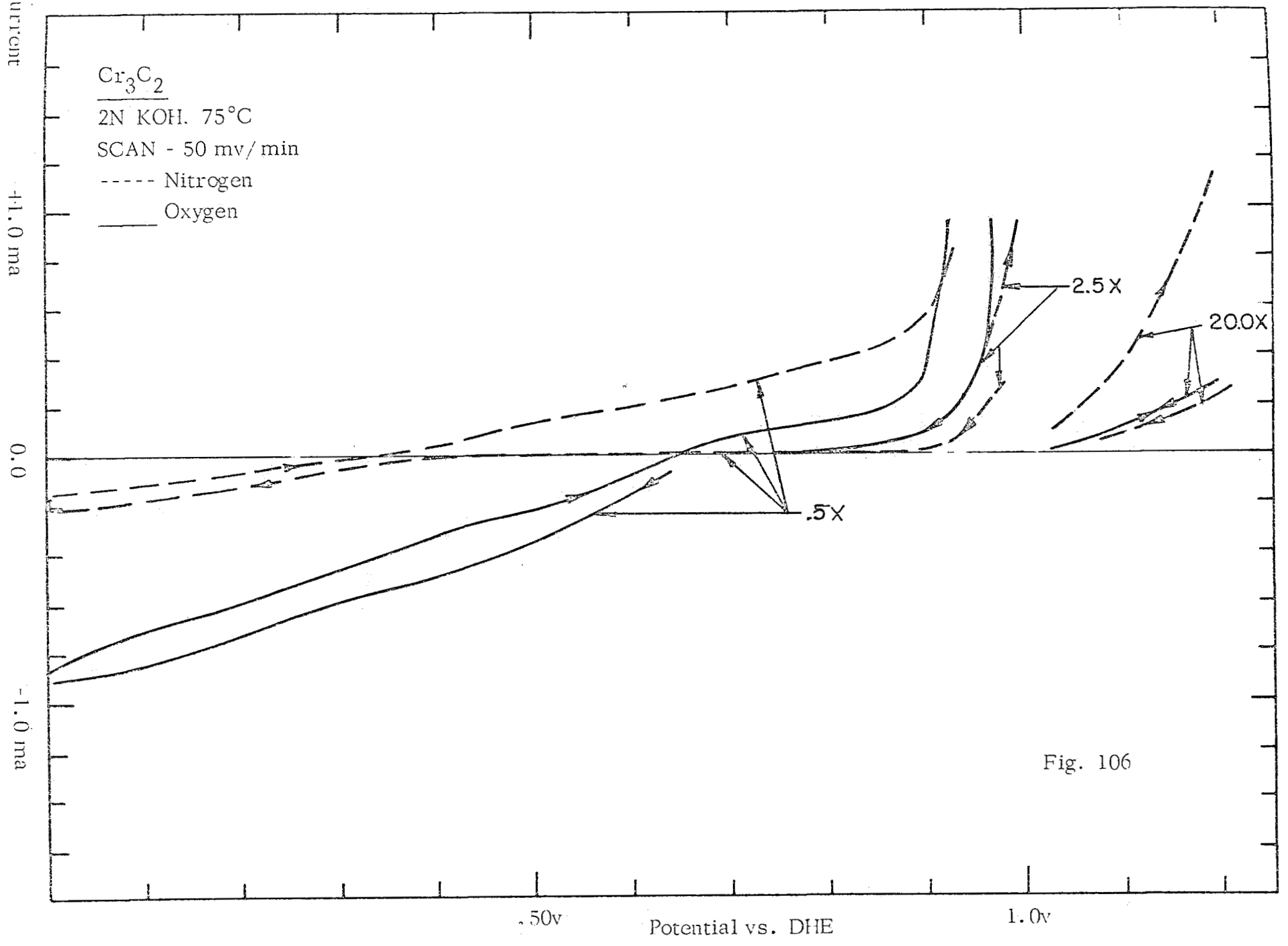
Cr_3C_2
2N KOH. 75°C
SCAN - 50 mv/min
----- Nitrogen
_____ Oxygen
2.5X
20.0X
.5X
Current
+1.0 ma
0.0
-1.0 ma
-.50v
Potential vs. DHE
1.0v

Fig. 106

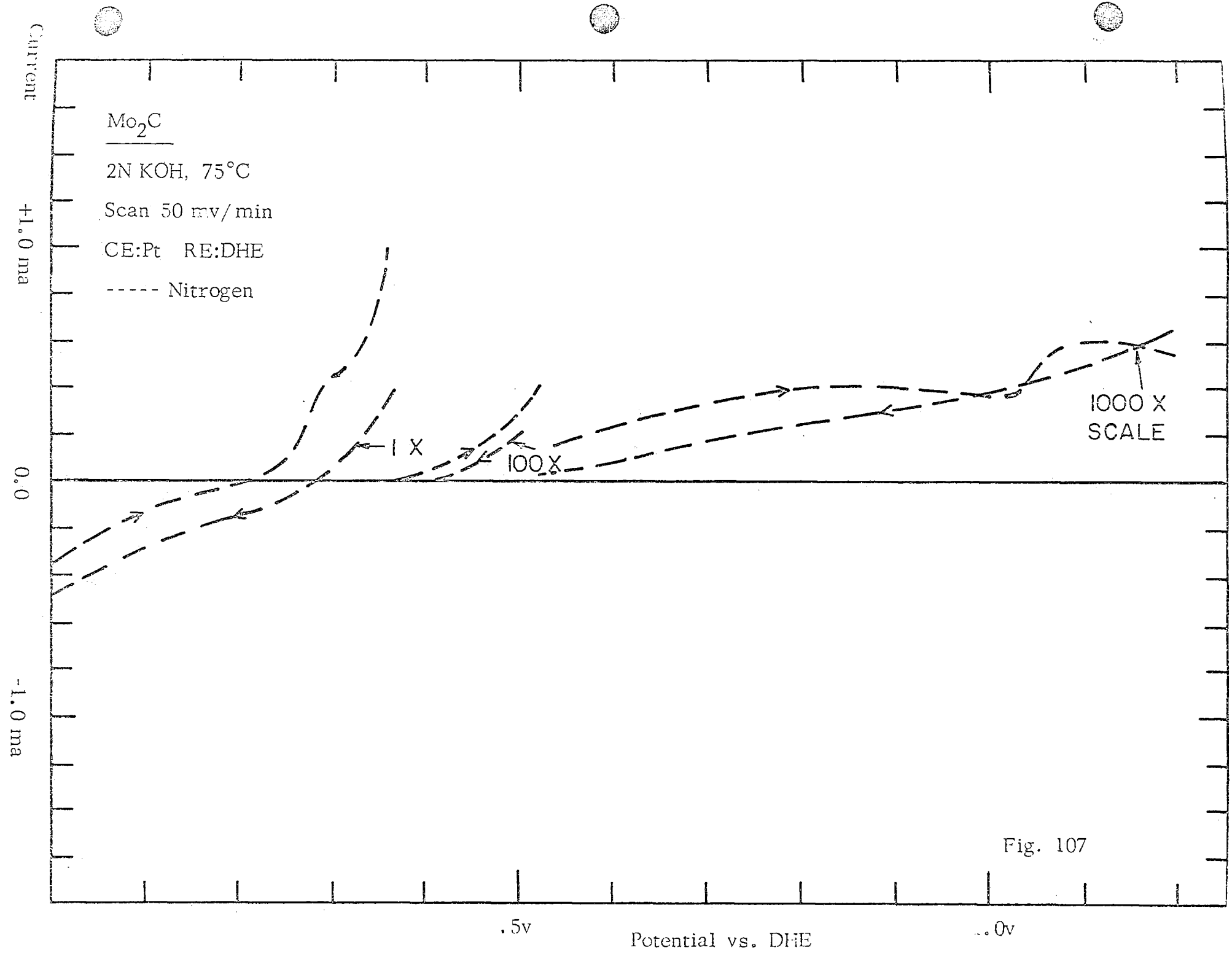
Current
+1.0 ma
0.0
-1.0 ma
Mo_2C
2N KOH, 75°C
Scan 50 mv/min
CE:Pt RE:DHE
----- Nitrogen
1 X
100 X
1000 X
SCALE
.5v
Potential vs. DHE
.0v

Fig. 107

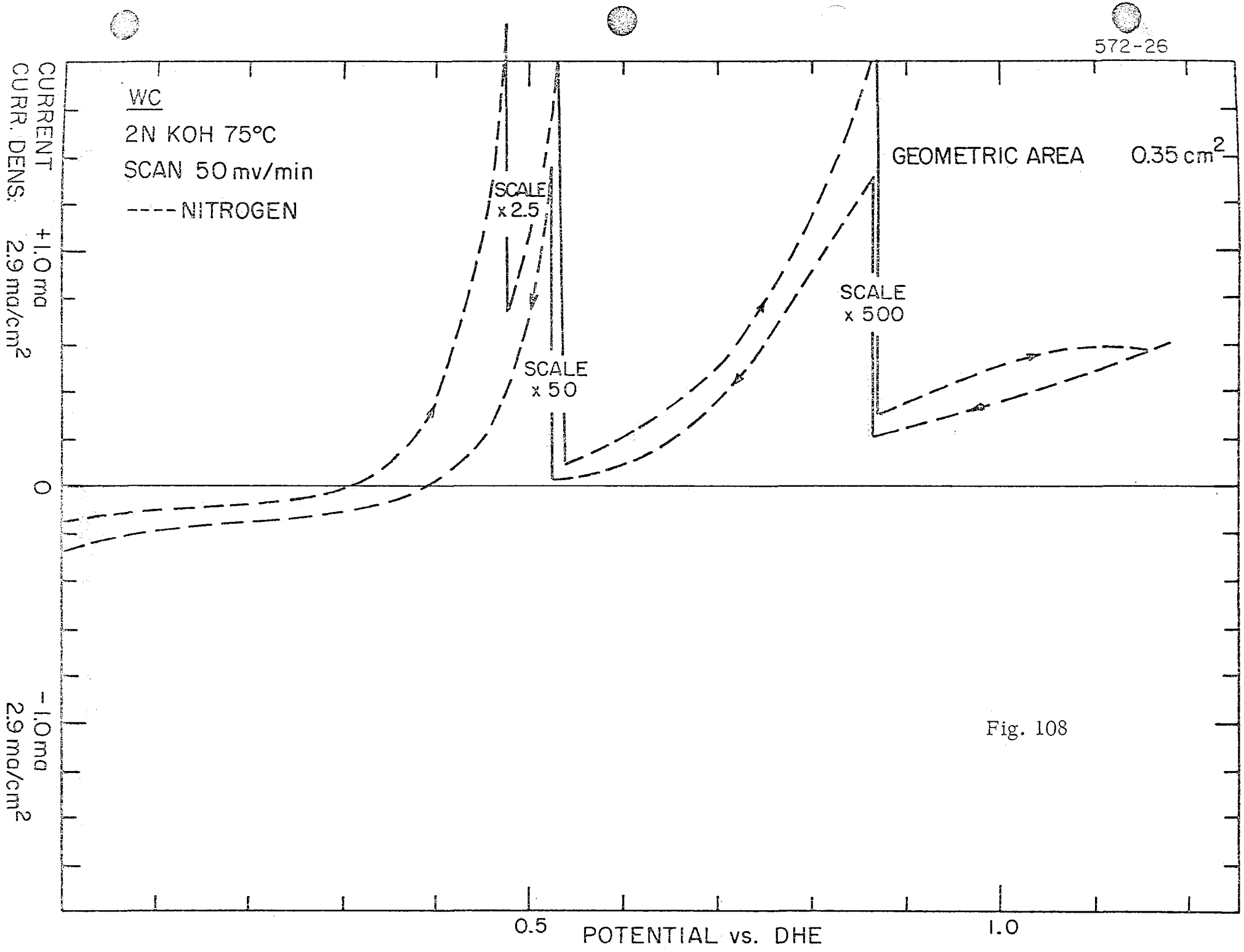
WC
2N KOH 75°C
SCAN 50 mv/min
----NITROGEN
GEOMETRIC AREA 0.35 cm²
SCALE x 2.5
SCALE x 50
SCALE x 500
CURRENT CURR. DENS. +1.0 ma 2.9 ma/cm²
0
-1.0 ma 2.9 ma/cm²
0.5
POTENTIAL vs. DHE
1.0

Fig. 108

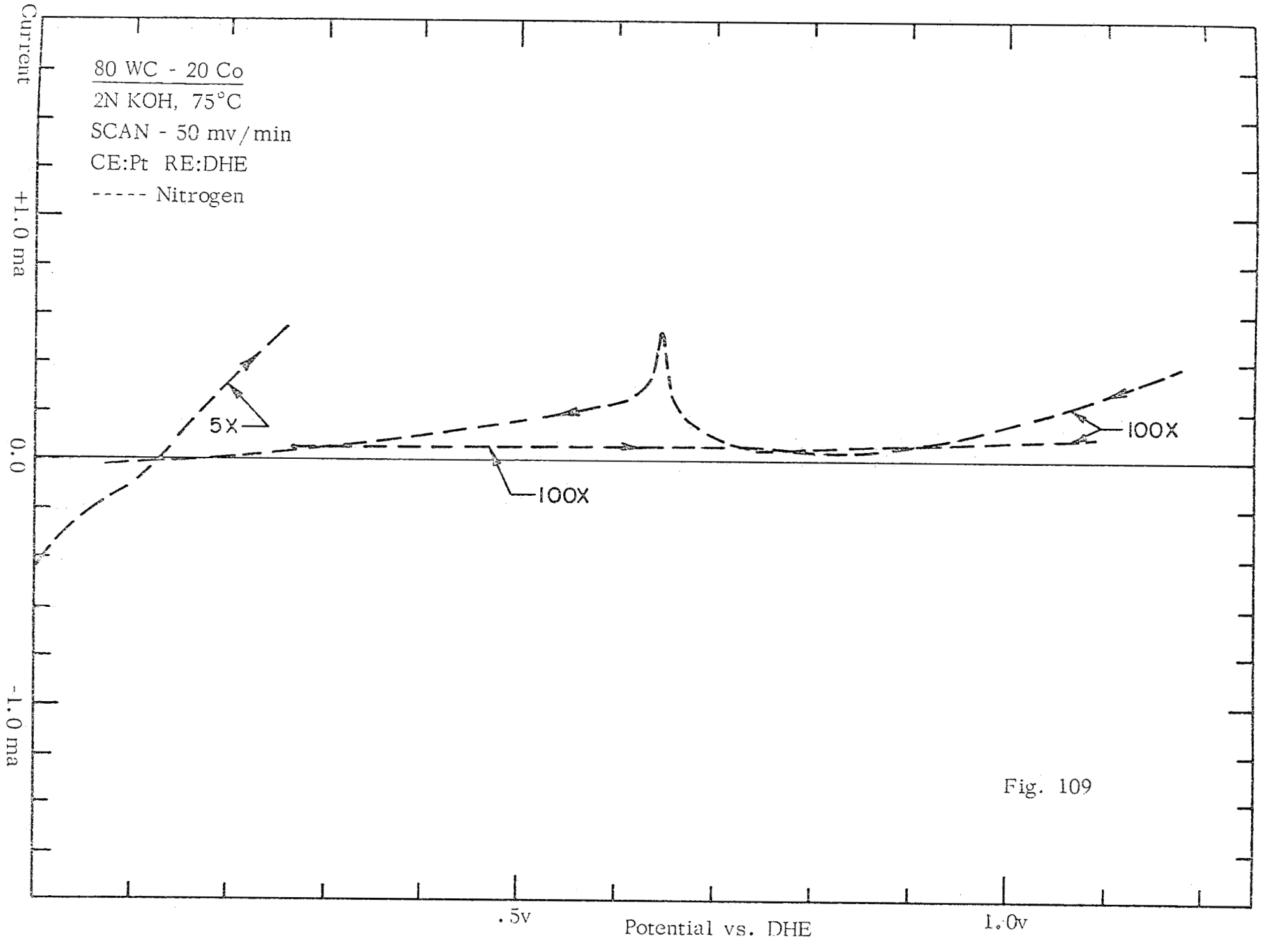
Current
80 WC - 20 Co
2N KOH, 75°C
SCAN - 50 mv/min
CE:Pt RE:DHE
----- Nitrogen
+1.0 ma
0.0
-1.0 ma
5X
100X
100X
.5v
Potential vs. DHE
1.0v

Fig. 109

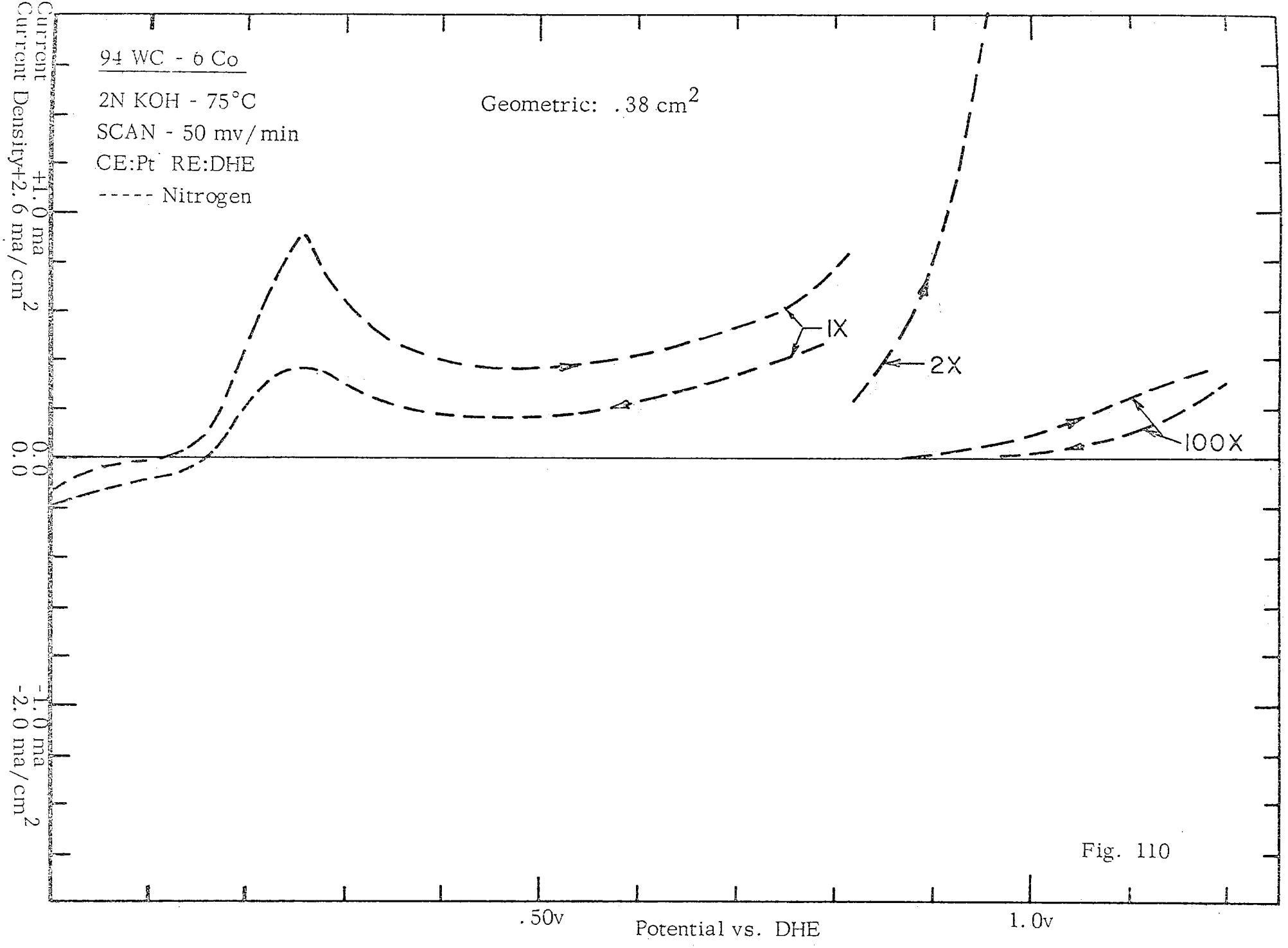
94 WC - 6 Co
2N KOH - 75°C
SCAN - 50 mv/min
CE:Pt RE:DHE
----- Nitrogen
Geometric: .38 cm2
Current
Current Density+2.6 ma/cm2
+1.0 ma
0.0
-1.0 ma
-2.0 ma/cm2
1X
2X
100X
.50v
Potential vs. DHE
1.0v

Fig. 110

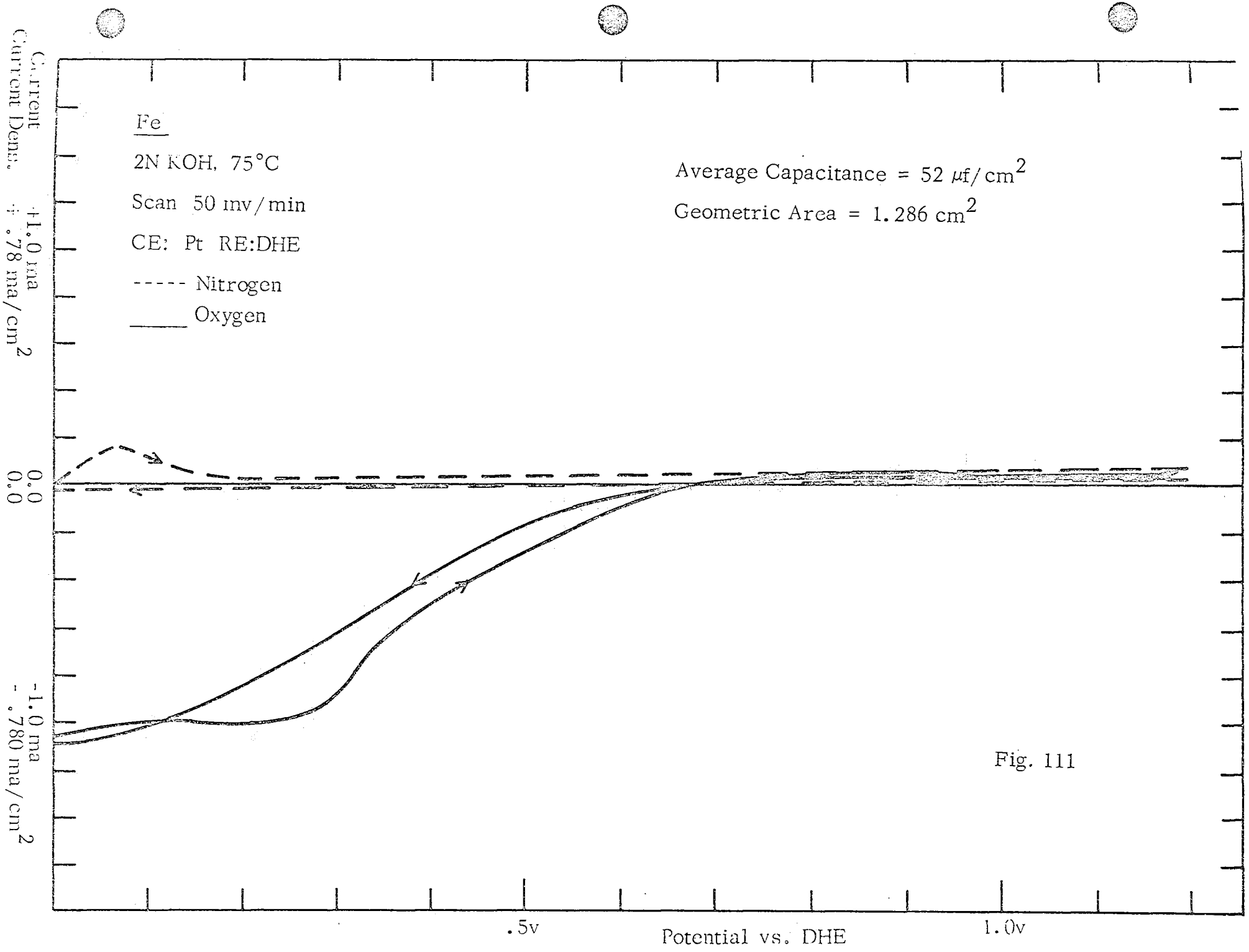
Fe
2N KOH, 75°C
Scan 50 mv/min
CE: Pt RE:DHE
----- Nitrogen
_____ Oxygen
Average Capacitance = 52 μf/cm²
Geometric Area = 1.286 cm²
Current
Current Dens.
+1.0 ma
+ .78 ma/cm²
0.0
0.0
-1.0 ma
- .780 ma/cm²
.5v
Potential vs. DHE
1.0v

Fig. 111

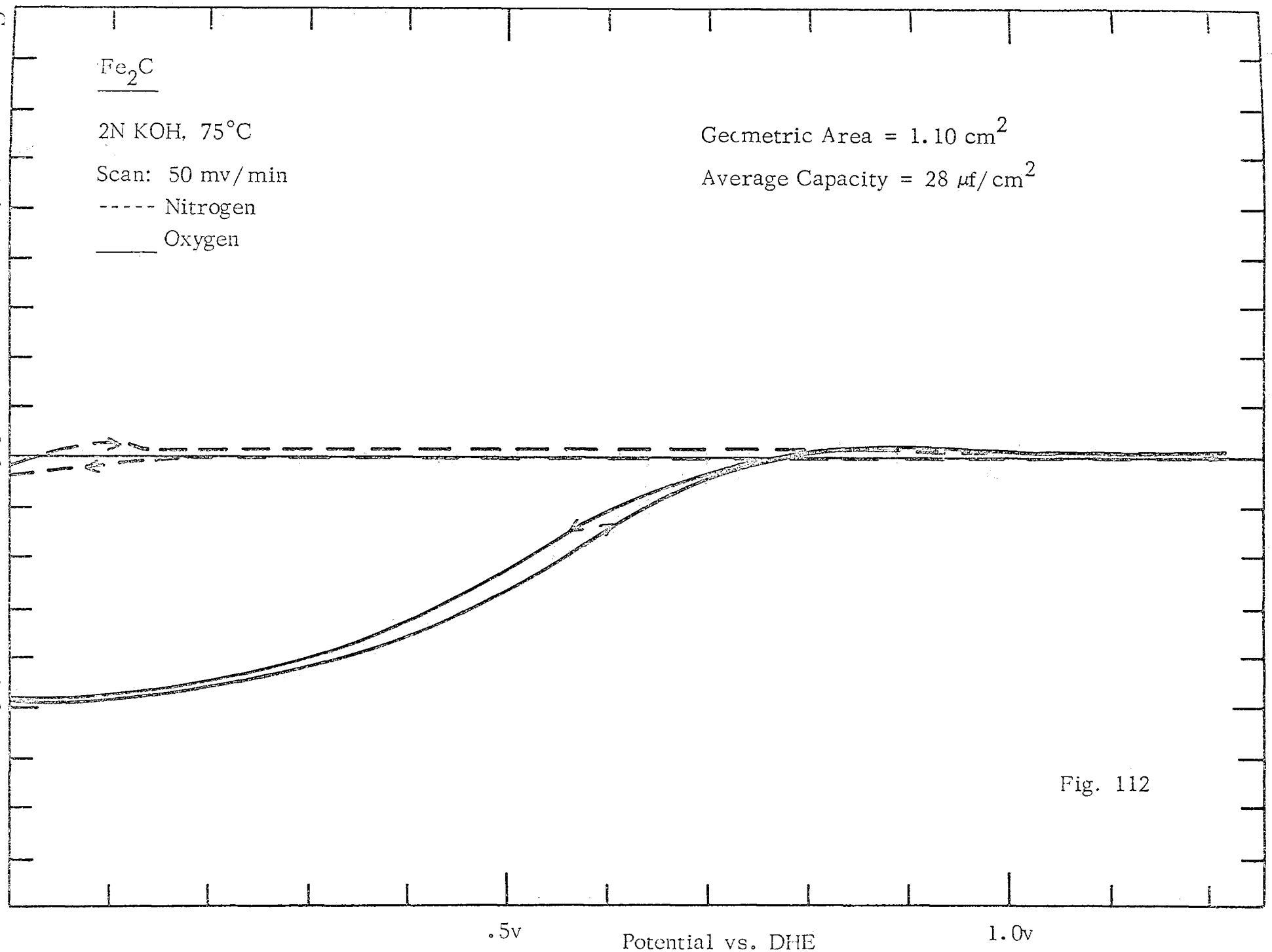
Fe2C
2N KOH, 75°C
Scan: 50 mv/min
----- Nitrogen
_____ Oxygen
Geometric Area = 1.10 cm2
Average Capacity = 28 μf/cm2
Current Dens.
+1.0 ma
+ .907 ma/cm2
0.0
0.0
-1.0 ma
- .907 ma/cm2
.5v
Potential vs. DHE
1.0v

Fig. 112

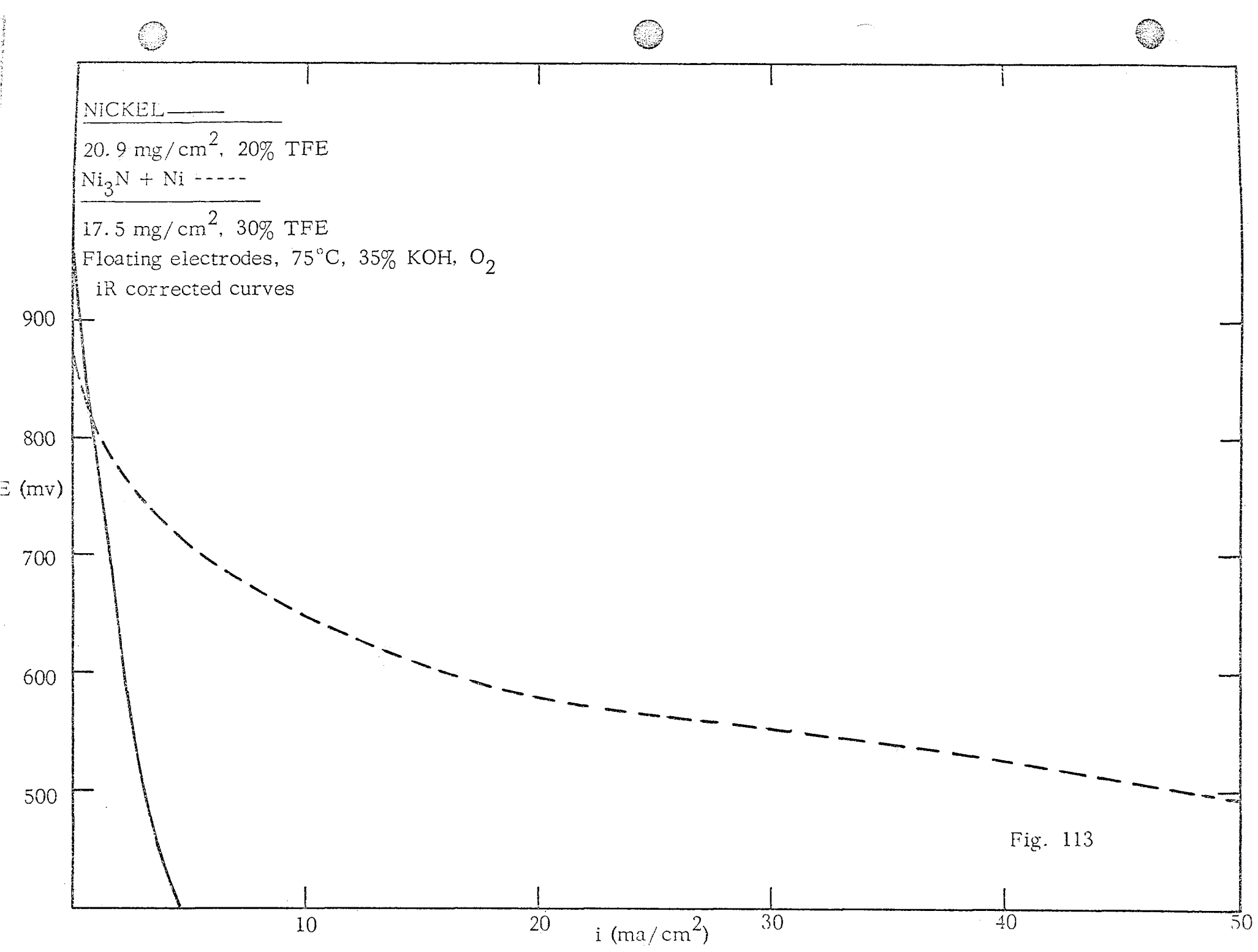
NICKEL
20.9 mg/cm2, 20% TFE
Ni3N + Ni -----
17.5 mg/cm2, 30% TFE
Floating electrodes, 75°C, 35% KOH, O2
iR corrected curves
900
800
E (mv)
700
600
500
10
20
30
40
50
i (ma/cm2)

Fig. 113

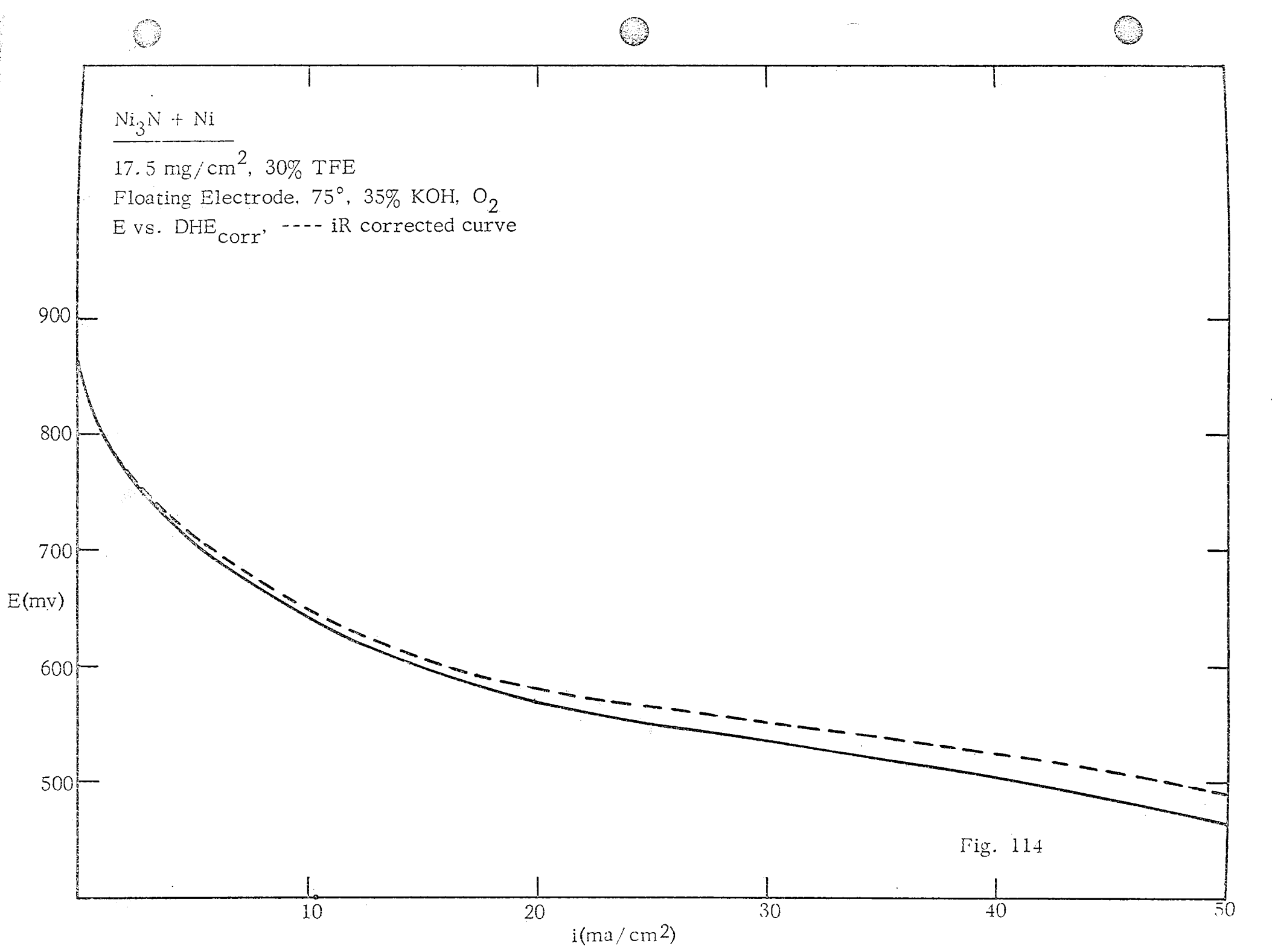
$Ni_3N + Ni$
17.5 mg/cm^2, 30% TFE
Floating Electrode, 75°, 35% KOH, O_2
E vs. DHE_{corr}, ---- iR corrected curve
900
800
700
600
500
E(mv)
10
20
30
40
50
i(ma/cm2)

Fig. 114

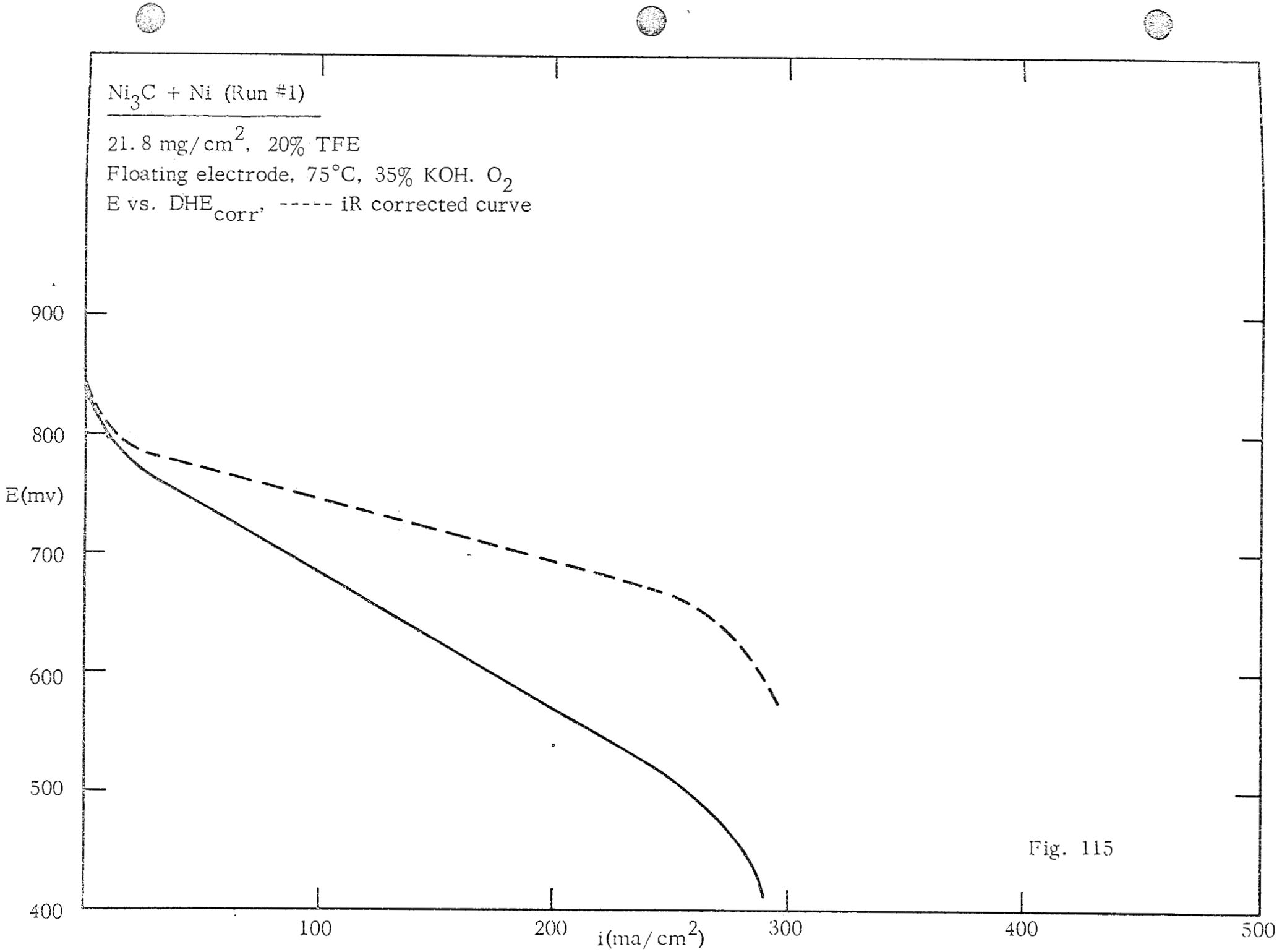
Ni_3C + Ni (Run #1)
21.8 mg/cm^2, 20% TFE
Floating electrode, 75°C, 35% KOH. O_2
E vs. DHE_{corr}, ----- iR corrected curve
900
800
700
600
500
400
E(mv)
100
200
300
400
500
i(ma/cm^2)

Fig. 115

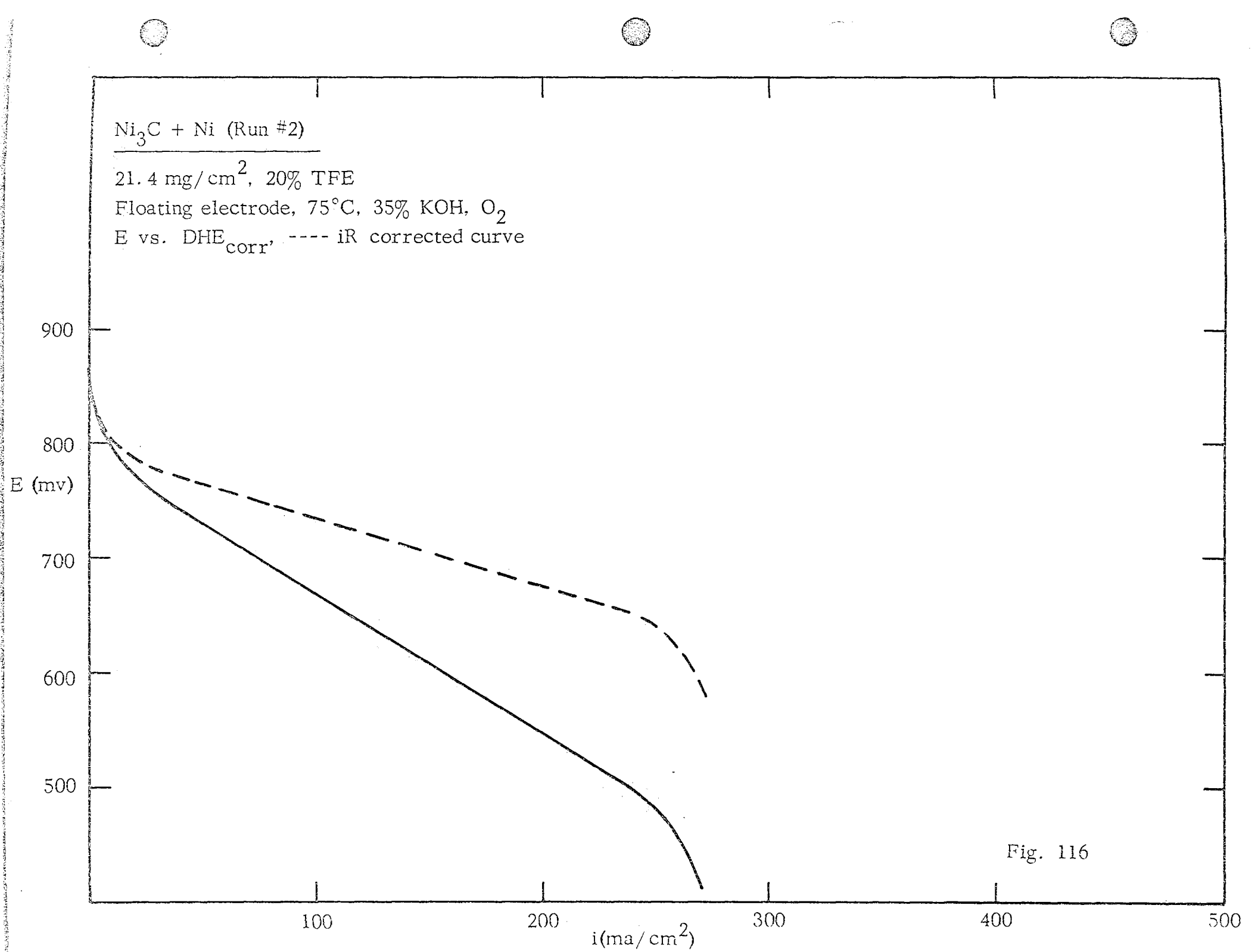
Ni_3C + Ni (Run #2)
21.4 mg/cm^2, 20% TFE
Floating electrode, 75°C, 35% KOH, O_2
E vs. DHE_{corr}, ---- iR corrected curve
900
800
700
600
500
E (mv)
100
200
300
400
500
i(ma/cm^2)

Fig. 116

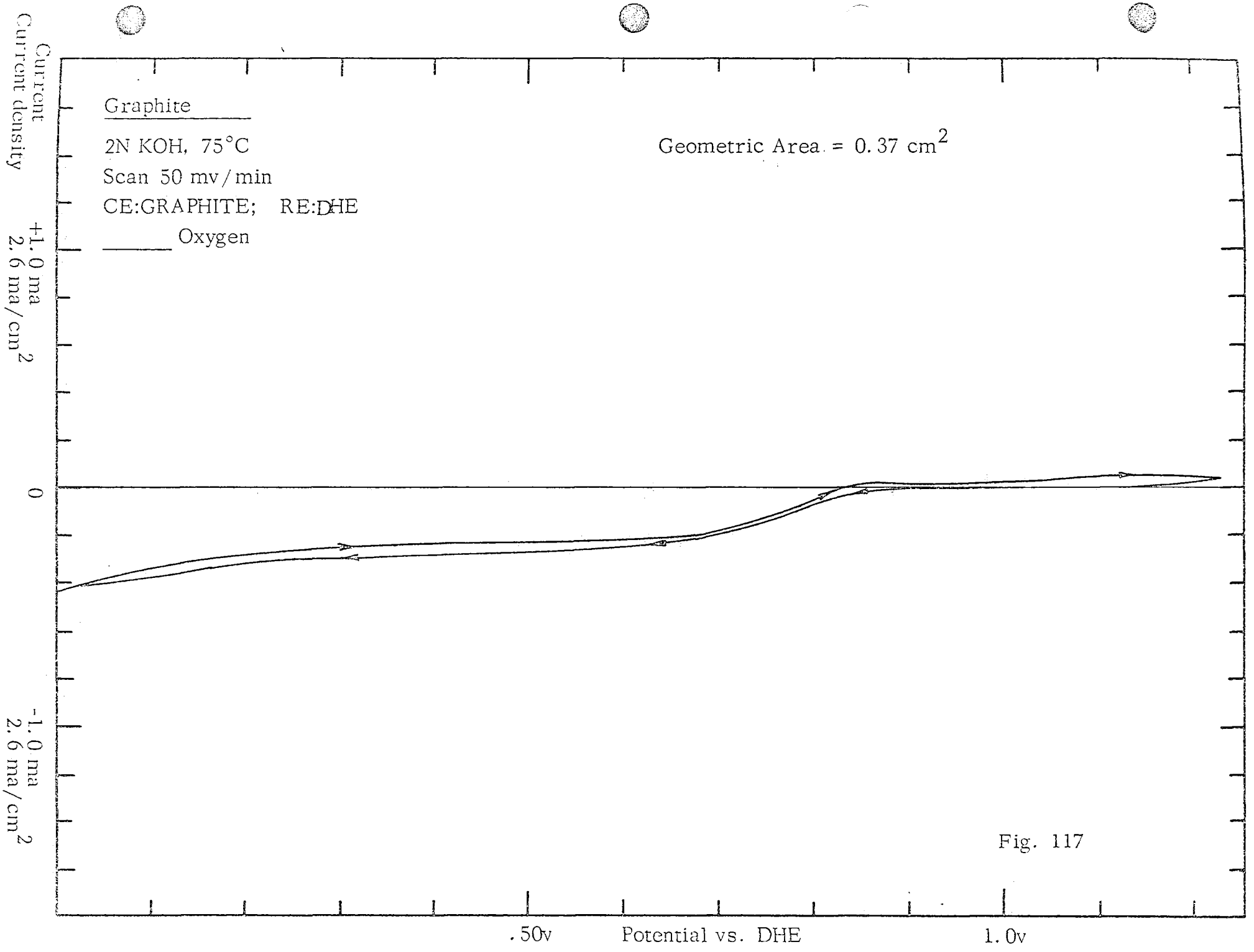
Graphite
2N KOH, 75°C
Scan 50 mv/min
CE:GRAPHITE; RE:DHE
Oxygen
Geometric Area = 0.37 cm2
Current density
+1.0 ma
2.6 ma/cm2
0
-1.0 ma
2.6 ma/cm2
.50v
Potential vs. DHE
1.0v

Fig. 117

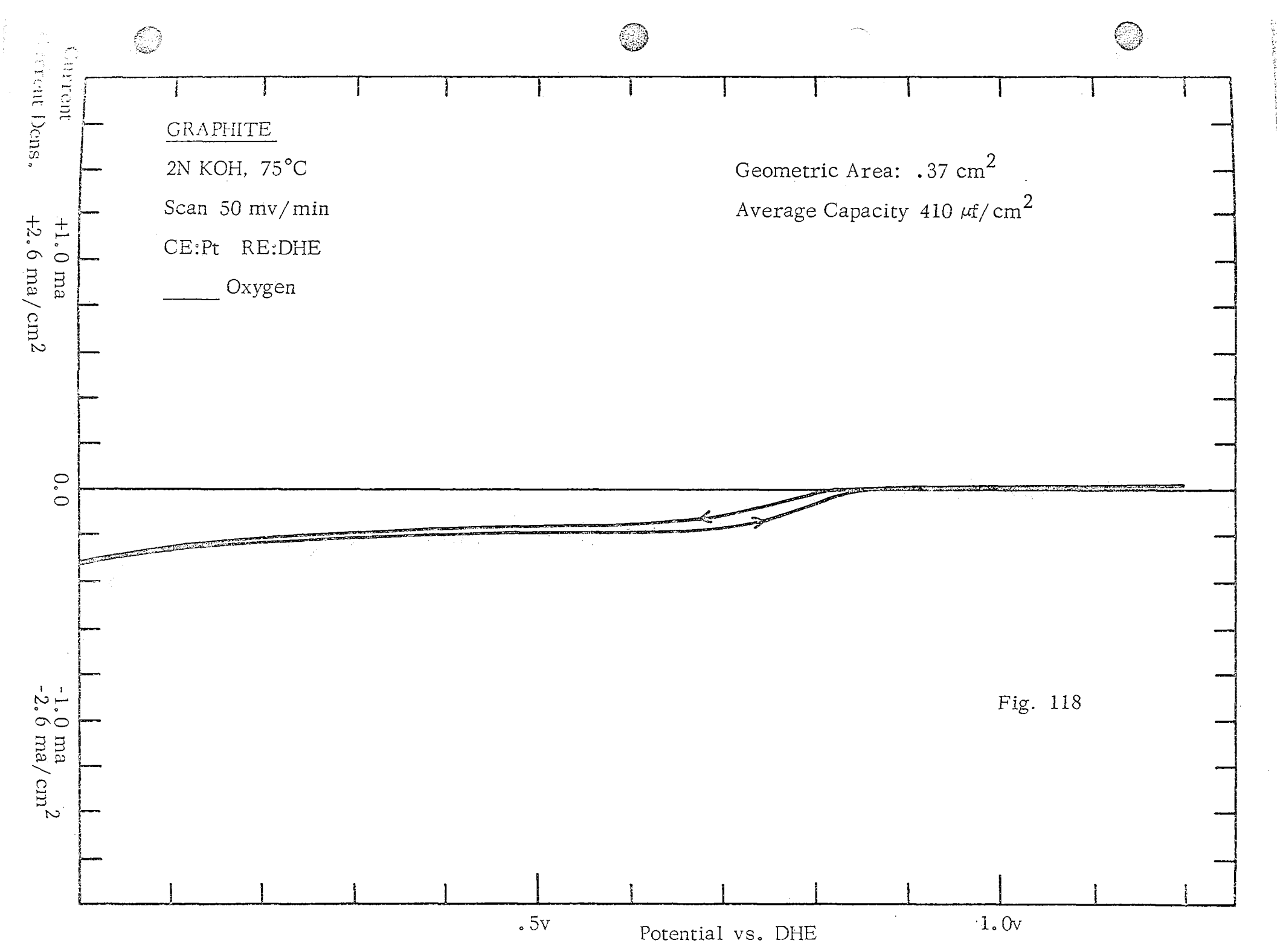
Current
Current Dens.
GRAPHITE
2N KOH, 75°C
Scan 50 mv/min
CE:Pt RE:DHE
_____ Oxygen
Geometric Area: .37 cm2
Average Capacity 410 μf/cm2
+1.0 ma
+2.6 ma/cm2
0.0
-1.0 ma
-2.6 ma/cm2
.5v
Potential vs. DHE
1.0v

Fig. 118

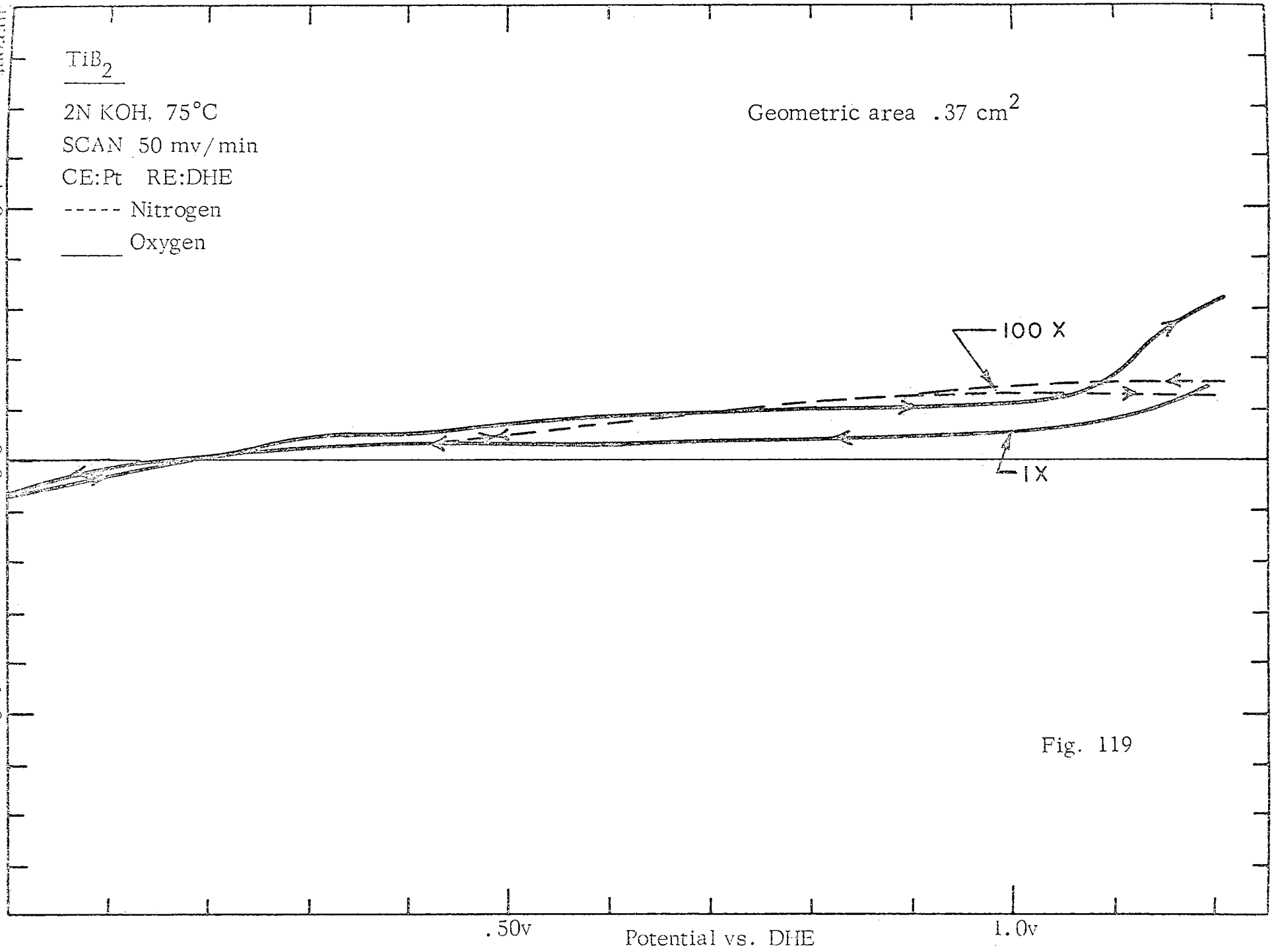
TiB2
2N KOH, 75°C
SCAN 50 mv/min
CE:Pt RE:DHE
----- Nitrogen
_____ Oxygen
Geometric area .37 cm2
100 X
1X
Current density
-1.0 ma
-2.7 ma/cm2
0.0
0.0
+1.0 ma
+2.7 ma/cm2
.50v
Potential vs. DHE
1.0v

Fig. 119

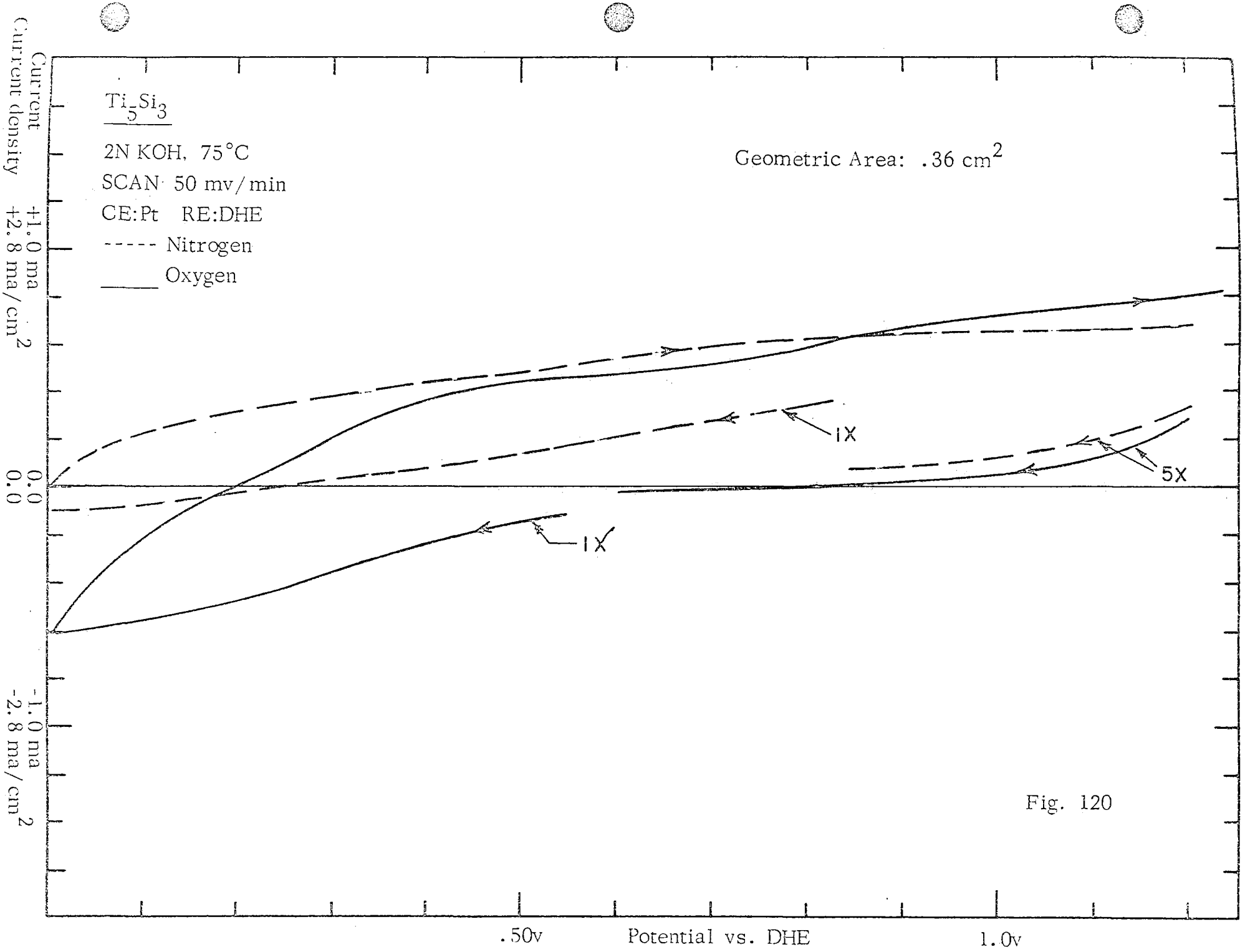
Current density
+1.0 ma
+2.8 ma/cm2
0.0
0.0
-1.0 ma
-2.8 ma/cm2
Ti5Si3
2N KOH, 75°C
SCAN 50 mv/min
CE:Pt RE:DHE
----- Nitrogen
_____ Oxygen
Geometric Area: .36 cm2
1X
5X
1X
.50v
Potential vs. DHE
1.0v

Fig. 120

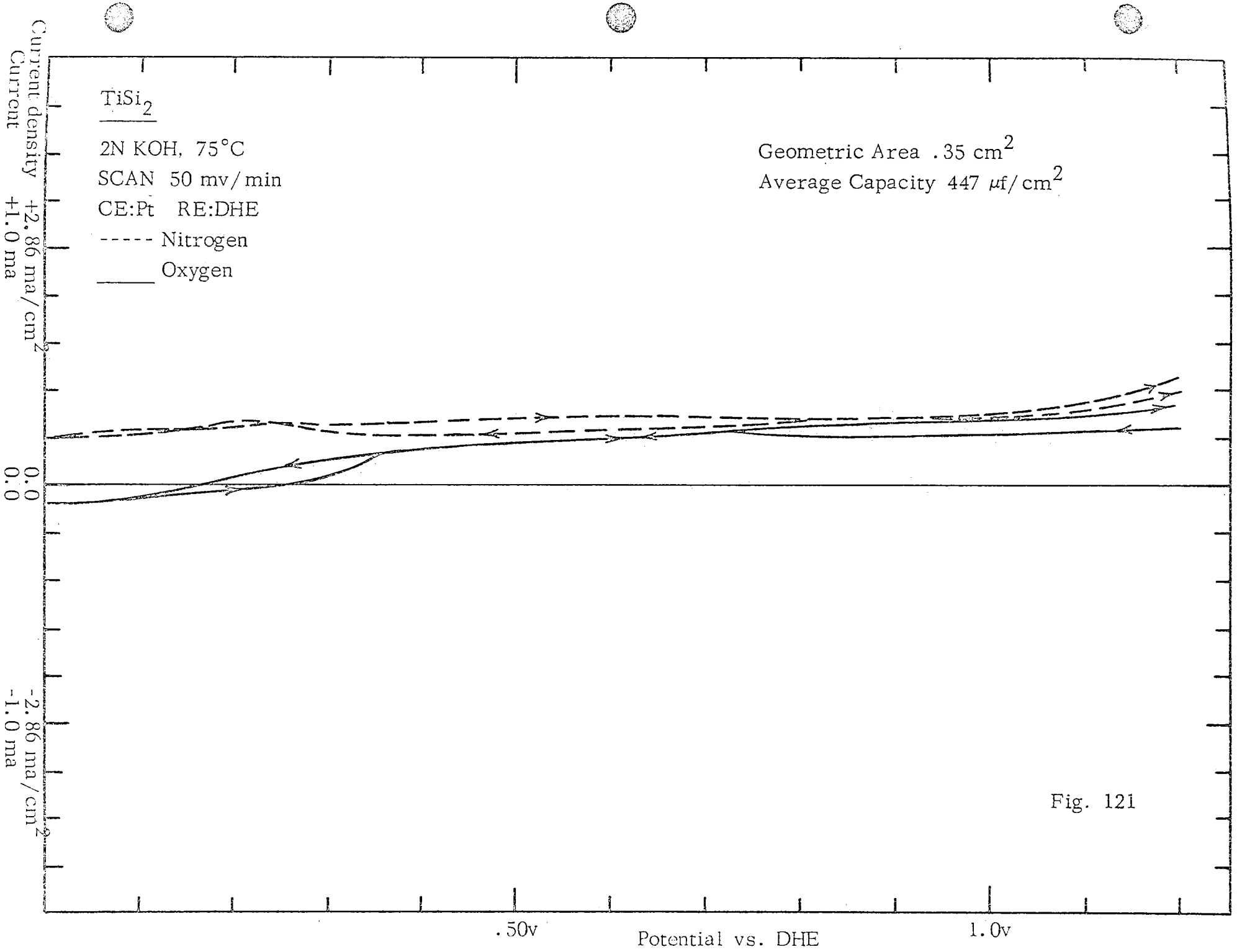
Current density
Current
+2.86 ma/cm²
+1.0 ma
0.0
0.0
-2.86 ma/cm²
-1.0 ma
TiSi2
2N KOH, 75°C
SCAN 50 mv/min
CE:Pt RE:DHE
----- Nitrogen
_____ Oxygen
Geometric Area .35 cm²
Average Capacity 447 μf/cm²
.50v
Potential vs. DHE
1.0v

Fig. 121

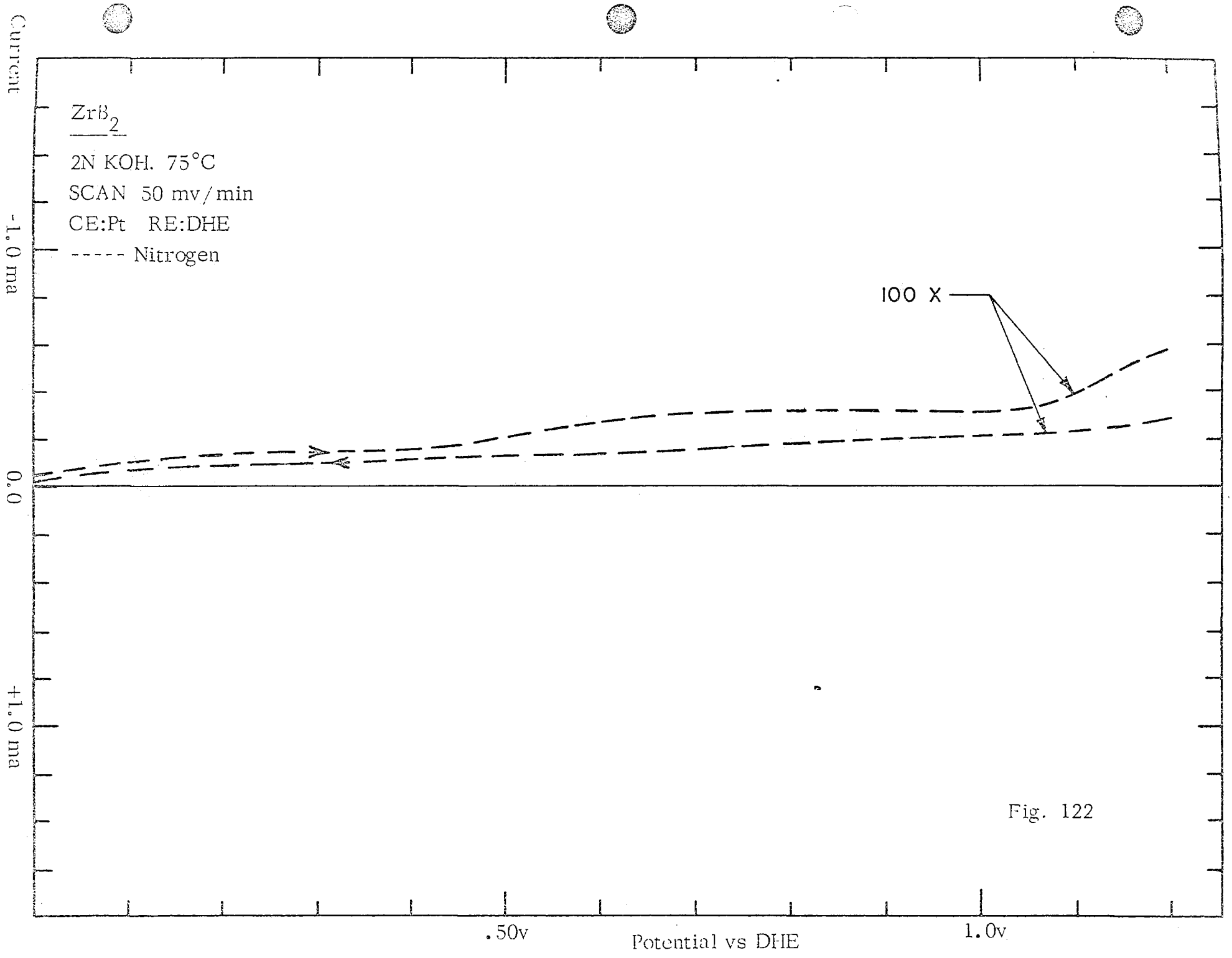
Current
-1.0 ma
0.0
+1.0 ma
ZrB_2
2N KOH. 75°C
SCAN 50 mv/min
CE:Pt RE:DHE
----- Nitrogen
100 X
.50v
Potential vs DHE
1.0v

Fig. 122

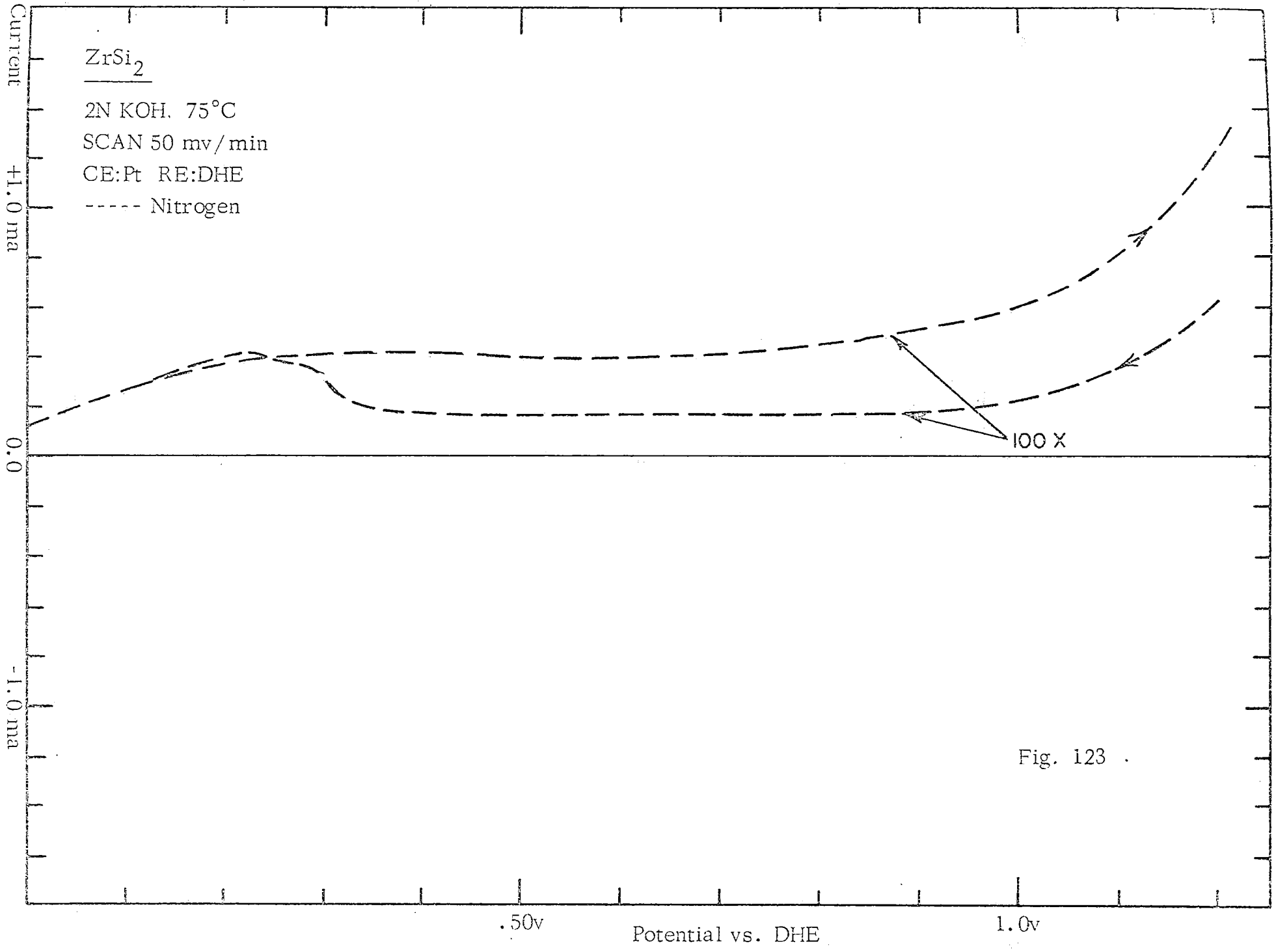
Current
$ZrSi_2$
2N KOH. 75°C
SCAN 50 mv/min
CE:Pt RE:DHE
----- Nitrogen
+1.0 ma
0.0
-1.0 ma
100 X
.50v
Potential vs. DHE
1.0v

Fig. 123 .

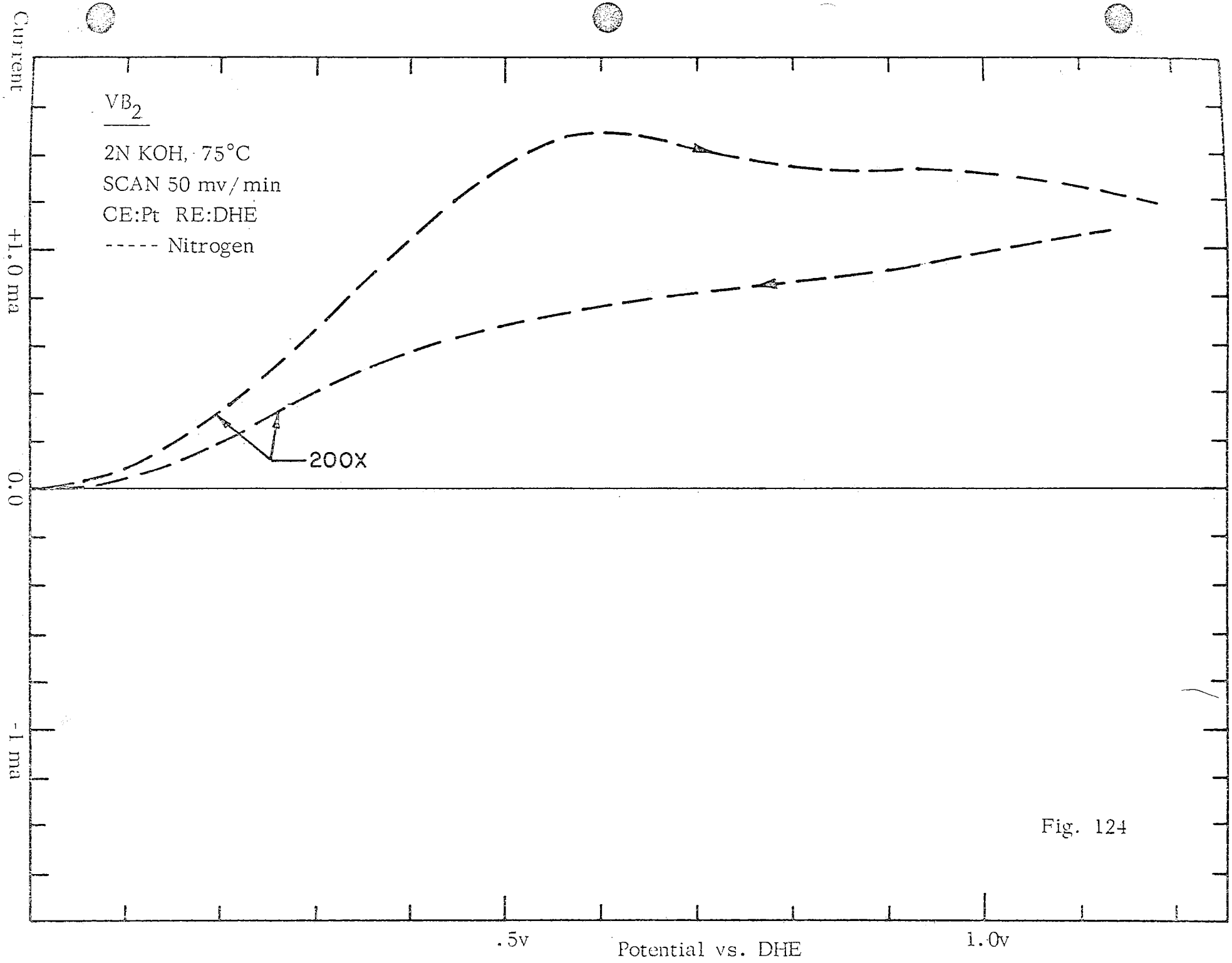
Current
+1.0 ma
0.0
-1 ma
VB_2
2N KOH, 75°C
SCAN 50 mv/min
CE:Pt RE:DHE
----- Nitrogen
200X
.5v
Potential vs. DHE
1.0v

Fig. 124

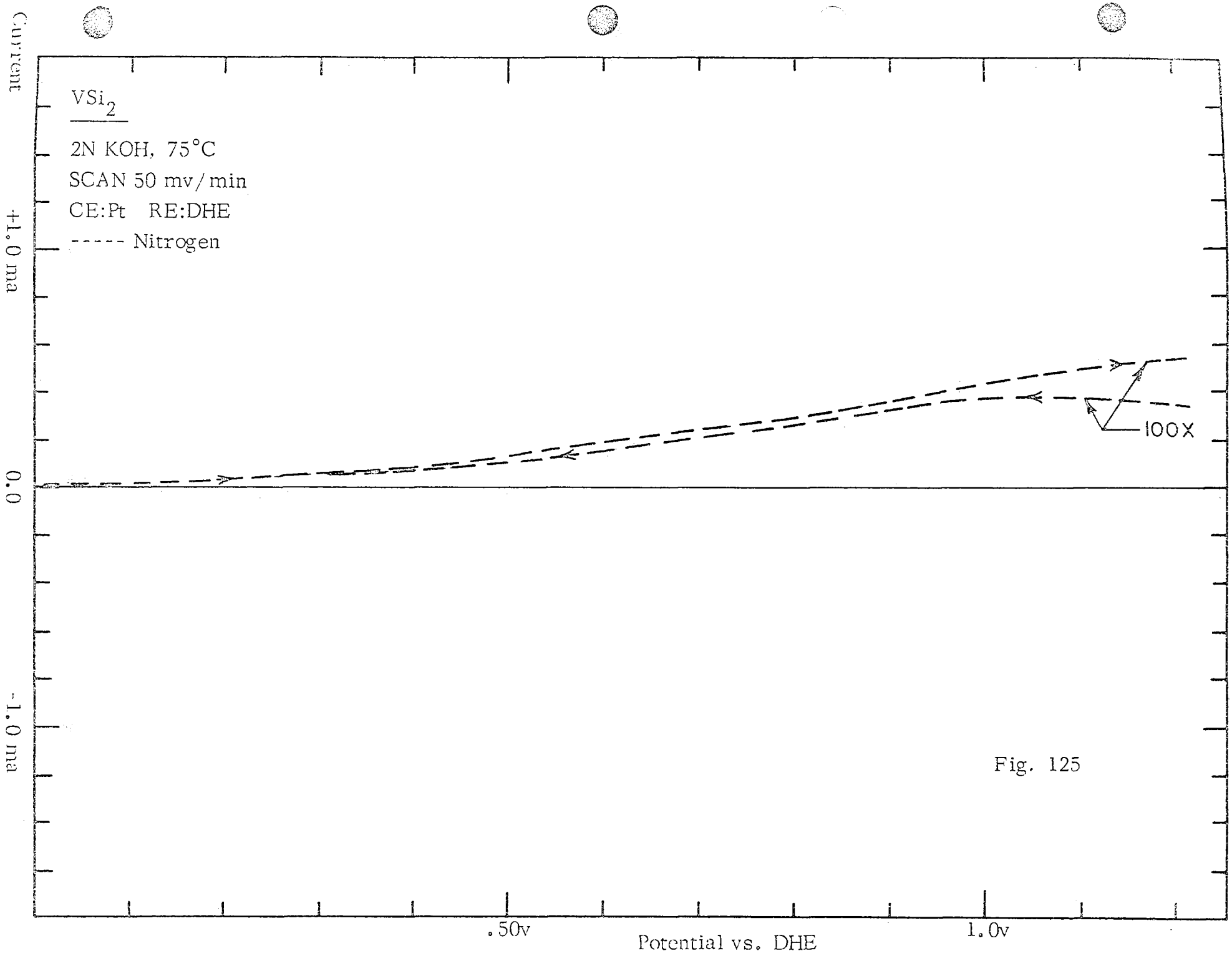
Current
+1.0 ma
0.0
-1.0 ma
VSi_2
2N KOH, 75°C
SCAN 50 mv/min
CE:Pt RE:DHE
----- Nitrogen
100X
.50v
1.0v
Potential vs. DHE

Fig. 125

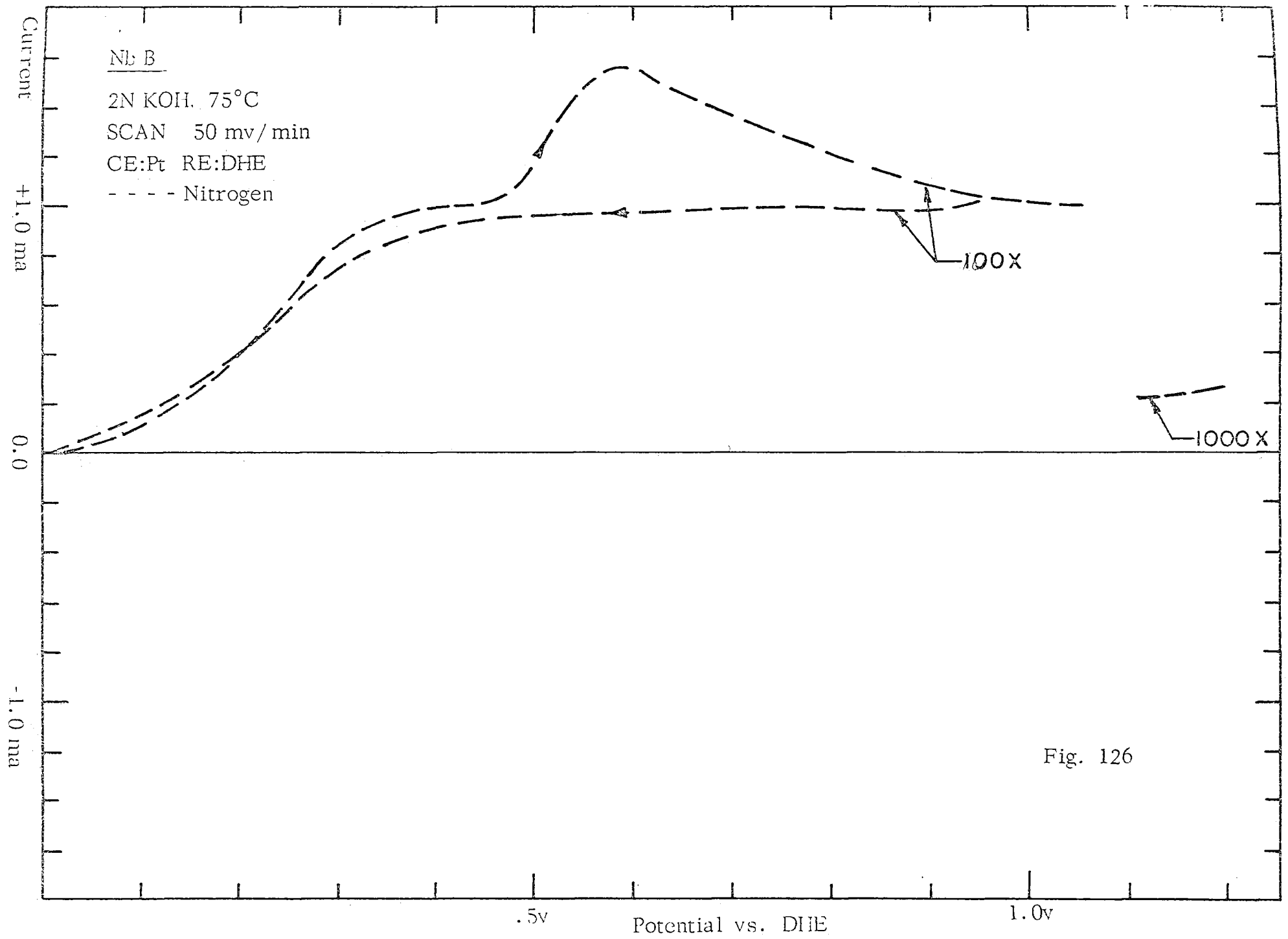
Nb B
2N KOH. 75°C
SCAN 50 mv/min
CE:Pt RE:DHE
- - - - Nitrogen
100X
1000X
Current
+1.0 ma
0.0
-1.0 ma
.5v
1.0v
Potential vs. DHE

Fig. 126

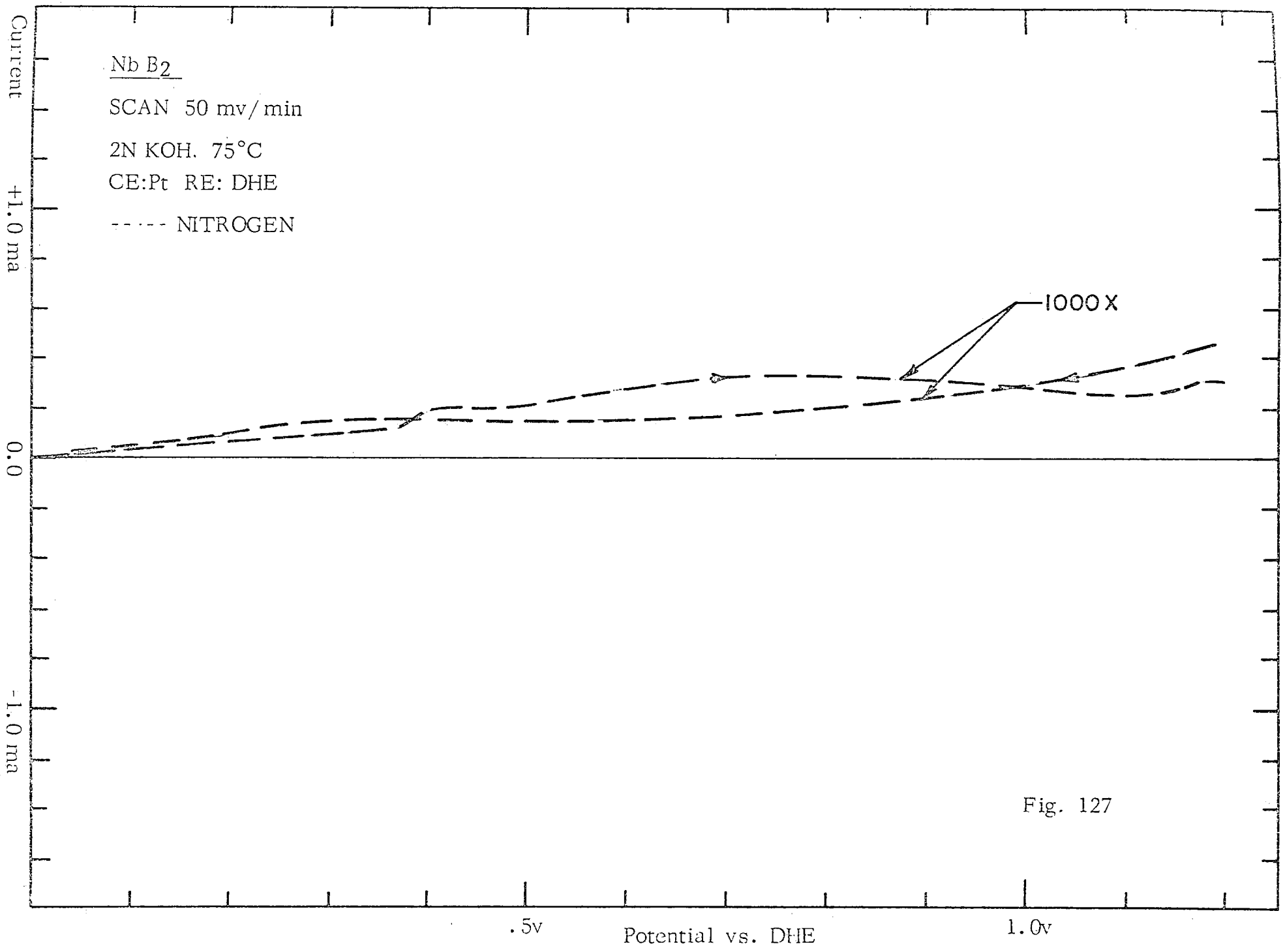
Nb B_2
SCAN 50 mv/min
2N KOH. 75°C
CE:Pt RE: DHE
----- NITROGEN
1000 X
Current
+1.0 ma
0.0
-1.0 ma
.5v
Potential vs. DHE
1.0v

Fig. 127

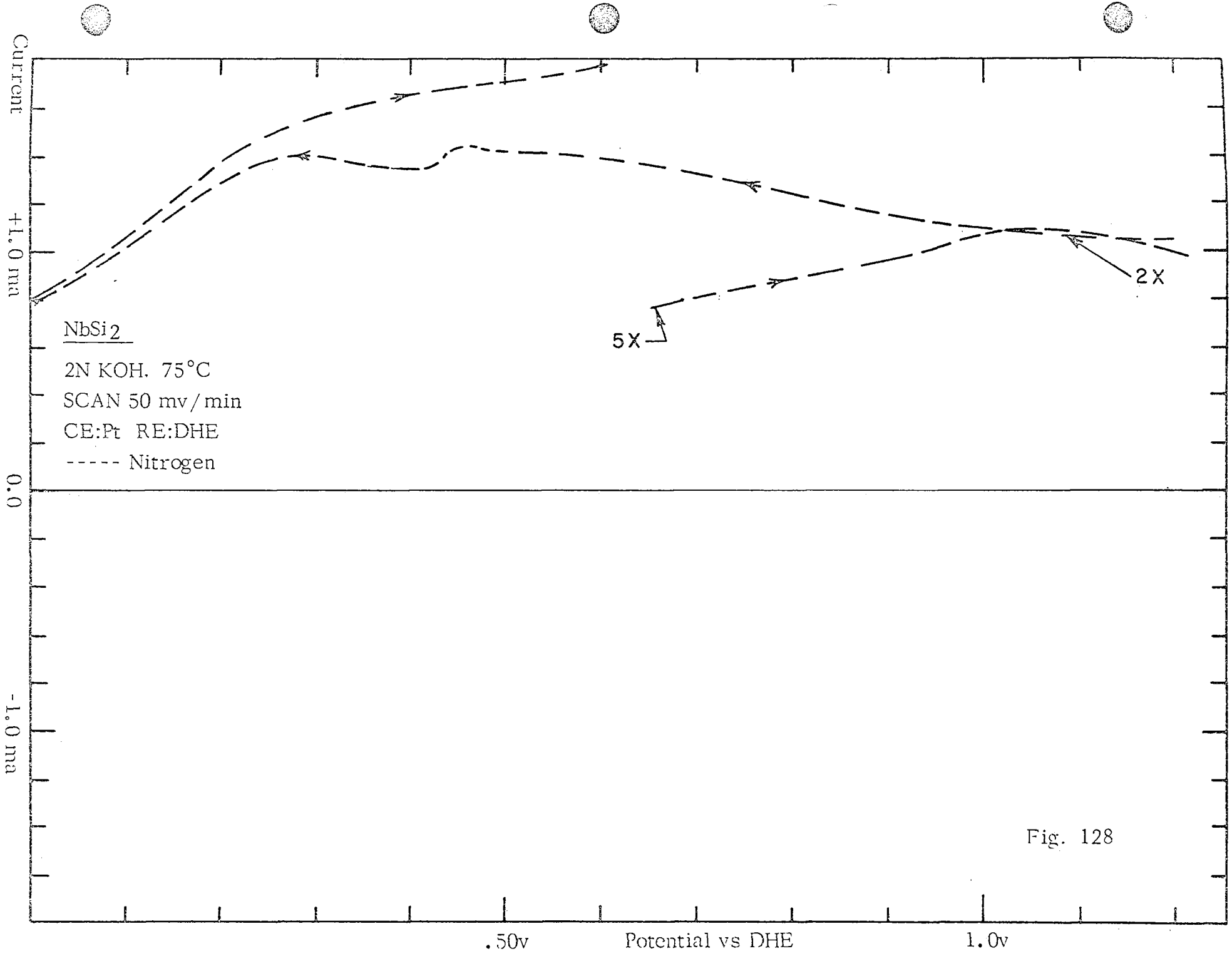
Current
+1.0 ma
0.0
-1.0 ma
NbSi2
2N KOH. 75°C
SCAN 50 mv/min
CE:Pt RE:DHE
----- Nitrogen
5X
2X
.50v
Potential vs DHE
1.0v

Fig. 128

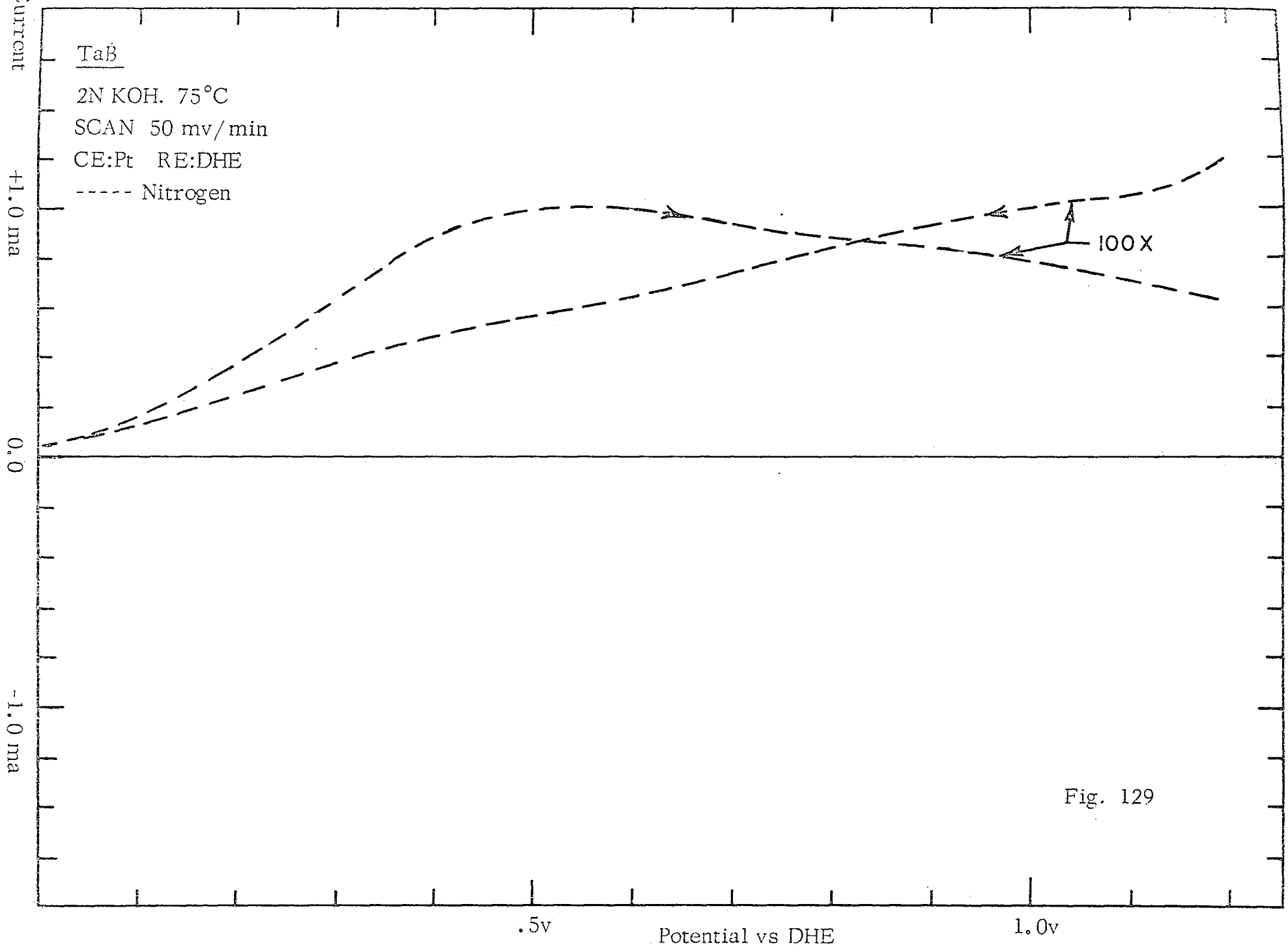
TaB
2N KOH. 75°C
SCAN 50 mv/min
CE:Pt RE:DHE
----- Nitrogen
100 X
Current
+1.0 ma
0.0
-1.0 ma
.5v
Potential vs DHE
1.0v

Fig. 129

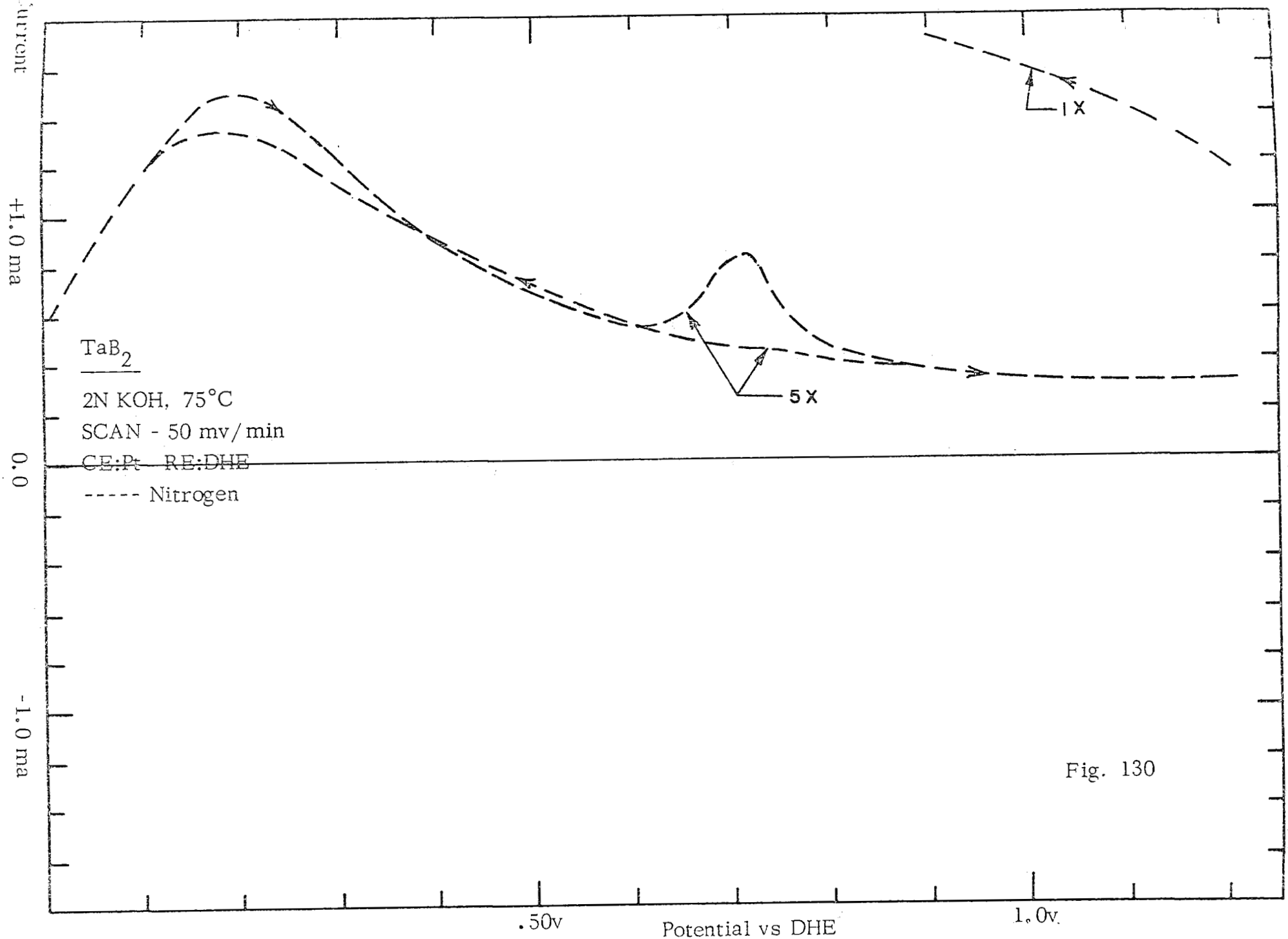
Current
+1.0 ma
0.0
-1.0 ma
1X
5X
TaB_2
2N KOH, 75°C
SCAN - 50 mv/min
CE:Pt RE:DHE
----- Nitrogen
.50v
Potential vs DHE
1.0v

Fig. 130

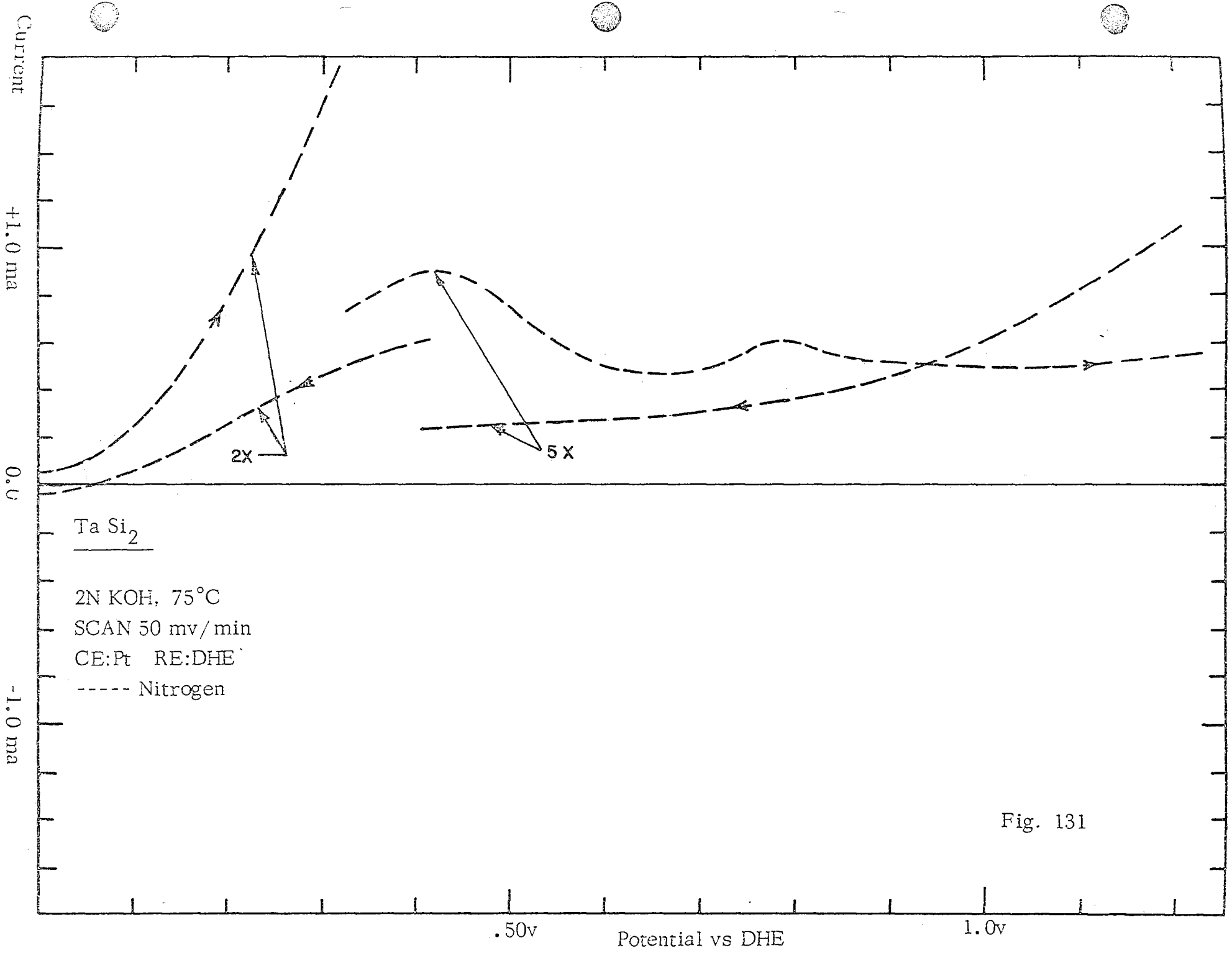

$Ta\ Si_2$

2N KOH, 75°C
SCAN 50 mv/min
CE:Pt RE:DHE
----- Nitrogen

Fig. 131

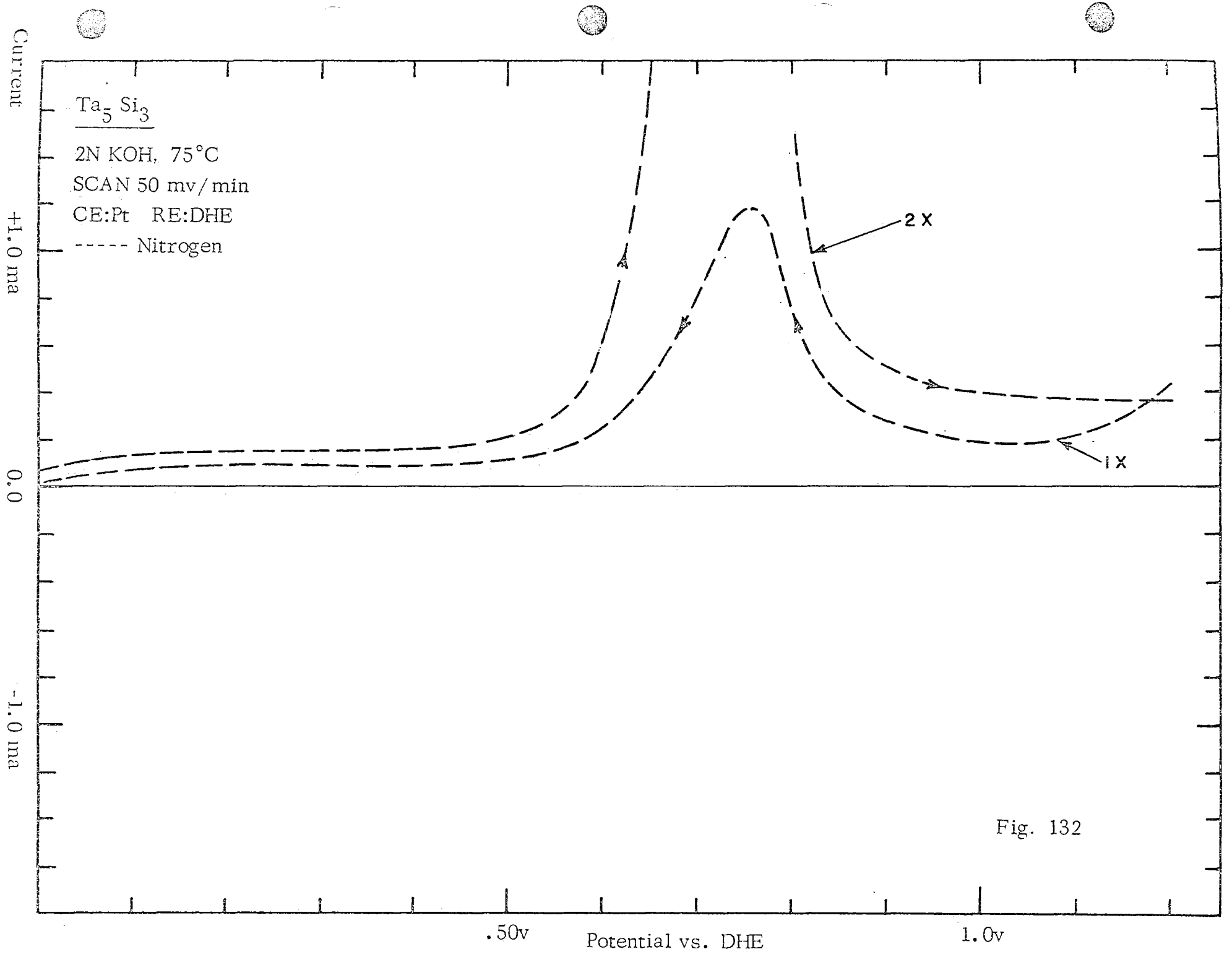
Current
+1.0 ma
0.0
-1.0 ma
$Ta_5 Si_3$
2N KOH, 75°C
SCAN 50 mv/min
CE:Pt RE:DHE
----- Nitrogen
2 X
1 X
.50v
Potential vs. DHE
1.0v

Fig. 132

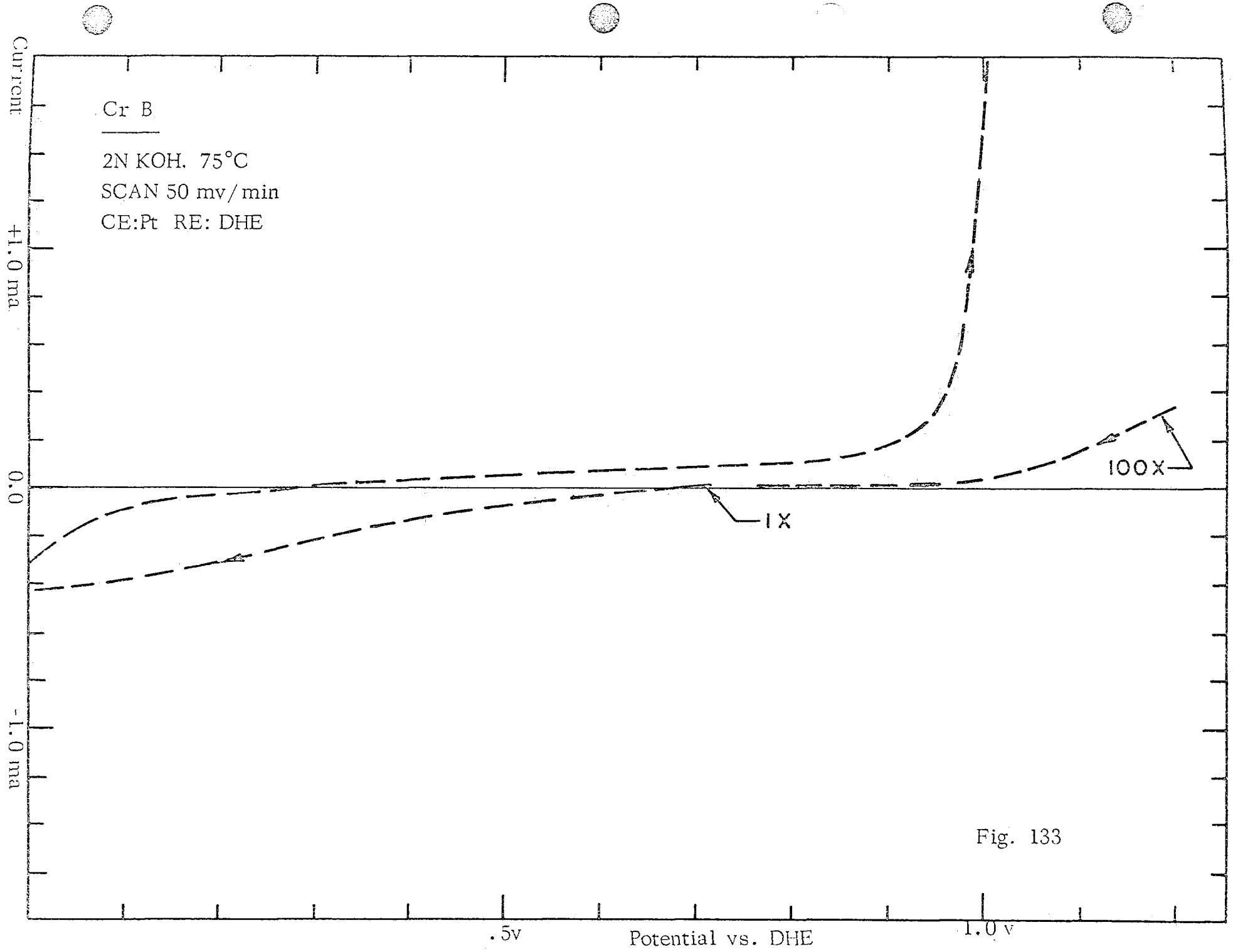
Cr B
2N KOH. 75°C
SCAN 50 mv/min
CE:Pt RE: DHE
Current
+1.0 ma
0.0
-1.0 ma
100X
1X
.5v
Potential vs. DHE
1.0 v

Fig. 133

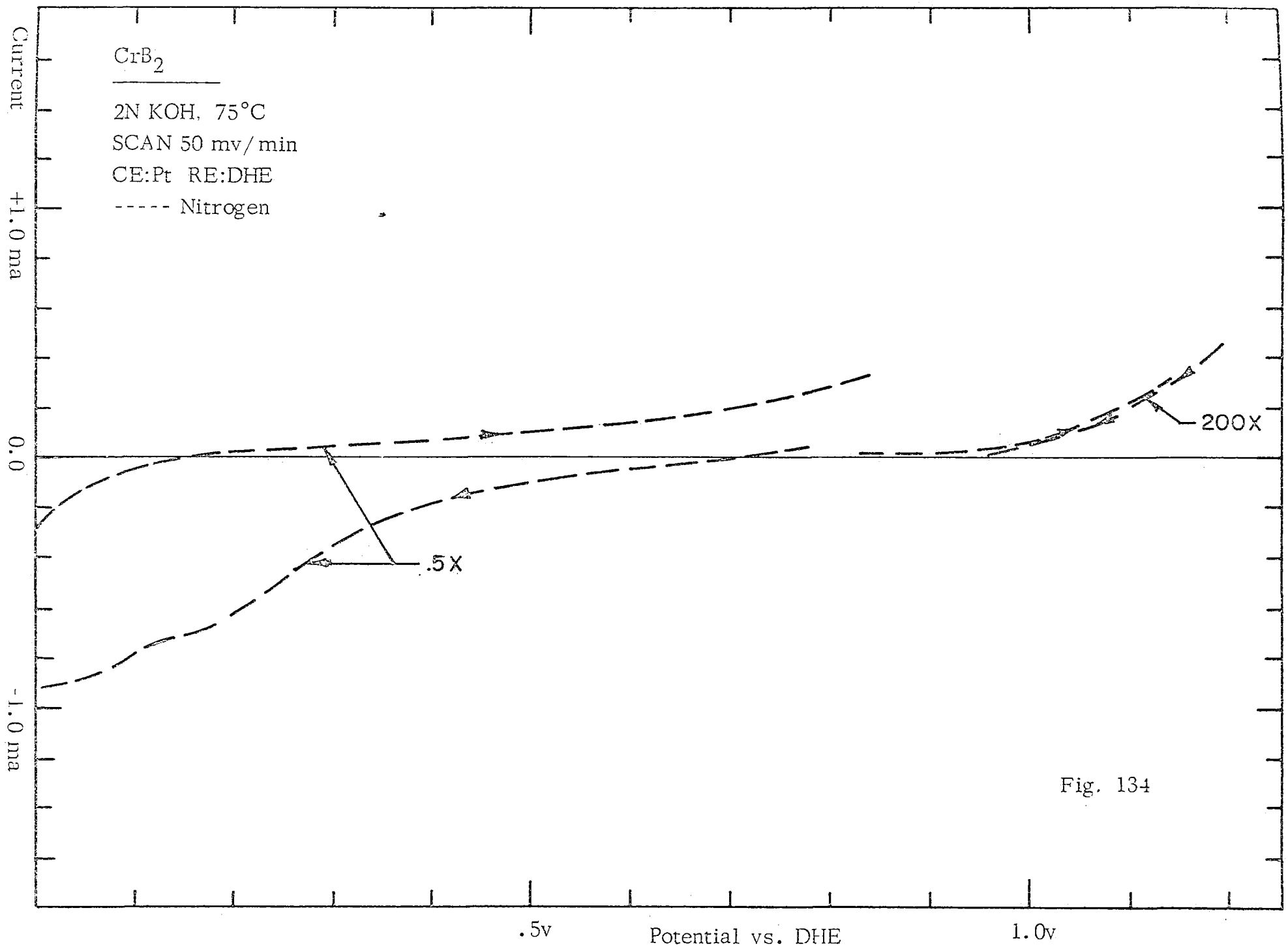
CrB_2
2N KOH, 75°C
SCAN 50 mv/min
CE:Pt RE:DHE
----- Nitrogen
Current
+1.0 ma
0.0
-1.0 ma
200X
.5X
.5v
Potential vs. DHE
1.0v

Fig. 134

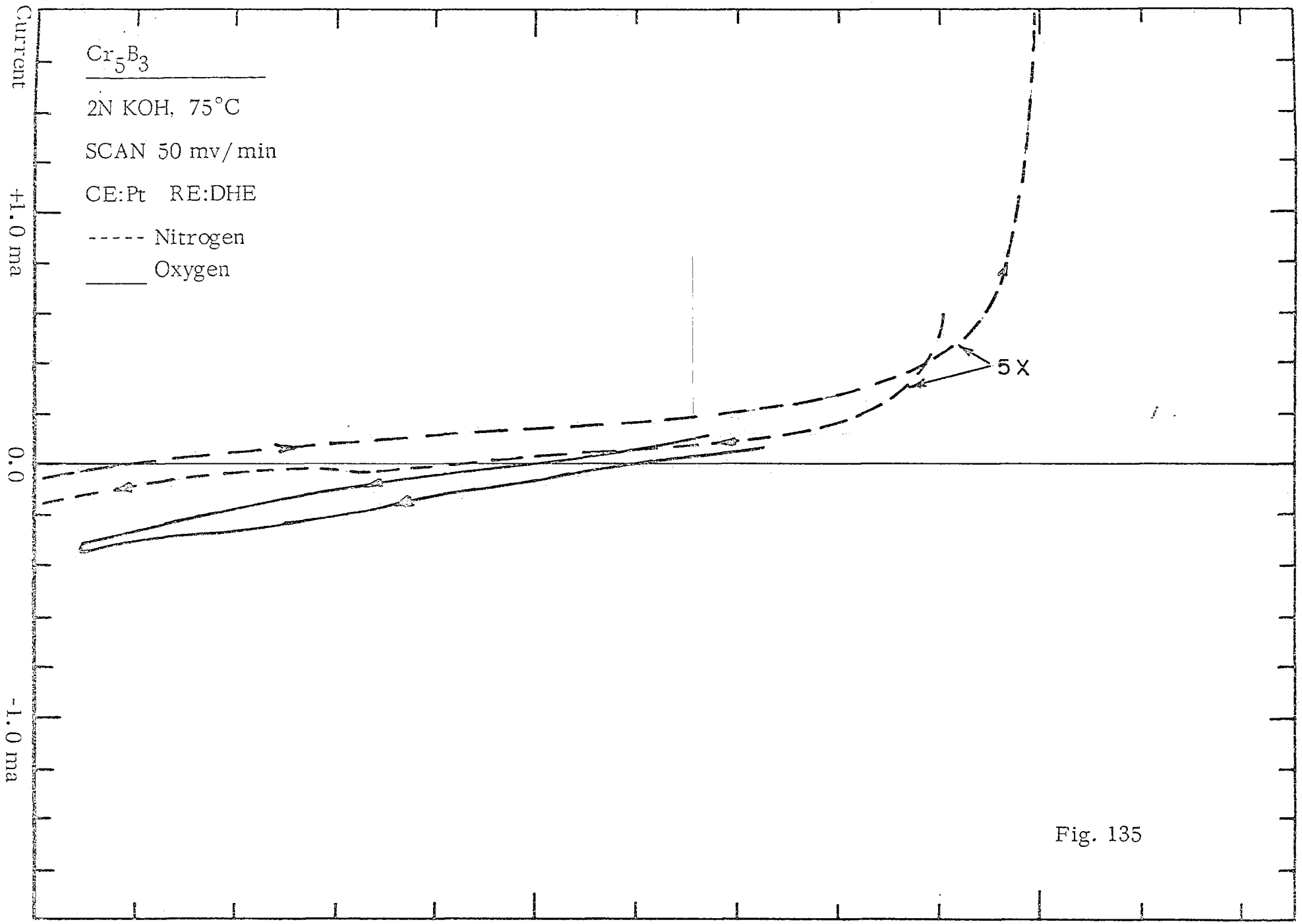
Cr_5B_3
2N KOH, 75°C
SCAN 50 mv/min
CE:Pt RE:DHE
----- Nitrogen
_____ Oxygen
5X
Current
+1.0 ma
0.0
-1.0 ma
.50v
Potential vs DHE
1.0v

Fig. 135

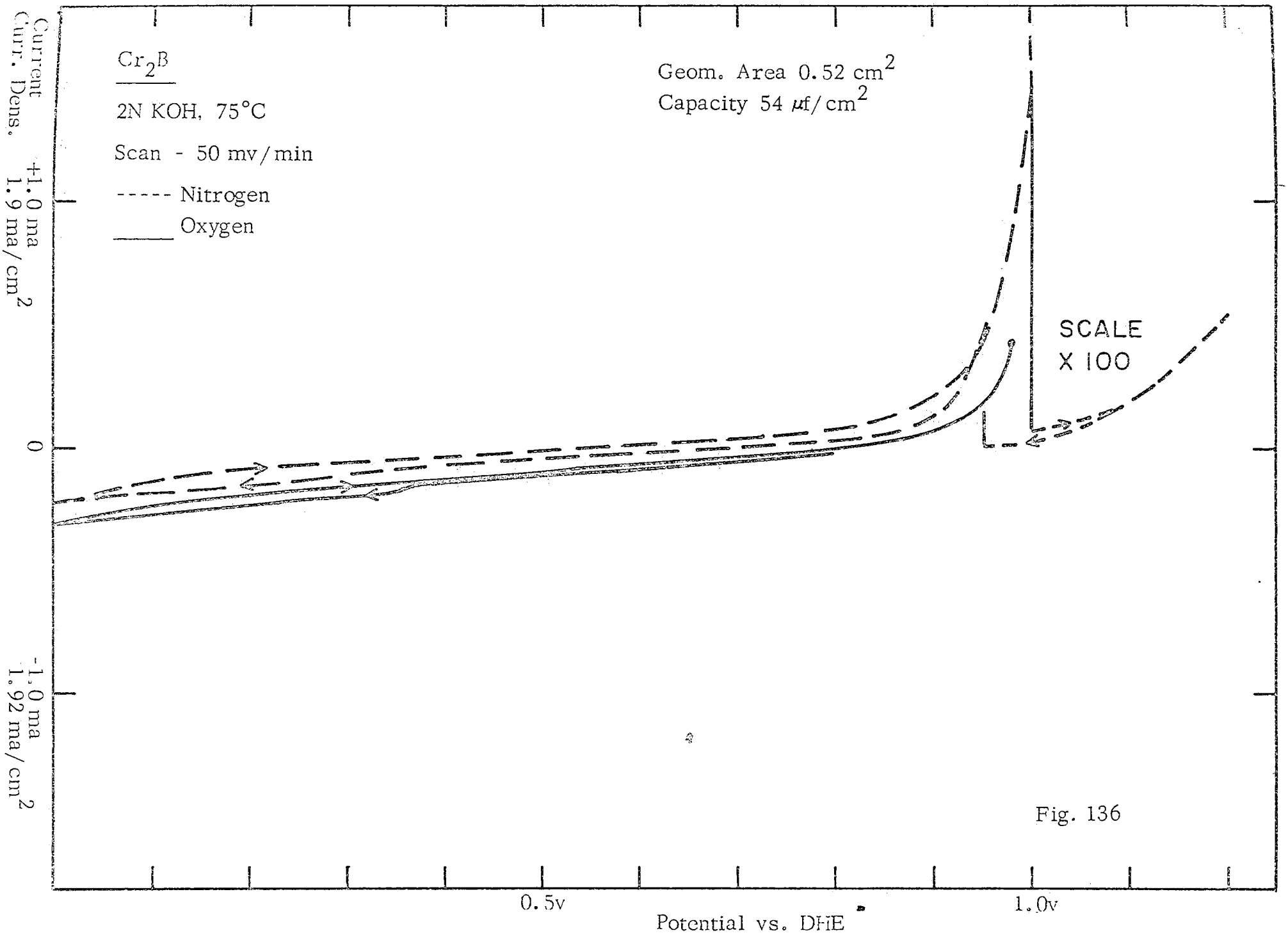
Cr2B
2N KOH, 75°C
Scan - 50 mv/min
----- Nitrogen
_____ Oxygen
Geom. Area 0.52 cm2
Capacity 54 μf/cm2
SCALE
X 100
Current
Curr. Dens.
+1.0 ma
1.9 ma/cm2
0
-1.0 ma
1.92 ma/cm2
0.5v
1.0v
Potential vs. DHE

Fig. 136

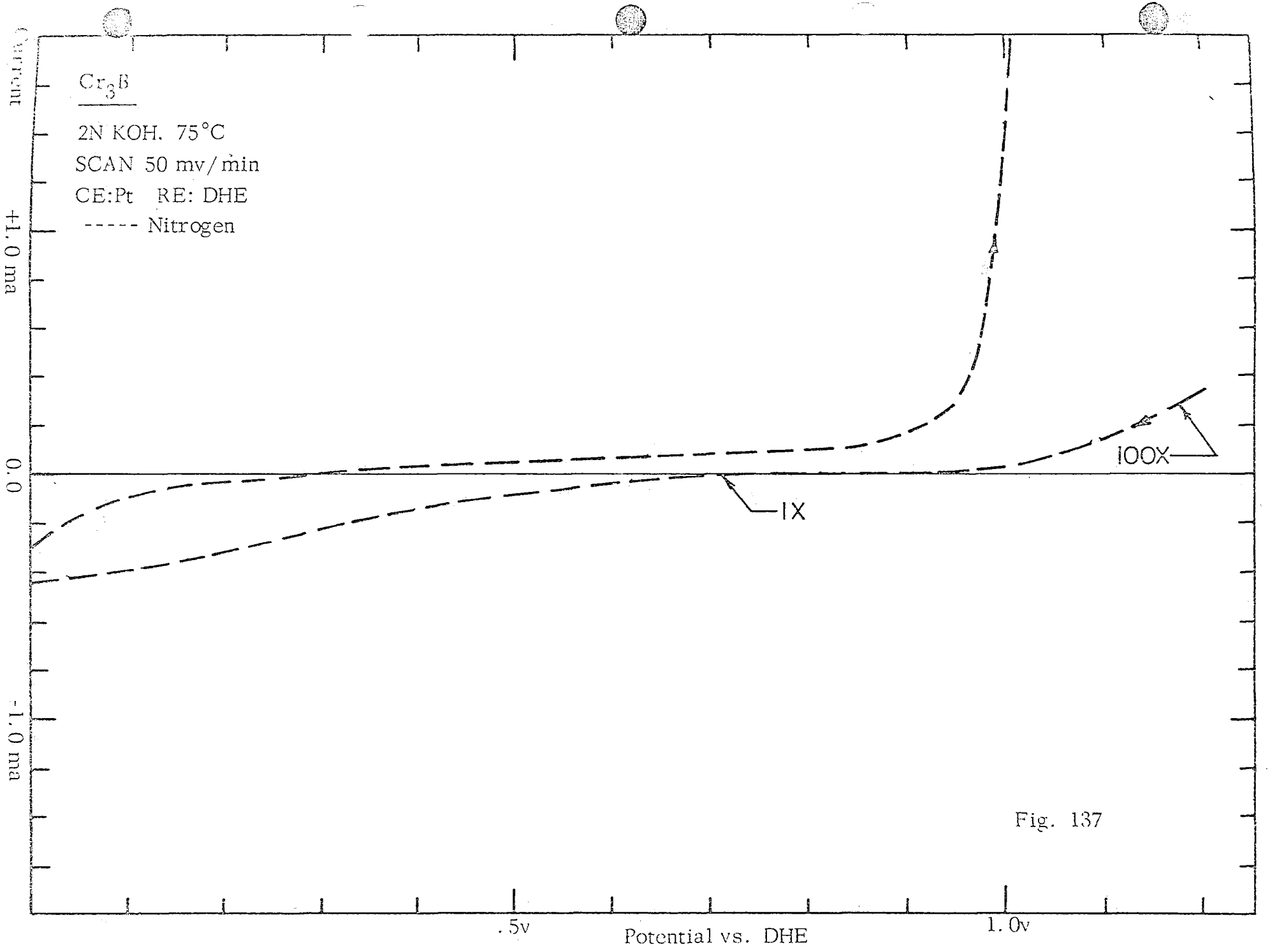
Cr_3B
2N KOH. 75°C
SCAN 50 mv/min
CE:Pt RE: DHE
----- Nitrogen
Current
+1.0 ma
0.0
-1.0 ma
100X
1X
.5v
1.0v
Potential vs. DHE

Fig. 137

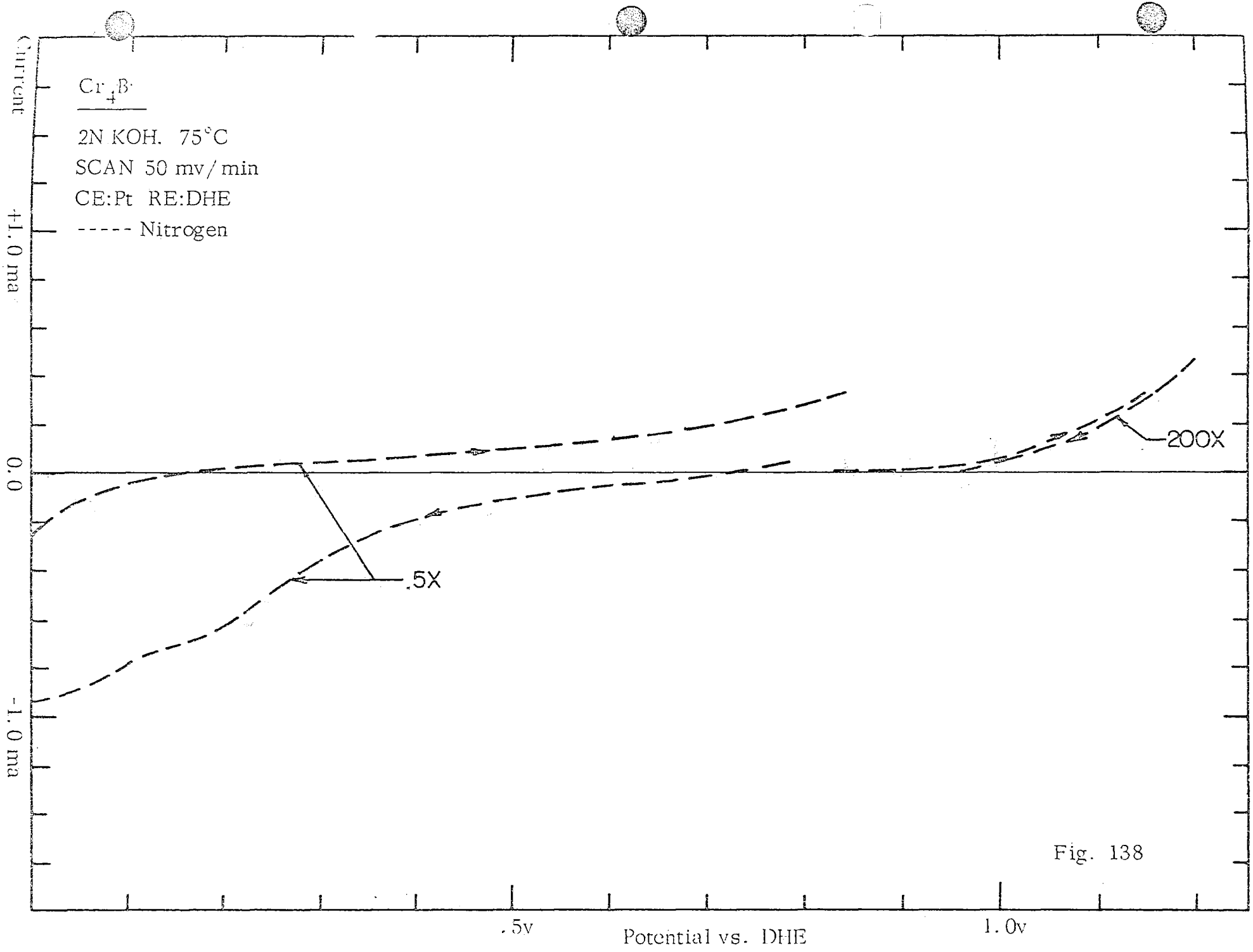
Current
+1.0 ma
0.0
-1.0 ma
$Cr_{+}B$
2N KOH. 75°C
SCAN 50 mv/min
CE:Pt RE:DHE
----- Nitrogen
200X
.5X
.5v
Potential vs. DHE
1.0v

Fig. 138

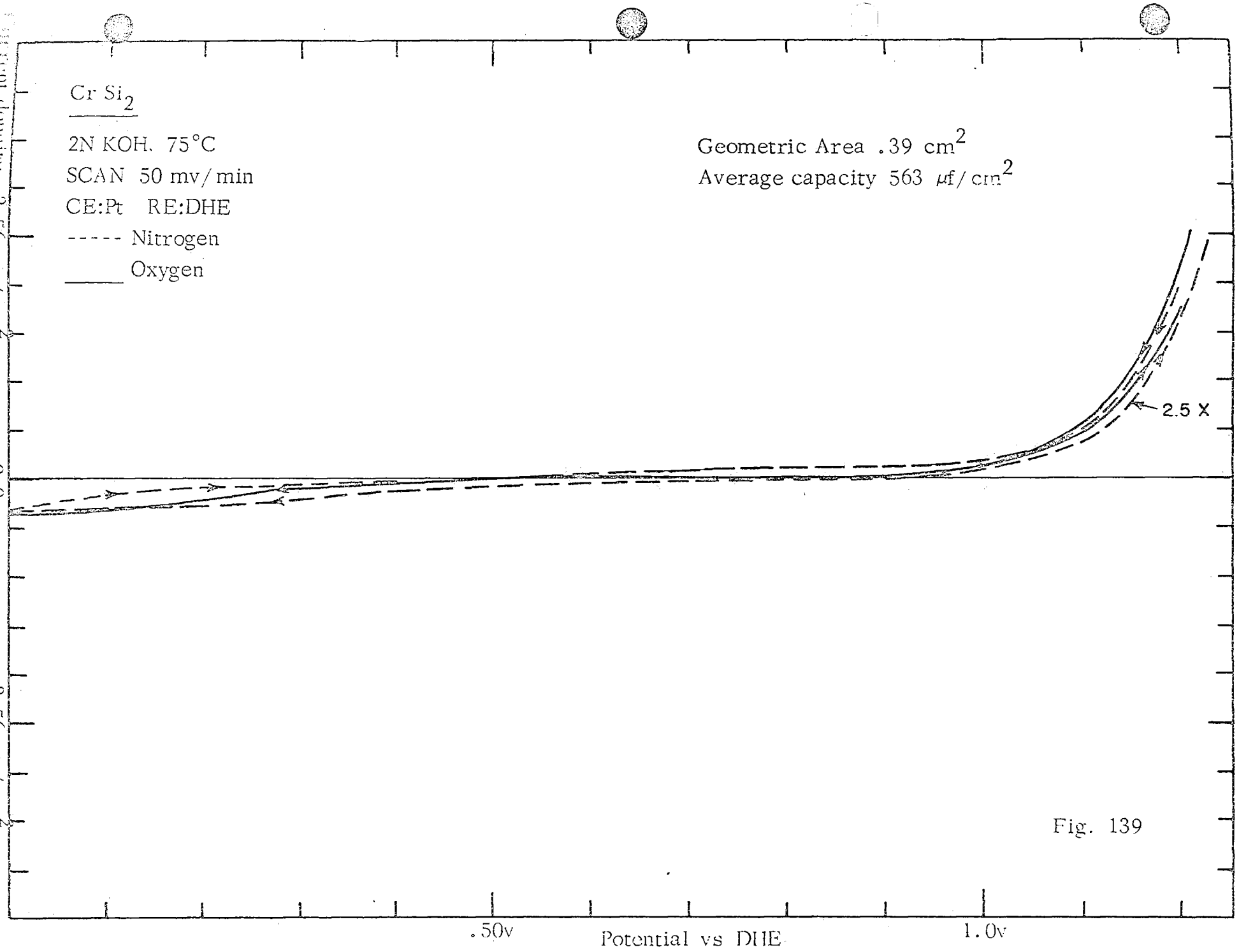
Cr Si_2
2N KOH. 75°C
SCAN 50 mv/min
CE:Pt RE:DHE
----- Nitrogen
_____ Oxygen
Geometric Area .39 cm^2
Average capacity 563 $\mu f/cm^2$
2.5 X
Current density
+2.56 ma/cm^2
+1.0 ma
0.0
0.0
-2.56 ma/cm^2
-1.0 ma
.50v
Potential vs DHE
1.0v

Fig. 139

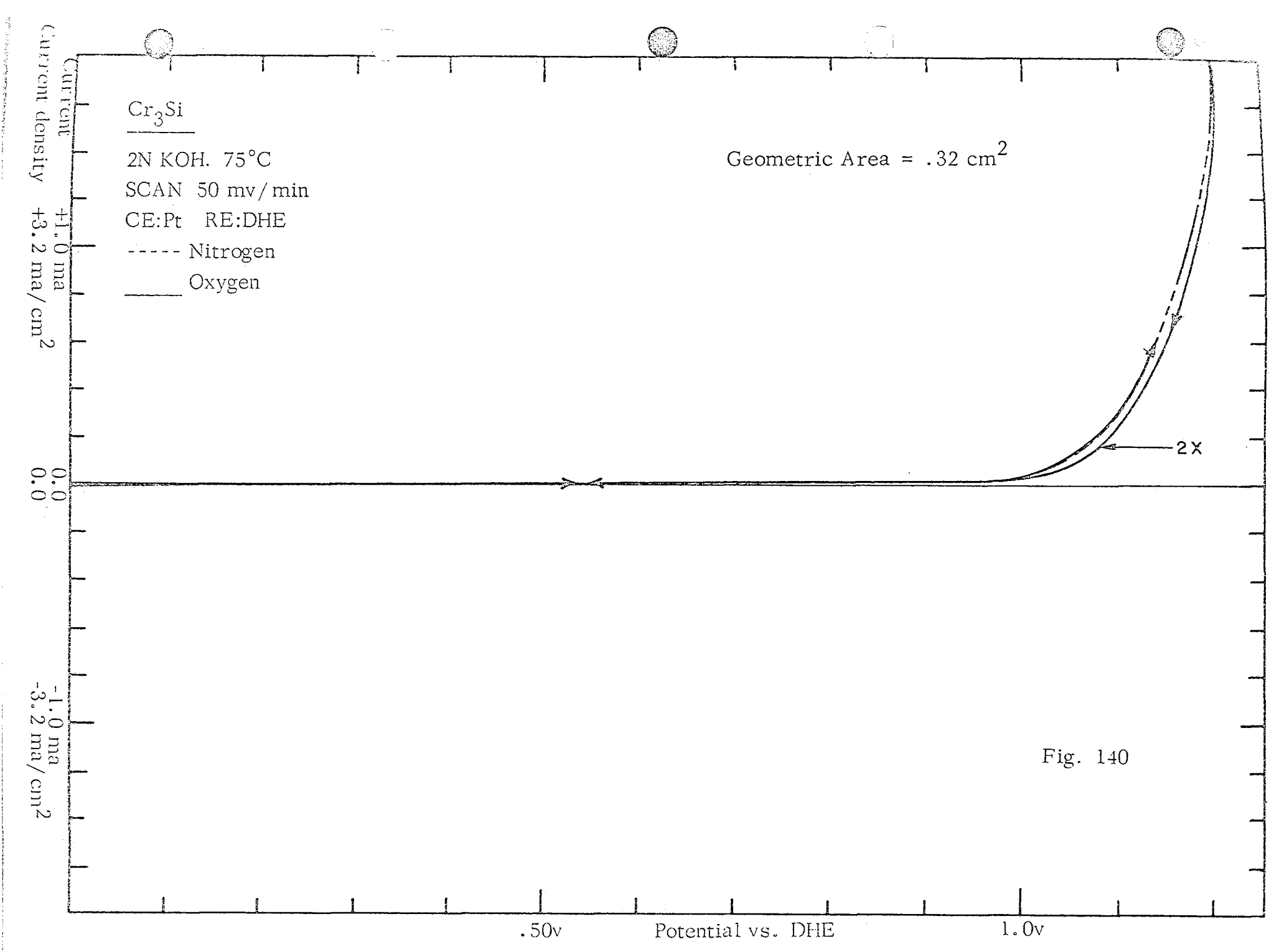
Current density
+1.0 ma
+3.2 ma/cm2
0.0
0.0
-1.0 ma
-3.2 ma/cm2
Cr3Si
2N KOH. 75°C
SCAN 50 mv/min
CE:Pt RE:DHE
----- Nitrogen
_____ Oxygen
Geometric Area = .32 cm2
2X
.50v
Potential vs. DHE
1.0v

Fig. 140

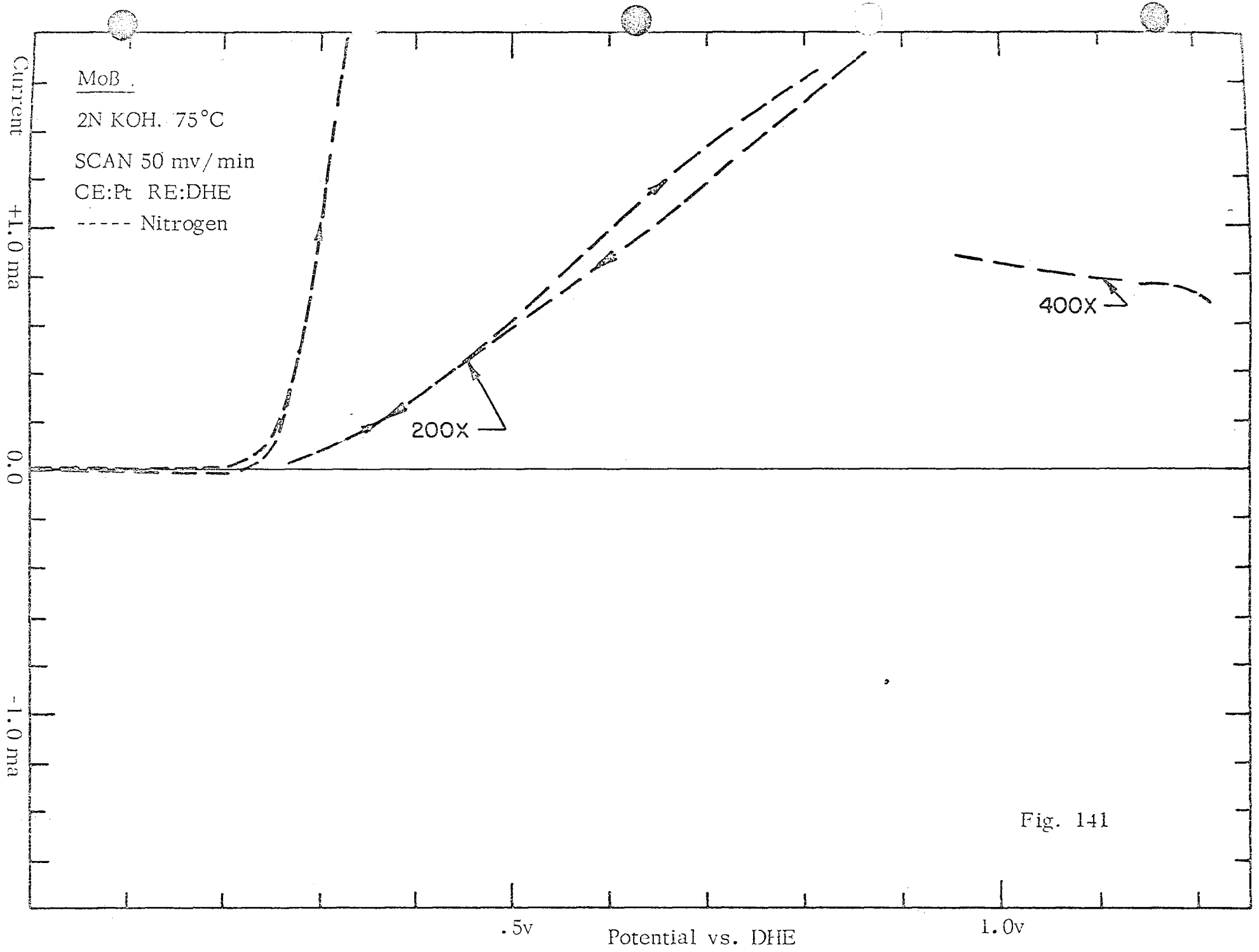
Moß .
2N KOH. 75°C
SCAN 50 mv/min
CE:Pt RE:DHE
----- Nitrogen
Current
+1.0 ma
0.0
-1.0 ma
200X
400X
.5v
1.0v
Potential vs. DHE

Fig. 141

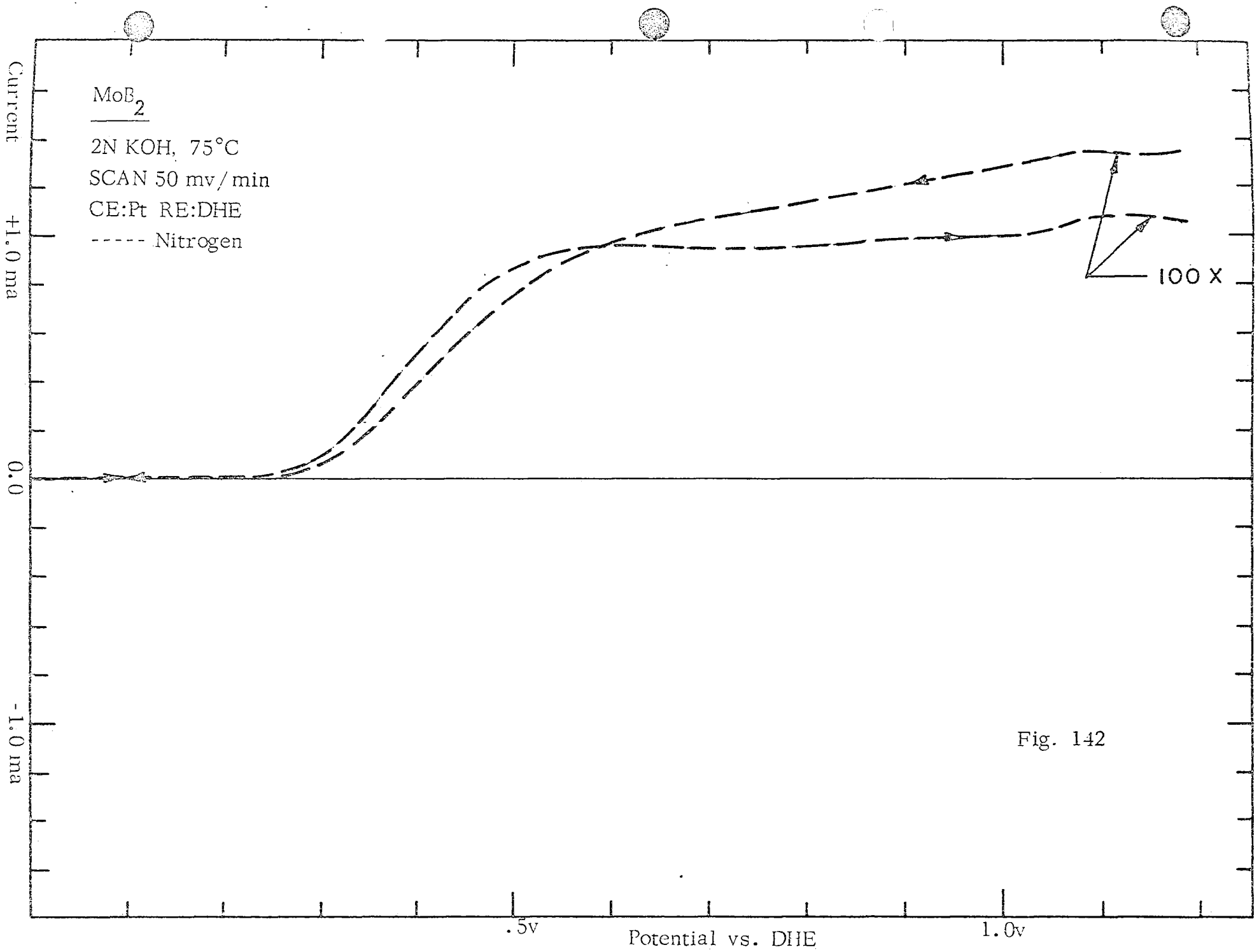
MoB_2
2N KOH, 75°C
SCAN 50 mv/min
CE:Pt RE:DHE
----- Nitrogen
100 X
Current
+1.0 ma
0.0
-1.0 ma
.5v
Potential vs. DHE
1.0v

Fig. 142

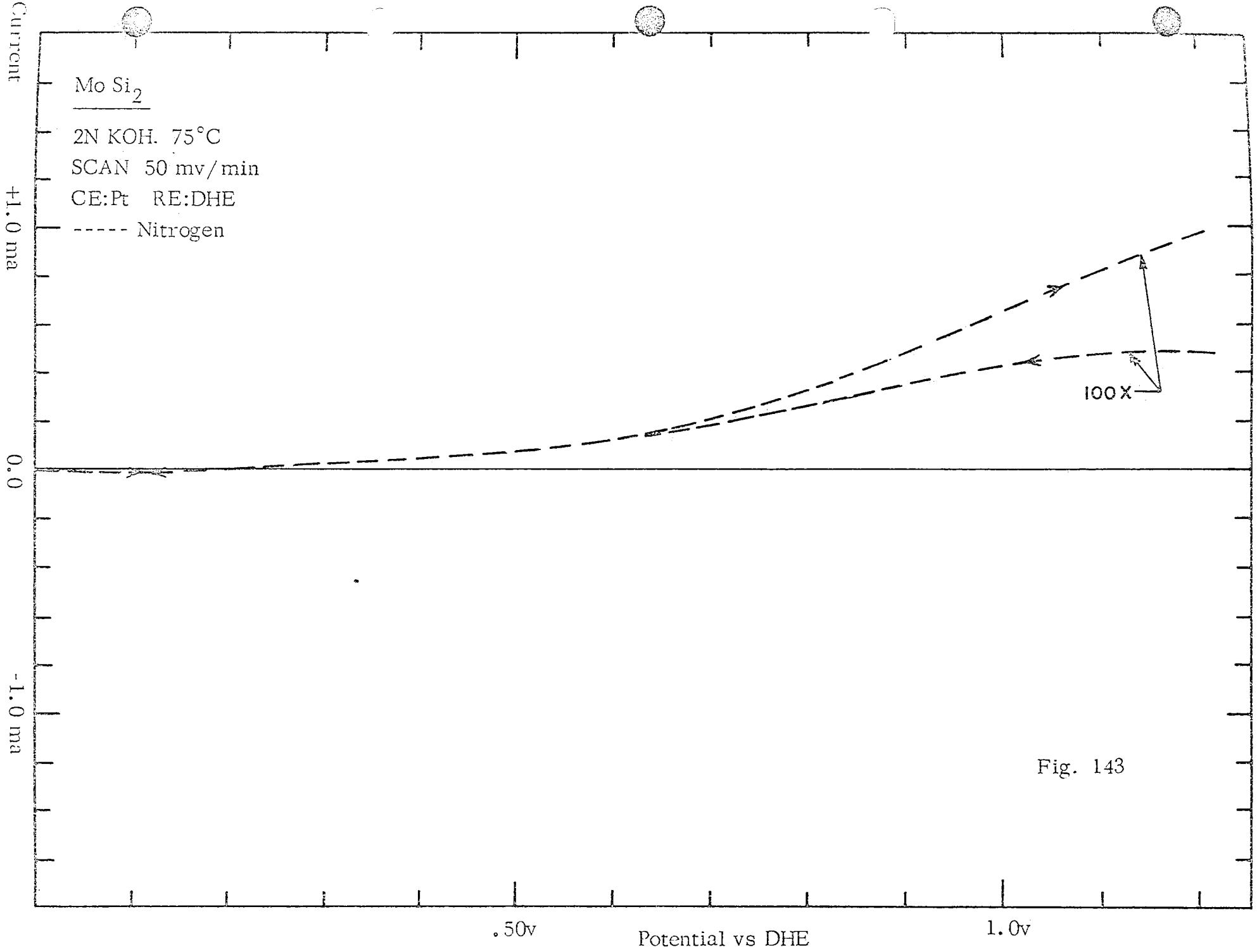
Current
Mo Si2
2N KOH. 75°C
SCAN 50 mv/min
CE:Pt RE:DHE
----- Nitrogen
+1.0 ma
0.0
-1.0 ma
100 X
.50v
Potential vs DHE
1.0v

Fig. 143

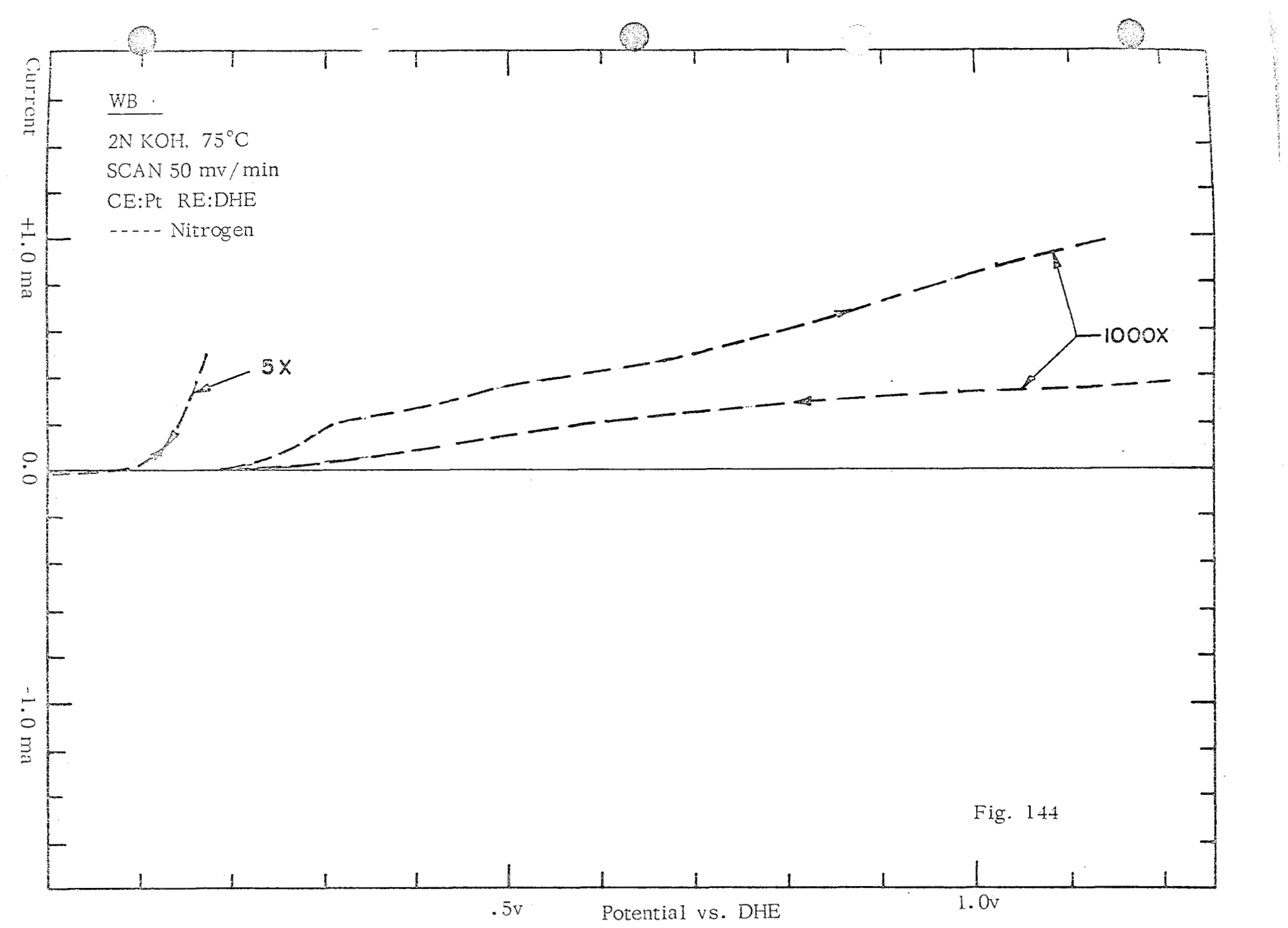
WB
2N KOH, 75°C
SCAN 50 mv/min
CE:Pt RE:DHE
----- Nitrogen
5X
1000X
Current
+1.0 ma
0.0
-1.0 ma
.5v
Potential vs. DHE
1.0v

Fig. 144

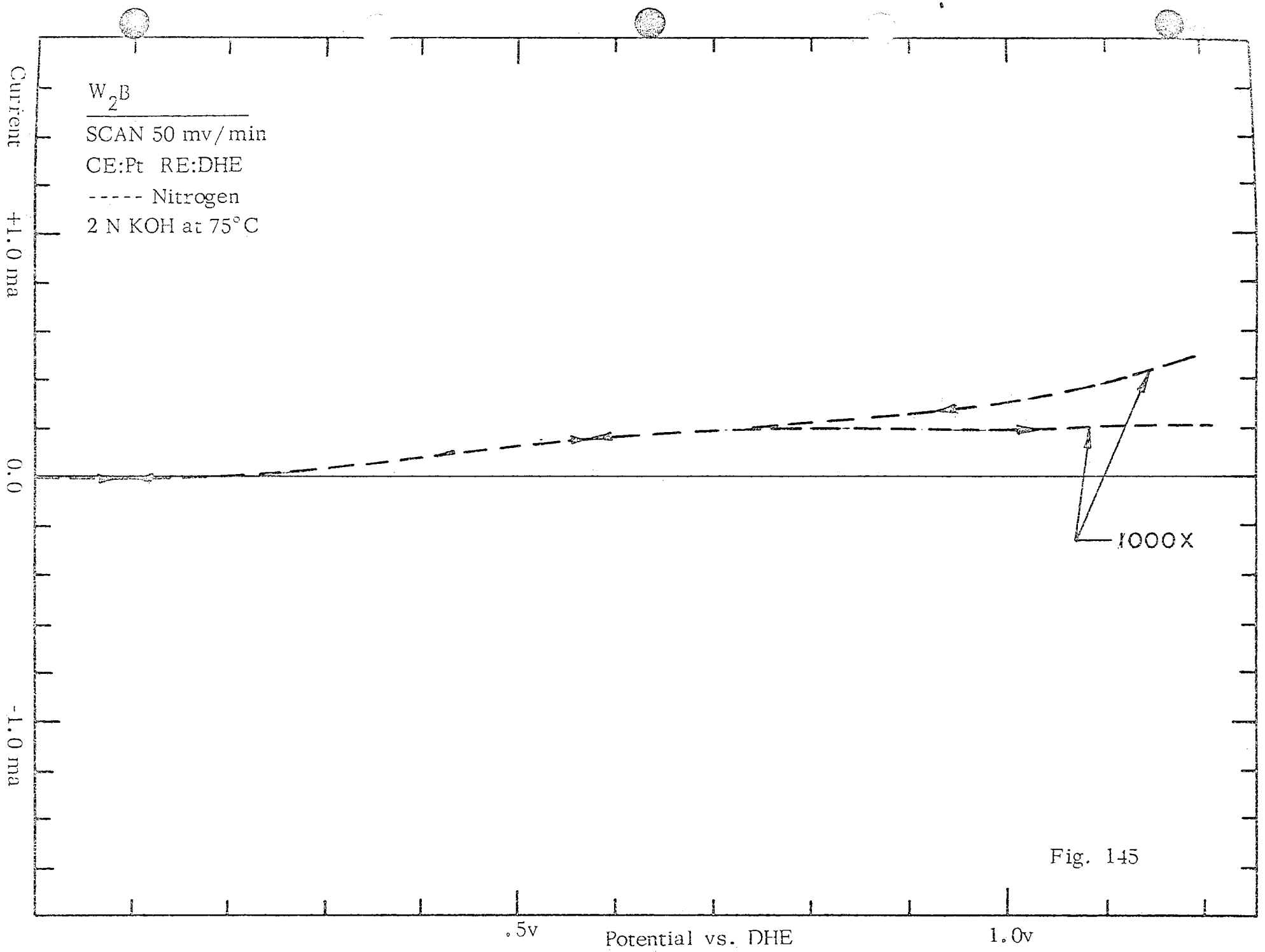
W_2B
SCAN 50 mv/min
CE:Pt RE:DHE
----- Nitrogen
2 N KOH at 75°C
Current
+1.0 ma
0.0
-1.0 ma
1000X
.5v
Potential vs. DHE
1.0v

Fig. 145

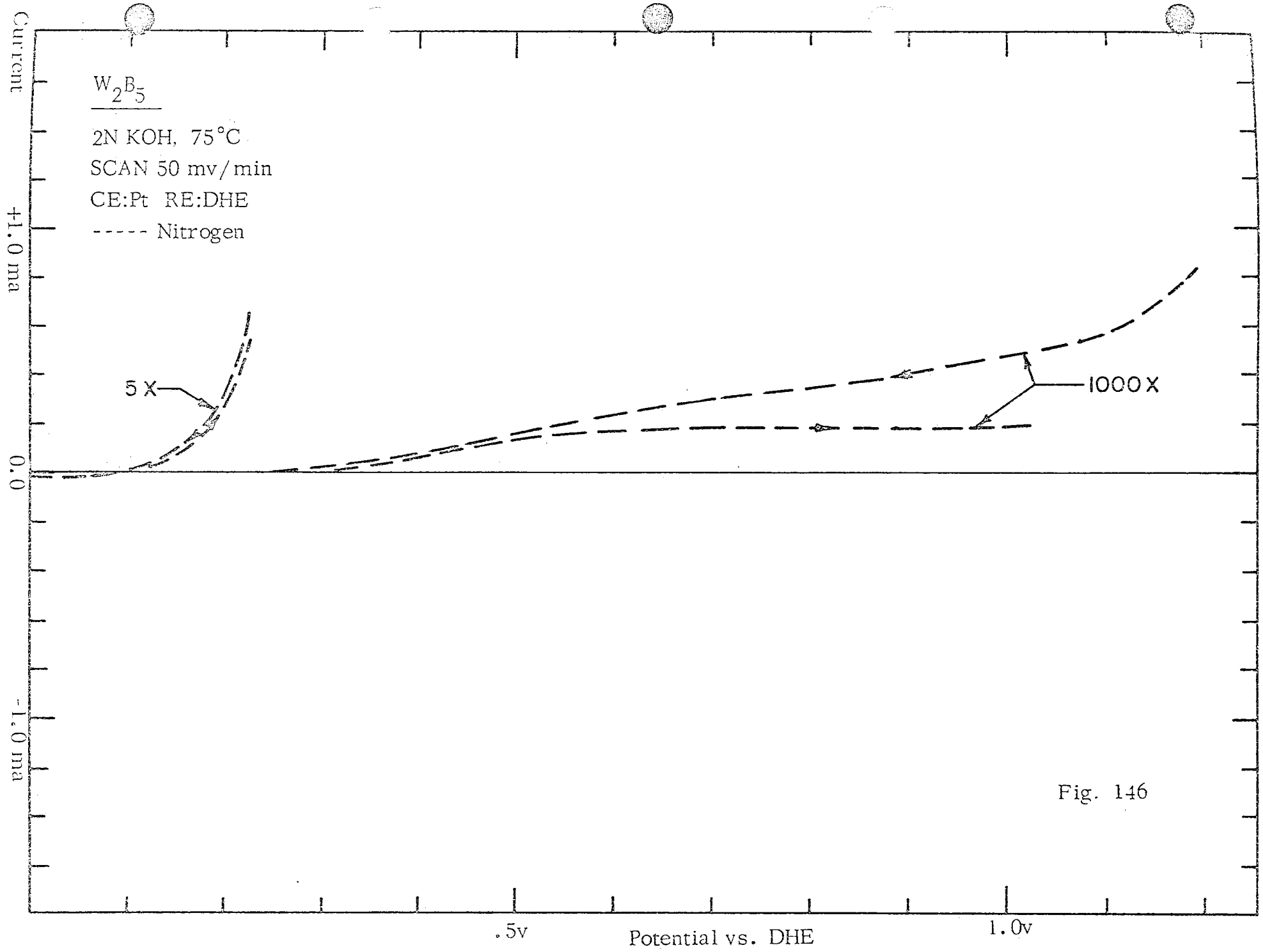
Current
+1.0 ma
0.0
-1.0 ma
W_2B_5
2N KOH, 75°C
SCAN 50 mv/min
CE:Pt RE:DHE
----- Nitrogen
5 X
1000 X
.5v
Potential vs. DHE
1.0v

Fig. 146

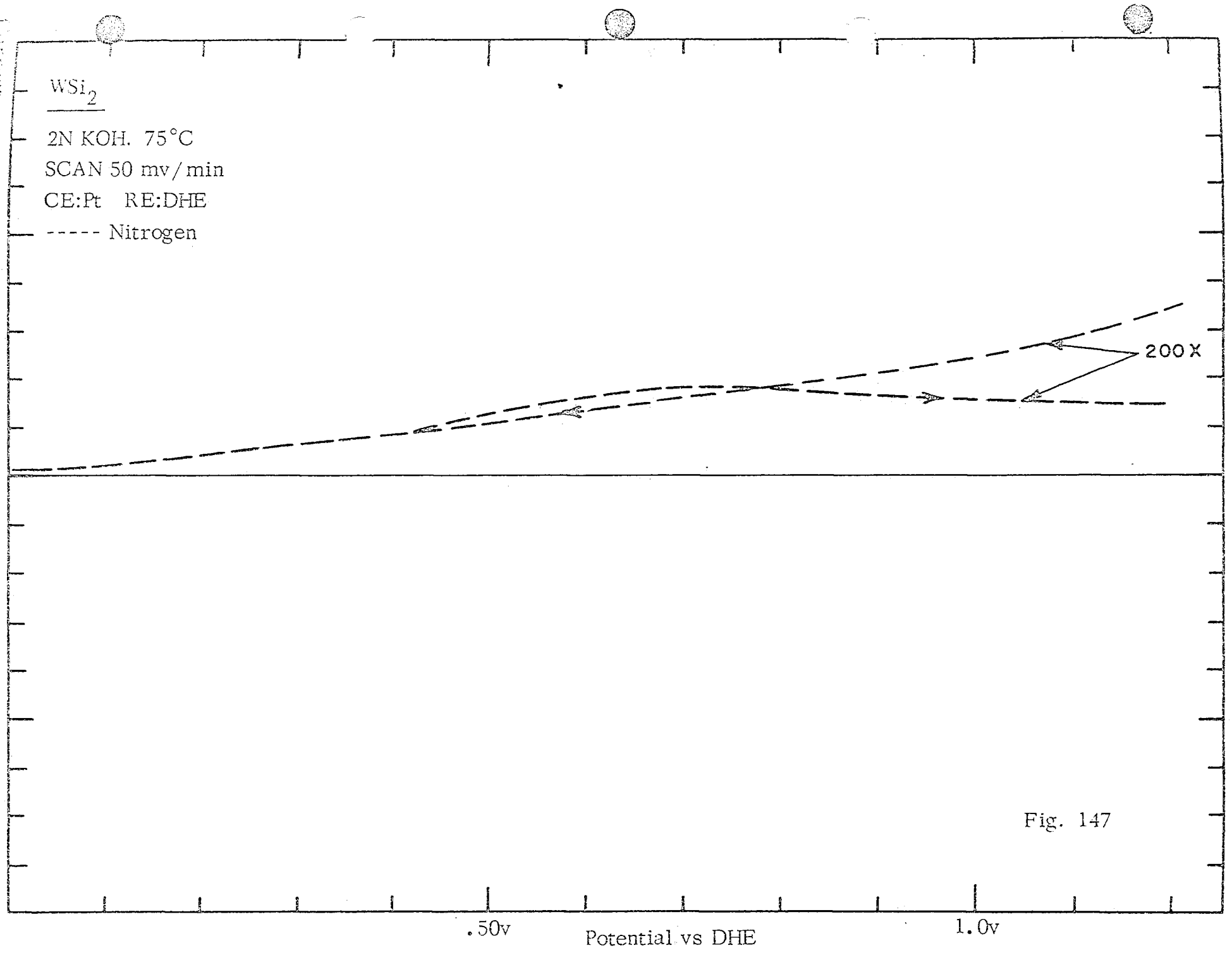
WSi_2
2N KOH. 75°C
SCAN 50 mv/min
CE:Pt RE:DHE
----- Nitrogen
200X
+1.0 ma
0.0
-1.0 ma
.50v
Potential vs DHE
1.0v

Fig. 147

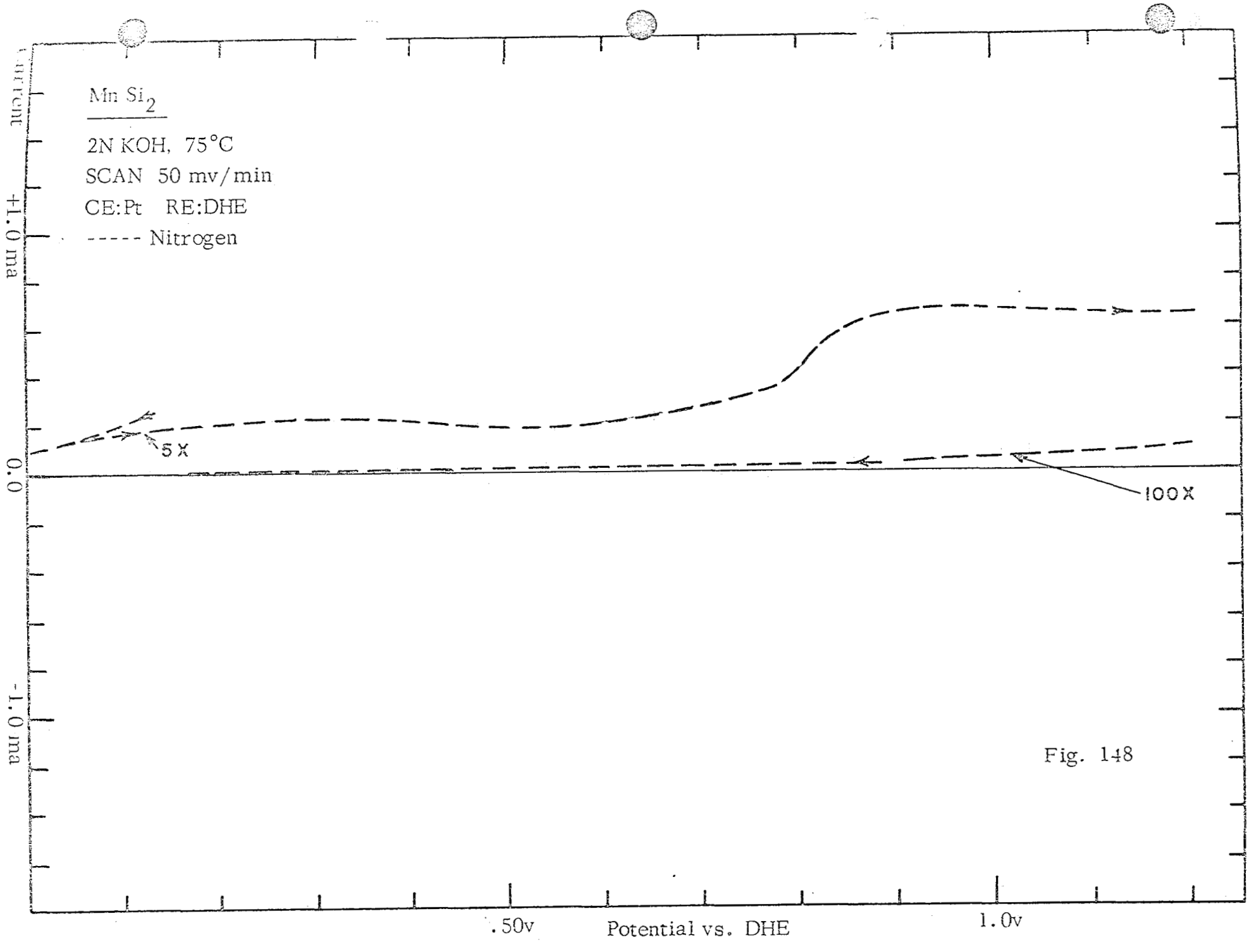
Mn Si_2
2N KOH, 75°C
SCAN 50 mv/min
CE:Pt RE:DHE
----- Nitrogen
Current
+1.0 ma
0.0
-1.0 ma
5X
100X
.50v
Potential vs. DHE
1.0v

Fig. 148

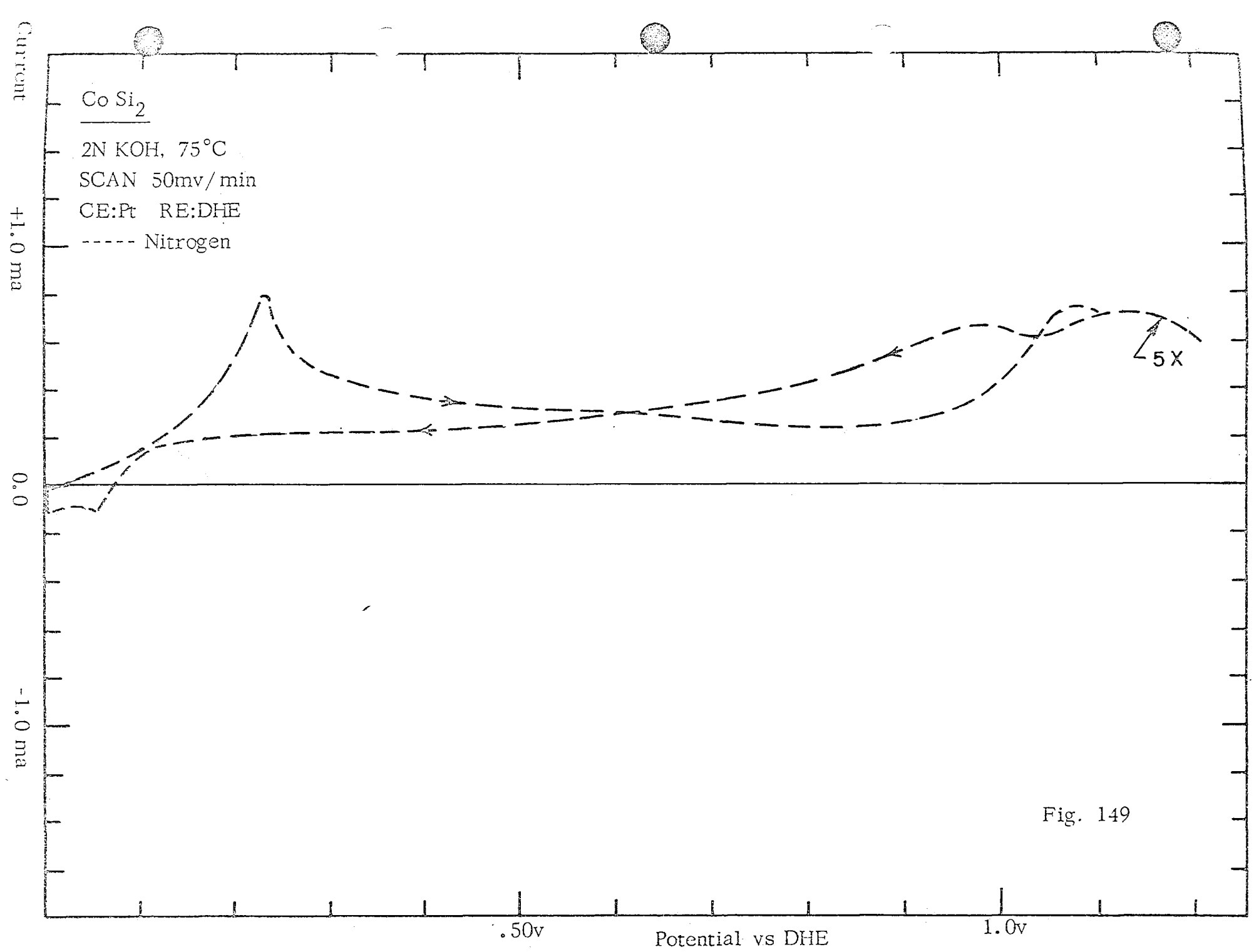
Current
+1.0 ma
0.0
-1.0 ma
Co Si_2
2N KOH, 75°C
SCAN 50mv/min
CE:Pt RE:DHE
----- Nitrogen
5X
.50v
Potential vs DHE
1.0v

Fig. 149

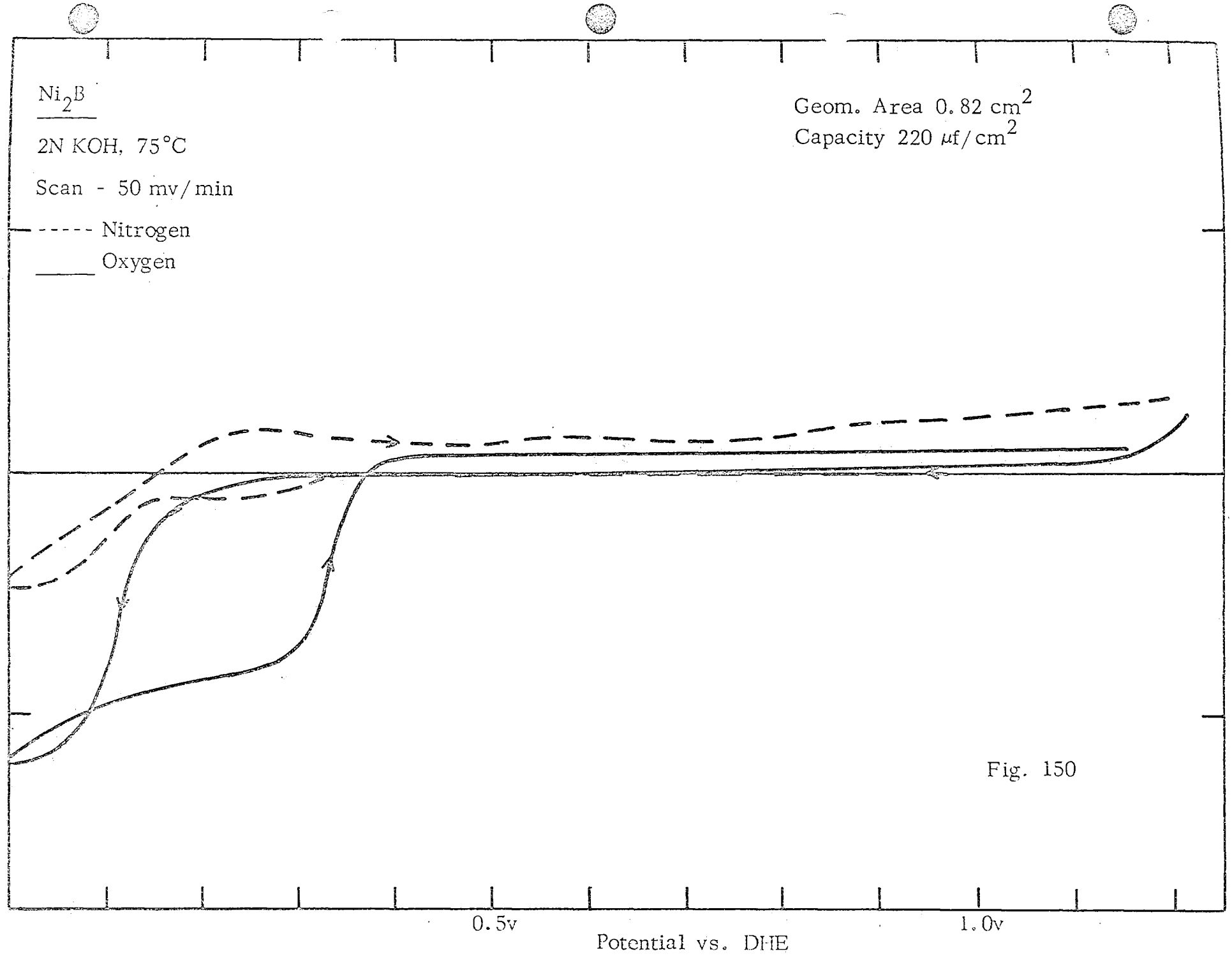
Current
Curr. Dens.
+1.0 ma
1.22 ma/cm2
0
-1.0 ma
1.22 ma/cm2
Ni2B
2N KOH, 75°C
Scan - 50 mv/min
----- Nitrogen
_____ Oxygen
Geom. Area 0.82 cm2
Capacity 220 μf/cm2
0.5v
1.0v
Potential vs. DHE

Fig. 150

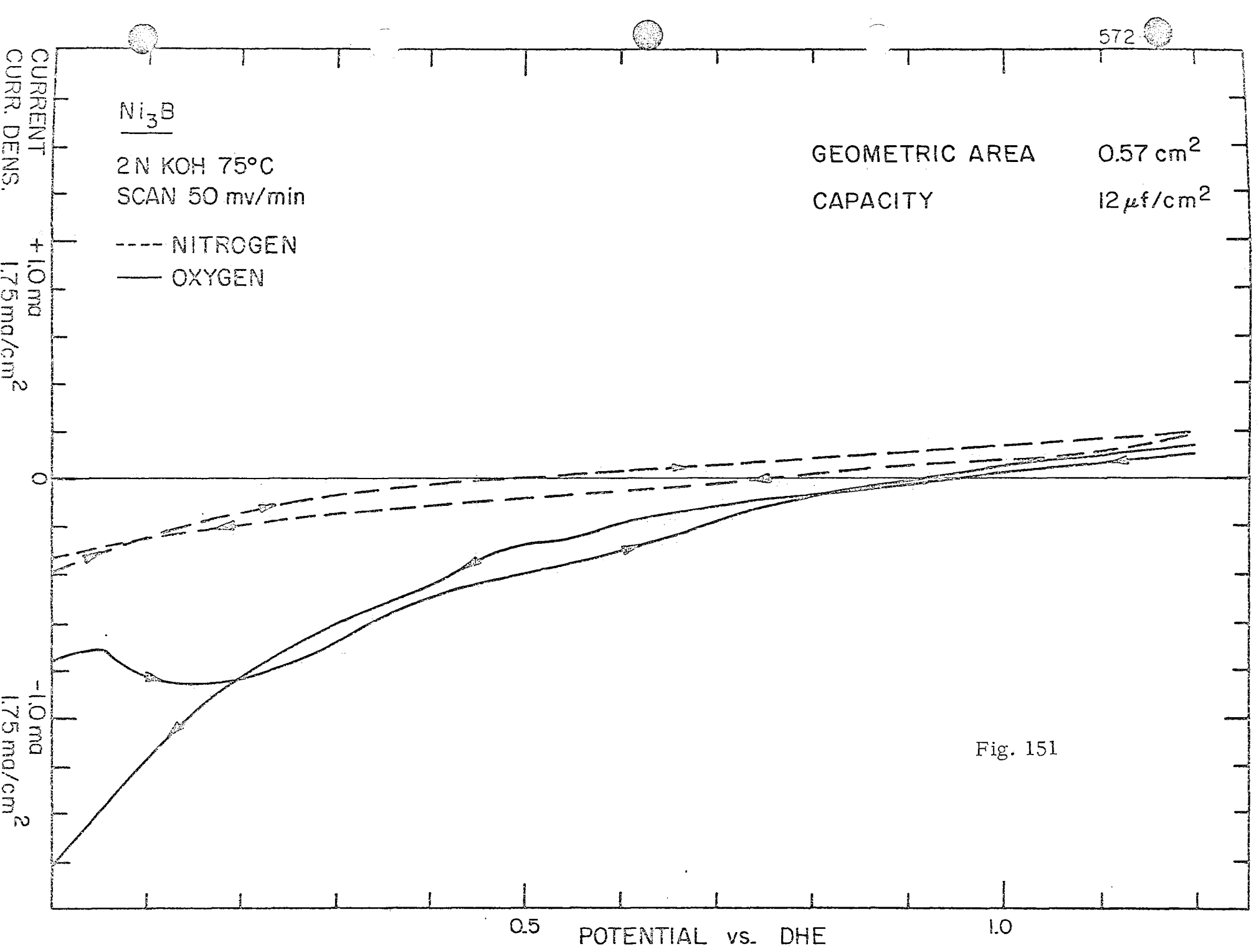
Ni_3B
2 N KOH 75°C
SCAN 50 mv/min
---- NITROGEN
—— OXYGEN
GEOMETRIC AREA 0.57 cm^2
CAPACITY 12 $\mu f/cm^2$
CURRENT
CURR. DENS.
+1.0 ma
1.75 ma/cm^2
0
-1.0 ma
1.75 ma/cm^2
0.5
POTENTIAL vs. DHE
1.0

Fig. 151

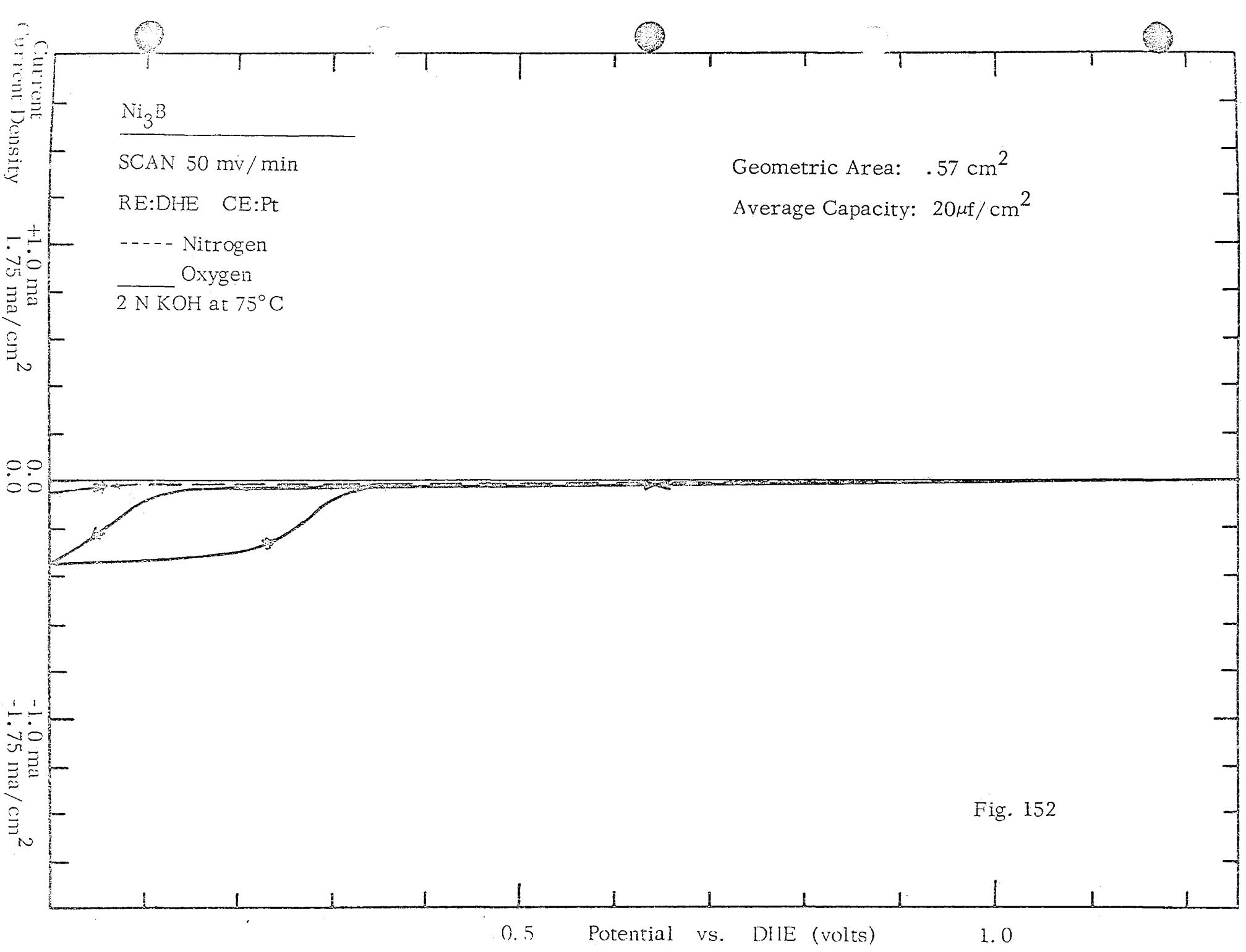
Current Density
+1.0 ma
1.75 ma/cm2
0.0
0.0
-1.0 ma
-1.75 ma/cm2
Ni3B
SCAN 50 mv/min
RE:DHE CE:Pt
----- Nitrogen
_____ Oxygen
2 N KOH at 75°C
Geometric Area: .57 cm2
Average Capacity: 20μf/cm2
0.5
Potential vs. DHE (volts)
1.0

Fig. 152

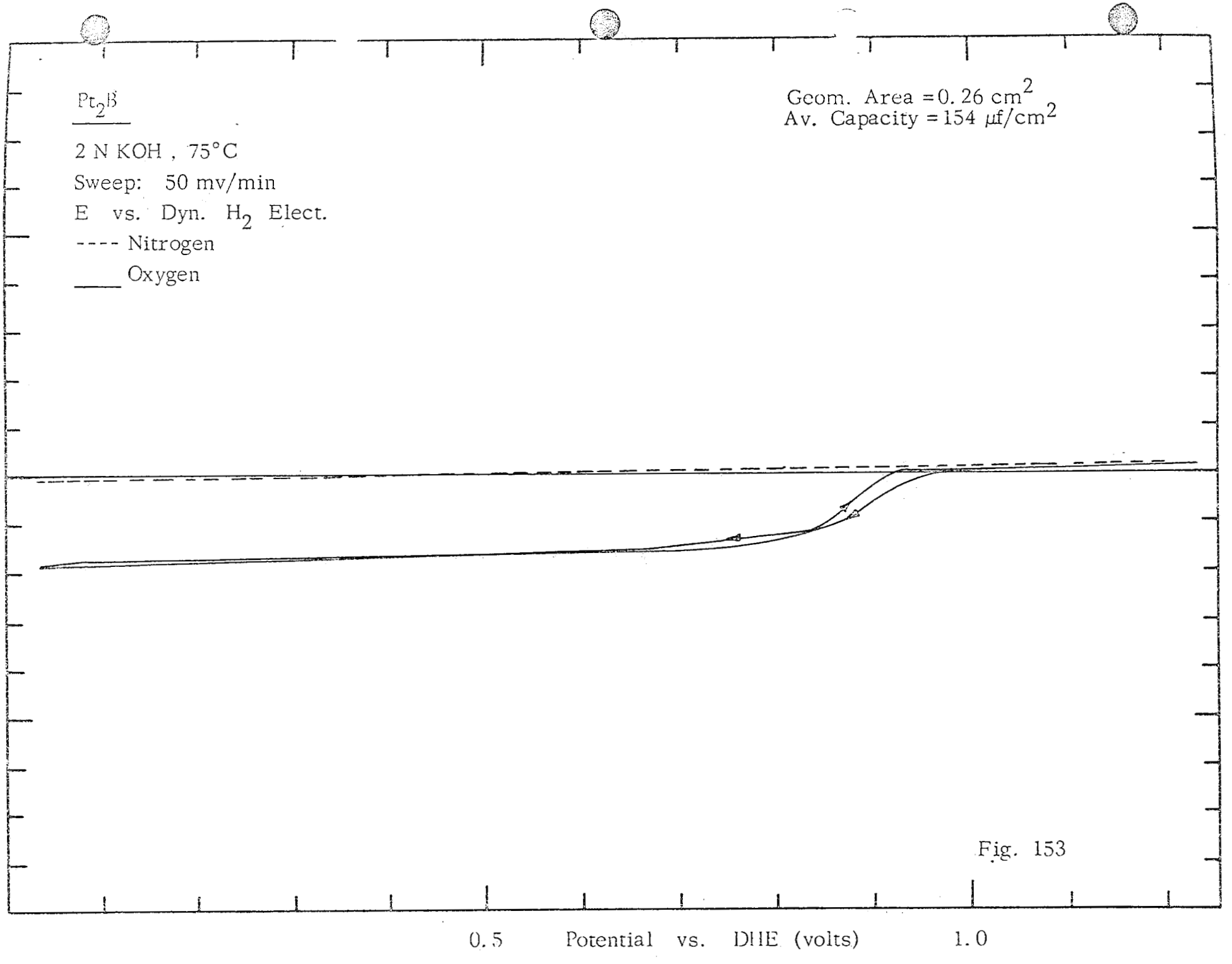
Pt2B
2 N KOH , 75°C
Sweep: 50 mv/min
E vs. Dyn. H2 Elect.
---- Nitrogen
____ Oxygen
Geom. Area = 0.26 cm2
Av. Capacity = 154 μf/cm2
+1.0 ma
0
- 1.0 ma
0.5
Potential vs. DHE (volts)
1.0

Fig. 153

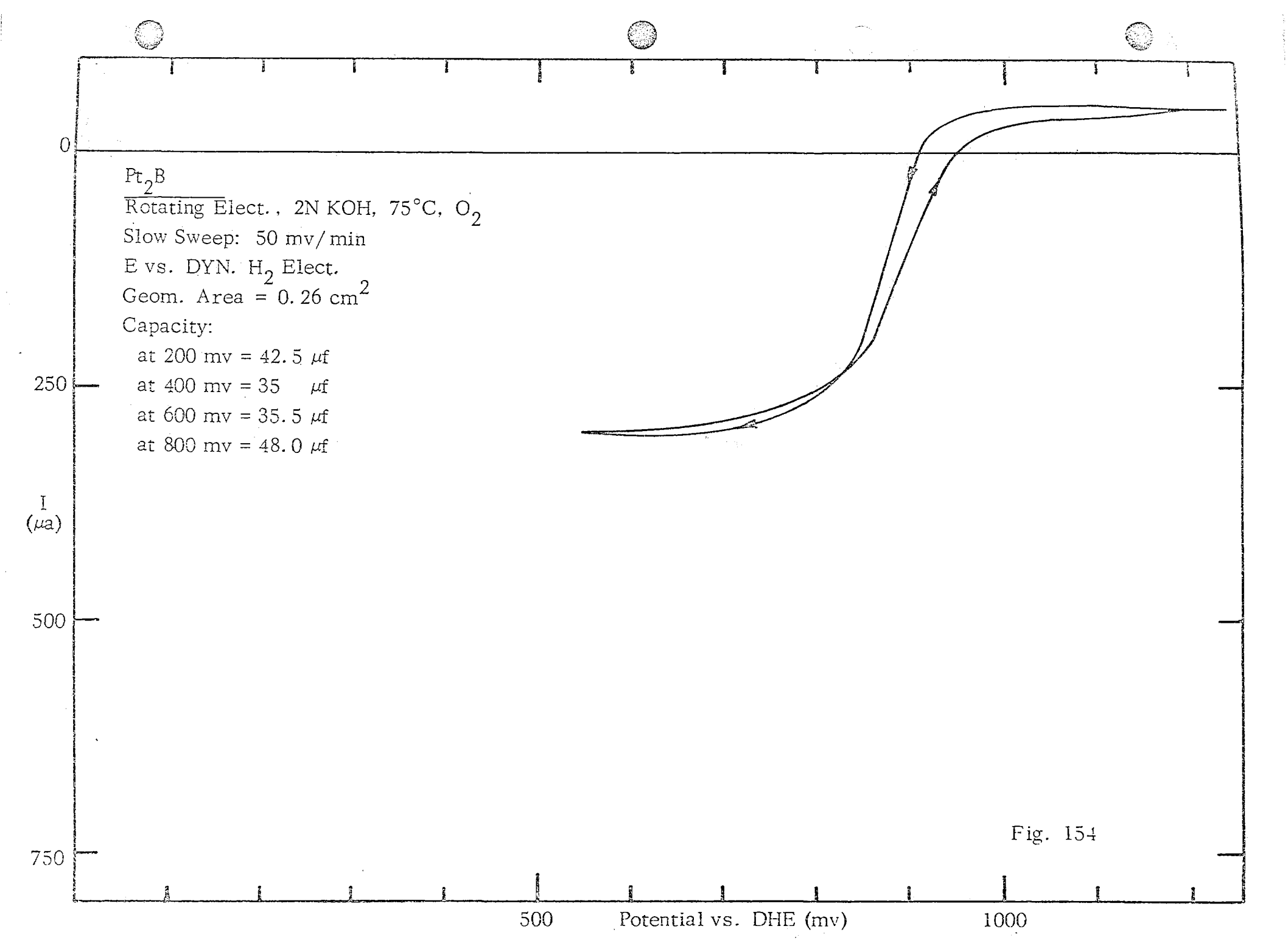
0
250
500
750
I
(μa)
Pt2B
Rotating Elect., 2N KOH, 75°C, O2
Slow Sweep: 50 mv/min
E vs. DYN. H2 Elect.
Geom. Area = 0.26 cm2
Capacity:
at 200 mv = 42.5 μf
at 400 mv = 35 μf
at 600 mv = 35.5 μf
at 800 mv = 48.0 μf
500
Potential vs. DHE (mv)
1000

Fig. 154

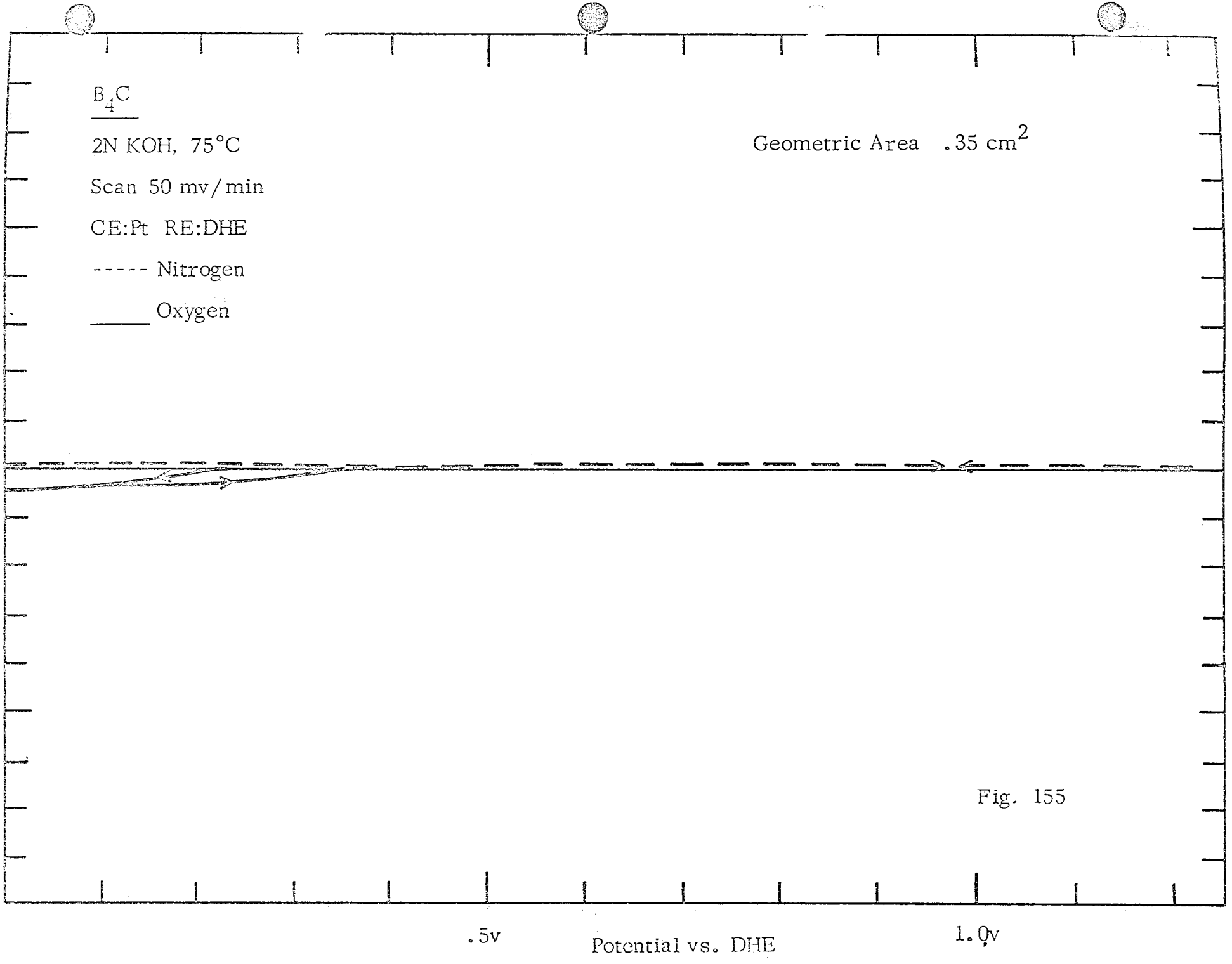
Current
Current Dens.
+1.0 ma
+2.84 ma/cm2
0.0
-1.0 ma
+2.84 ma/cm2
B4C
2N KOH, 75°C
Scan 50 mv/min
CE:Pt RE:DHE
----- Nitrogen
_____ Oxygen
Geometric Area .35 cm2
.5v
Potential vs. DHE
1.0v

Fig. 155

APPENDIX B

METALLURGICAL CHARACTERIZATION OF INTERMETALLIC COMPOUNDS

The extent to which a particular electrode sample is actually made up of a given intermetallic compound can be determined by metallographic analysis. In many cases a small amount of a second phase - either a metallic solution or an intermetallic compound - may be present in a particular sample, but the sample usually contains 90% or more of the compound to be tested.

In metallographic preparation the sample is ground flat through a series of progressively finer SiC grit papers. It is then fine-polished on Microcloth wheels using either diamond pastes or alumina slurries, depending on the hardness of the particular compound. Next, the sample is etched to delineate the actual metallographic structure.

Due to the large number of elements involved in the synthesis of these intermetallic compounds, there is no general etchant which is applicable to all compounds. Instead, each compound must be treated separately, and a suitable etchant must be found for each. This is generally based upon the elements and the particular amount of each metal in the compound.

Representative photomicrographs of some of the intermetallic compounds studied in this program are given below. A general description of the compound, its etchant, and its heat-treatment (if any) accompanies each photomicrograph.

Of the eighteen samples shown below, only three show any significant amounts of second phase, viz. Mo_3Pt, Ni_3B, and $MoNi_4$. The reasons for the presence of the second phase are included with the description of the particular photomicrograph. The remainder are almost all uniformly single phase in nature. With proper melting procedure (so that there are no significant weight losses) and adequate heat treatment times and temperatures (for proper homogenization), single phase intermetallic compounds are usually attained.

AB_2 Stoichiometry (From 1st Quarterly Report)

Sample No. 572-25

$TaPt_2$ (c.p. orthorhombic phase) 150X.

Electrolytically etched in 20% HCl solution at approximately 3v (a.c. source) with Pt electrode.

The compound forms according to a congruent reaction. Due to small losses of Pt, a small amount of the compound TaPt has formed along the grain boundaries of $TaPt_2$.

Fig. 1

AB_3 Stoichiometry (From 1st Quarterly Report)

Sample No. 572-31

$TiPt_3$ ($AuCu_3$ - type, $L1_2$ structure) 100X.

Electrolytically etched in 20% HCl solution at approximately 3v (a.c. source) with Pt electrode.

The compound forms according to a congruent reaction. Extremely small precipitate particles of TiPt are seen, possibly due to some loss of Pt during melting.

Fig. 2

AB_3 Stoichiometry (From 1st Quarterly Report)

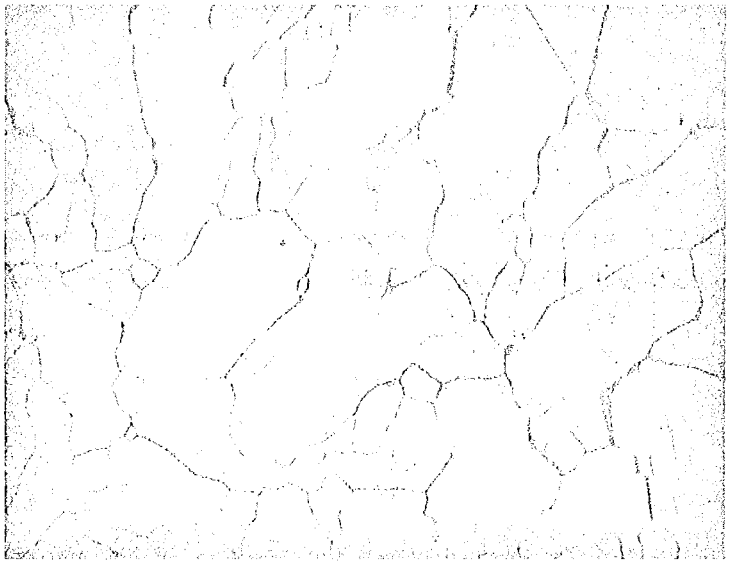

Sample No. 572-29

$TaPt_3$ (12 lsh stacking type; DOa structure) 100X.

Electrolytically etched in a 20% HCl solution at approximately 3v (a.c. source) with Pt electrode.

This compound forms according to a congruent reaction, and is entirely $TaPt_3$.

Fig. 3

AB_3 Stoichiometry (From 1st Quarterly Report)

Sample No. 572-17

$NbNi_3$ ($TiCu_3$ - type, orthorhombic structure) 50X.

This photomicrograph was taken under polarized light, as chemical etching seemed ineffective.

This compound forms according to a congruent reaction, and is entirely $NbNi_3$.

Fig. 4

AB_3 Stoichiometry (From 1st Quarterly Report)

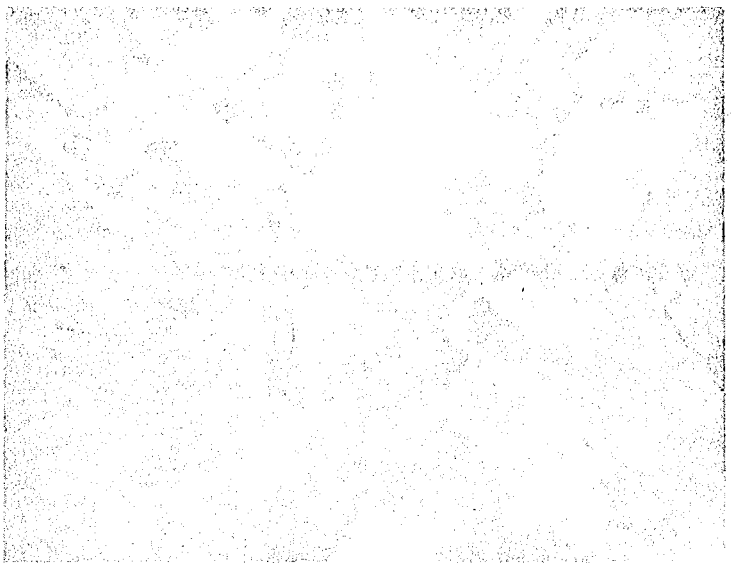

Sample No. 572-21

$TiNi_3$ (DO_{24} structure) 75X.

Chemically etched in 15 parts HCl, 5 parts HF, 5 parts HNO_3, and 15 parts glycerol. Photomicrograph taken under polarized light.

This compound formed according to a congruent reaction. The sample is almost entirely $TiNi_3$, except for minute particles of TiNi, or the Ni solid solution phase.

Fig. 5

Interstitials (From 1st Quarterly Report)

Sample No. 572-30

Ni_3B (DO_{11} structure) 250X.

Chemically etched in 50 parts HCl, 5 parts HCl, and 25 parts H_2O.

During arc-melting, large losses of boron were noted. The resultant sample is therefore a two-phase alloy, consisting of primary dendrites of Ni_3B, plus a eutectic mixture of Ni_3B and Ni solid solution.

Fig. 6

A_3B Stoichiometry

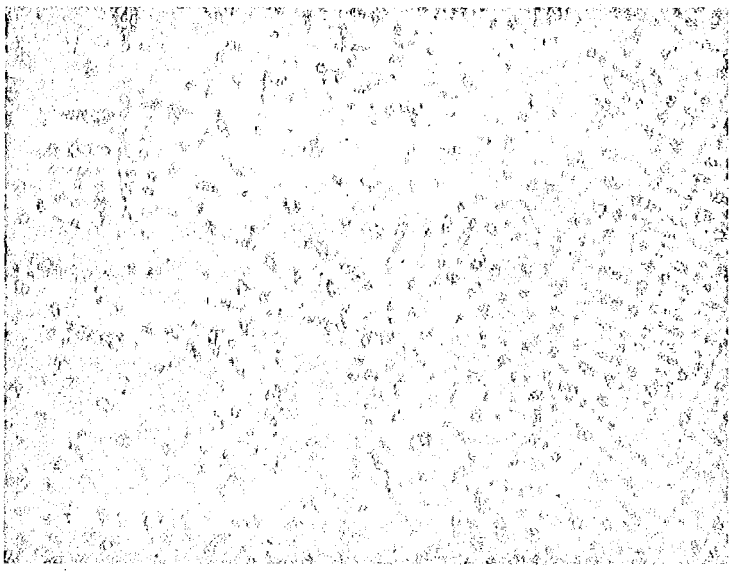

Sample No. 572-55

Mo_3Pt (β - W type, A15 structure) 85X.

Chemically etched in 5 grams $CuSO_4$, 10 cc NH_4OH, 20 cc H_2O.

The β-W-type compound, based on Mo_3Pt, actually forms peritectically at 1650°C at approximately 16 atomic % Pt. This particular sample was made at a composition of 25 atomic % Pt, and heat-treated in vacuum at 1600°C for 40 hours. The actual sample consists of primary grains of the β-W phase (Mo-16 atomic % Pt), plus a mixture of the β-W and the epsilon (MoPt) phases.

Fig. 7

A_2B Stoichiometry

Sample No. 572-62

Ti_2Cu ($MoSi_2$ - type, C11 b structure) 75X.

Chemically etched in 5 parts HNO_3, 5 parts HF, 40 parts H_2O.

Ti_2Cu forms peritectically at 990°C. This sample was heat-treated in an evacuated quartz cylinder (10^{-5} mm Hg) at 800°C for 160 hours; it is virtually all Ti_2Cu.

Fig. 8

AB Stoichiometry

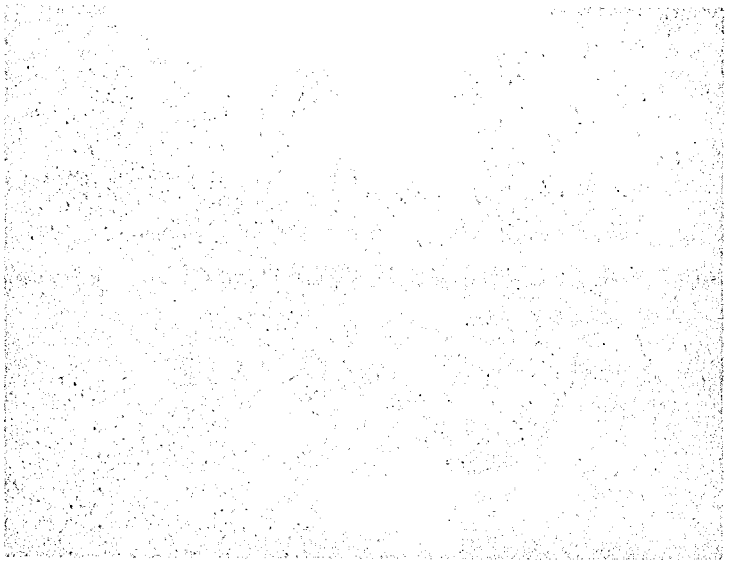

Sample No. 572-61

TiCo (CsCl type; Be structure) 100X.

Chemically etched in 10 parts HNO_3, 10 parts HF, 10 parts glycerin, and 1 part H_2O.

The reaction according to which TiCo forms is not definitely known. This sample was heat-treated at 800°C for 160 hours in an evacuated quartz cylinder (10^{-5} mm Hg). The small particles of second phase precipitate may be Ti_2Co, due to a small weight loss of CO during arc-melting.

Fig. 9

AB Stoichiometry

Sample No. 572-59

NiAl (CsCl type, B2 structure) 50X.

Chemically etched in 25 parts HCl, 5 parts HNO_3, and 10 parts H_2O.

The compound forms according to a congruent reaction. The sample is entirely NiAl.

Fig. 10

AB Stoichiometry

Sample No. 572-73

CoAl (CoAl type, B2 structure) 75X.

Chemically etched with 25 parts HCl, 10 parts H_2O, 5 parts HNO_3, 1 part HAc.

The compound is formed according to a congruent reaction. The sample is entirely CoAl.

Fig. 11

AB Stoichiometry

Sample No. 572-38

MoPt (Hexagonal close-packed structure) 100X.

Electrolytically etched in 20% HCl solution at approximately 3v (a.c. source) with Pt electrode.

The compound forms according to a congruent reaction. The sample is entirely MoPt.

Fig. 12

AB_3 Stoichiometry

Sample No. 572-48

$CoPt_3$ ($AuCu_3$ type, Ll_2 structure) 50X.

Electrolytically etched in 20% HCl solution at approximately 3v (a.c. source) with Pt electrode.

This compound forms according to an ordering reaction at 750°C from the Co-Pt solid solution of this composition. After melting, the sample was heat-treated at 700°C, 66 hours, in an evacuated quartz cylinder (10^{-5} mm Hg). The sample is entirely $CoPt_3$.

Fig. 13

ABn, n > 3 Stoichiometry

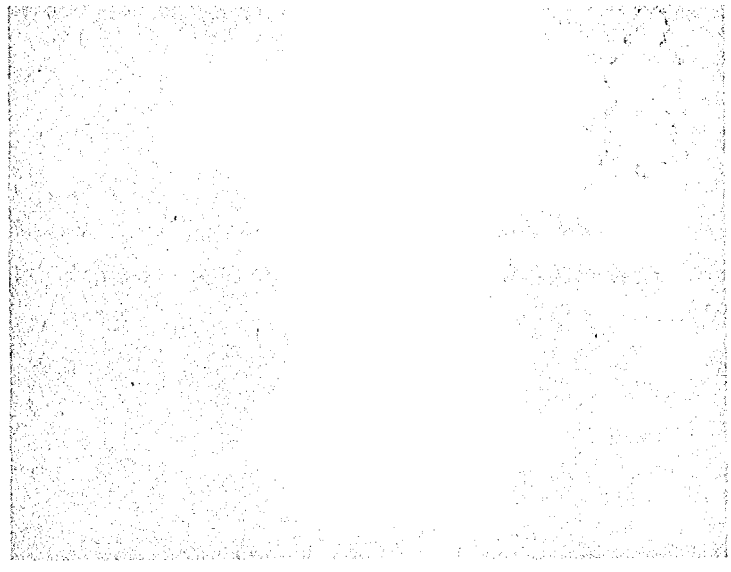

Sample No. 572-49

$MoNi_4$ (Face-centered tetragonal superstructure) 200X.

Chemically etched.

The compound forms according to a peritectoid reaction at 840°C. The melted sample was heat-treated in an evacuated quartz cylinder (10^{-5} mm Hg) at 700°C for 66 hours. The heat-treatment was insufficient to transform the as-melted material entirely to the actual compound, and the sample is most likely a mixture of $MoNi_4$ and Mo solid solution.

Fig. 14

Solid Solutions

Sample No. 572-44

Ta - 66.7 atomic % V (TaV_2) 50 X

Chemically etched with 10 parts HF, 10 parts HNO_3, 20 parts glycerin.

At elevated temperatures, Ta and V form a complete series of solid solution alloys. At the composition TaV_2, the alloy orders below 1320°C to form a compound with a Laves phase ($MgCu_2$-type) structure. The above photomicrograph shows that particular composition in its solid solution state.

Fig. 15

Solid Solution

Sample No. 572-33

Co - 33.3 atomic % Ni (Co_2Ni) 50X.

Chemically etched.

Co and Ni form a complete series of solid solution alloys. This sample is an alloy corresponding to the composition 66.7 atomic % Co, 33.3 atomic % Ni.

Fig. 16

Interstitials

Sample No. 572-39

Ni_2B ($CuAl_2$ type, C16 structure) 100X.

Chemically etched with 50 parts HCl, 5 parts HNO_3, 25 parts H_2O.

The compound is formed according to a congruent reaction. The sample is primarily Ni_2B with some small amounts of Ni_3B at the grain boundaries due to boron loss during melting.

Fig. 17

Ternary compound
AB Stoichiometry

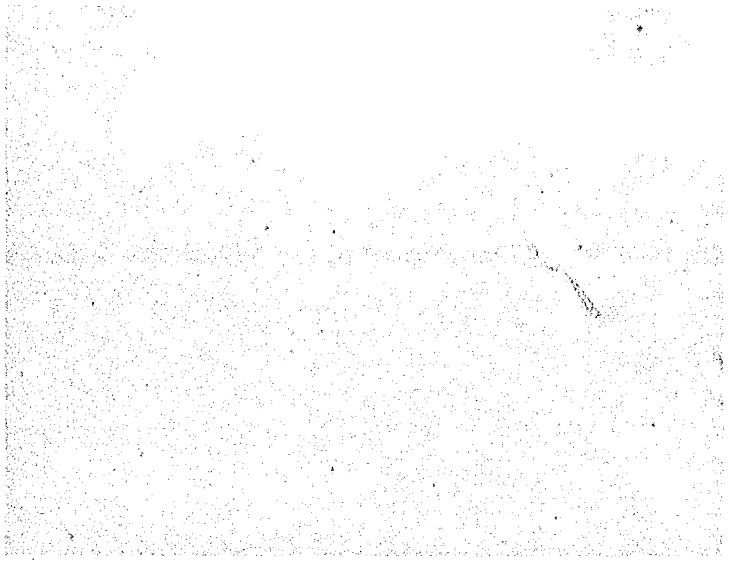

Sample No. 572-72

$(Co_{.67}Ni_{.33})Al$ (CsCl type, B2 structure) 75X.

Chemically etched with 5 parts HNO_3, 25 parts HCl, 1 parts HAc, 10 parts H_2O.

This compound is based upon CoAl and NiAl which are mutually soluble in one another, i.e., Co and Ni can readily substitute for one another. No second phase was present in the sample.

Fig. 18